The Response of Textile Composites Subjected to Elevated Loading Rates

by

Brian Patrick Justusson

A dissertation submitted in partial fulfillment
of the requirements for the degree of
Doctor of Philosophy
(Mechanical Engineering)
in The University of Michigan
2015

Doctoral Committee:

Professor Anthony M. Waas, Chair
Associate Professor Samantha Daly
Associate Professor Veera Sundararaghavan
Assistant Professor Mark R. Pankow, North Carolina State University
Chian-Fong Yen, United States Army Research Laboratory

To Karen and Jerald Justusson

ACKNOWLEDGEMENTS

I would like to express my gratitude toward a number of people who contributed to the completion of this work. In particular, Prof. Waas, for his support throughout the years. Additionally, I am appreciative of the guidance of Mark Pankow and Chian-Fong Yen. I would also like to thank Prof. Samantha Daly and Prof. Veera Sundararaghavan for serving on my committee.

I wish to acknowledge the assistance I have received from Composite Structures Lab members past and present, and in particular, the mentorship of Christian Heinrich, Paul Davidson, and Pavana Prabhakar. My contemporaries in the group, including Pascal Meyer, Dianyun Zhang, Royan D'mello, Zach Kier, Cyrus Kozstowny, and Lucas Hansen offered great advice and set high bars for quality research. I am also thankful to the various experimentalists who worked and trained in the lab including Solver Thorsson, Jaspar Marek, Sunil Pai, Stewart Boyd, and Amit Salvi.

The University of Michigan staff of Terry Larrow, Tom Griffin, Dave McLean, Aaron Borgmann, Eric Kirk, Denise Phelps and Cindy Enoch provided the technical and logistical support needed to create an agile and highly responsive experimental environment. The United States Army Research Laboratory staff of Jian Yu, Ashiq Quabili, Brandon McWilliams, Ryan Karkainnen, and Mike Neblitt offered tremendous insight into textile composites and experimental techniques. I wish to thank Prof. Steve Nutt, Lessa Grunnenfelder, Nik Kar, Micahel Asfaw, and Chris Fischer of the University of Southern California for teaching me the manufacturing and NDE side of composites.

I would like to thank my mom and dad (Karen and Jerry Justusson) as well as my brothers (Adam, Kevin, and Brad Justusson) for their support through this entire process.

Finally, I would like to thank the United States Army Research Laboratories for their financial support of this effort via ORISE and ARO.

TABLE OF CONTENTS

CHAPTER

LIST OF FIGURES

Figure

LIST OF TABLES

Table

LIST OF APPENDICES

Appendix

ABSTRACT

Response of Textile Composites Subjected to Elevated Loading Rates

by

Brian Justusson

Chair: Anthony M. Waas

The United States military is involved in a number of peacekeeping and combat operations throughout the world. In an effort to increase the deployability and agility of the military, a number of novel technologies are being developed. Lightweight combat vehicles have relied on thick structural members, typically made of metallic materials, to defend against specific threats including Improvise Explosive Devices (IEDs) and live fire munitions. While these techniques have proven successful in the past, the weight considerations greatly affect the mobility of these vehicles. Modern armoring techniques have been developed that include the use of Fiber Reinforced Polymer Composites (FRPCs) that offer high structural rigidity while reducing the weight of the vehicle. Because traditional composite laminates suffer from delamination which does not allow the material to reach its full mechanical performance, a new class of 3D composite materials, referred to as 3D textile composites, have been developed. 3D Textile composites involve the interweaving of fiber yarns in a number of preforms to achieve a desired mechanical performance. In this thesis, the high strain rate tensile response of 3D textile composites is addressed. Traditional 1-dimensional high strain rate tensile testing of composite materials is used to understand the failure mechanics of a single fiber tow and to develop constitutive models that are subsequently used to explain the results of textile composites under single and multi-axial load states at quasi-static and high rates of loading. Plain woven textile composites are subjected to shock loading in a shock tube facility to produce biaxial tensile load states. The deformation response is measured using digital image correlation. Experimental results are used as motivation to construct finite element models, including different length scales to understand and explain the observed deformation response and failure mechanics of textile laminates.

CHAPTER I

Introduction

1.1 Motivation

With the United States Military engaged in a number of peacekeeping and combat operations throughout the world, the Department of Defense is actively seeking to increase the agility and deployability of its vehicles, land, water, and aerial based, through the use of advanced materials. While many unmanned vehicles have been developed for aerial operations such as UAVs, it is sometimes necessary to have active combat members within the areas of concern. To minimize the threat to these military personnel, light combat vehicles, such as that shown in Figure 1.1, are often the first line of defense between them and specific threats. When mobilized, servicemen and women are faced with specific threats from gunfire and Improvised Explosive Devices (IEDs). In order to minimize the threat, the Department of Defense spends millions annually developing new armoring techniques.

One such such way of improving deployability and agility of these light combat vehicles is the reduction of weight. Typical armoring techniques rely on using thick, steel members to prevent attacks. While this technique has proved reliable against gunfire, the IED threat has not been sufficient addressed due to the lack of energy absorption and dissipation by the steel members and also due to the presence of significant shrapnel. In order to reduce the weight, novel armoring techniques must

Figure 1.1: A typical light weight combat vehicle used by the United States Military (photo courtesy of CF Yen)

be developed. One such way is through the incorporation of Fiber Reinforced Polymer Composites (FRPCs). FRPCs have higher specific strengths than steel or aluminum, and could provide significant reduction in weight to military vehicles, while having better mechanical performance to specific threats.

Outside of military applications, there is continued growth of composite material use in the aerospace industry, sporting goods, automotive, and other industrial sectors (such as in wind energy systems), however, full adoption has been slow outside of the aerospace industry. In order for mass implementation to occur, a detailed understanding of the deformation response and failure is needed. Typical laminated composites fail in the delamination mode, which greatly reduces the structural integrity. This mode of failure is critical to mass implementation of composite materials and the delamination mode must be limited. Various techniques have been developed such as stitching, z-pinning, and the development of textile composites known as 2D in plane weaves such as plain and 5-harness satin to defeat the delamination mode.

Another class of textile composites are made by 3D weaving which has shown great promise by using mechanical binding through the thickness to prevent delamination from occurring and propagating rapidly through the material. This technology came from the industrial revolution where looms were used to make textiles and use of the looms for production of composites requires little alterations from their original manufactured state. These integral woven materials, known as preforms, can be woven in one process to include a series of warp and weft fibers with a reinforcing fiber. This preform, once removed from the loom, is then infused with a matrix material using Vacuum Assisted Resin Transfer Modeling (VARTM) to create a structural panel. 3D composites have been shown to have increased mechanical performance [90] and the ability to prevent the spread of delamination or completely eliminate this mode altogether [80] [20]. Hybridization via incorporation of different yarns or fiber tows can result in a number of increases in mechanical performance including increased energy absorption [12] [62] and improved tensile properties characterized by increases in failure strain [47]. Hufenbach et. al. have shown hybrid 3DWC can be tailored for specific structural performance [39]. While 3DWC show great promise as structural materials, design of internal microstructure is much more difficult due to lack of proper predictive tools and a limitless designspace. In order to design these microstructures effectively, a clear understanding of yarn failure is needed. An example of several different 3DWC architectures is shown in Figure 1.2 in which multiple yarns have been used in a traditional Z-fiber architecture.

When designing composite structures, the allowables are generally dictated by the compressive strength given that it is the lesser of the tensile and compressive strengths, however, in certain loading and service configurations, it is very important to maximize the tensile strength. An example of this occurs during blast and ballistic loading in which a projectile or blast wave impacts a structure. While the structure undergoes a large degree of multiaxiality with respect to loading and experiences high shear stresses, the limiting factor for full penetration is the tensile strength of the outer surface of the structure as seen in Figure 1.3.

(a) A carbon panel with a glass fiber z-yarn (b) An all glass plate

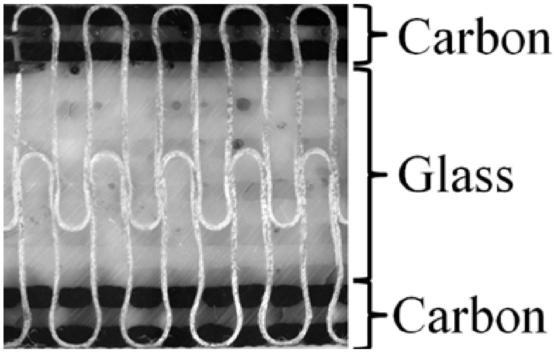

(c) A symmetric carbon, glass, carbon panel with a kevlar z-yarn (d) An assymetric carbon and glass panel with a kevlar z-yan

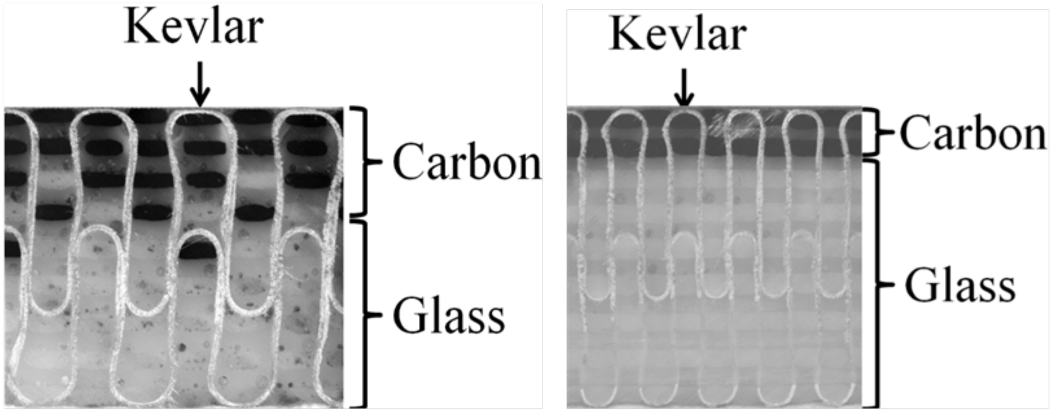

(e) A functionally graded carbon and glass panel with a kevlar Z-yan (f) A thick assymetric carbon and glass panel with a kevlar z-yan

Figure 1.2: Examples of various 3DWC architectures woven by the United States Army Research Laboratory (photos courtesy of Mark Pankow)

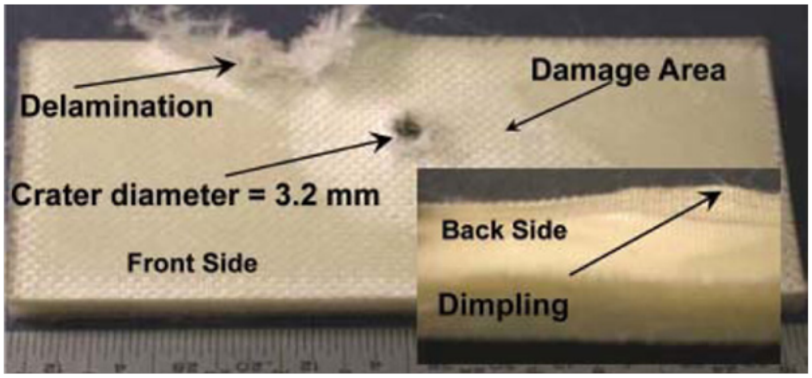

Figure 1.3: A composite panel subjected to ballistic impact (photo courtesy of CF Yen)

To further complicate this problem, depending on the type of projectile and/or the strength of a blast, large strains accumulate in the sample over a very short time duration (microseconds) resulting in appreciably high strain rates. For this reason, it is necessary to further understand composite materials, and in particular textile composites, failing at high tensile strain rates.

	Testing Type		
Applicable Strain Rates (/s)	**Compression**	**Tension**	**Shear and Multiaxial**
<0.1		Conventional Load Frame	
0.1-100		Special Servohydraulic Frames	
0.1-500	Cam Plastomer & Drop Test		
10-1000			Torsional Impact
100-1,000		Hopkinson Bar In Tension	
100-10,000	Hopkinson Bar in Compression		Hopkinson Bar in Torsion
10,000-100,000	Taylor Impact Test	Expanding Ring & Flyer Plate	Double-notch Shear & Punch Test
>100,000			Pressure-shear Plate Impact

Table 1.1: Types of testing techniques for a range of strain rate testing (modeled from ASM Handbook [71])

Table 1.1 shows a number of different tests that are widely used and accepted for high strain rate testing for compression, tension, and shear. Many research efforts have been conducted on the compressive response because of its importance in design but also because the Hopkinson bar test in compression can be used over a wide range of strain rates relative to the equivalent tensile and shear configurations. With respect to the tensile response of materials using traditional load frames in concert with Hopkinson bar in tension, a wide range of strain rates can be examined and have been studied by researchers in the past. A key issue that remains is the interpretation of the experimental data which is best exemplified by the great disparity amongst the reported tensile response of composite materials under high strain rate.

Common fibrous material systems that have been investigated are glass, carbon, and kevlar, and the results are inconclusive and dependent on the material system. In general though, the glass response has been more consistent than the carbon. In a review paper by Jacob et al. [43] the strain rate effects on the mechanical properties of polymer composite materials were examined and the results seemed to indicate no real agreement amongst many researchers over decades of time. (Note that in this introduction, the references are specific to the review paper by Jacob and years given distinguish between which experiment is discussed) Davies and Magee (1975, 1977) reported an increase in tensile strength with increasing loading rate in a glass/polyester system, however, glass and epoxy have been studied in greater detail. Rotem and Lifshitz (1976), Okoli and Smith (1999-2001), Armenakas and Sciamarella (1973), Staab and Gilat (1995, 1993) have all reported an increase in tensile strength of glass and epoxy. Hayes and Adam (1982) observed a general strain rate insensitivity while Kawata et al. (1981, 1982) reported that the tensile strength decreased with an increase in strain rate.

While the majority of work for glass tends to suggest strain rate hardening, the results for carbon are less clear. Groves et al.(1993), Kawata et al. (1982), Tzeng and Abrahamian (1998), and Cazeneuve and Maile (1985) each reported an increase in tensile strength as a function of increasing strain rate. Daniel et al. (1978, 1995), Chamis and Smith (1983), Daniel and Liber (1976), Harding and Welsh (1984) all observed what they described as rate insensitivity. Finally, Hayes and Adams reported strain rate softening (1982). Of particular note, many of these efforts failed to achieve strain rates that are comparable to those observed in metallic samples with many significantly less than 400/s, but to understand these effects further, a careful analysis is needed of each researchers work and considerations must be made with respect to available evaluation equipment.

Subsequent efforts have been used to study the validity of these results. Eskandari and Nemes [15] performed high strain rate tensile tests on composites, but noted that due to the complexity of their fixture to clamp the sample, traditional Split Hopkinson Tensile Bar (SHTB) analysis, similar to the techniques reported by the previous researchers, would not suffice because a 1D wave assumption is no longer correct. To remedy this, the authors needed to introduce a correction factor or the testing would yield inaccurate results. Gilat et al. [22] studied the high strain rate response of carbon fiber composites and noted a discrepancy between between the strain measurements taken from the strain gage bonded directly to the sample and the traditional analysis with the traditional analysis yielding a strain that is nearly 50% higher than that measured in the sample. These two efforts, combined with the inconsistencies in the literature begin to underscore the need to understand how applicable traditional testing techniques are to composite materials. For this reason, there is a clear need to develop, modernize, and create novel testing techniques for composite materials to identify how composite materials, and in particular yarns, deform, damage, and fail under high rates of loading.

1.2 Research Objectives

Design tools for textile composites are minimal. While certain finite element based codes exist to predict the manufactured state of a textile composite, they typically only give information about the architecture, often in an idealized sense. Softwares such as TexGen or WiseTex can mimic an architecture of a composite, however, in order to not have idealized geometries, significant scripting of the source code is required. Other programs rely on digital fiber links to allow for simulation of the weaving process such as Digital Fabric Mechanics Analyzer (DFMA), but suffer from difficulties of being able to generate usable meshes.

Typical modeling techniques for textile composites can occur on one of three scales exclusively or in concert as a multiscale approach. In general, modeling of textile composites has been identified in the following scales:

1. Microscale - Constituent level modeling of the fiber and matrix - This technique offers the highest degree of fidelity, but is also very computationally expensive. Additionally, it is heavily reliable on having accurate experimental data of the fiber and matrix and may not consider in-situ effects.

2. Mesoscale - Fiber tow and matrix level of modeling - This technique uses homogenized properties of the tow and models it independently of the matrix. This allows for a level of fidelity needed for evaluation of damage evolution. It has high fidelity, but less computationally expensive in comparison to the Microscale

3. Macroscale - Fully homogenized properties - This technique treats the tows and matrix as a single entity with uniform properties throughout. The macroscale does not give information about damage and failure events on lower scales. This technique has lower fidelity and low computational costs.

Because a large design space exists, there needs to be a methodical way to design textile preforms to optimize mechanical response prior to weaving. The goal of this research is to determine if 1D tests can be used to develop failure criteria for a tow that will subsequently be applied to multiaxial loading. More specifically, this research will address a major design consideration for textile composites by determining if a rate dependent constitutive model for a composite yarn can be used as a failure criteria when a composite is subjected to multiaxial loading.

Traditional 1D testing techniques will be used to determine failure laws for the tows. To validate these failure laws for multiaxial situations, novel test methods and techniques will be developed to induce a state of biaxial tension on the crown of a plate subjected to transverse loading. Through the development of a finite element model at the mesoscale, the applicability of the 1D damage and failure laws to multiaxial testing will be assessed.

1.3 Dissertation Outline

The aforementioned research goals will be addressed in the following chapters:

Chapter 2: Material Systems and Quasistatic Mechanical Characterization - This chapter addresses all of the quasistatic mechanical tests that were completed on the project to understand basic material properties. It includes testing of the matrix material in tension and compression and determining the in-situ matrix response. It also motivates the need to test crossplies to determine fiber rupture strengths as opposed to unidirectional composites.

Chapter 3: Development and Validation of a Split Hopkinson Tensile Bar for High Strain Rate Testing - This chapter discusses the development and implementation of the SHTB testing framework that was done for this dissertation. It introduces an Enhanced Split Hopkinson Tensile Bar data analysis technique that incorporates non-contact measurements of the strain time history directly from the sample. Information is provided on how the enhanced technique offers unique insight into a sample as it fails.

Chapter 4: High Strain Rate Tensile Failure of Crossplies - Using crossply glass and carbon samples, high strain rate tensile properties are analyzed. The results of the testing pose a interesting questions regarding the validity of SHTB results with respect to heterogeneous, orthotropic materials.

Chapter 5: Use of a Shock Tube for Generation of High Strain Rate Multiaxial Tensile Stress States - This chapter demonstrates how a shock tube can be used to generate a state of multiaxial tension in the crown of a sample subjected to shock loading. It introduces the shock loading method and discusses how high strain rates can be generated in the sample. A finite element model is developed to show how this test can be used with inverse analysis to determine rate dependent failure.

Chapter 6: Shock Loading of 2D Plain Woven Textiles - This chapter analyzes the high strain rate properties of plain woven textile composites subjected to multiaxial tensile strains. Using the techniques developed in chapter 4, plain woven glass and carbon samples are examined at two different states. As the pressure is increased, so too are the through thickness shear stresses. To combat this effect, a new technique of thinning the samples to cause tensile failure is presented and validated.

Chapter 7: Creation of a Finite Element Model for IM7 Plain Woven Material - This chapter examines how a mesoscale model was developed to predict the tensile response of woven textile composites. Microscopic images are taken to extract geometrical information about the as nested material of a carbon plain weave. A Representative Volume Element (RVE) is developed, and virtually tested to obtain homogenized material properties. Results are compared against experimental data

Chapter 8: Modeling of Shockwave Loading Carbon Plates - Using the model and material properties developed in chapter 7, a global-local model is used with the mesoscale model of the a plain weave to examine multiaxial response. The pressure-time history from the experiment is used as an input to the model to generate tensile failure within the thin section.

Chapter 9: Concluding Remarks - Conclusions and a discussion of recommended future work are presented in this section.

1.4 Unique Contributions in this Dissertation

The orthotropic nature of composite materials make them interesting candidates for high performance applications since they can be designed for a known service state. The high rate tensile failure of textile composites has received relatively little attention throughout literature, and the results show large discrepancies between researchers and techniques and also greatly limits the implementation of composite materials. While repeatability of static tensile testing has difficulties, these effects are exacerbated when moving from the intermediate (0.1/s-100/s) to high strain rate regime(100/s-10,000/s). Traditional high strain rate testing techniques typically offer insight into failure mechanisms, however, there has not been sufficient analysis of these results, and their relation to the composite material microstructure in order to gain a better understanding of the failure mechanics of composites under high tensile straining rates. Therefore, this thesis focuses on some of these aspects and has provided the following unique contributions:

1. Use of modern data acquisition techniques coupled with traditional testing techniques to provide novel insight into tensile failure mechanisms of composites at high strain rates
2. Developed capabilities to use a Split Hopkinson Tensile Bar (SHTB) for uniaxial testing of composites
3. Developed and validated a technique to create a high strain rate multiaxial test
4. Used finite element analysis to better understand the high strain rate mechanics of composite materials. In particular, the response of textile composite plates to high rate flexural loading, including damage development and failure, is addressed in chapter 6, providing a unified modeling approach.
5. Developed predictive tools for design and analysis of textile composites

CHAPTER II

Material Systems and Quasistatic Mechanical Characterization

In this chapter, the material system of interest will be introduced and studied in great detail. Firstly, the properties of the constituents will be presented as determined from literature. Due to variations that occur because of the prescribed curing cycle, a detailed analysis of the epoxy-resin system will be conducted to determine its stress-strain response in tension and compression for the neat epoxy, and the in-situ tensile properties as extracted from a tensile test. Finally, an investigation in the proper technique of employing cross-ply versus unidirectional laminate testing will be presented.

2.1 Constituent Properties from Literature

The material systems of interest for this work are SC-15 matrix, S2 glass fibers and IM7 carbon fibers. IM7 is a widely used carbon fiber for aerospace and military applications, whereas the S2 Glass fiber is preferred to the E-glass fiber because of its superior stiffness and energy absorption/dissipation. SC-15 is a low-viscosity, two-phase toughened epoxy resin consisting of two parts: Part A is a resin mixture utilizing diglycidylether epoxy toughener, and Part B is a cycloaliphaic amin poluoxy-

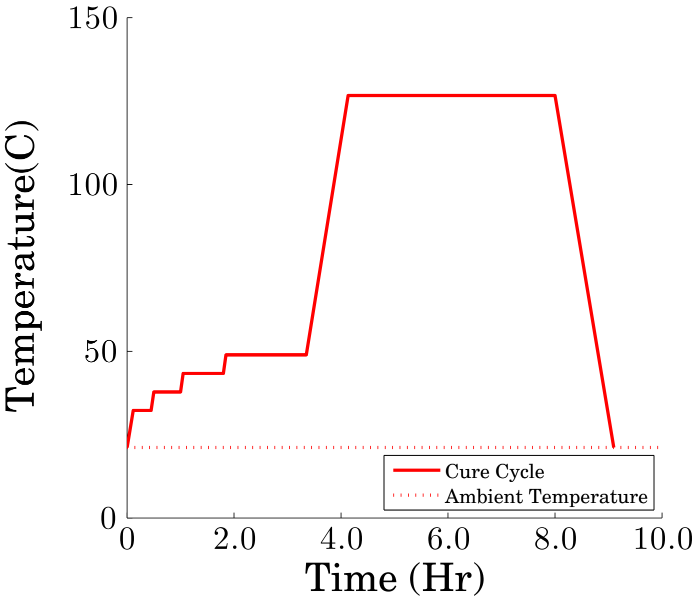

Figure 2.1: Cure cycle used for SC-15 matrix

lalkylamine hardener [136]. In general, SC-15 is shown to have brittle characteristics when subjected to mechanical loading, but is selected because it is particularly well suited for Vacuum Assisted Resin Transfer Molding (VARTM) due to its low viscosity. The composite is typically cured in a two part process that includes an initial cure as well as a post-cure at an elevated temperature to maximize the cross-linking of the polymers. The cure cycle for all the composites listed in this thesis is shown in Figure 2.1. The cure cycle uses a series of ramps instead of a continuous ramp because it has been found previously to have better thermal properties during the cure by the United States Army Research Laboratory (USARL) manufacturing staff.

IM7 is a PAN based fiber with high performance and intermediate modulus in comparison to other commercially available carbon fibers. It can be surface treated with a coating to allow for a number of different textile type applications such as weaving, prepregging, filament winding, braiding, and pultrusion [34]. It is commercially available in a number of different sizes for fibers per tow.

S2 glass is a second generation of S-glass which has higher tensile strength and modulus, lower weight, and better high temperature properties than traditional E-glass [63]. S2 glass has better performance than S1 due to higher silica content. It is commercially available in a number of different forms including yarns with sizing on the fiber, rovings, mat, or chopped fibers.

The properties from literature for each of the constituents are shown in Table 2.1.

Constituent	E_1 (GPa)	E_2 (GPa)	ν_{12}	G_{12} (GPa)	$G_{23}(GPa)$
SC-15 [83]	2.487	2.487	0.35	0.921	0.921
IM7 Carbon Fiber [33]	276.0	15.0	0.279	12.0	5.02
S2 Glass Fiber [33]	114.2	114.2	0.22	46.8	46.8

Table 2.1: Mechanical properties of the fibers and matrix systems used in this research effort

2.2 Matrix Material Testing

Since the mechanical performance of the matrix is dependent on the curing cycle and the information in literature is varied, it was determined that it would be best to measure the properties directly using ASTM standards. To test this, a panel was fabricated and cured into a 50.8 x 50.8 x 0.3175 cm (20 in. x 20 in. x 1/8 in.) sample. From this, both tension and compression samples were extracted via waterjet cutting to the ASTM standard. From the tensile tests, four major mechanical properties were determined: the modulus of elasticity, the ultimate tensile strength, the failure strain, and the Poisson's ratio. The modulus of elasticity was determined by taking the slope of the linear portion of the response. The linear elastic portion of the curve was generally between 0.5% and 1.0% strain. The ultimate tensile strength was determined by the maximum stress experienced by the sample before failure. The failure strain was determined by the average longitudinal strain at failure. The Poisson's ratio was determined by taking the slope of the longitudinal strain versus the transverse strain curve during the elastic loading.

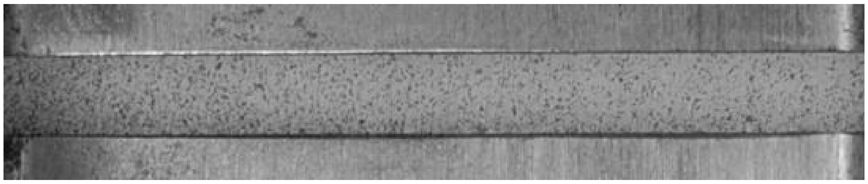

Figure 2.2: Side image showing the applied speckle and cropped raw image for compressive tests of the SC15

2.2.1 Compression Response of Neat Epoxy

Compression tests for the matrix were performed to the ASTM D695 specification [18]. The samples were loaded at a rate of 0.05 in/minute. Strain gauges were not used for this testing because strains beyond the failure strain of the gauges were expected. Instead, a speckle pattern was applied to the side of the sample using Krylon fusion paint. Images were then taken every two seconds using a Nikon D100 digital SLR camera with 4.0+ megapixel resolution. The images were then cropped using a MatLab script and were analyzed using the ARAMIS DIC software [112]. A sample of the raw image is seen in Figure 2.2.

ARAMIS DIC software then calculated the corresponding strain fields. This was used to generate a stress-strain response in compression. The results of the testing for the 5 samples are shown in Figure 2.3. From this figure, the 5 tests show a high degree of agreement in terms of the initial slopes, modulus of elasticity, failure strain and failure strength. While the matrix material is generally brittle, two-piece failure is not observed. When the material is fully compressed, it ultimately develops an instability that results in a shearing response. At this point, the test was stopped the sample was considered to have failed and the failure stress is considered to be the maximum nominal stress.

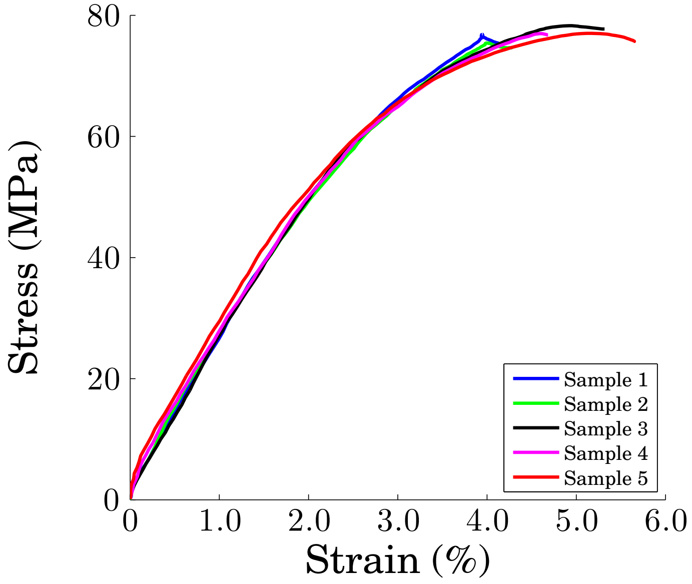

Figure 2.3: A comparison of the response of the 5 tests

2.2.2 Tension of Neat Epoxy

Tensile tests were performed to the ASTM D638 [17] specification; however, strain was measured optically instead of the use of a digital strain gage. Photographs were taken by a Grasshopper camera at a rate of 10 Hz. Load and displacement was also recorded by the DAQ at a rate of 10 Hz. The strain was measured using the commercial software ProAnalyst [123]. From the analysis software, 9 points were selected for analysis. A sample of how the points were selected is shown in Figure 2.4. Three of the points were aligned on the tensile axis in the center of the specimen, and six are selected on the side of the sample. From the center axis, three strains were gathered and averaged to give the total strain in the sample in the longitudinal direction. Additionally, three strains were averaged to get the transverse strain. These measurements are equivalent to what would be measured by the strain gauge. However, since this technique is not limited to a single point, as strain gages are, the strain measured actually covers a broader area of the specimen.

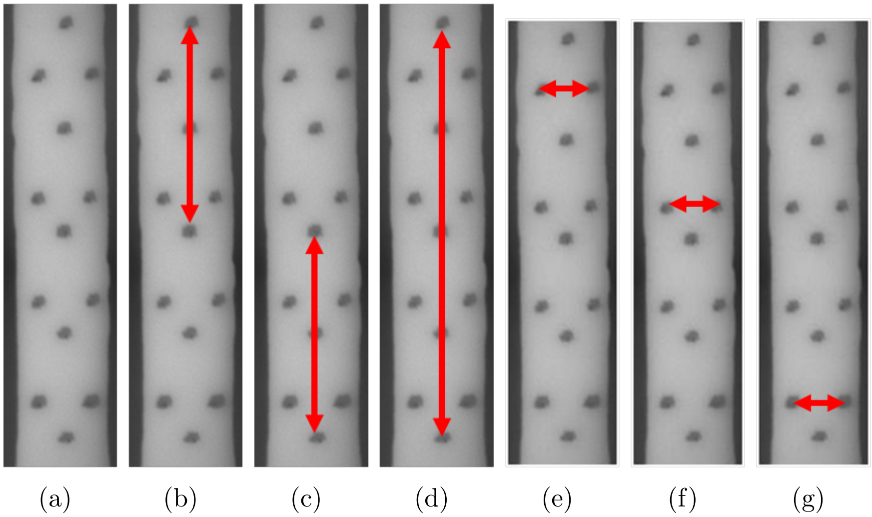
(a) (b) (c) (d) (e) (f) (g)

Figure 2.4: Schematic showing how the 6 different strain measures were taken in the SC-15 Samples

The stress-strain tensile mechanical response of SC-15 is shown in Figure 2.5. The eight samples that were tested until failure are shown in Figure 2.5(a). Of particular interest, the results are fairly consistent in modulus of elasticity and ultimate tensile strength. The modulus was determined to be 2.20±0.18 GPa and the UTS was 58.31±2.24 MPa. The sample generally showed a bilinear response with some pronounced plasticity like effects. Necking however, was not observed. The samples generally failed at strains of less than 5% which demonstrates there is not a particularly high amount ductility. This however, was to be expected as SC-15 is a thermoset plastic. This type of behavior is similar to other matrix materials used in polymer matrix fiber composites. A comparison between the tested material and that of Pankow [83] is shown in Figure 2.5(b).

The results of both the current effort and the results of previously published values for SC-15 are shown in Table 2.2. The work of Pankow was completed using a torsion test and tensile properties were extracted. Additionally, two tests were conducted on SC-15 by Zhou in both flexural testing (2005) [136] and tensile testing (2007) [135]. The modulus of elasticity as determined by the compression test is nearly identical to that of Pankow, however the Poisson's ratio is not. The failure strain is

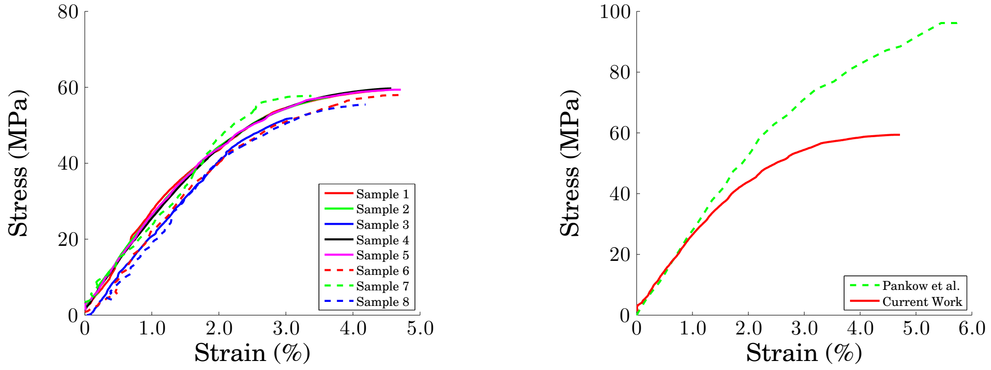

(a) Results of current study for tensile response (b) Average response against previously reported data

Figure 2.5: The stress strain response of the SC-15 for (a) the current work and (b) against previous reported data

perhaps the most interesting of the mechanical data. Both Pankow and Zhou report a failure strain above 6.0% however, in neither compression or tension within this testing protocol achieved strains larger than 6.4%.

The failure strains in the current work are similar to previous data reported by Zhou (2007) but not in earlier data reported by the same author in [136] (2005). Additionally, Zhou reports two failure strengths that differ by as much as 50%. This could be attributed to two possibilities. First, this may be an artifact of the testing. In the work of 2005, the stress-strain behavior was determined by the use of a flexural test, whereas the 2007 work was related to a tensile test. In general, the tensile test mechanical properties are similar to those of the current work. It is possible that deviations in the test setup could lead to improper interpretations of the results. Secondly, the author does not report a curing cycle. The curing cycle has a significant effect on the amount of cross-linking that occurs in the polymer and could ultimately be responsible for differences in mechanical performance.

Reference	Modulus of Elasticity (GPa)	Failure Strength (MPa)	Poisson's Ratio	Failure Strain (%)
Pankow	2.487	110	0.35	6.4
Zhou, et al. (2005)	2.25±0.11	85.0±4.3	n/a	6.0
Zhou, et al. (2007)	2.31±0.12	53.01±2.79	n/a	4.86±0.34

Table 2.2: Results of current SC-15 against previously published data

2.2.3 In-situ Matrix Tensile Response

While the neat epoxy response is important to know, it may not always be the best description of what is occurring in the material itself. This is because the neat epoxy response differs from the epoxy response in the composite due to curing kinetics. The curing processes is affected by a number of parameters and can frequently result in a difference in the mechanical response of the matrix due to induced cure damages and changes the cross-linking density. The resulting matrix properties are termed the in-situ matrix properties. The in-situ matrix response considers all damages and the effects of voids in creating a response that describes properties of the matrix within the material itself. The process by which the in-situ response is determined is described by Ng and Salvi [72].

In this publication, Ng and Salvi show that the in-situ matrix properties can be determined by creating a composite laminate that is $[+45/-45]_s$ and subjecting it to a simple tensile test. Because the fibers are oriented at 45°relative to the axial direction, it loads the matrix in shear. The shear response of a lamina can then be determined and using a stress and strain transformation to the principal material frame, the equivalent uniaxial tensile response can be determined.

The in-situ matrix response is determined by a 5 step process as described by Ng and Salvi [72]:

1. Determine the strain-time history in both the axial and transverse direction
2. Determine the axial stress-strain response of the composite lamina
3. Determine the shear stress-shear strain response of the composite lamina

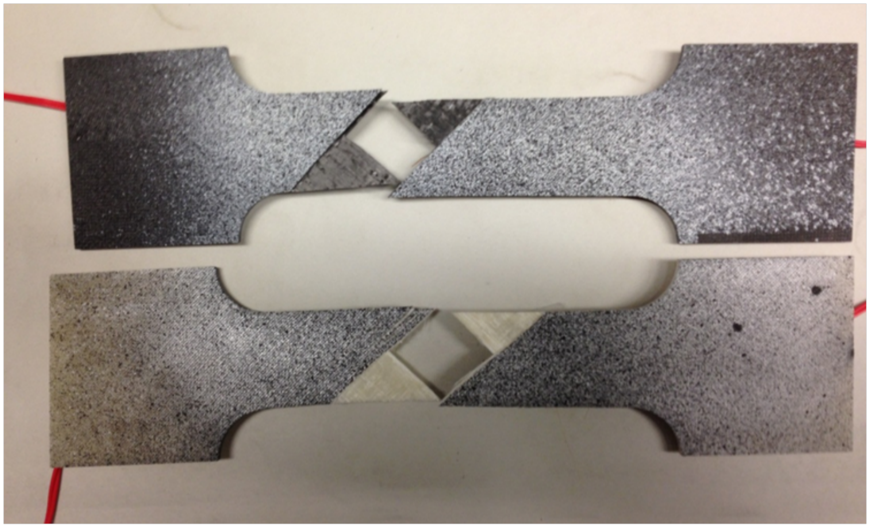

Figure 2.6: Typical failure for in-situ matrix sample

4. Determine the secant modulus versus shear stress response of the lamina
5. Using the expression for the lamina shear modulus in terms of the matrix shear modulus based on the concentric cylinder model for fiber reinforced medium [13], determine the in-situ matrix response

To determine this response, an 8 ply sample was created with a layup of $[+45_2/-45_2]_s$ was created to give a reasonable thickness to the sample. For this experiment, the samples had a thickness of approximately 0.10”. Panels of S2 glass and IM7 were fabricated using what is termed ’sticky string’ dry fibers. This string is used as a binding fiber to keep the dry fabric together to lay it up. The dry preform was then infused with SC-15 matrix and cured using the previously shown cycle. Samples were extracted via waterjet cutting. During loading, the composite’s strain was measured with both a strain gage and DIC. The strain gage data is neglected because as the material fails, it results in matrix microcracking between the fibers and causes premature failure of the strain gage. An average strain in the section is used for this testing.

Five tests were completed with each sample to assess the repeatability. With a

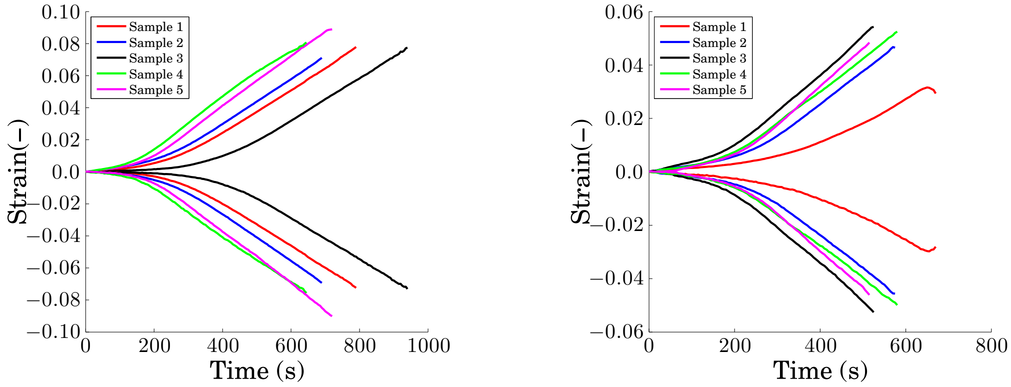

(a) The strain-time history for the S2 glass samples

(b) The strain-time history for the IM7 samples

Figure 2.7: Axial and transverse strain-time histories for the in-situ matrix testing

typical test, the sample develops microcracking in the laminae. After a sufficient amount of strain is applied, the sample separates into two pieces with a repeatable failure pattern. A sample failure is shown in Figure 2.6.

Figure 2.7(a) and 2.7(b) show the axial and transverse strain for the results for each of the five tests for both the S2 glass and IM7 respectively. In this figure, the positive strains are the axial strains and the negative strains are the transverse strains as a result of Poisson's effects. Under ideal circumstances, the axial and transverse strains would be identical, however, can differ due to deviations within the sample. Both of the samples do not show a high degree of agreement and this is most likely a result of the VARTM process leading to differences in compaction and local properties. The carbon samples showed a higher degree of repeatability with 4 samples showing similar failure strains. In general, the glass was more compliant than the carbon samples.

From the axial and transverse strains, the shear response can be determined by using the following sets of equations as explained earlier. Equation 2.1 describes the lamina shear stress in terms of the applied axial stress, and Equation 2.2 is the simple transformation from the two strain measures.

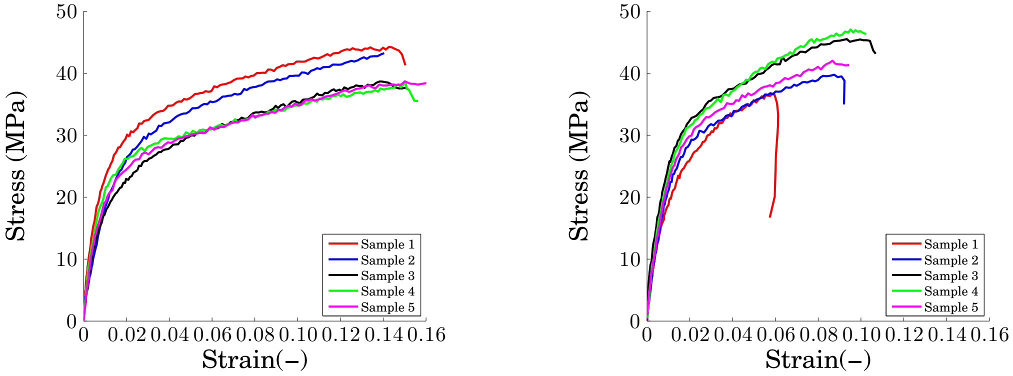

(a) The shear stress-strain history for the S2 glass samples

(b) The shear stress-strain history for the IM7 samples

Figure 2.8: The shear stress-shear strain for the composite

$$\tau_{12} = \pm\frac{\sigma_1}{2} \tag{2.1}$$

$$\gamma_{12} = -(\varepsilon_2 - \varepsilon_1) \tag{2.2}$$

The results of the transformation from axial stress-strain to shear stress-strain is shown in Figures 2.8(a) and 2.8(b). From these stress-strain response, it is clear that while the failure strengths are very similar, the failure strains are not. The S2 glass samples show a higher amount of energy absorption in comparison to the carbon.

From the results shown in Figures 2.8(a) and 2.8(b), the secant lamina shear modulus can be determined as a function of the applied shear stress. The secant modulus is determined by the taking the instantaneous shear stress divided by the instantaneous shear strain. This effectively is giving the modulus to a specific point in the curve.

The secant shear modulus versus the applied shear stress is shown in Figures 2.9(a) and 2.9(b). Both samples show that over a large range of applied shear stress, there is a linear relationship with the secant shear modulus. The slopes of the samples within

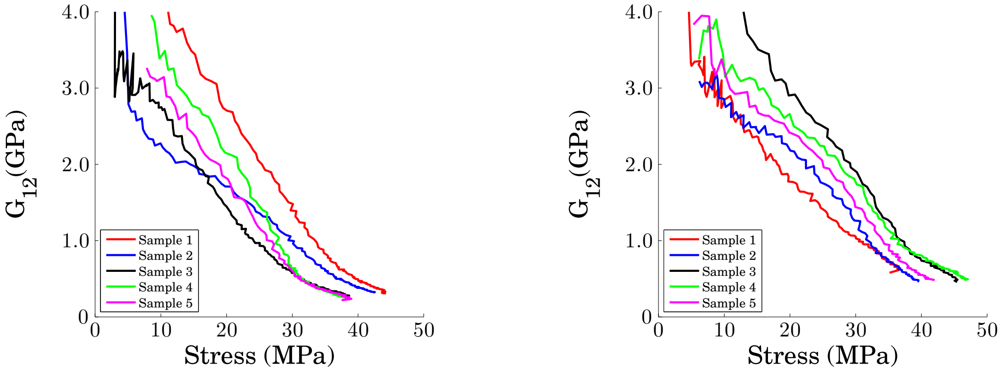

(a) The secant shear modulus-applied shear stress response for the S2 glass samples

(b) The secant shear modulus-applied shear stress response for the IM7 samples

Figure 2.9: The shear stress-shear strain for the composite

each group are in agreement over a number of samples and begins to show much more similar behavior.

The in-situ matrix response can then be determined by using Equation 2.3 where V_f is the volume fraction, and G_m is the shear response of the matrix. This equation can then be solved for the matrix response. For textile composites, it is not uncommon to have volume fractions of less than 45% and for this work, a volume fraction of 47% was used. It should be noted that this is an approximation of the fiber volume fraction as it was not explicitly measured. The shear modulus of the fiber was used from the previously described properties.

$$G_{12,c} = \frac{G_{12,f}(1+V_f) + G_m(1-V_f)}{G_{12,f}(1-V_f) + G_m(1+V_f)} G_m \tag{2.3}$$

The in-situ shear stress-strain response can be determined and this response is shown in Figures 2.10(a) and2.10(b). The effect of the deviation between samples begins to appear less, however, there is still some deviation.

For further clarification, the average response for both the samples is shown in Figure 2.11 The results indicate that the in-situ matrix response is dependent on the type of fibers that it is being co-cured with. The S2 glass shows a different

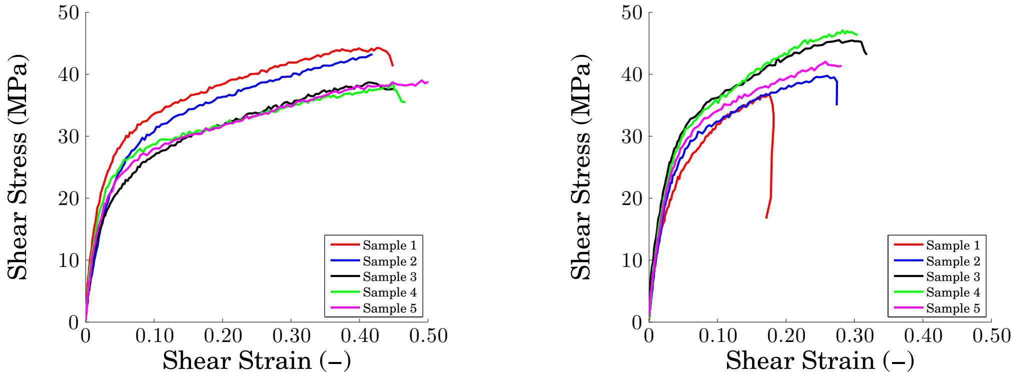

(a) The in-situ matrix shear stress-strain response with S2 glass fibers

(b) The in-situ matrix shear stress-strain response with IM7 carbon fibers

Figure 2.10: The shear stress-shear strain for the in-situ matrix

response than the carbon. The in-situ matrix properties of the glass show higher energy absorptions, but lower yield stresses.

In order to compare this result to the results of previous work including neat epoxy and the work of Pankow, the response must be converted to a uniaxial response using a Mohr's circle transformation. After transformation, the equivalent uniaxial response is shown in Figure 2.12. From this, it is clear that the neat epoxy response can differ greatly from the in-situ response. Interestingly though, the ultimate tensile strength was in between the tensile strength and compressive strength of the neat epoxy. The yield stresses for the in-situ matrix are much lower than that of the neat epoxy which is a result of the cure damage. Each of the responses though was significantly less than the results reported by Pankow. One point of note is that while the strains to failure are quite large for the in-situ problems, this might not actually be a physical effect. This may be the result of some of the textile geometry causing artificially high strains as a result of the ply cracking, however, this does not affect the initial response.

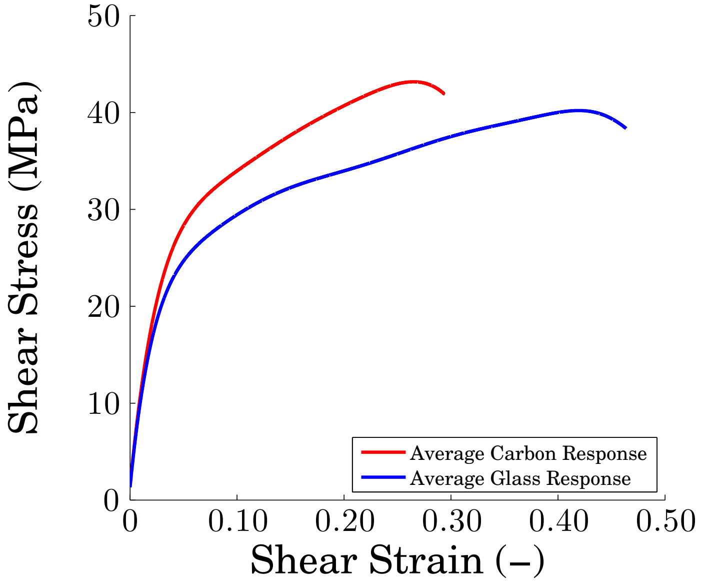

Figure 2.11: A comparison of the average in-situ response for the glass and carbon samples

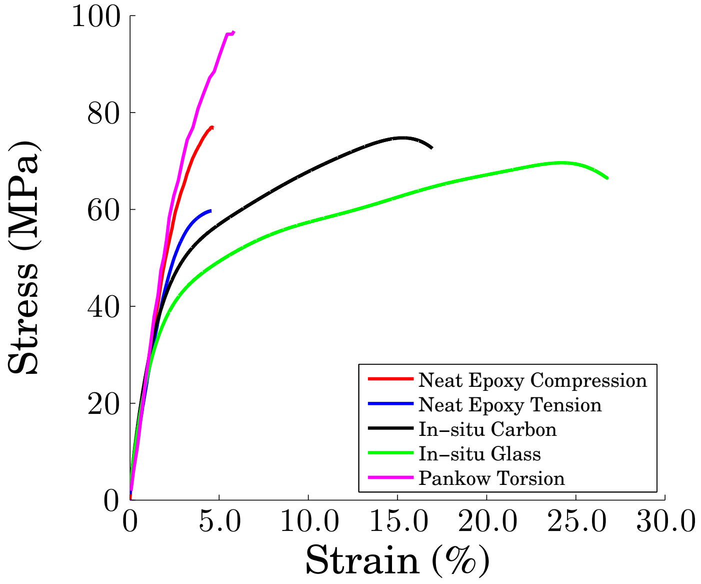

Figure 2.12: A comparison of all responses of the SC15 testing

Figure 2.13: Photograph of the cured carbon composite showing the cotton yarn

2.3 Testing of Fibrous Composites

Inducing tensile rupture in yarns is a very difficult mechanical test to perform. This is because other damage mechanisms are apparent during testing. To attempt to determine the tensile rupture strength of a yarn, two testing protocols are examined. The first is a modified version of the ASTM D3039 Standard [16]. Due to testing difficulties experienced in practice with this testing protocol, The Suppliers of Advanced Composite Materials Association, SACMA, developed a testing protocol for cross-plied composites to determine the tensile rupture of a ply or yarn. While SACMA is now defunct, the developed standard (SACMA-RM9 [75]) is still widely used as an accepted protocol.

2.3.1 Unidirectional Testing

To first determine the tensile strength of a ply, a unidirectional sample with thickness 2.54 mm (0.10 in.) of both IM7 carbon and S2 glass were tested. Because the preferred manufacturing process for textile composites is VARTM, the same process was used to manufacture the unidirectional samples tested here. While traditional prepreg composites utilize the tack of the uncured resin to hold together the ply, this is not possible to do with the dry fibers used in the unidirectional samples. To hold the dry fibers together, an additional cotton yarn, termed sticky string, runs transverse to the yarns. An image of this can be seen in Figure 2.13. The equivalent thicknesses of both of the samples were approximately 4 plies.

Samples were extracted via waterjet cutting to a length of 25.4 mm (10 in.) × 12.7 mm (0.5). It should be noted that width of 12.7 mm differs from the ASTM

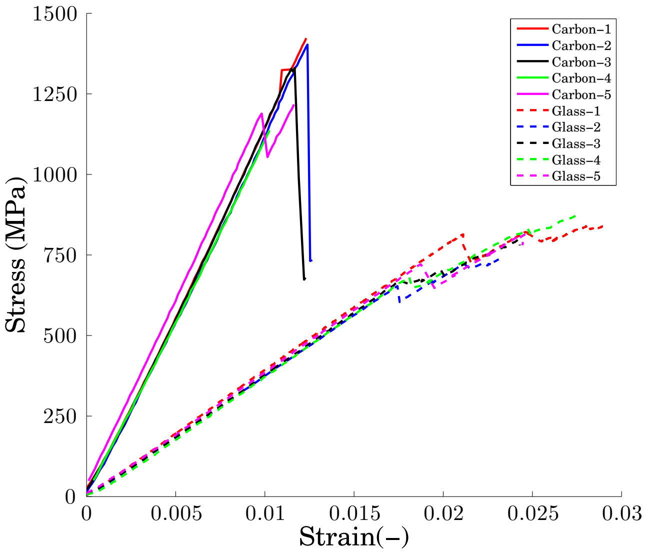

Figure 2.14: The results of the unidirectional testing using the ASTM D3039 standard

D3039 standard and was selected because of demonstrated success from prior material systems. The samples were pulled at a rate of 0.0004 in/s and emery cloth was used in the gripping mechanism. Five tests were performed for each of the material systems. The load-time history was measured via the test frame load cell and the strain-time history was determined by using DIC. To eliminate the effects of the localized damage, a line strain measure was used. The results of the stress-strain responses are shown in Figure 2.14.

While the results are generally in agreement with respect to failure stress, failure strain, and modulus of elasticity, there were apparent issues with the testing. Test results are presented in Table 2.3. The issues experienced in testing are evidenced by the load drops that are seen in the testing that occur both within the IM7 and S2 glass systems. One reason for this is because there is a large amount of energy dissipation due to fiber splitting. Fiber splitting is an energy dissipation mechanism that results in cracks propagating along the fiber tow itself.

Additionally, an image showing the five failed glass samples can be seen in Figure

Material	Modulus (GPa)	Tensile Strength (MPa)	Failure Strain(%)
Carbon	114.0±3.2	1400±200	1.2±0.1
Glass	37.7±0.8	800.5±39.3	2.6±0.2

Table 2.3: Material properties determined by ASTM D3039 Standard

Figure 2.15: Photograph of experimentally tested unidirectional samples showing a high degree of fiber splitting

2.15. While many of the samples do show a two piece failure, it is clear that there is significant brooming failures which is characteristic of splitting. Additionally, the yarns are very apparent in the image. Since the carbon was more brittle, when the sample begins to split, it breaks off in large pieces that are ejected from the test piece. When examining the DIC results, it is clear that local damage occurs followed by splitting in the sample. However, it is necessary to understand why this occurring.

Figure 2.16 demonstrates the splitting effect in a unidirectional carbon fiber panel. Plotted are both the normal strain distributions and the shear strain distributions within the gage section of the field. The normal stress distribution allows for visualization of the cracks as they begin to form and shear stress gives information about the location and periodicity of the cracks. At relatively early loading, marked point A in Figure 2.16(a), there are not clear discernible features within the strain fields. After further loading, it is seen in the Figures 2.16(e) and 2.16(f) that localization is beginning to occur. It becomes more noticeable in the strain fields at the point marked C, where there begins to be very apparent periodic behavior with respect to the locally high strain concentrations. As it is loaded further, the area around which the damage localizes in a small area becomes larger and progresses. Finally, at point E, there becomes failure in 3 pieces as the middle piece splits. Because of the brittle nature of the carbon material, as the fiber splits, it is not able to dissipate the elastic energy and it fractures, thusly, ejecting the split fiber from the failed sample. It is clear though that the periodicity of the large strain concentrations is may contributing to the splitting effects because the path of failure is along the samples themselves.

The use of optical microscopy sheds further light on this periodic cracking effect. When examining micrographs shown in Figures 2.17(a) and 2.17(b), it is clear that there are resin rich areas on either side of the tow. The resin rich areas are shown in red boxes. These resin rich areas correspond to points where the sticky-string passes through the samples. As it binds the yarns together, tension must be placed on the sticky string to hold the yarn tight. This tension deforms the yarn locally. These areas allow an natural crack initiation point and the area between fiber yarns provides a pathway for the crack to propagate. Since the resin rich areas are periodic, it favors the splitting mechanism.

The stress-strain response coupled with DIC analysis and optical microscopy demonstrates why the ASTM D3039 standard might not give an accurate tensile response of this material. For this reason, it is advantageous to examine the SACMA RM-9 standard to determine the rupture strength of a yarn.

2.3.2 Crossply Testing

Because of the propensity of fiber splitting, the SACMA RM-9 standard was developed to give a more accurate measurement of the failure strength of a yarn. The ASTM D3039 data analysis is very straight forward as the stress on the longitudinal yarns is the load divided by the measured cross-sectional area, however, the RM-9

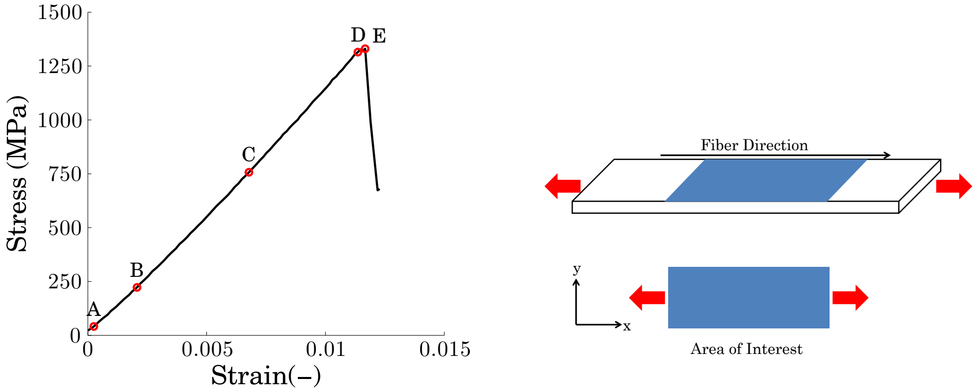

(a) A typical stress stress response for a unidirectional carbon composite (b) A schematic of the test showing the DIC contours

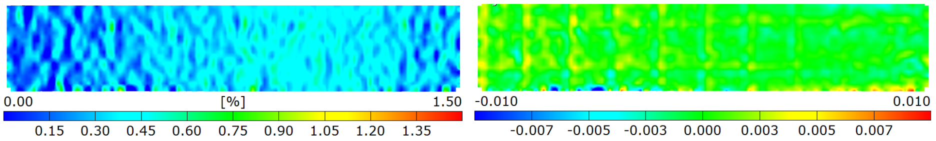

(c) Normal strain at point A (d) Shear strain at point A

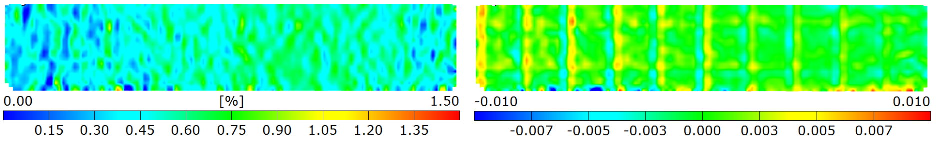

(e) Normal strain at point B (f) Shear strain at point B

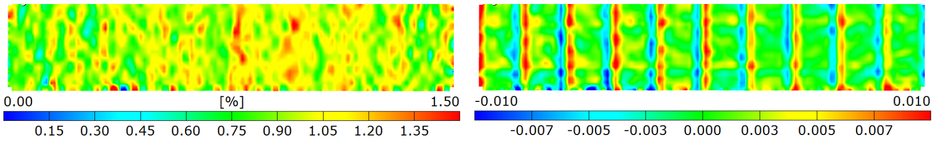

(g) Normal strain at point C (h) Shear strain at point C

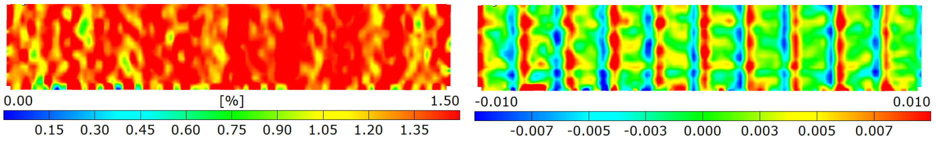

(i) Normal strain at point D (j) Shear strain at point D

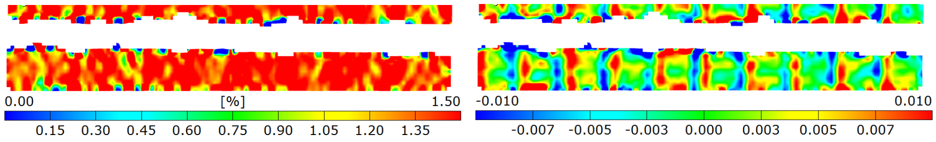

(k) Normal strain at point E (l) Shear strain at point E

Figure 2.16: Schematic showing the progression of damage transverse to the fiber direction

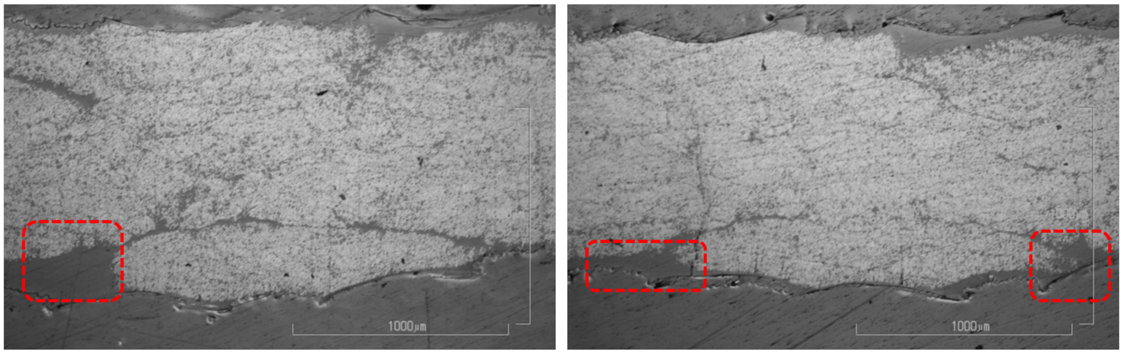

(a) Resin rich areas in a unidirectional glass sample

(b) Resin rich areas in second unidirectional glass sample

Figure 2.17: Two micrographs showing resin rich areas within the unidirectional samples

standard is not as straight forward and requires additional analysis relative to classical lamination theory. The SACMA RM-9 requires a cross-ply layup of $[0/90]_s$ where the 90°is the longitudinal ply and the 0°is the transverse ply on the outside. As the sample is subjected to an external strain, the outer 0°plies crack similarly to what is seen in the unidirectional sample. As the sample's crack density is saturated (the limit at which the ply that cannot crack more) all of the load is carried by the middle longitudinal plies. The longitudinal plies do not split as seen before because the cracks are now bridged by the outer fibers.

To determine the failure stress of the ply, classical lamination theory can be used to determine the strength using what is termed the back out factor. The strength of the longitudinal plies is determined by Equation 2.4.

$$\sigma_{ULT,yarn} = BF * \sigma_{ULT,composite} \tag{2.4}$$

where,

$$BF = \frac{2E_{11}}{E_{11} + E_{22}} \tag{2.5}$$

with E_{11} and E_{22} being the longitudinal and transverse stiffness of a ply. However, using the assumption that when the outer plies are completely saturated in cracks, they no longer contribute to the stiffness, the backout factor, BF, simply becomes 2. Therefore, Equation 2.4 can be written as follows:

$$\sigma_{ULT,yarn} = 2 * \sigma_{ULT,composite} \tag{2.6}$$

Strip samples of length 254 mm (10 in.) by 25.4 mm (1 in.) were extracted from a 4 ply plate via water jet cutting. They were tested on the same Shore Western load frame at the rate described earlier. The samples were tested in triplicate and showed good agreement. The stress strain response is shown in Figure 2.18. The mechanical properties are shown in Table 2.4. Post test analysis did not show any brooming effects. Two piece failure was observed in the carbon samples, however, the glass samples did not show the same type of failure. Instead of showing a clear transverse crack path, many of the fiber tows failed internally, and then began to pull out. Due to frictional effects, a finite load was still able to be carried, however, the tow failure is considered to correspond to the maximum stress.

Material	Modulus (GPa)	Tensile Strength (MPa)	Failure Strain(%)
Carbon	62.2±3.3	903.5±46.4	1.45±0.05
Glass	18.8±1.6	486.7±48.5	2.60±0.30

Table 2.4: Material properties determined by SACMA RM-9 Standards

The progressive failure of a typical carbon fiber crossply sample tested with the RM9 standard is shown in Figure 2.19. The response shows a characteristic linear elastic response, which is to be expected since the transverse ply offers little strength and stiffness in comparison to the the longitudinal plies. When examining the progressive failure analysis in the subsequent images, it is clear that transverse cracks develop on the surface of the sample in a progressive manner. Figure 2.19(b) shows the strain distribution in the sample prior to point A. At the two ends, the transverse cracks have already formed and are beginning to open more while cracks in the center

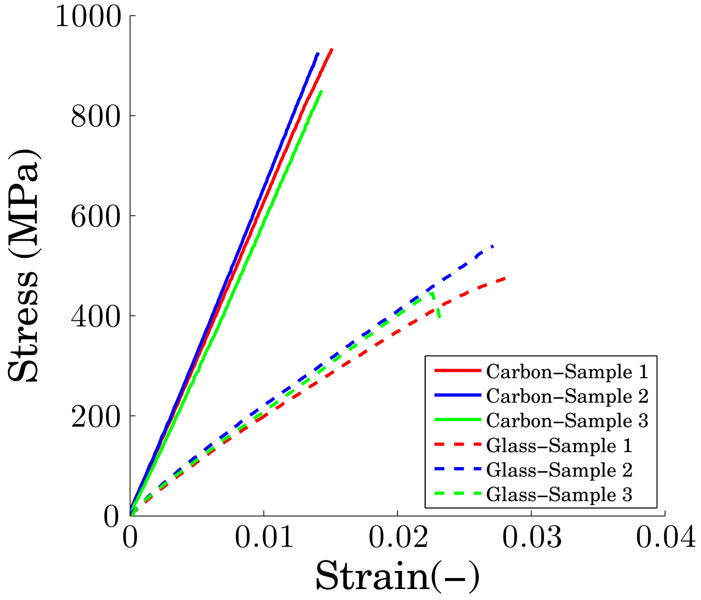

Figure 2.18: Results of the SACMA RM9 testing

of the sample are only beginning to form. This continues until between point B and C, all the cracks have been developed and are beginning to open. This opening of cracks is well characterized by the periodic spacing of the transverse cracks seen in Figure 2.19(e). The relative time during loading at which the cracks appear is related to the thickness of the of the red lines since as the cracks open, the width will appear larger. As stated earlier, cracks on either end formed first whereas cracks in the middle appeared later. By the point of final failure, the width of the cracks is relatively equal as seen in Figure 2.19(g) and no further energy dissipation can occur via crack opening. At this point, the longitudinal fibers are being loaded directly and no load transfer is taking place to the longitudinal plies. After point E, two piece failure occurs with a clean break transverse to the loading direction taking place. Splitting was not observed during the RM-9 testing.

Figure 2.20 shows two crossply carbon samples that were tested to the RM-9 standard. From this image, it is clear that two piece failure is observed in the gage section and not at the grips. Of note, it some cases, more than three or more sections

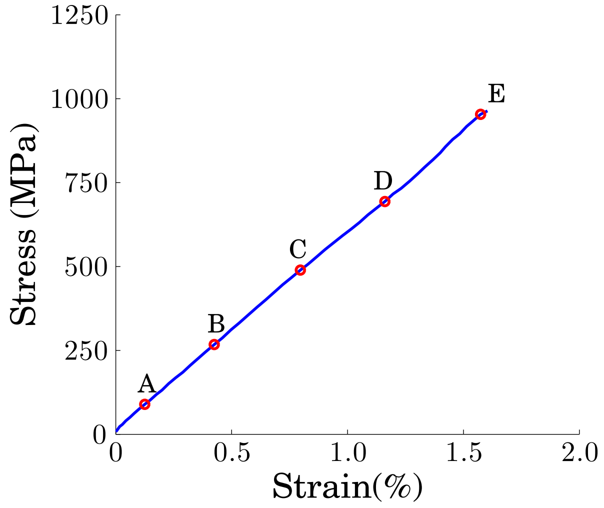

(a) A typical stress strain response for an RM9 carbon crossply composite

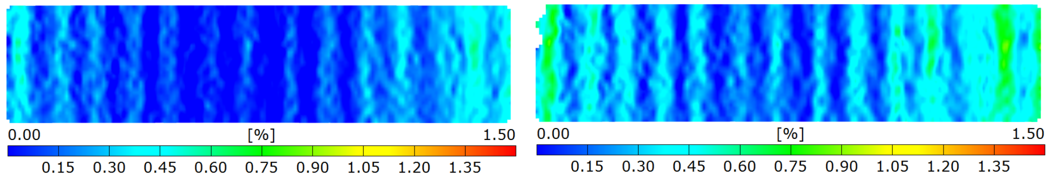

(b) Normal strain prior to point A

(c) Normal strain at point A

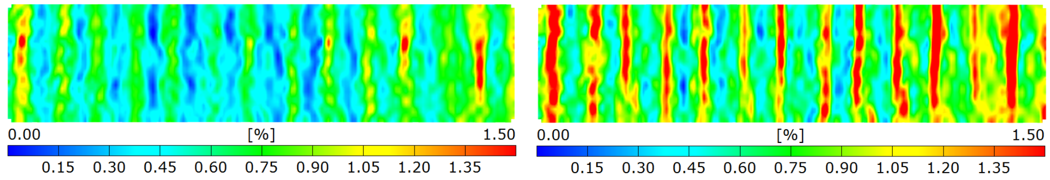

(d) Normal strain at point B

(e) Normal strain at point C

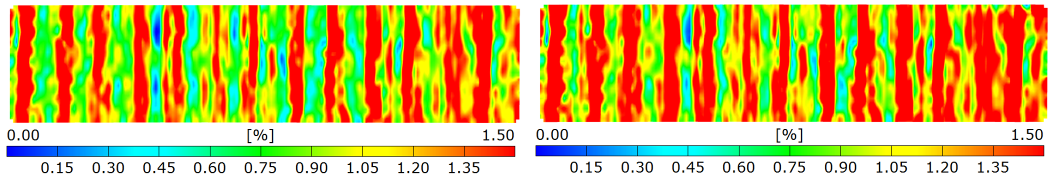

(f) Normal strain at point D

(g) Normal strain at point E

Figure 2.19: Schematic showing the progression of damage in the $[0/90]_s$ composite that has been tested to the SACMA RM9 standard

Figure 2.20: An image of failed carbon crossply samples

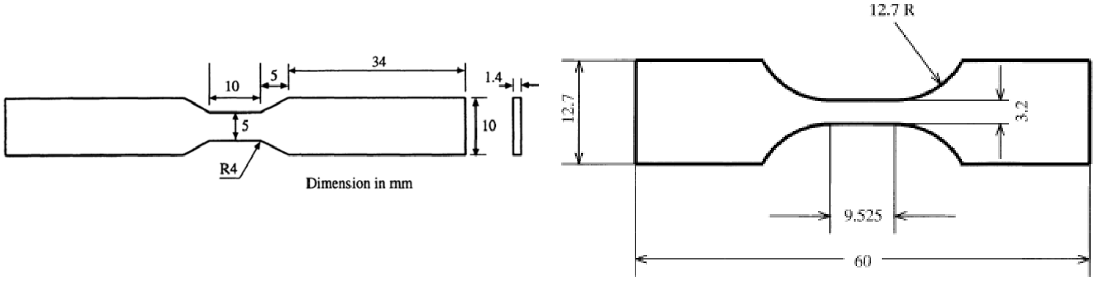

(a) Example of a bowtie specimen used for composites

(b) Example of a dogbone specimen used for composites

Figure 2.21: Two common geometries used for testing composite materials

are recovered post failure. This is a due to the release of large amounts of strain energy creating a cascade fracture type behavior in the material and is characteristic of a brittle material.

2.3.2.1 Dogbone Shaped Specimens

Because the RM-9 sample is relatively large (25.4 mm) it is not possible to test this at high rates, a reduced cross-sectional sample needed to be engineered to allow for use in high strain rate testing, but also to use as little material as possible. In general, there are two types of samples that are typically used. The first is a the bowtie sample and the second is a dogbone sample. The main difference between the two samples is that the bowtie (Figure 2.21(a)) uses a taper to reduce the cross-section whereas the dogbone (Figure 2.21(b)) uses a radius.

To engineer the proper dogbone to mimic the results of the RM-9 with reduced material, namely uniform stress within the cross-sectional area without a stress concentration, a parametric study was performed to determine the effects on key aspects

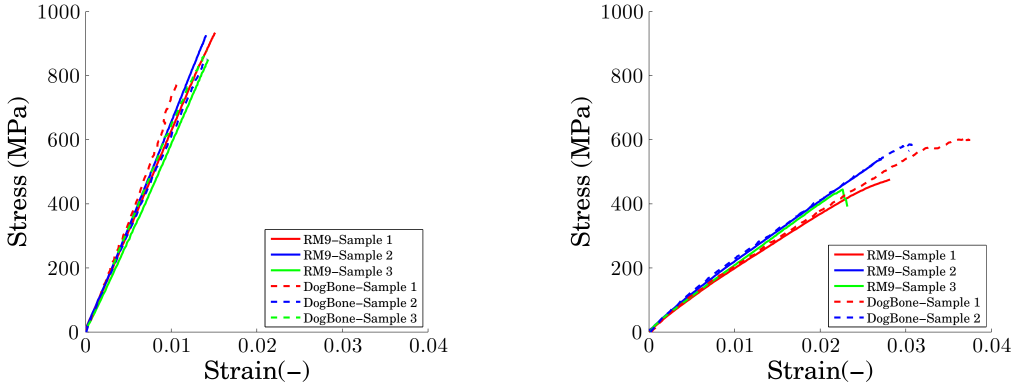

(a) Comparison of the carbon dogbone specimen to the RM9 sample

(b) Comparison of the glass dogbone specimen to the RM9 sample

Figure 2.22: Results of the dog bone testing

of the geometry. To do this, the effects of the width of the gage section, the length of the gage section, the angle/length of the taper, and radius of the neck were examined. From the finite element analysis, it was determined that the bowtie sample resulted in a stress concentration at the point where the taper met the gage section and could be eliminated. Furthermore, it was determined that to mimic the results of the RM-9 the sample width must be decreased as FE analysis showed that the deviation in stress across the samples decreased with width. Secondly, it was determined that as the gage length increases, the stress deviation decreases. Finally, as the sample's radius to the gage section increases, the deviation in stress decreases. Using this information, a dogbone geometry was developed and tested to determine if the results capture the proper mechanics of the RM-9 samples.

The dogbone was tested with the same parameters as the RM-9 samples, and the results are shown in Figure 2.22(a) for the carbon samples and Figure 2.22(b) for the glass samples.

The comparison of the mechanical properties between the RM9 samples and the dogbone are shown in Table 2.5. There is generally good agreement between the samples in terms of all three metrics for the carbon, however, a discrepancy exists between the failure strain and ultimate tensile strength of the glass samples. This is because as the cross-section of the sample is reduced, it eliminates the effect of the sticky string as the sample width approaches the width of a single yarn. This gives a closer comparison of the true strength of the yarn. The failure modes were consistent between samples as the carbon dogbone exhibited two piece failure in the gage section in both the RM9 and the dogbone. In the glass samples, different types of failure were observed. While there are two pieces that are developed between the inner plies, the 90°on the outer ply is still adhered to the 0°ply. This adherence allows for residual strength, however, it still has a negative tangent stiffness. This effect was not seen in the dogbone sample.

Material	Modulus (GPa)	Tensile Strength (MPa)	Failure Strain(%)
Carbon RM9	62.3±3.3	903.5±46.4	1.45±0.05
Carbon Dogbone	64.4±6.2	838.5±46.6	1.31±0.18
Glass RM9	18.8±1.6	486.7±48.5	2.6±0.30
Glass Dogbone	18.5±1.2	581.5±45.3	3.14±0.18

Table 2.5: Material properties determined by SACMA RM-9 Standard

While the mechanical properties appear to be consistent, it is important to ensure that the mechanics of the failing specimen are correct. To do this, the progressive damage development from the DIC images need to be examined. The progressive damage images are shown in Figure 2.23 for a typical carbon test. As discussed previously, the onset of cracking in the outer transverse ply begins very early on in the loading as evidenced by the image shown in Figure 2.23(b). The damage then propagates and progresses to show the same periodic spacing between the fibers as seen with the SACMA standards. When the crack density reaches a saturation point, the sample fails in a two piece failure. The failure point is in the gage section of the sample.

By comparing the stress-strain response, mechanical properties and the qualitative/quantitative information from the DIC analysis, it was determined that the

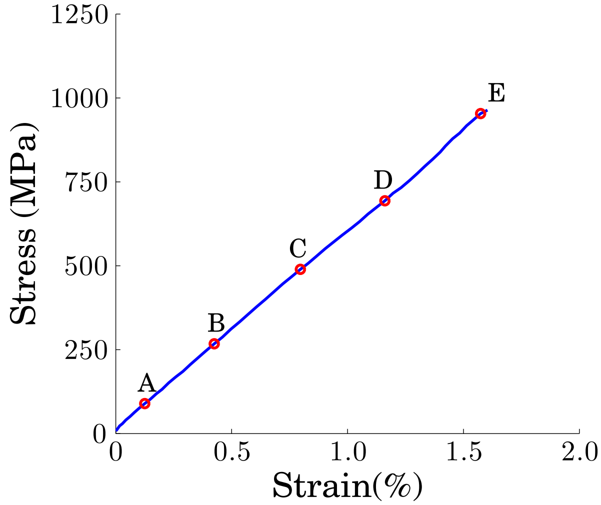

(a) A typical stress strain response for a dogbone carbon crossply composite

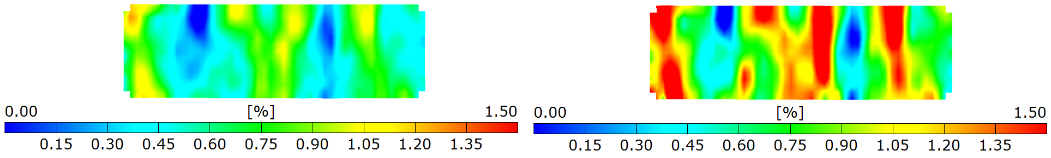

(b) Normal strain prior to point A

(c) Normal strain at point A

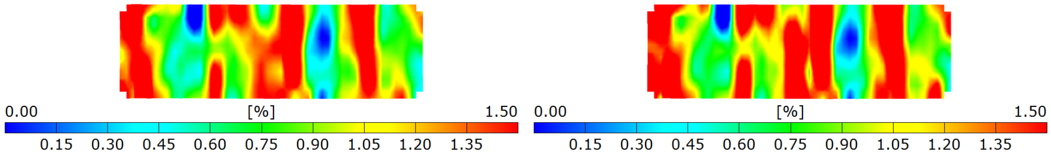

(d) Normal strain at point B

(e) Normal strain at point C

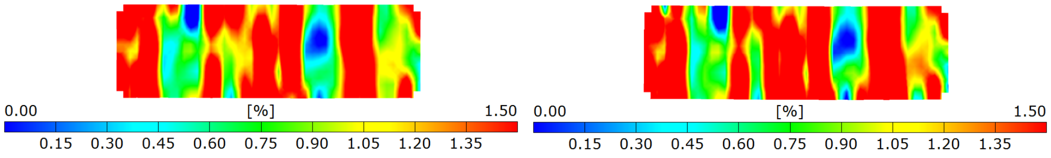

(f) Normal strain at point D

(g) Normal strain at point E

Figure 2.23: Schematic showing the progression of damage in the $[0/90]_s$ dogbone composite

dogbone sample and SACMA samples could be used interchangeably for mechanical testing.

2.4 Conclusions

The quasistatic mechanical properties of constituents and basic composite lay-ups were determined. The matrix material, SC-15 was examined for its neat tension and compression response and found to be material dependent, however, the in-situ matrix properties were determined by performing a $[45/-45]_s$ test. The in-situ properties differed greatly from the neat epoxy as curing kinetics affected the as cured properties of the matrix. The unidirectional properties of an S2 glass and IM7 carbon fiber in an SC-15 matrix were tested per ASTM D3039 standards and it was determined that the preferred mode of failure is fiber splitting and a true measure of the strength of the composite was not obtained. It was also found that the sticky string that was used to hold the dry fabric together provided a starting point for cracks to propagate along the gage section. To obtain a true measure of the rupture strength of the composite, the SACMA RM-9 standard was used and found to create consistent failure within the composite. To ensure transferability between between the SACMA standards and other testing protocol, a dogbone samples was developed and tested. It was found that the dogbone samples captured the unique mechanical features of the SACMA standard and replicated the results.

CHAPTER III

Development and Validation of a Split Hopkinson Tensile Bar for High Strain Rate Testing

One of the most common testing techniques to determine the high strain rate mechanical response of materials is by use of a Split Hopkinson Pressure Bar (SHPB) for compressive response or Split Hopkinson Tensile Bar (SHTB) for tensile response. Relying on 1-dimensional wave theory, SHTB testing techniques allow a tensile sample to achieve a dynamic equilibrium at a constant strain rate, and a dynamic stress-strain response can be extracted. By varying the testing parameters, a wide variety of mechanical responses over a range of strain rates can be determined.

While the more common compressive or pressure version of the testing apparatus is well known, the SHTB is often more difficult to understand and requires more analysis. The purpose of the current chapter is to define all necessary testing parameters as they relate to the engineered test. In this chapter, a thorough analysis of the design, set-up, and implementation of the SHTB setup will be explained.

3.1 Introduction

The study of strain rate dependent behavior has been of great interest since the second half of the 19th century. Widely recognized within the field as a pioneer of strain rate dependent testing is John Hopkinson (1849-1898). Hopkinson became interested in the strain-rate rupture response of wires and employed a system of dropping a weight to cause two-piece failure in the wire [37]. The original motivation was to study the stress wave transfer within the wire, however, measurements were extremely difficult at that time.

The interest in stress wave analysis and measurement was passed onto his son, Bertram (1874-1918). B. Hopkinson was interested in studying the stress wave propagation in an axial bar and noted the results in his 1914 paper [36]. Hopkinson studied the stress in an axial bar by creating a stress wave with an explosive charge or impacting it with a bullet. The bar was suspended in the air by wires and was free to move along its axis. Without the aide of modern measuring techniques, Hopkinson used pencil and paper to measure how the wave propagated past fixed locations on the bar. Motivated by the inability of Hopkinson to measure the stresses directly, Davies incorporated the first electronic data acquisition system to measure the stress-time history in his 1948 work [14]. Davies's work was able to better understand the work of B. Hopkinson and developed the necessary tools to begin modern dynamic testing techniques.

Modern split pressure bar testing techniques were pioneered from the earlier work of the Hopkinsons and Davies, and first introduced by Harold Kolsky in 1949 [50]. Kolsky theorized and proved that based on the wave propagation through elastic media, a material can be wedged between two bars, and the dynamic stress-strain properties can be determined. Kolsky showed that dynamic stress-strain responses of many materials such as natural rubbers, PMMA, copper, and lead can be extracted using these techniques. To honor the innovators in the field, Kolsky named the experiment the Split Hopkinson Pressure Bar (SHPB). Since this time, Split Hopkinson Bar testing techniques have been modified for a number of capabilities including torsion, shear, and tension.

In this chapter, a detailed explanation will be given for the development and validation of a Split Hopkinson Tensile Bar (SHTB). This SHTB was designed according to principles of the original formulation of Kolsky, and others. The chapter will then include an evaluation of a novel SHTB analysis technique that relies directly on the measurement of the strain-time history using modern measurement techniques from the sample as opposed to the traditional SHTB analysis. Finally, a validation study will be shown using a commercially available aluminum to show that the bar is completely operational.

3.2 Design of a Split Hopkinson Tensile Bar for Planar Samples

The following sections describe key components of the development of the tensile Hopkinson bar. Included is a basic introduction to the 1D wave theory that is used for data analysis in Hopkinson bar testing as well as a description of the bar developed for this work. Then a thorough analysis is shown for how a sample is gripped for testing and finally, a novel data analysis technique is shown.

3.2.1 Basic Split Hopkinson Bar Theory

The analysis of Split Hopkinson Bar Theory was first developed by Kolsy ([50]) and is based on 1D wave propagation through elastic medium. While the entire derivation has been shown in numerous references (for example, ref. [71]), only a few key concepts of the testing govern the data analysis.

For Hopkinson Bar testing, it is necessary to develop a strain wave or pulse in the bar. The strength of the strain pulse should be strong enough to not dissipate due to damping in the system but weak enough such that the strain pulse remains elastic and does not dissipate energy through plastic deformation. The bar strain associated with pulse has been developed through a variety of methods including generation of a blast through a denotation, impact with a bullet, however, the general accepted standard is to generate the pulse via impact with an auxiliary bar or tube ejected from a gas gun. The pulse that is generated is generally termed the incident pulse and is denoted by the symbol ε_i. As the wave propagates down the length of the bar and reaches the sample, the pulse splits into a reflected pulse (ε_r) and a transmitted pulse (ε_t).

The key assumption for the validity of Hopkinson bar analysis is that dynamic equilibrium exists. Dynamic equilibrium indicates that the forces on each end of the sample is the same. From a pulse standpoint, this is validated by Equation 3.1. The importance of dynamic equilibrium is that it ensures that inertial effects from the bar moving are negligible.

$$\varepsilon_t = \varepsilon_i + \varepsilon_r \tag{3.1}$$

Once dynamic equilibrium has been satisfied, the strain rate history can be determined from Equation 3.2, where C_{bar} is wave speed of the incident bar and L_s is the length of the sample.

$$\dot{\varepsilon}(t) = \frac{2 * C_{bar}}{L_s}\varepsilon_r(t) \tag{3.2}$$

By integrating Equation 3.2 the strain-time history can be determined. The strain-time equation is shown in Equation 3.3

$$\varepsilon(t) = \int \frac{2 * C_{Bar}}{L_s}\varepsilon_r(t)dt \tag{3.3}$$

The sample stress-time history can be determined from the geometrical properties of the bar as well as the transmitted pulse. Since dynamic equilibrium exists, the stress time history can be determined by Equation 3.4 where A_s is the area of the

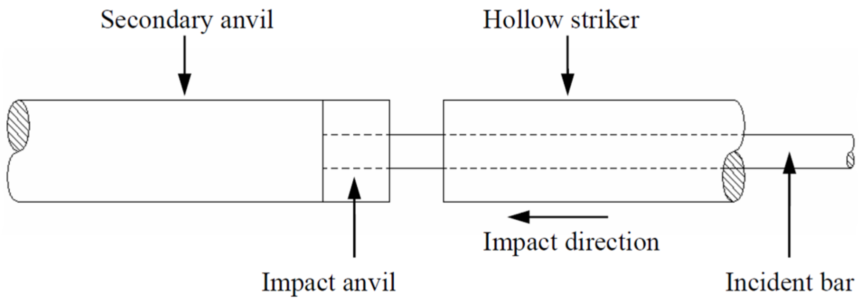

Figure 3.1: A schematic of the Owens SHTB

sample, A_{bar} is the cross-sectional area of the bar, and E is the modulus of elasticity of the bar.

$$\sigma(t) = \frac{A_{bar}E}{A_s}\varepsilon_t(t) \tag{3.4}$$

3.2.2 Setup of a Split Hopkinson Tensile Bar

The bar that was developed was based on the one developed by Owens in ref. [78] as part of a masters thesis at Auburn University. The selected setup of the Split Hopkinson Tensile Bar is based on the striker tube/anvil technique. For illustration purposes, the setup is shown schematically in 3.1 and photographically in Figure 3.2 which shows the barrel, striker tube, anvil setup.

In order to generate a tensile pulse, a 0.45 m (18 in.) steel striker tube is ejected from a 1.14 m (45 in.) barrel. The barrel and striker tube are concentric with a 38.1 mm (1.5 in.) diameter 1566 steel bar of length 2.44 m (96”). A dovetail profile was cut into the bar using an Electric Discharge Machining Process (EDM) and that profile will be discussed further in the subsequent section. The steel is not case hardened as seen with most Hopkinson bars. The reason for this is twofold. Because this is a tensile setup, it is not susceptible to barreling effects that are often seen in compression bars, e.g. it is not necessary to prevent the barreling that occurs in compression. Secondly, a dovetail profile cannot be cut into the bar accurately

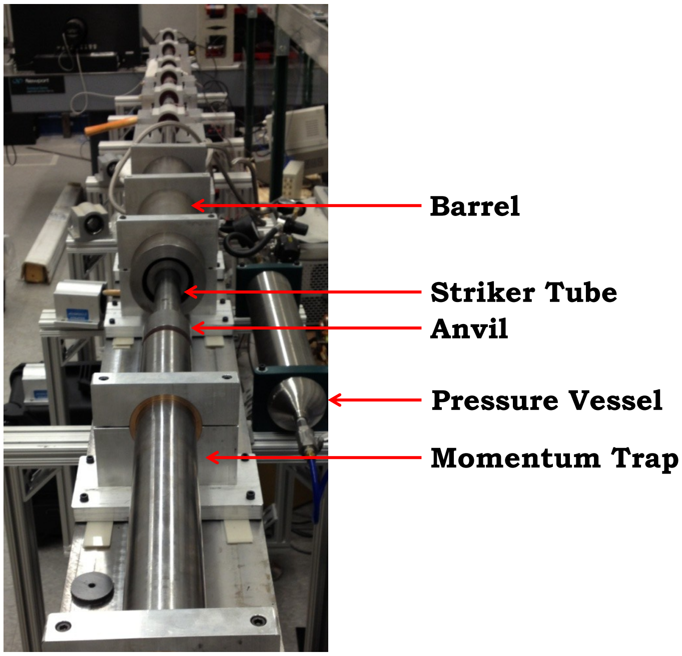

Figure 3.2: A photo of the SHTB setup

because the additional thermal stresses from the EDM process relieve the internal stresses from the case hardening.

An anvil is bolted into the end of the bar and butted against a momentum trap. A circular piece of urethane wedged between the anvil and the momentum trap to allow for a large impedance mismatch and ensure that any wave that is transmitted into the momentum trap does not get retransmitted into the bar. The use of the urethane also allows for a characteristic trapezoidal pulse to be developed. When the anvil is struck by the tube, it creates a compressive pulse in the anvil. As the pulse transmits through the anvil, it is reflected back at the surface and transmitted as a tensile pulse along the bar. The transmitted bar is 1.524 m (60 in.) in length and is made of the same material as the incident bar.

3.2.3 Gripping of Sample

Gripping of a planar sample is perhaps one of the most important aspects SHTB testing. This is because traditional SHTB analysis is based upon strain signals that

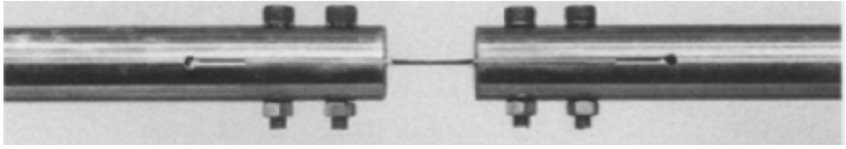

Figure 3.3: Huh et. al used 2 bolts to secure the sample during testing

are incident and reflected in the incident bar and transmitted in the second bar. In order to adequately analyze the signal, the initial strain pulse must be transmitted without distortions through the bar. Traditional SHTB tests on cylindrical samples allow for the samples to be threaded into the bars which creates a condition in which the strain wave can pass through the sample with relative ease. Since planar samples can generally not be manufactured with threaded ends, a different way is needed to grip the samples. This has traditionally been approached in one of three ways:

1. Use of a dowel pin or screw through the bar
2. Direct adhesion of the sample to the bar
3. Wedges in the bar or in a wedge assembly

The first type of technique as been used by Huh, Kang, and Hun in their investigation of sheet metals [40]. The particular interest in this analysis was looking at metal forming limits. To do this, the researchers created a SHTB that employed 2 screws through the sample in both bars to grip the sample. A sample of this type is shown in Figure 3.3. In the paper, it is noted that the grip does change the wave dynamics, but not significantly. While the technique proved successful for sheet metals, it is not particularly well suited for composites as the likelihood of the damage causing shearing failure at the grips is much higher than that of a metallic sample.

Direct adhesion to the bar is a suitable option for composites as it eliminates the need to include mechanical fasteners and with the right epoxy, can achieve very high strengths. This technique has been used by Gilat et. al [22] and Eskandari and Nemes

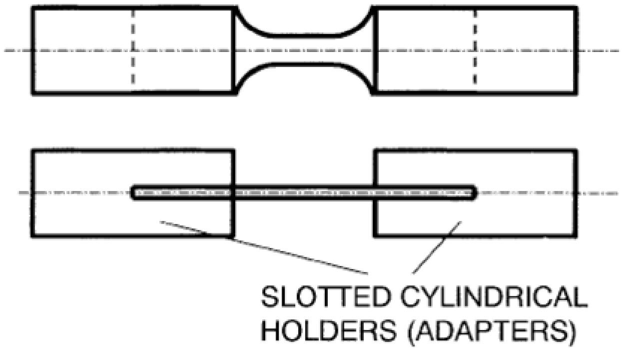

(a) SHTB setup by Gilat using epoxy to mount sample

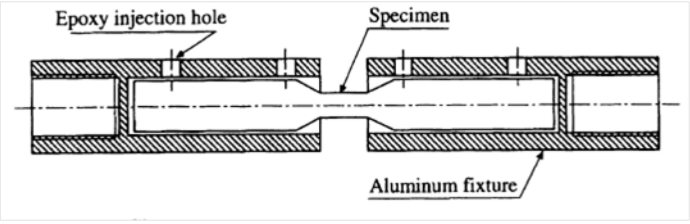

(b) SHTB setup by Eskandari using epoxy to mount sample

Figure 3.4: Comparison of two different epoxy methods to mount sample

[15]. A schematic of each setup is shown in Figures 3.4(a)and 3.4(b) respectively. Both techniques proved successful in obtaining failure of composite materials. Difficulty arises in using this technique for two reasons. First, the composites are adhesively bonded directly to an adapter that is then installed to the bar. The problem that arises from this is it creates an additional interface between the sample and the bar. In SHB testing, additional interfaces are locations in which the strain signals can be lost, distorted or reflected. Because of this, the fidelity of the signals can be jeopardized. Secondly, the test material itself is surround by a relatively low impedance material of the epoxy. Because of this, there will be many loses of the signal between the epoxy and the bar. In general, this was determined to not be an optimal technique for composite testing.

The final technique is a wedge grip. The novelty of the wedge grip is that it allows for mechanical gripping of the sample and can use materials that are of the same impedance as the bars, thus minimizing the losses during testing. The first

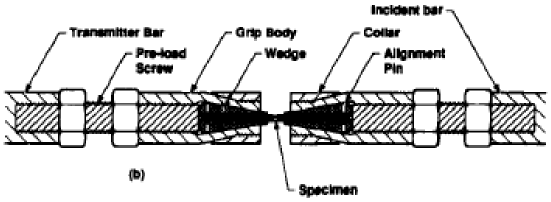

Figure 3.5: Leblanc and Lassila used a wedge grip to mechanical hold the sample

technique of this is seen in Leblanc and Lasilla who used a wedge grip profile to test sheet metal at a high strain rate [56]. A schematic of the tensile testing is seen in Figure 3.5. As seen in the figure, the wedge grip system is actually an extension of the bar through threaded adapters which allow the sample to be preloaded. To ensure further gripping, the researchers used a dowel pin as well.

This technique proved effective in creating tensile failure without the sample slipping, but not without issue. One issue that arises from the use of this technique is that the bar must transfer the load in a way that does not distort the signal and the inclusion of the threaded portions will cause distortions resulting in the strain wave that is measured in the bar to be different from what the test specimen actually experiences. Nevertheless, this proved to be an effective way to do the testing.

Using the lessons from the original Kolsky work, it is desirable to have the sample gripped as if it were an extension of the bar. To do this, an innovative design was developed that incorporated the wedge grip into the bar. This technique creates a unibody wedge gripping system that allows for better transmission of the signal. To incorporate the geometry, a 7° taper was cut into the end of the bar using Electric Discharge Machining (EDM). A sample of the bars with the wedge profile is shown in Figure 3.6. Note that both an aluminum and steel bar are shown in this sample, however, for actual testing, both bars are steel. To prevent opening of the profile as the wedges are pulled through, cylindrical steel clamps are used at the ends of the bar with a diameter equal to that of the bar.

Figure 3.6: The ends of the bars after EDMing showing the profile

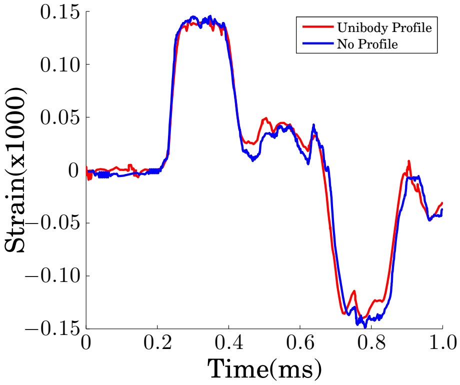

Figure 3.7: Finite element analysis showed that the unibody profile did not affect the strain waves in the incident bar

To ensure that that there was not any significant distortions in the bar due to the profile, a finite element analysis was performed on the bar with and without the unibody profile. The results are shown in Figure 3.7 which indicate that there is no significant distortion of the strain waves through the inclusion of the unibody profile. In addition to the finite element analysis, strain gauges were attached to the bar offset at 120° and showed that near the profile, there is no significant distortion of the wave radially. From the FE analysis and initial pulse testing, it was determined that this would be the ideal technique for gripping a planar sample.

With the profile complete, the only addition that was needed was the use of the wedges. The wedges were fabricated from a similar steel as the bars. To allow increased friction during the test, the wedges were coated with an industrial coating known as Carbinite. Carbinite is a surface treatment that hardens a surface while creating additional texture. The texture ranges from a fine coarseness of 1 to rough coarseness of 4. For this testing, a coating of 4 was chosen. Preliminary testing indicated that the initial release of pressure resulted in an initial movement to the system to frequently moved the sample out of pretension. To combat this effect, the sample is initially tensioned by using a Jacobs Taper drill chuck removal key to drive the wedges forward, and shim stock is placed behind it to maintain the tension. This technique ultimately proved successful.

3.2.4 Enhanced SHTB Analysis Technique

Because of the design features of having a large geometric impedance mismatch between the bars and the samples, relying on just the strain rates from the traditional theory, may not be the ideal way to perform data analysis. For this reason, a new analysis technique has been developed for this testing. This technique includes novel testing measurement techniques through the incorporation of modern technology, namely high speed photography. Similar techniques have been proposed in the past by Moulart et al. [65] and Gilat et al. [21]. While both rely on using optical measuring techniques for determination of the strain time histories in deforming materials at high strain rates, a complete analysis of the dynamic stress-strain response using strain-time history from DIC measurements has not been verified. The current data analysis is performed through a 4-step process (in the case for the validation of aluminum, a 5-step process was done).

1. Verify that a constant strain rate regime exists and measure the strain rate from the strain-time history
2. Verify that dynamic equilibrium exists
3. Identify the stress-time history by using the geometrical amplification technique in the transmitted bar
4. Use time shifting to create the dynamic stress-strain curves

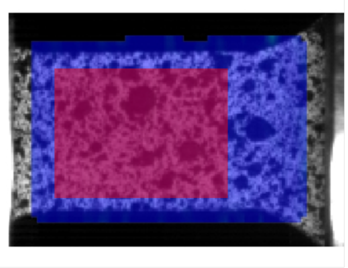

Figure 3.8: Schematic of the average strain definition as selected by the area of interest

5. Determine the yield stress by using a 0.2% plastic offset

In each of the following subsections, a sample data analysis will be done to show how the technique is viable and its advantages versus using the traditional signals.

3.2.4.1 Verification of a Constant Strain Rate Regime

In order to first determine the strain rate, it is first necessary to define the measure of strain. For this work, two strain measures will be presented, however, only one will be used for further data analysis. Strain will be defined as either the average strain or the line strain. A visual representation is shown in Figure 3.8 and 3.9. Within each facet of the DIC, there is a calculated strain measure that is based on the algorithm used by ARAMIS. The average strain reported is the average of the strains over all the facets in the gage section. The gage section used for the calculations is selected to eliminate edge effects.

The line strain is determined by creating two stage points at the ends of the gage section at the center of the width. From this, a line can be created that measures the distance as defined by a number of pixels. In subsequent stages, the change in length is determined. A simple 1D definition of strain is defined as follows:

$$\varepsilon(t) = \frac{\Delta L(t)}{L} \tag{3.5}$$

A schematic of the line strain is shown in Figure 3.9

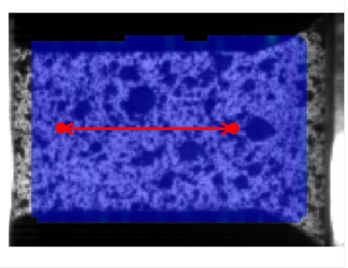

Figure 3.9: Schematic of the line strain definition

While there are two definitions of strain measure, they offer two unique perspectives of how the material strains. Since the 1D wave theory that governs Hopkinson Bar testing does not consider the heterogeneity of the strain rate measure of the material, the average strain gives more of a local information about the average strain in the sample as the material deforms. 1D wave theory is also related to the movement of the bar as the strain wave passes through it, therefore, the line strain is analogous to the measures the bar strains would yield.

Figure 3.10 displays results of a test on an aluminum 5083-0. In the figure, both the line strain and average strain are shown along with a line of best fit to display the strain rate that is observed during testing. Two general trends are seen with this type of analysis. The first is that the strain to failure is only accurately captured by the average strain. This is because the definition of line strain does not consider two-piece failure but rather just the straining that occurs before the two points. When constructing the stress-strain curves, this is an artifact that must be considered. The second trend is that the strain rate of the average strain is lower than the line strain. This is due to the fact that as the material damages locally, relaxation in the undamaged areas begin to occur. Therefore, the strain as measured in the undamaged areas will be lower. This is an effect of the damage causing heterogenous strain rates in the sample.

It is worth noting that the strain-time history that is measured by the line strain is nearly the same if 1D wave theory is considered. Figure 3.11 shows the results

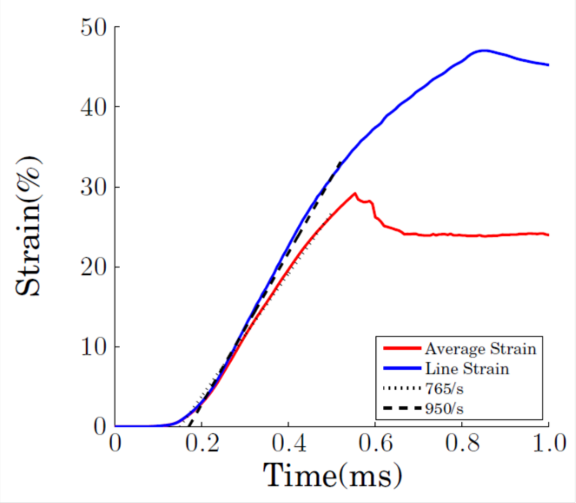

Figure 3.10: A comparison of the average strain and line strain within a strained section

of analyzing the raw strain signals with traditional SHTB analysis techniques to determine the strain-time history in comparison to the direct measure from the DIC. Additionally, agreement between the two measures is dependent on the identification of an 'effective gage length.' The effective gage length for this analysis differed by as much as 12.5% from the actual gage length of the sample. Determination of this effect makes traditional SHTB analysis more difficult.

3.2.4.2 Verification of Dynamic Equilibrium

Due to the aforementioned complications of the traditional strain analysis, determination of a state of dynamic equilibrium could not be gleaned from the signals alone. For this reason, a new way to determine that dynamic equilibrium exists is needed. Strain measurements can be determined directly from the sample itself. In traditional SHTB analysis, the strain is measured on each end and then a force is determined with respect to Figure 3.12. Force 1 is determined by adding the incident and reflected pulses. Force 2 is determined by examining the strain of the transmitted pulse. By using the mechanical properties of the bars, an argument is constructed that dynamic equilibrium exists if these forces are equal.

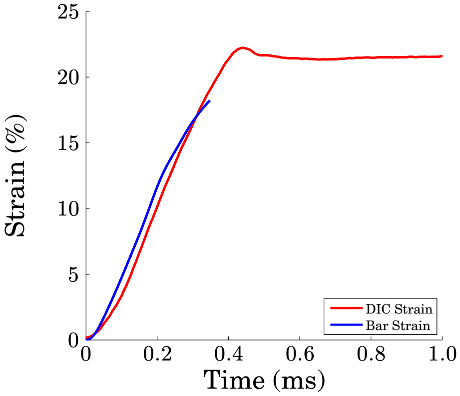

Figure 3.11: A strain-time plot showing the strain-time history that is measured from the bar is nearly identical to the line strain of the DIC

To establish that dynamic equilibrium exists, the average strain of each end of the gage section is measured by using the average strain of 20-30 facets through the width. A schematic is shown in Figure 3.12 From this, the strain-time history can be determined for the right and left end of the sample. If the strains are equal, then it can be concluded the forces on each end of the sample are equal since the material is the same.

Figure 3.12 shows the results of measuring the strain on both ends of the sample during the constant strain rate regime. From this figure, it is clear that the strain is nearly identical on both ends and well within the experimental error. It can therefore be concluded that the sample is in dynamic equilibrium and the creation of the stress-strain response that is determined is accurate and correct.

One of the advantages of this technique is that it eliminates the need to determine the effective gage length of the sample. This is because the extraction of the strain time history is an exact measure from the sample as opposed to using the traditional 1D wave theory. Additionally, this eliminates the need to have a complete separation of the incident and reflected pulses because they are not necessary for the creation of the dynamic stress-strain response.

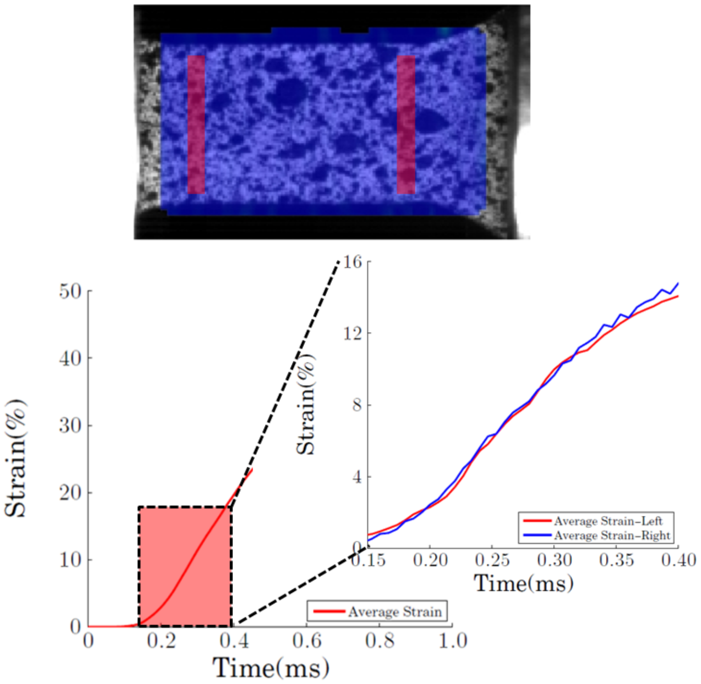

Figure 3.12: Dynamic equilibrium is determined by measuring the average strain on either side of the gage section

3.2.4.3 Determination of the Stress-Time History

Due to the large geometric impedance mismatch, only a small fraction of the incident pulse is transmitted. Due to the relatively large diameter of the bars, the force in the bars is quite low and only marginally above the noise level of the strain gages, thus an amplification of the strain is necessary to determine the stress-time history of the sample more accurately. This can be achieved in one of three ways. The first is to change the material of the transmitted bar. Using an aluminum bar instead of a steel bar can amplify the strain signal 3 times based on the difference in modulus of elasticity (210 GPa to 70 GPa for steel and aluminum respectively). This technique, however, is not a viable option for the present setup because in order to analyze the data, the incident, reflected, and transmitted pulses are needed for stress-strain analysis. For the same reason that the dynamic equilibrium cannot be determined from the strain signals, this technique will not work with the current

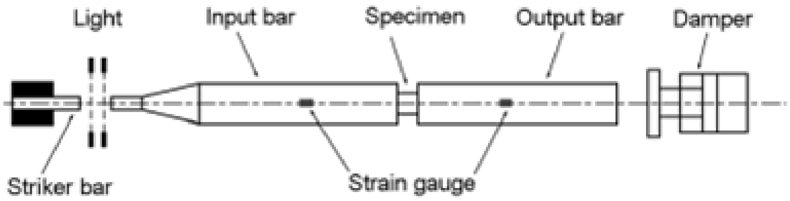

Figure 3.13: A schematic of Liu and Hu's conical bar setup (from Explos. Shock Waves)

setup due to frictional loses.

The second technique is to change the transmitted bar to a hollow shaft. Again, this is not a viable option for this setup due to the unibody gripping fixture. Since the wedge profile is directly manufactured into the bar, a hollow bar cannot be used because the material is needed to grip the sample and reduction of that area would result in reduced mechanical performance. Additionally, threading a solid wedge profile into the hollow bar is not viable because it again introduces additional artifacts that can affect the wave propagation and thusly, the strain/force measurements.

The final technique is a geometrical amplification of an existing bar. Liu and Hu have shown previously that a taper can be used to change the strain in the bar, however, their technique was to taper to a larger diameter [57]. In their effort, Liu and Hu were examining the effectiveness of using conical bars. A schematic of their setup is shown in Figure 3.13

The efforts by Liu and Hu led to the idea of using a taper to create a smaller cross-section. In this case, by reducing the diameter by two results in a four times amplification of the signal, and does require all three pulses to analyze the data. Through the use of finite element analysis, it was determined that a straight taper is necessary to ensure that there is no amplification of the force due to stress-concentrations. A schematic of the reduced geometry in the bar is shown in Figure 3.14. The two inch length allows for proper length for a strain gage to be attached and not be susceptible

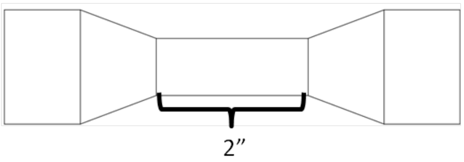

Figure 3.14: A schematic of showing how the bar is tapered to a reduced cross-section to amplify the strain. The total length of the taper is 4 in.

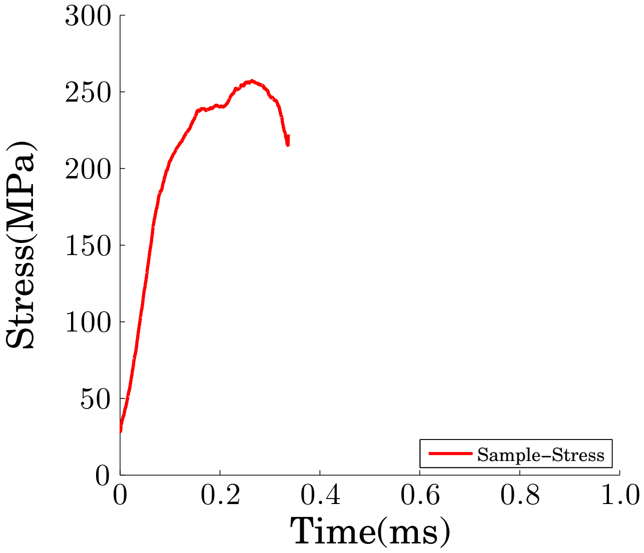

Figure 3.15: The stress time history extracted via MatLab analysis

to false readings due to the transition zone. The finite element analysis confirmed that the force was constant throughout the bar as the stress wave transmitted through the bar.

Since it was determined that the sample is in dynamic equilibrium, it is acceptable to measure the force from only one side of the sample as is the case with the traditional Hopkinson bar theory. A MatLab script (Appendix B has a library of scripts that were used in this dissertation) was written to extract the stress-time history using cross-sectional area of the sample and the strain-time history measured on the transmitted bar. A sample stress-time history is shown Figure 3.15.

3.2.4.4 Time Shifting of Stress/Strain-Time Histories

In order to properly create a strain rate sensitive stress-strain response, time shifting of the stress-time (or strain-time) history must be done to accommodate the losses in the signal and to ensure that the proper points are taken [10]. In general, the time for time shifting can be determined by Equation 3.6 and Equation 3.7 where L_o is the location of the strain gage on the incident bar, L_i is the location of the strain gage on the transmitted bar, C_b is the wave speed of the bar, and C_s is the wave speed in the sample.

$$T_r = T_i + \frac{2L_o}{C_b} \tag{3.6}$$

$$T_t = T_i + \frac{L_o + L_i}{C_b} + \frac{L_s}{C_s} \tag{3.7}$$

Since the enhanced Hopkinson Bar analysis technique has been developed and the strain gage on the incident bar is no longer used, time shifting occurs by normalizing the stress and strain time history by their respective maximum values. The peaks are then aligned such that the maximum occurs at the same point. Similar to what is reported in ref. [10].

3.2.4.5 Determination of Yield Stress

For this validation, the metric of interest is the yield stress as a function of strain rate to determine the high strain-rate response of the aluminum. To do this, a 0.2% plastic strain offset is used to define the yield stress since a clear proportional limit cannot be determined from the plot. A line with a slope of 68.9 GPa (the modulus of elasticity as determined by the static test on the material) was drawn with an x-intercept of 0.2% strain. the point at which the plastic offset line intersects the stress-strain curve is taken as the yield stress. A sample determination for a strain rate of

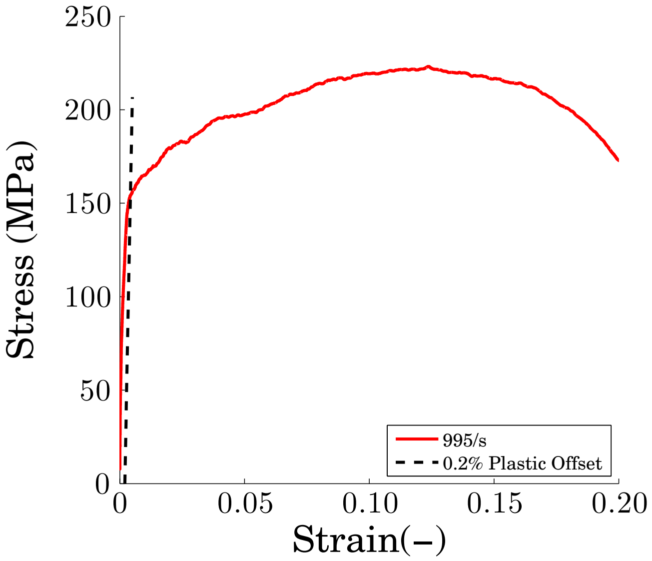

Figure 3.16: A schematic of showing how the yield stress is extracted from the dynamic stress strain curve

955/s is shown in Figure 3.16 where the yield stress is 155 MPa, or approximately 15% higher than the value determined from the quasistatic response as seen in Figure 3.18.

3.3 The High Strain Rate Response of Aluminum 5083-0

While many commercially available aluminum are thought to be strain-rate independent, aluminum 5083-0 has been examined previously by Lloyd [58] in 1980. Over a range of strain rates from 0.1-100/s, aluminum 5083 and other commercial Al-Mg allows show similar strain rate dependent behavior characterized with an increase in yield stress as a function of strain rate. The composition of the alloy is shown in Table 3.1. The -0 suffix indicates that the material has not been work hardened. Since the aluminum 5083-O was shown to have rate dependence in the past, it was selected as the material to be used to validate the SHTB setup.

Mg	Mn	Cr	Fe	Si
4.46	0.84	0.08	0.25	0.15

Table 3.1: Alloy composition for Al-5083

3.3.1 Experimental Details

The SHTB bar that was for this application is relatively large by Hopkinson Bar standards, therefore, a large dogbone sample has been developed for use with the bar. A large gripping section is required to hold the sample in place without slipping. Prior to firing, the sample was pretensioned to prevent slipping by using a Jacobs Drill Chuck removal key to drive the wedges further into the dovetail profile. Afterwards, shim stock was placed behind the wedges to ensure that they did not fall out. The samples were extracted from a rectangular plate using water jet cutting. Prior to testing, samples were examined to ensure no damage in the gage section to act as an initiation point for failure.

Based on 1D wave theory, the strain rate in a deforming sample is related to the inverse of the sample length as shown in Equation 3.4. In order to take advantage of this, the gage length of the sample varied between 6.34 mm (0.25 in.) to 12.7 mm (0.5 in.). Since the striker tube velocity is not measured directly in this test, the firing pressure of the gas gun is used as a de facto measure of striker tube velocities. The pressure vessel was initially loaded with a prescribed pressure between 0.52-2.93 MPa (75-425 PSI). This was determined to be the maximum allowable firing pressure as it was found that pressures above this range created a force larger than the tensile strength of the bar and/or the bolt.

3.3.2 Experimental Results

Quasistatic tests were performed prior to determine the static yield stress in the sample. After testing 15 different firing pressures, it was found that strain rates in

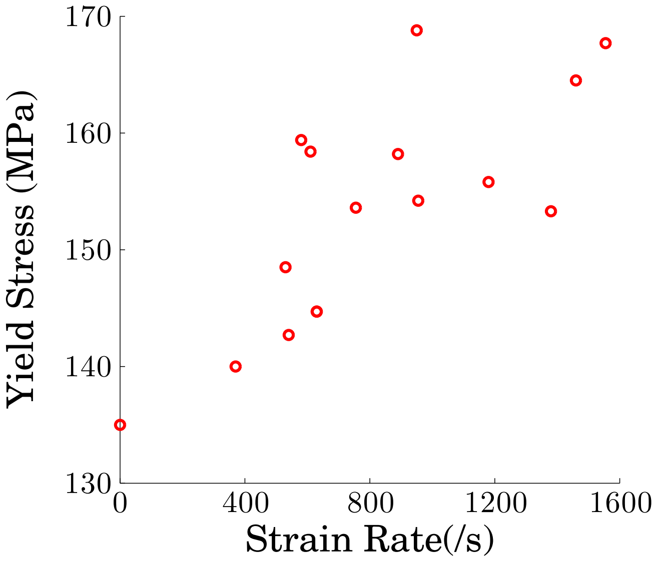

Figure 3.17: The results of high strain rate testing showing rate dependent hardening of the yield stress

the aluminum ranged between 370-1550/s. The results of the yield stress variation as a function of strain rate is shown in Figure 3.17. It is clear from this figure that the yield stress increases with increasing strain rate. The data analysis technique that was developed and presented previously was used to determine this information. The sample was in dynamic equilibrium throughout the loading event and the DIC images offered insight into the failure event itself. This result is consistent with the previous work of Lloyd.

Also of interest is the elevated strain rate, stress-strain response. The results of this are shown in Figure 3.18. As the strain rate increases, so too does the yield stress. It should be noted that the test result shown for the sample at 370/s does not lead to two-piece failure because the strength of the pulse in concert with the length of the pulse did not allow for strain to be fully accumulated in the sample. This could be remedied by having a longer striker tube, but since the metric of interest was the yield stress as a function of strain rate response, this was not pursued.

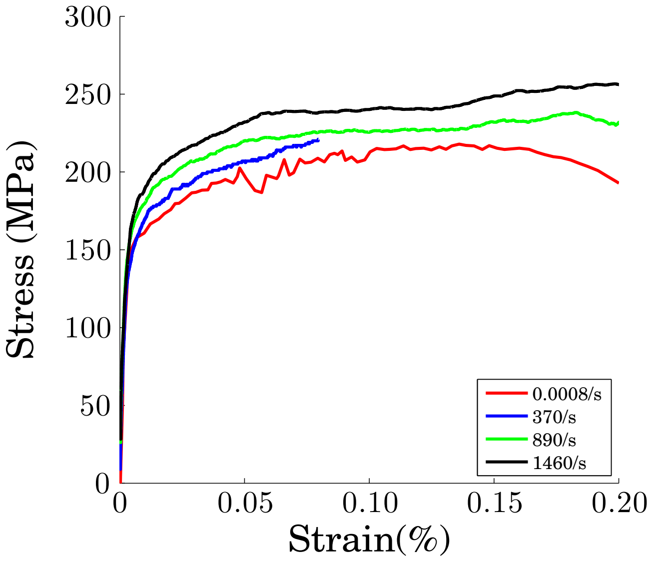

Figure 3.18: The stress-strain response of Al-5083-0

3.4 Conclusions

A Split Hopkinson Tension Bar was developed for planar samples. After surveying the literature, it was determined that to maximize strain wave transfer, it is necessary to have a mechanical connection between the grips and the bar to allow for optimal wave transfer. To do this, a dovetail profile was cut into the bar via Electric Discharge Machining to allow a wedge to be inserted. To validate the setup, a novel Hopkinson bar data analysis technique was developed to extract strains from the sample instead of the bar strains which allowed for the elimination of the need to determine an effective gage length in the sample. Using the new analysis technique, the strain rate dependent properties of a commercial grade aluminum were determined and consistent with prior reported data in the literature [58].

CHAPTER IV

High Strain Rate Tensile Failure of Crossplies

In the previous chapter, a novel analysis technique was applied to the traditional Split Hopkinson Bar testing protocol to shed new insight on high strain rate failure of flat samples. Past literature shows no clear consensus regarding the response of fiber reinforced composite materials under high tensile loading rates. In this chapter, simple layups will be examined to determine their strain rate dependent properties and assess the applicability of the traditional testing techniques to determine their respective mechanical performance.

4.1 Introduction

In the beginning of the dissertation, it was shown that there is no clear consensus within the literature about the strain rate dependent properties of a carbon and glass fiber tow when subjected to high rates of tension. Glass samples were generally found to be rate independent or rate hardening with respect to either the modulus of elasticity or failure strength. The carbon was much more varied with both rate dependence and independence reported. In order to understand the difference between what was reported by each researcher, it is important to understand the testing techniques and the material systems as the difference in the way that the load is introduced into the specimen may lend further insight into the results that have been reported. In general, there are four major techniques that are used to determine these results.

1. Servo-Hydraulic Load Frames
2. Direct Impact Techniques
3. Hybrid Impact/Wave Propagation Techniques
4. Split Hopkinson Tensile Bar (Wave Propagation Techniques)

Servo-Hydraulic techniques are widely used and are highly repeatable, however, the results from the testing tend to be limited in terms of strain rate. Direct Impact Techniques involves directly impacting a text fixture in which the sample is strained very quickly. This is accomplished using a drop weight impact tower or a Charpy impactor. This method does not facilitate dynamic equilibrium in the sample. The Hybrid Impact/Wave propagation relies on a direct impact of a fixture with some sort of striker, generally a hollow tube. The impact results in a tensile wave that is transmitted into the sample, and relies on Hopkinson bar analysis to determine mechanical properties. Finally, the last method is modern Split Hopkinson Tensile bar techniques such as that described in the previous chapter. The latter facilitates a check on dynamic equilibrium in order to extract material properties at elevated loading rates

4.1.1 Strain Rate Dependence from Direct Impact Techniques

A number of researchers have used a Direct Impact Technique to examine the strain rate dependence. Hayes and Adams used a Charpy impact tester to measure the energy absorption of a unidirectional composites [30] and determined that the carbon/epoxy system showed rate softening in the modulus and failure strength while the glass/epoxy system displayed a hardening effect in both modulus and failure strength, however, the carbon fiber was AS4 and the glass was S2. Chamis and Smith presented a technique that involved composite rings subjected to pressures generated by controlled explosions and the strain rate was measured by strain gage attached to the sample [9]. While strain rates of 400/s were achieved, it was found that the carbon/epoxy tensile rupture strength was rate insensitive. Daniel et al. used a similar system and found that strain rates of up to 500/s were acheived in carbon/epoxy system. Daniel observed initial stiffening of the modulus of elasticity and an increase in failure strength. However, both modulus of elasticity and failure strength decreased at the highest rates. They concluded that the composite response was rate insensitive. It should be noted though that while results were similar between the two tests, data analysis is complicated, and it may not be an accurate representation of the material response under high tensile loading rates.

In a series of studies by Al-Zubaidy et al., carbon fiber sheets were tested using a modified drop weight impact tower. It was found that the carbon fiber samples experienced stiffening in the modulus as well as an increase in failure strength up to rates of 100/s [3],[27]. It was reported that there was an increase in strain to failure. A similar setup was used by Shokrieh and Omidi for unidirectional glass samples [99] which determined that the modulus increases, the failure strength increases, and the strain to failure generally remains the same. A study by Armenakas et al. used a similar system of concentric tubes, however, a blast was used to accelerate the tube that impacted the hanging glass/epoxy sample [4] reported the modulus of elasticity increased, however the strain to failure and ultimate tensile strength decreased. This setup, however, is not well suited for high strain rates as it does not allow for the establishment of dynamic equilibrium.

4.1.2 Strain Rate Dependence from Hybrid Impact/Wave Propagation Techniques

Initial work in high strain rate properties focused on Hopkinson Tensile Bar like testing techniques which relied on wave propagation through the material, but did not necessarily reflect the proper mechanics as described by Kolsky. Harding and Welsh used a modified SHTB test in which a hollow bar was launched into a stationary bar in a manner that is similar to a drop weight test [29], [28]. They reported stiffening of the modulus, increase in strength, and an increase in strain to failure. A similar technique with the same findings was observed by Kimura et al. [49]. Groves et al. used a hybrid drop tower and SHTB setup to examine the strain rate effects on DER332-T403 carbon/epoxy material system and reported significant hardening in tension at rates about 50/s, however, no data is reported after 100/s after a nearly 3 times increase in the peak stress from the static results. One key issue in their setup remains that dynamic equilibrium is not able to be easily established due to the fact that wave separation cannot be measured.

4.1.3 Strain Rate Dependence from Split Hopkinson Tension Bar (Wave Propagation) Techniques

The modern Split Hopkinson Tensile bar techniques were developed by Staab and Gilat in ref. [107], however, they relied on a clamp on the bar to generate the pulse. This device was used to test glass/epoxy angle-ply laminates [105], [106] and the authors reported increases in tensile strength and strain to failure. Gilat continued the work and reported that carbon/epoxy laminates at 10°displayed little rate dependence. In general though, Split Hopkinson Tension Bar testing techniques have not been widely used to examine the tensile failure of a unidirectional ply. This is most likely due to gripping and pretensioning issues with the samples

4.1.4 Chapter Overview

While the mechanical testing and analysis techniques are varied throughout the literature and, to date, no researchers have determined the tensile rupture strength of IM7/SC-15 and S2 Glass/SC-15 material system. In this chapter, strain rate dependency will be demonstrated using an intermediate loading rate on a servo-hydraulic load frame. Using this as a motivation, Split Hopkinson Tensile bar testing techniques are used on cross-ply samples to determine the response over a wide range of strain rates. Stress-strain curves are generated and a discussion of the validity of results is framed by using DIC strain fields to examine the mechanics in the static and elevated rate regimes.

4.2 Intermediate Loading Rate Testing

To understand whether or not strain rate dependency exists, an intermediate loading rate between static and dynamic rates of the Split Hopkinson Tension Bar was examined. The dogbone samples discussed in Chapter 2 were tested on a Shore Western loading frame at a rate of 25.4 mm/s (1 in./s). Instead of using a high resolution Digital SLR, a Photron High Speed Camera was used at a framing rate of 60 FPS. The data analysis technique that was used was identical to that described previously in Chapter 2.

The stress-strain response of the glass samples is shown in Figure 4.1. From this figure, the response at increased loading rate is similar to that of the static response. The failure stress is elevated as well as the strain to failure. The slope is generally higher than that of the static samples and the sample still demonstrates a linear elastic response up until failure without damage.

The extracted material properties from the two loading rates are shown in Table 4.1. The modulus of elasticity increase is not shown to be statistically significant

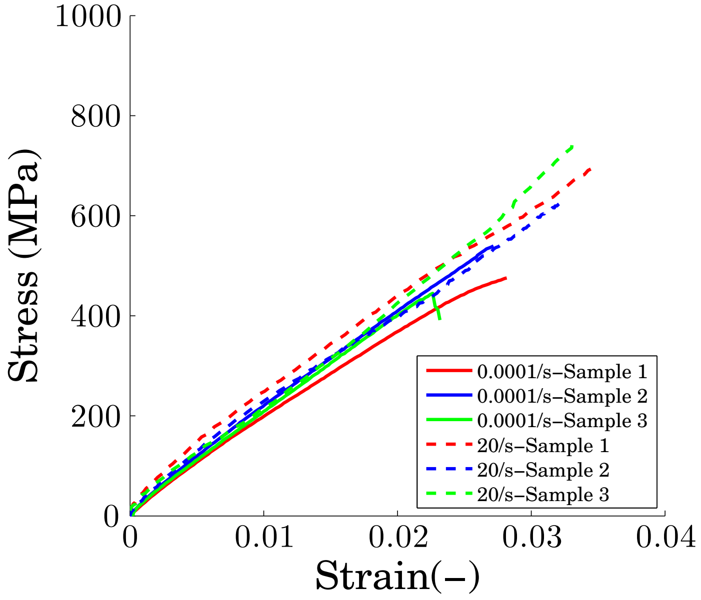

Figure 4.1: The stress-strain response of the glass crossplies at an intermediate loading rate

Sample Strain Rate	Modulus (GPa)	Failure Strain (%)	Failure Stress (MPa)
0.0001	18.5±1.2	3.14±0.18	581.5±45.3
20	20.6±1.5	3.33±0.12	686.0±55.1

Table 4.1: The difference in material properties at elevated rates for the glass crossply

because it is within the experimental error of the measurements. The increases in failure stress and strain are significant and represent a strain rate hardening effect.

The stress strain responses for the carbon samples are shown in Figure 4.2. The response between the intermediate loading rate and quasistatic rate is very similar, however, the statistical analysis shown in Table 4.2 indicate that there is a rate hardening effect in the failure stress as it is statistically significant.

Sample Strain Rate	Modulus (GPa)	Failure Strain (%)	Failure Stress (MPa)
0.0001	64.4±6.2	1.31±0.18	838.5±46.6
20	58.9±1.6	1.62±0.03	955.7±11.2

Table 4.2: The difference in material properties at elevated rates for the carbon crossply

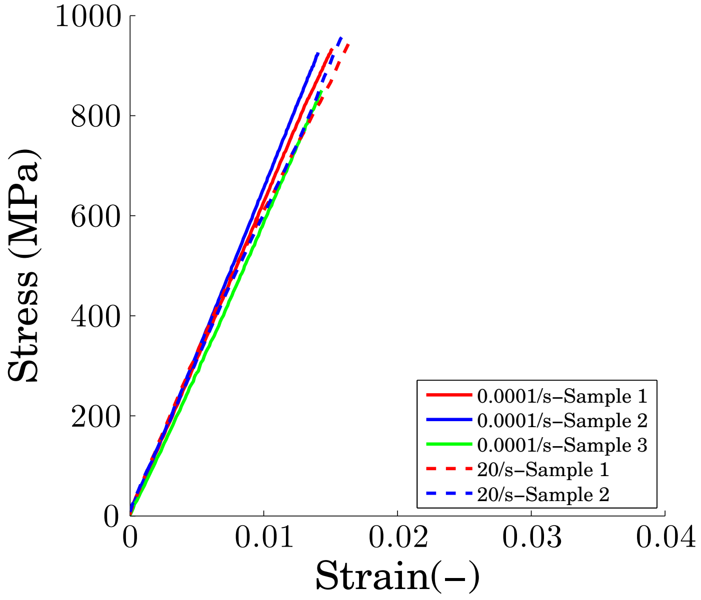

Figure 4.2: The stress-strain response of the Carbon crossplies at an intermediate loading rate

4.3 High Loading Rate Testing

After establishing the initial failure properties of the crossplies at low and intermediate loading rates, the high loading rate response could be examined. In the previous chapter, SHTB testing techniques were introduced and it established the validity of using mechanical contact to introduce the load into the sample. Additionally, it established novel testing techniques that showed that high speed imaging can be used to measure the strain-time history of a sample without having to rely on determination of the so called effective gage length, traditionally used in SHB data analysis.

4.3.1 Experimental Details

Due to extremely large impedance mismatches between the sample and the bar material and a series of tests it was determined that a 38.1 mm (1.5 in.) diameter bar was not ideal for testing the composite samples due to low transmission of strain

Figure 4.3: The Split Hopkinson Tensile Bar at the BLAST Lab (Photo courtesy of M. Pankow via REL)

signals in the bar and losses due to friction. For this reason, experimentation took place at the Ballistic Loading and Structural Testing Laboratory (BLAST Lab) at North Carolina State University under the direction of Dr. Mark Pankow. The Split Hopkinson Tensile Bar that is used at the BLAST Lab conforms to the same mechanics as the bar discussed on Chapter 3, and is a striker tube and anvil type setup. A view of the bar is shown in Figure 4.3

The BLAST Lab experimental setup is made of a 2.13 m (84 in.) incident bar and a 1.83 m (72 in.) transmitted bar. Both bars have diameters of 19.05 mm (0.75 in.) and are made of maraging steel (E=210 GPa, ρ=8100 kg/m^2). While the wave speed of the bar is similar to that in Chapter 3, the geometric impedance mismatch is greatly reduced. Additionally, because of the reduced weight of the setup, there are few losses due to frictional effects. The striker is 300 mm (12 in.) in length. The bar is supported by precision machined bronze bearings.

The gripping mechanism is similar to that of Gilat and other researchers in the way that it uses a collar to attach directly to the bar and is shown in Figure 4.4.

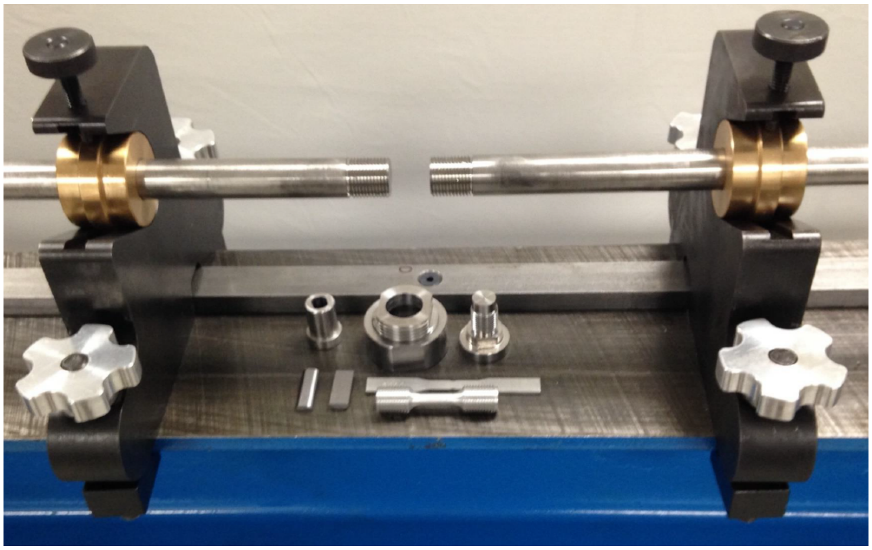

Figure 4.4: The gripping end of the bars at the BLAST Lab (Photo courtesy of M. Pankow via REL)

Force transmission is maximized when an outer thread is machined into the shaft. The collar is threaded on both ends and allows an additional gripping mechanism to be included in the end. The gripping mechanism is a threaded collet with wedge profile on the inside that allows for gripping of the samples via serrated edges. A schematic of the gripping mechanism is shown in Figure 4.5 The wedges are 25.4 mm (1 in) in length and 9.53 mm (0.375 in) in width. Since the samples have a propensity to slip out of the grips, the wedges must be driven into the collet with a pre-tension pressure. For this range of testing, the pre-tension pressures ranged from 6.9-9.0 MPa (1000-1300 PSI) and was applied with a hand operated hydraulic pump. This pressure was found to not damage the sample.

Composite specimens were extracted from $[0/90]_s$ crossply plates in strips via waterjet cutting. The strips were 9.525 mm in width and 60 mm in length (0.375 x 2.36 in). Tabs that were the length of the serrated grips were bonded to the samples using Locktite H3151. Locktite H3151 is an acrylic adhesive that is optimized for bonding steel and aluminum to polymer based materials. Both steel and aluminum tabs were tested, however, it was determined that the aluminum tabs allowed for

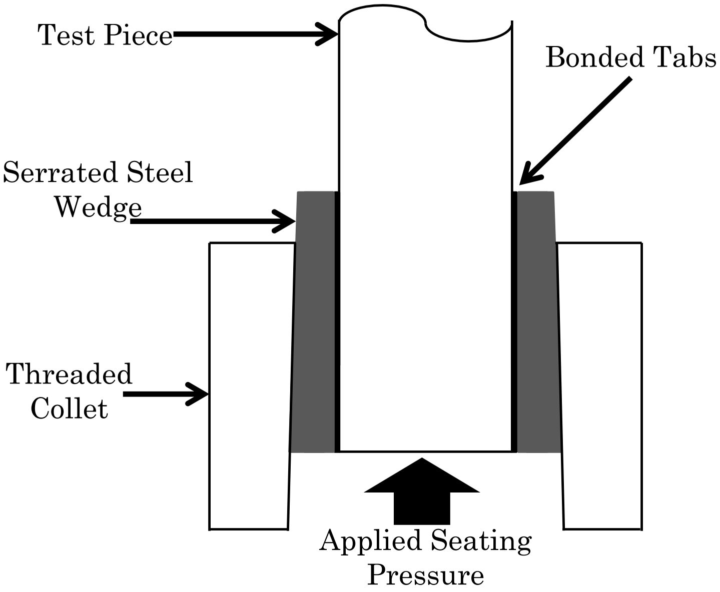

Figure 4.5: A schematic of the gripping mechanism used at the NCSU BLAST Lab

better gripping. The samples were tested over a range of firing pressures from 206-655 kPa (30-95 PSI).

Like the tests discussed previously, high speed imaging in concert with DIC was used to determine the strain time history. A Photron SA.X2 camera was used at a frame rate of 120 kFPS to image the event. The camera was triggered by a TTL signal that was generated when the strain wave passed the strain gage mounted on the incident bar. The stress-time history was determined using the transmitted signal. The data analysis technique that was described in the previous chapters was used for this testing as well.

Of note, the strain rate is measured using the strain-time history that was described in the previous chapter, however, two measures were presented in the average and line strain. In the aluminum samples, the line strain differed from the average strain, however, in the composite samples, there is no discernible difference between them. For this reason, the strain rates that are being reported can be considered to be a structural level or macro-strain that is being applied to the sample.

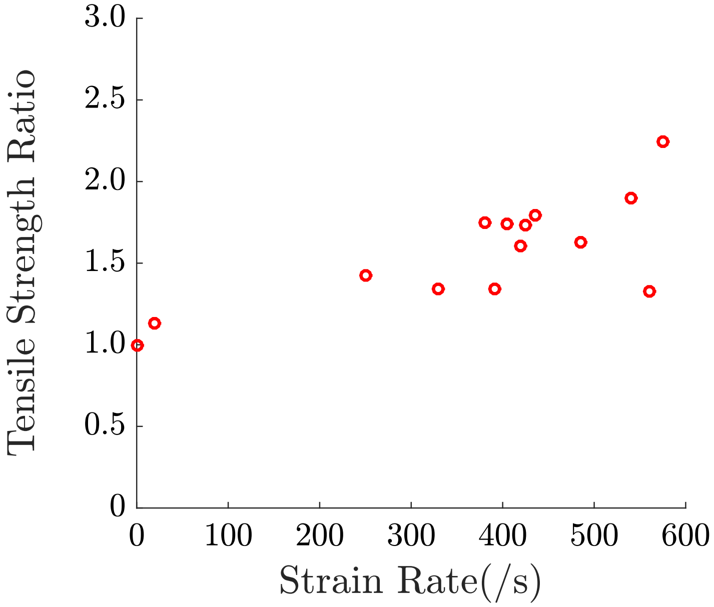

Figure 4.6: The failure stress ratio as a function of strain rate for the IM7/SC-15 material system)

4.3.2 Tensile Response of IM7/SC-15 Crossplies

Samples were tested over a range of strain rates from 250-575/s. From the data analysis, the tensile strength showed an increase with respect to increasing strain rate over the range of rates tested. In order to compare the hardening effects, the samples are normalized by the static rupture strengths. The results of this are shown in Figure 4.6. From this figure, it is clear that strain rate hardening is occurring within this sample and is similar to that of power-law strain rate hardening. Variations exist in the samples because of manufacturing defects and the relatively small size of the sample.

Following the data analysis techniques described previously, stress-strain curves are generated and shown in Figure 4.7. Interestingly enough, two other trends are observed as strain rate is elevated. The first is that the strain to failure generally decreases, and also there is appreciable hardening in the instantaneous modulus (i.e. the tangent modulus increases with increasing rate). Additionally, the mechanics of

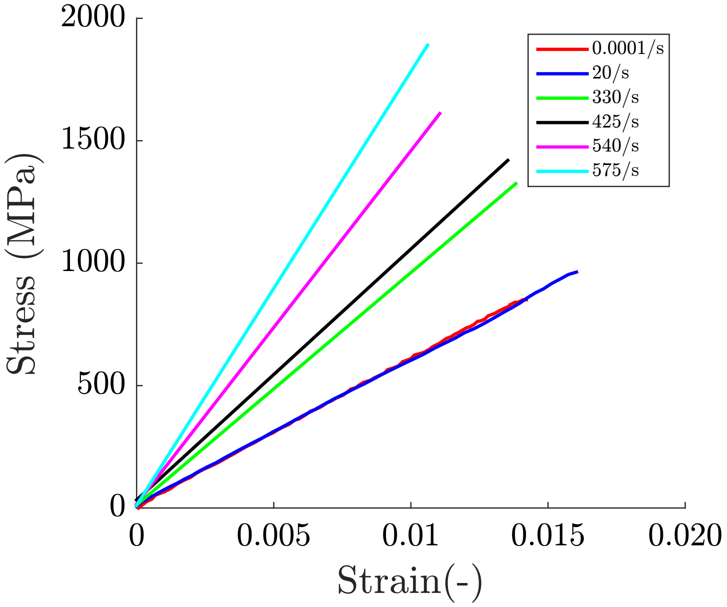

Figure 4.7: The stress-strain response of the IM7/SC-15 material system at various strain rates

the composite remained the same as that of the quasi-static response. In both the low strain rate and high strain rate testing, damage via transverse cracking was observed. This is shown in the subsequent section with the progression of damage.

The increasing stiffness in modulus is generally well accepted within the polymeric materials community [68], however, the validity of it for fiber composites has not been fully established. The best comparison for the validity of the response is to examine the results from literature. Two key studies have examined the effects of elevated loading rate on unidirectional carbon fiber systems. The first study of interest is by Gilat [22] who studied the general response of carbon/epoxy systems using SHTB techniques. Of interest is the fiber dominated response of the IM7/977-2 system. In the 10 degree off-axis loading case, at the stiffness increased with increasing strain rate and the strain to failure decreased up to rates of 400/s.

In a separate study by Taniguchi et al. [111], unidirectional carbon/epoxy composites are examined to determined the effect of ply angle on the response of the composites. By testing a variety of off-axis loading angles with respect to the fiber direction, the tensile strength can be examined further as a function of rate. The authors examine two strain rates: static and 100/s. Their results show that as the angle approaches a unidirectional configuration, there is a significant increase in tensile strength. At 100/s, the tensile strength increases from 382.3 MPa to nearly 635.5 MPa in a 10 degree sample. This is a 1.6x increase in strength.

A comparison can be made between the current work and that reported by Gilat and Taniguchi by examining the results of the modulus of elasticity, yield ratio, and strain to failure. Both Taniguchi and Gilat report an increase in failure strength for the 10°sample. For the two types of carbon/epoxy systems examined by Taniguchi, the 10°off-axis samples increased in strength by 63% and 66% from the static rate to a strain rate of 100/s. Similarly, Gilat reported an increase of about 25% at a rate of 400/s for his samples. In the present work, at a rate of 400/s, there is approximately a 75% increase in the failure strength. Taniguchi does not present stress-strain responses for the materials, however, Gilat observes both lower strains to failure (1.3% for static rates and 0.6% for 400/s) and increased tangent modulus. From these results, it is reasonable to assume that the findings are consistent with previous published results.

4.3.3 Progressive Damage Analysis of IM7/SC-15 Material System

To further examine the validity of the results, it is necessary to examine the progressive failure analysis of the sample at elevated strain rates to ensure that the mechanics are captured correctly for the testing. The DIC results from a crossply test is shown in Figure 7.2(a). In this figure, the sample was tested at a strain rate of 575/s and experienced a significant hardening effect as a function of both modulus of elasticity and the failure stress.

When examining the progressive failure of the sample, it is clear that many of the

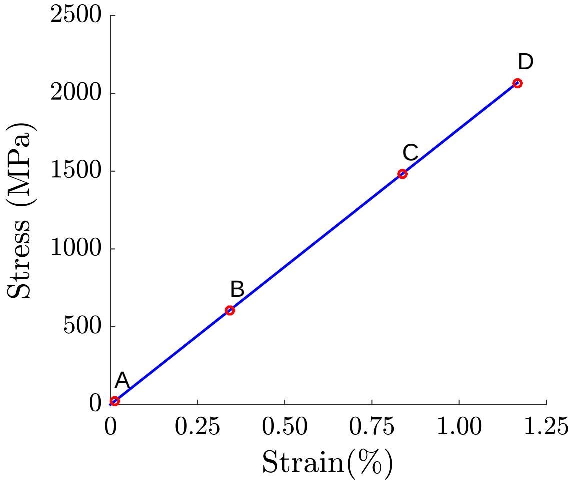

(a) The stress-strain response of a carbon sample

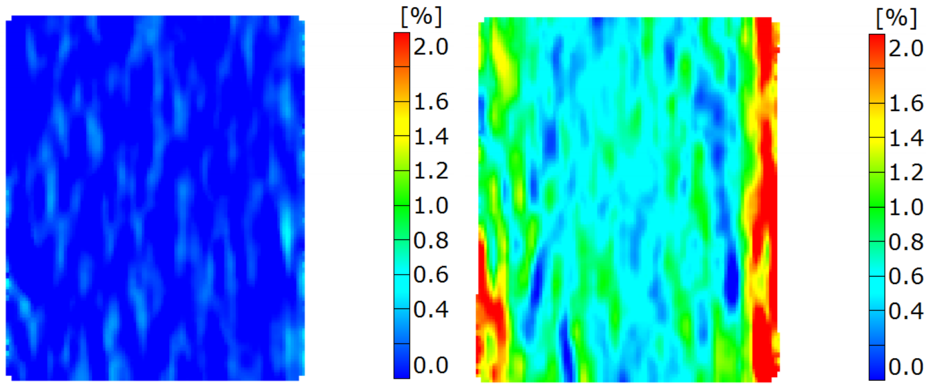

(b) Normal strain at point A (c) Normal strain at point B

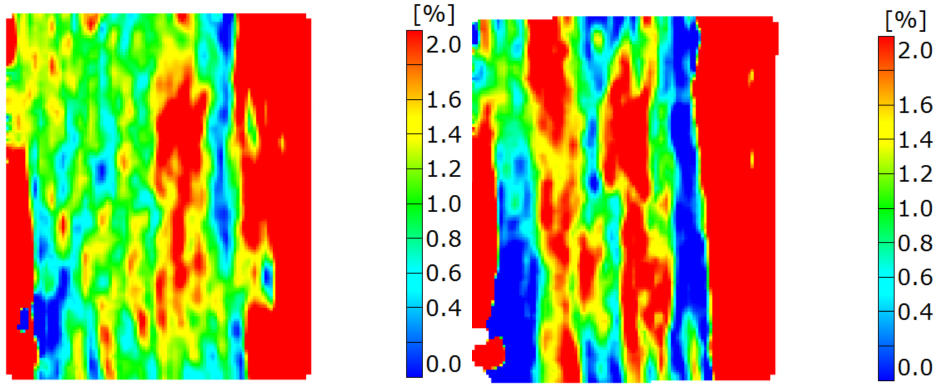

(d) Normal strain at point C (e) Normal strain at point D

Figure 4.8: Schematic showing the progression of damage to a crossply carbon sample at a strain rate of 575/s

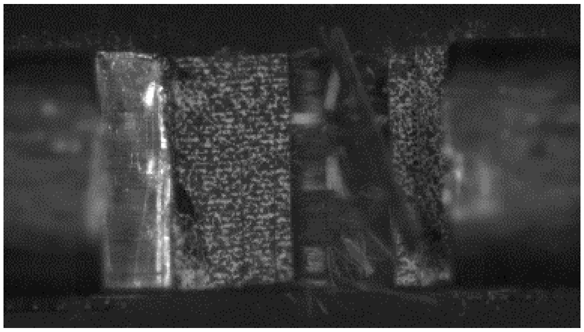

Figure 4.9: Photograph of the sample just after failure, at the gage section away from grips

mechanics that were observed in the static tests presented in Chapter 2 are visible in the failure at high strain rate. In particular, the transverse cracking is very apparent. Figure 7.2(b) shows the initial loading of the sample, however, when strain begins to accumulate in the sample, cracking first occurs near the end of the samples as shown in Figure7.2(c). This effect is expected because much of the clamping force after the wedges have been seated tends to be at the end of the sample in the center section. However, as strain further accumulates, the characteristic cracking pattern is observed as shown in Figure 7.2(d). Finally, at the point of failure shown in Figure 7.2(e), further cracking in the center of the gage section is seen. Five sections are visible with two experience high strains relative to the other regions. This is the full development and opening of the cracks on the outermost ply. This result is consistent with previous testing at lower strain rates.

It should be noted at this time that while the DIC showed that high strain was developing near the tabs and the end of the fixture, final failure occurred in the gage length of the sample and not at the grip. The result of this was two piece failure. This is evident by a comparison of the raw photographs after the failure shown in Figure 4.9.

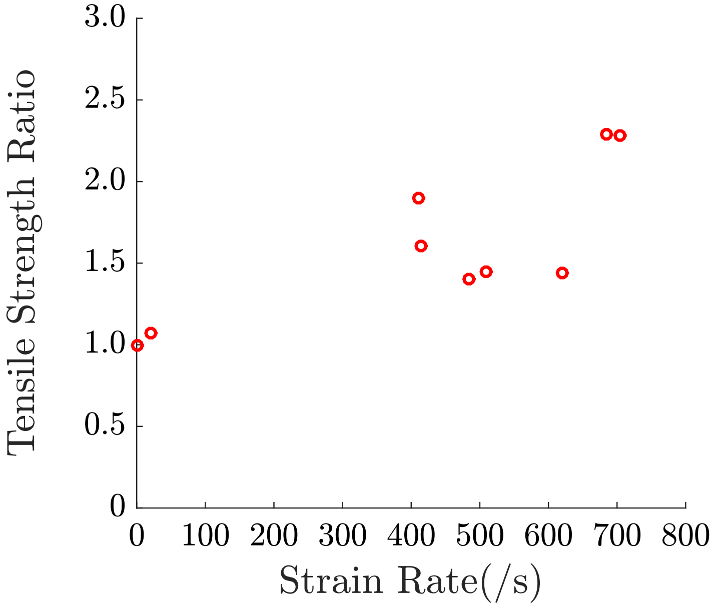

Figure 4.10: The failure stress ratio as a function of strain rate for the S2-Glass/SC-15 material system

4.3.4 Tensile Response of S2 Glass/SC-15 Crossplies

Glass cross-plies were tested in the same manner as the carbon samples and strain rates of 380-705/s were achieved. The results of the tensile strength ratio of the glass samples as a function of strain rate are shown in Figure 4.10. Much like the carbon, there is an increase in tensile strength with increasing strain rate.

The stress-strain responses of the high loading rates are shown in Figure 4.11. Of particular interest is that at increasing strain rates, there is an increase in modulus as well as the ultimate tensile strength, however, the failure strain remains relatively unchanged.

These results show an interesting behavior, and while the literature for glass samples significantly less than that of carbon samples, other studies in the past have looked at glass composites. Yazici [125] studied individual S2 and S2/epoxy interfacial behavior at elevated loading rates. From these findings using the ASTM standard for a single fiber testing, it was shown that a single S2 Glass fiber exhibits a strong

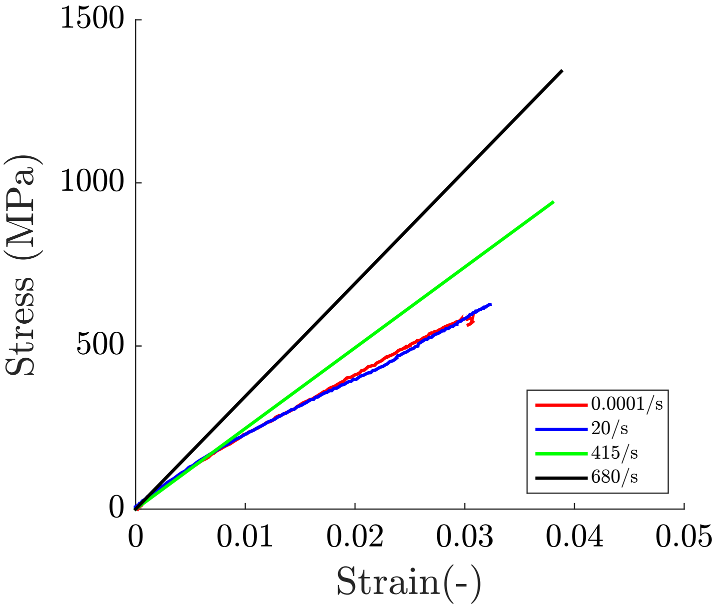

Figure 4.11: The stress-strain response of the S2-Glass/SC-15 material system at various strain rates

dependence on loading rate. In low to intermediate rates (0-25 mm/min), the fiber's tensile strength increases greatly, followed by modest hardening (25-100 mm/min) before decreasing at the highest end of loading rates (>100 mm/min). Of importance though, the strength was still higher than the lowest loading rate. This same trend was observed with the modulus of elasticity of a single fiber.

A note should be made at this point that the rupture of glass fibers is difficult to do experimentally because of the relatively poor interfacial bonding between the glass tows and the SC-15 matrix itself. While two piece failure was observed in the high rate tests, two-piece failure was not observed as clearly in the low strain rate tests. The low rate tests may be more fiber pull-out and interfacial dominated failure than a true ruptured failure. For this reason, it may be to better to consider only the trend from the high strain rate regime. A conclusion that the glass samples harden at a greater rate than the carbon samples relative to the static stress cannot be made without further experimentation to ensure that clear tensile rupture occurs within the quasi-static samples.

4.3.5 Progressive Damage Analysis of S2/SC-15 Material System

Much like the carbon samples, the glass samples displayed the same type of progressive damage pattern that was seen in the static tests. The progressive damage is shown in Figure 4.3.5. The stress-strain curve for a sample subjected to a strain rate of 705/s is shown in Figure 4.12(a). The initial analysis of the unstrained sample is shown in Figure 4.12(b), however, the sample quickly strains and the characteristic cracking is observed and propagates in Figures 4.12(c), 4.12(d), and 4.12(e). At the point of crack saturation, the outer ply fails and two piece failure is observed in the sample.

While the crossply carbon and glass display similar mechanical behavior, the progression of damage is much more apparent in that of the glass than the carbon. This is a function of the strain to failure difference between the two samples. In the carbon samples, cracks occur and saturate prior to failure, however, at the reduced resolution of the camera, the DIC is not able to resolve it as well as the high resolution images of the static tests. This effect is more pronounced in the glass samples because as the outer ply cracks, it then opens as the material is strained further. Since the glass sample experiences higher strains to failure, it results in larger openings in the cracks and gives the appearance in the damage analysis of a much more pronounced appearance.

4.3.6 Tensile Response of In-situ Matrix Properties using Crossply Samples

In Chapter 2, a discussion about how the in-situ matrix properties can be determined by performing a simple $[+45_2/-45_2]_s$ tension was presented. This test was shown to be highly repeatable and offered consistent failure in the gage section of

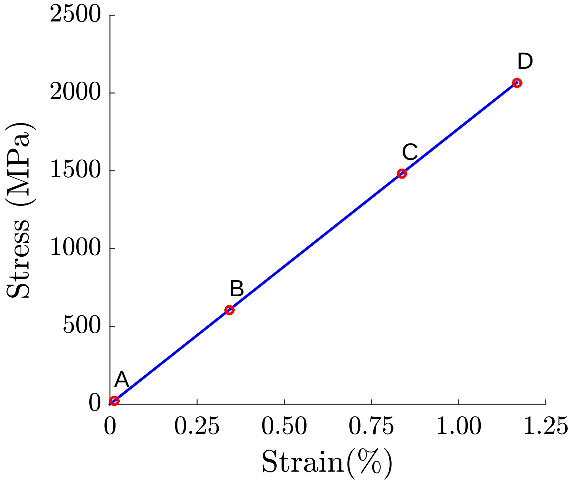

(a) The stress-strain response of a glass sample

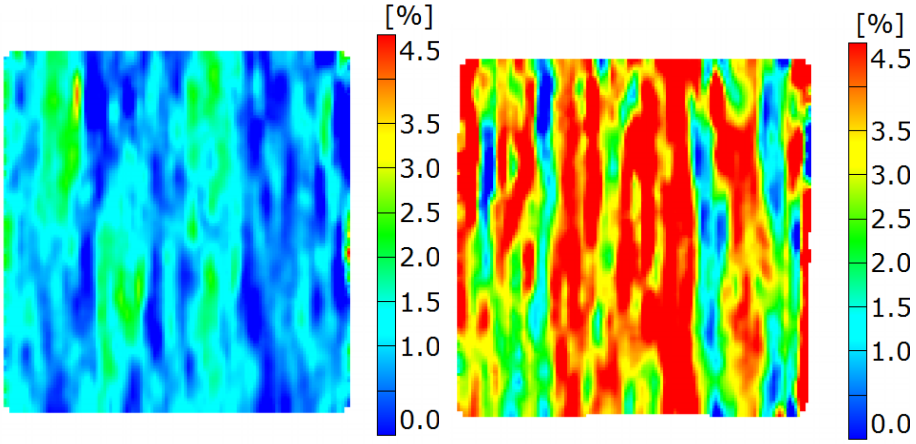

(b) Normal stress at point A

(c) Normal stress at point B

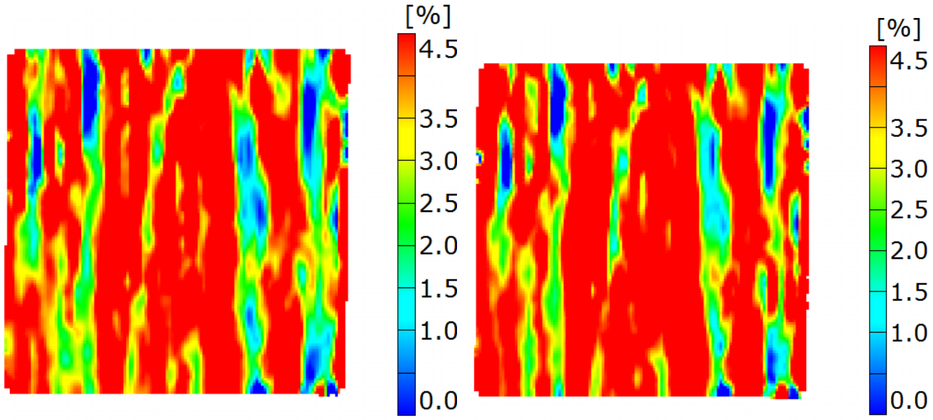

(d) Normal stress at point C

(e) Normal stress at point D

Figure 4.12: Schematic showing the progression of damage to a crossply glass sample at a strain rate of 705/s

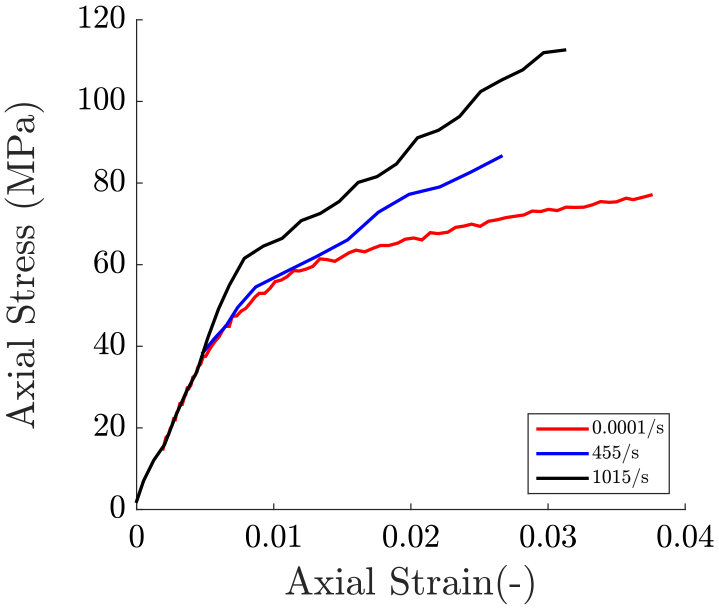

Figure 4.13: The stress-strain response of the $[+45_2/-45_2]_s$ at various strain rates

the sample. The mechanics of this test are captured correctly if the ratio of the gage length to the width of the sample is three or greater. This is because it allows to for transverse cracking to occur entirely within the gage section.

To date, there is no known study that has examined the rate dependency of the in-situ matrix properties, namely whether or not rate dependency exists. For this reason, one final set of tests was performed on the SHTB on a $[+45_2/-45_2]_s$ using the geometry that was used previously by Gilat in ref. [22].

While in excess of 10 samples were tested, the test results presented difficulties to extract data for a number of reasons. In order to ensure the validity of the results, the strain fields need to be properly examined to determine if the sample alignment is correct. If the sample is misaligned, it eliminates the state of shear in the gage section in which the matrix is loaded. Additionally, because it is a matrix dominated response, the strain signals in the transmitted bar needs significant amplification which can be achieved through the amplification of the signal or mechanical amplification. Furthermore, in order to determine the strain rate dependence of in-situ matrix response, there is a necessary requirement to go through the transformations described in Chapter 2. These transformations require a sizable amount of data and measurements for the axial and transverse strains, and cannot be taken at the necessary rate to do this. Figure 4.13 shows the results of 3 tests without transformation of the coordinates (the response of the composite, not the matrix properties). While the exact response of the in-situ matrix properties at rate cannot be determined, these curves suggest that the in-situ matrix properties are rate dependent.

4.4 Conclusions

Cross-ply samples of IM7/SC-15 and S2 Glass/SC-15 were subjected to a variety of strain rates to determine the rupture strength of a tow as a function of strain rate. It was shown that in both material systems there is significant hardening effects that occur with elevated strain rates. In particular, a stiffening effect is observed in the modulus and the failure stress is higher than the static strength by as much as twofold. The carbon samples showed increasing brittle behavior as the strain to failure decreased with increasing loading rate, however, the failure strain of the glass samples appeared to have no effect from the strain rate. The mechanics of the sample were analyzed through examination of the DIC measurements and images. It was observed that the materials displayed the same transverse crack saturation prior to two piece failure was occurring in the sample as it did with the static testing. Finally, an attempt to determine if the in-situ matrix properties were rate dependent was unsuccessful in generating stress-strain responses that yielded useful data. The limited amount of data was inconclusive

CHAPTER V

Use of a Shock Tube for Generation of High Strain Rate Multiaxial Tensile Stress States

The previous two chapters have been used to provide a framework for traditional 1D high strain rate testing. This chapter is concerned with the need to understand the multiaxial response of composite materials. While shock wave mechanics and shocktubes have been around for over 150 years, the loading of flat plates using a shock tube is relatively new. In this chapter, shockwave transverse loading of a flat thin plate is introduced in the context of a commercially available aluminum plate. To validate the experimental setup, a finite element model is presented with material rate dependence included to demonstrate how high strain rate properties can be extracted through test measurement and associated analysis.

5.1 Introduction

Traditionally, extraction of rate dependent stress-strain relationships is performed using a Split Hopkinson Pressure Bar (SHPB) testing techniques as shown in Chapters 3 and 4. This technique has been widely used to obtain stress strain response of aluminum in both thin [101] and in thick samples, [77, 133, 11]. While the response of aluminum and other metals at elevated rates is well established by SHB under uniaxial strain states, limitations occur in the test due to reliability of data in the intermediate strain rates. This is due in part to the relatively fixed setup of the SHPB testing apparatus since it is difficult to change bars, striker bars, etc. Because of the fixed nature of the setup, it is difficult to measure strain waves at low to intermediate strain rates without modifying the existing test apparatus. For example in [26], three rates are used in the range $\leq 10^{-1}s^{-1}$ using simple conventional quasi-static tests, and three points for rates $\geq 10^{3}s^{-1}$ were determined. In the range of strain rates 10^1-10^3, no data is reported, and in the design of primary structures for automotive or aerospace applications, it may not be wise to design by use of interpolation or curve fitting between the strain rates.

The limitation at intermediate strain rates is also observed in previous work with automotive sheet form aluminum alloys[101] where the lowest strain rate value reported is $600s^{-1}$. Measuring the material response at low to intermediate strain rates can be done through proper amplification of the strain wave in the transmitted bar. Amplification of the signal can occur by using a material with a lower modulus of elasticity. For example, the use of bars made from viscoelastic materials such as nylon have been used and shown to be able to be used for the SHPB setup [133]. Intermediate strain rate stress-strain behavior presents challenges because of the wave propagation time in long bars. The use of nylon bars for example, greatly decreases the wave speed within the bar and can allow for intermediate strain rate testing.

The difference in mechanical behavior between multiaxial and uniaxial response has been of great interest, particularly in the field of manufacturing for sheet metal forming. The static multiaxial response of sheet metal has been examined in great detail using the so called "bulge test." This test is used to understand the forming limits of sheet metal. The bulge test consists of applying a hydrostatic pressure to a circular specimen. Traditionally, the bulge test is a static test, however, the need for dynamic characterization was first addressed by Broomhead and Grieve [8] in 1982 in which a drop-tower and water hammer-rig was used to load the specimen at a variety of strain rates. A similar testing rig was used by Pickett et. al. [86]. More recently, researches have combined the appreciable features of the SPHB with the bulge test to create a dynamic bulge test. First completed by Grolleau et. al. [25], the authors modified a traditional SHPB by incorporating a so called "bulge cell" and viscoelastic bars. The bulge cell acted like a traditional hydraulic bulge test, but allowed the input bar to dynamically compress the fluid resulting in elevated strain rates. Ramezani and Ripin further refined this method by eliminating the fluid by adding a rubber pad to load the material [91]. Both investigations incorporate an inverse modeling technique to determine the material properties, however, in the case of ref. [91], this is more difficult due to the added complexity of the rubber in contact with the specimen. Grolleau notes, that the method is limited due to strain inhomogeneities through the thickness due to the small specimen size and notes that incorporation of Digital Image Correlation methods (DIC) would be an added benefit that may eliminate the need for inverse modeling.

Other techniques have been developed to examine a multiaxial response including blast or shock loading where out of plane measurements can be recorded using DIC [116]. Blast loading of aluminum has been examined with explosives using thin aluminum [121], and aluminum welded plates in [7]. Shock loading has been studied in detail and is generally well understood as shown in [118] and with respect to aluminum in [41], however, it has not been used for extraction of rate dependent multiaxial material properties.

In this chapter, aluminum 3003 is shock wave loaded using a conventional shock tube. Specimens with different thicknesses are used to obtain a range of strain rates. The strain fields and displacements are recorded using DIC and the results are compared against a finite element model of the test configuration to extract the bi-axial rate dependent constitutive response of aluminum. This chapter demonstrates the ability to use a shock tube to extract bi-axial strain rate dependent mechanical properties.

5.2 Material

Aluminum 3003, an aluminum/manganese alloy, has been shown to have little rate dependence at strain rates lower than $10^{-3}s^{-1}$ [35], but has a significant strain rate dependence at rates above this threshold as shown in [26]. The samples were obtained by cutting shim stock to a 108 mm (4.25 in.) by 108 mm (4.25 in) specimen using a shearing press. Three thicknesses were used for testing with nominal thicknesses of 0.51 mm (0.020 in.), 0.64 (0.025 in.), and 0.76mm (0.030 in.). The thicknesses were accurate to within 10% as specified by the manufacturer. Within the specifications given by the manufacturer, it was determined that the treatment on the 3003 aluminum was H-12, view Table 5.1. The stress-strain response for Al-3003-H12 curves and material properties were obtained from the Atlas of Stress Strain Curves [1] and are shown in Figure 5.1. In addition to the stress-strain behavior, the atlas of Stress Strain response curves also gives the materials yield stress. This yield stress was used as the static yield stress.

Type of Aluminum	Density	Modulus, GPa (MSI)	Yield Stress, MPa (KSI)
3003-H12	170 (2730)	68.9 (9.99)	119 (17.3)

Table 5.1: Material Properties Used for Testing

5.3 Experimental Method

Shock loading of plates can be thought of as equivalent to performing a standard bulge test with air instead of a fluid. This technique has a number of advantages and disadvantages in comparison to a traditional bulge test. In a standard bulge

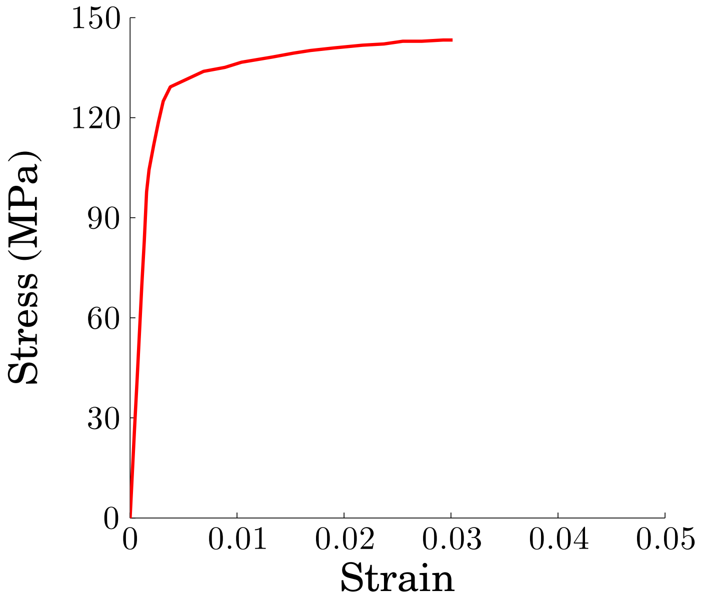

Figure 5.1: The stress-strain response of Aluminum 3003-H12

test, a finite volume of fluid is compressed to allow hydrostatic loading on a circular plate. Traditionally, this is limited to static testing rates and only recently has been adapted to high rate testing. Since the bulge test is typically used for determining sheet forming strain limits, it is often tested to failure. This results in fluid being released from the failed surface.

The shock tube consists of two parts, the driver section and the driven section as shown in Figure 5.2. These sections are separated by a diaphragm, which controls the burst pressure. For this testing, mylar sheets of a constant thickness were used as diaphragms because of the repeatability of burst pressures. The driver section is filled rapidly with helium until a pre-determined burst pressure is reached. The difference in pressures between the driver and driven sections causes a shock wave to form which is propelled down the shock tube in excess of Mach 1, the shock velocity being based on the pressure ratio between the drive and the driven section. When the shock wave impacts the plate situated at the end of the driven tube, it creates a large uniform pressure on the plate, situated at the end of the driven tube, and is subsequently, reflected back down the shock tube. More detail can be found in [79].

While the fluid based bulge test is generally limited to low rates, the shock tube is well suited for determination of intermediate to high rates due to the large amount of control over developing a shock wave and subsequent pressure within the tube. The equations describing pressure waves are well described in ref. [92]. There are a number of controls that can be applied to achieve a variety of rates including using heavier gases and depressurizing the shock tube. Heavier gasses travel more slowly down the the tube and result in lower pressures whereas lighter gases allow for higher pressures. Additionally, by applying a vacuum to the tube prior to bursting, higher plate pressures can be achieved. This type of control is more difficult to obtain in other testing techniques.

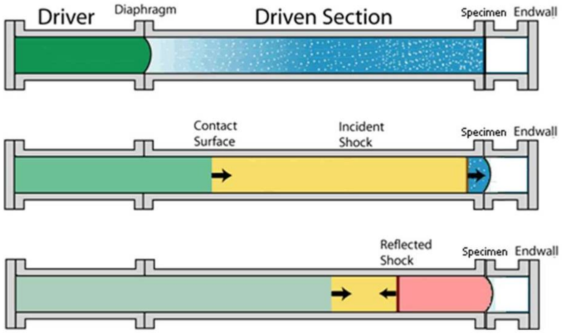

Figure 5.2: Schematic showing the shock tube setup [79]

Information about the shock wave speeds and pressures were determined from pressure transducers implanted in the shock tube. A stereo pair of Photron High Speed Cameras were used to capture a series of images used for digital image correlation (DIC) and determination of the out of plane plate displacement and strain fields from a random speckle pattern that is applied to the surface of the plate material. A framing rate of 100,000 fps was used which allowed an image size of 320x192 pixels. A sample speckle map is shown in figure 5.3. The facet size used for the DIC software was 17 pixels with a step size of 2 pixels.

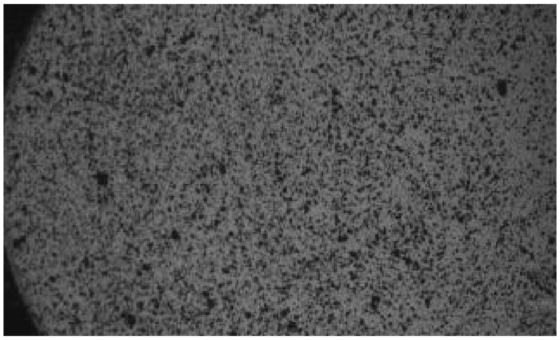

Figure 5.3: Sample Speckle pattern as seen from left stereo camera

For each of the three thicknesses, three burst pressures were used to create a range of strain rates in the plate specimen. The burst pressures were determined by the number of stacked sheets of mylar used for the diaphragm. Each burst pressure and plate thickness test were run in triplicate to ensure repeatability, producing results from 21 shock tube tests.

5.3.1 Calibration of Shock Plate and Determination of Pressures

In order to ensure the uniformity of the shock across the plate surface, a shock calibration plate was developed. The plate had pressure transducers placed radially and was made from 19.05 mm (0.75 in.) thick 1018 steel. A schematic of the shock tube setup with the calibration plate is shown in Figure 5.4, which shows a schematic of how the pressure transducers are implanted in the shock tube and in the calibration plate. Due to the thin nature of the tested samples, calibration took place at shock waves generated from burst pressures of 0.779 MPa, 1.63 MPa, 2.28 MPa (113, 237, 330 PSI). The pressure traces for one of the tests is shown in Figure 5.5. The data has been filtered using a simple moving average to allow for visualization of the signals.

Of particular interest from the results shown in Figure 5.5 are the pressure traces from transducers (3) and (4) which are on the plate. Since these two pressure traces are in agreement, a uniform pressure on the plate can be expected. Additionally, the pressure seen by the plate is also recorded by transducer (2). This is important

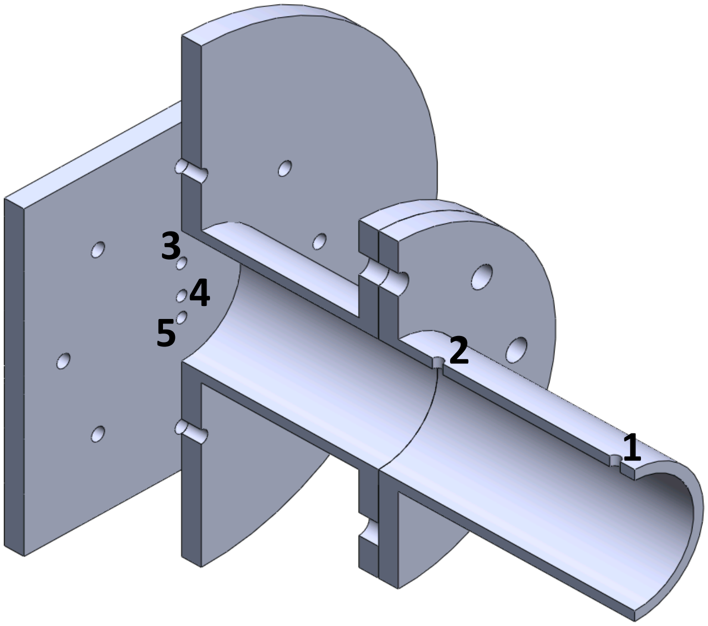

Figure 5.4: Location of pressure transducers in calibration plate (numbers correspond to pressure transducer numbers)

because as the shock wave reflects back, it allows for an accurate time/pressure history trace to be recorded without the transducers on the plate. This signal will ultimately be used as an input for the finite element model. The results showing the maximum pressures for the transducer signals are given in Table 5.2. The raw signals were used when reporting these averages. It should be noted at this point that while, 5 pressure transducers are shown in setup, only four are shown due to the channel limitations of the oscilloscope. Additional tests were run in other configurations to ensure that the a uniform pressure wave occurs on the sample.

Burst Pressure, MPa	Pressure Transducer 3, MPa	Pressure Transducer 4, MPa	Pressure Transducer 2, MPa
0.78	0.76 ± 3.13%	0.76 ± 6.80%	0.71 ± 3.25%
1.63	1.33 ± 3.68%	1.32 ± 3.32%	1.34 ± 1.49%
2.28	1.89 ± 1.55%	1.88 ± 2.70%	1.78 ± 1.41%

Table 5.2: Maximum pressure comparisons for all three burst pressures

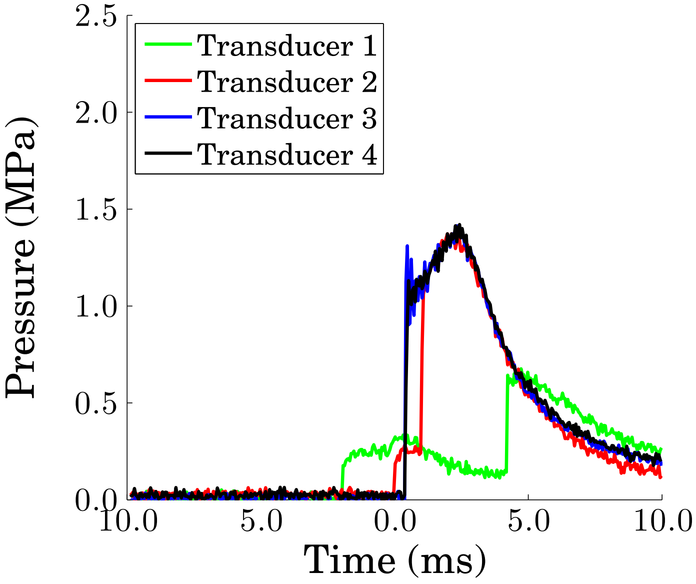

Figure 5.5: Pressure time history for flat plate

5.4 Experimental Results

Each of the samples was subjected to a shock load and the average burst pressure and out of plane displacement for the triplicate tests for each specimen was recorded as shown in table 5.3.

Nominal Thickness, mm	Burst Pressure, MPa (PSI)	Plate Pressure, MPa (PSI)	Out of Plane Displacement, mm (in)
0.020	0.78 (111)±2.25%	0.68 (98.6)±8.29%	6.84 (0.27)±2.64%
0.020	1.48 (214)±1.42%	1.16 (168.2)±2.49%	11.53 (0.45)±9.54%
0.025	0.75 (108)±2.44%	0.62 (90.1)±3.00%	6.64 (0.26)±7.89%
0.025	1.49 (215)±0.71%	1.15 (166.8)±1.01%	10.1 (0.40)±3.98%
0.030	0.76 (108)±3.20%	0.67 (97.8)±1.08%	4.84 (0.19)± 4.38%
0.030	1.49 (217)±2.24%	1.19 (172.6) ±2.73 %	7.67 (0.30)±3.43%
0.030	2.34 (339)±4.64%	1.83 (265.4)±5.33%	11.83 (0.47) ±6.94%

Table 5.3: Average results for the tests

Full-field measurements were made using commercially available Digital Image Correlation software, ARAMIS. These measurements provided the deflection time-histories and strain time-histories. These results together with the pressure time-history was used in the comparisons against the finite element simulation reported later.

The out of plane displacements results for two thicknesses are shown in the following section. Of particular interest is the shape of the response. When subjected to a shock load, the plate responds with an oscillatory behavior. This is only observed in a case where plasticity has not completely occurred. In general, if the plate is fully plasticized, it does not oscillate due to the plastic energy dissipation that overcomes the inertia, and begins to pull out of the clamping ring. This will be discussed in greater detail in conjunction with the computational model. The cause of pullout was generally well understood, and was not observed in all tests. In order to ensure the validity of the experiment, pull-out needed to be examined. The methods for determining whether or not pull-out occurred will be discussed in the following sections. A test was only considered a valid test if pull-out did not occur or was minimal.

5.4.1 Out of Plane Displacement Time-Histories

The out of plane displacement results were taken from each of the corresponding DIC data. Each of the three tests for a specific specimen thickness were examined to determine the out of plane displacement distribution for the same burst pressure. Tests which exhibited pull-out were not considered. While the burst pressures are similar, the plate pressures may differ due to the gas loading rates of the driver section. Some sample plots showing the distribution for the out of plane responses is given in Figure 5.6. The response is dependent on the plate pressure, although the burst pressure may not always correlate with the plate pressure. Plate pressures that are the same show a similar response, as seen in Figure 5.6(b). There can however, be larger distributions based on changes on pressures. Since the specimen pressure is measured from the transducer closest to the specimen clamp, this pressure time history is used in further discussions. The final deformed shapes can be seen in Figure 5.7.

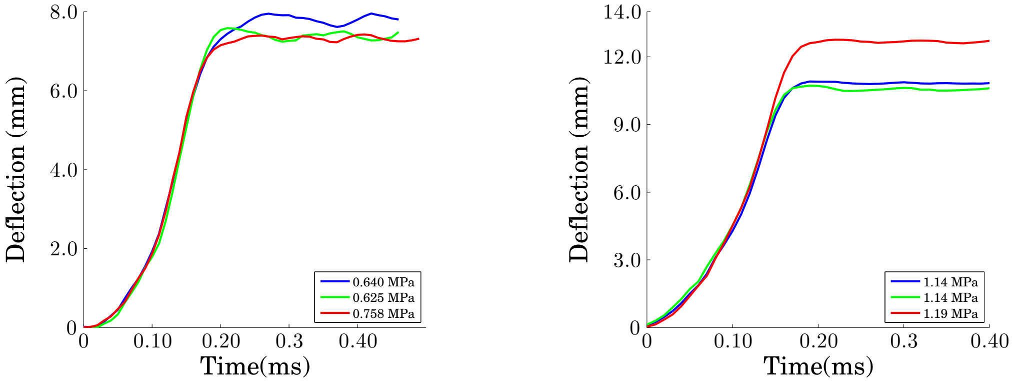

(a) Deflection response for 0.76 mm sample at same burst pressures

(b) Deflection response for 0.51 mm sample at same burst pressure. The out of plane displacement for the highest pressure is large due to pull-out of the sample from the clamping ring

Figure 5.6: Variation in experimental results for similar burst pressures

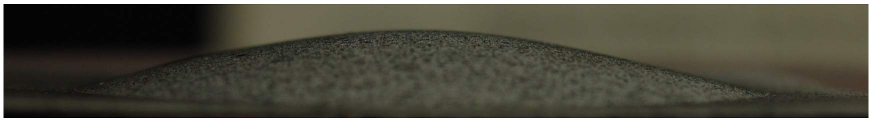

(a) Final deformed state for 0.84 mm at 1.186 MPa

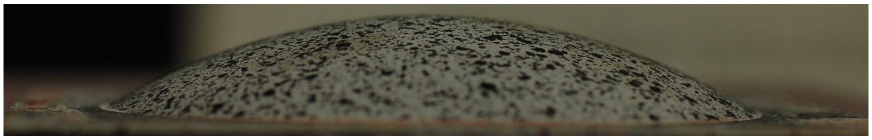

(b) Final deformed state for 0.82 mm at 1.94 MPa

Figure 5.7: Final deformed shapes for two samples at different plate pressures, viewed from the side.

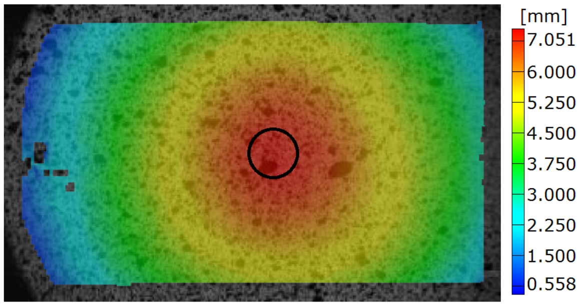

Figure 5.8: Strains and displacements were averaged over crown of plate using an averaging box similar to the one shown here

5.4.2 Strain Fields and Strain Rates

To determine the maximum strain, a small square area of interest of 45-50 facets was examined and the average and standard deviation were recorded. This area of interest was 29 x 29 pixels, or approximately 7.0 mm x 7.0 mm. An example of area of interest is shown in figure 5.8 which was also used for out of plane displacements. The standard deviation of the out of plane displacement is negligible. The strains measured are raw strain values and include error. For this reason, an average over the crown of the plate was used with 45-50 facets included in the calculation.

The strains in the x and y direction were averaged at the crown of the plate and the results were typically within agreement as shown in Figure 5.9. The results of the strain time history show a similar behavior as the previous work of Grolleau et. al. [25] This shows two behaviors that were observed in the strain fields; pull-out of the sample, Figure 5.9(a), and no pullout, Figure5.9(b). In the pull-out case, the relatively large out of plane displacements induced by plastic deformation leads to the specimen being pulled out of the clamping ring and occurs within a short duration for the inception of loading. Higher pullout was observed with higher plate pressures and smaller thicknesses. In Figure 5.9(a) no pull-out is seen because of the relatively low burst pressure resulting in agreement amongst the strain fields in the x and y direction. In the pull-out case, there is agreement within experimental error as shown in Figure 5.11(b) in the strain fields, however, not at the peak of the strains. Because the difference is small within experimental error in the strain fields, it does not have a significant effect on the out of plane displacement. Samples showing large deviations in the strain fields, an indication that pull-out has occurred, were not considered for the inverse modeling technique.

The pullout was also seen in the strain rates as some strain rates were significantly higher in one direction than another. Pull out is the case where the material no longer deflects, but pulls away from the clamping ring resulting an artificially high out of plane displacements. The results of pull out can be in in Figure 5.10 which shows the typical images of samples that have experienced pull out and no pull out. This was another indication of an invalid test. In Figure 5.10(a), no pull out is observed. In this photo, the results of the interaction with the clamping ring are shown and a fine line is evident. Additionally, the edge, shown by the dotted line, has not changed from the cut shape. In contrast, pull out is shown in Figures 5.10(b) and 5.10(d). In this case, it can be seen that the direction that experiences the pull out becomes curved a as a result of the material being pulled through the clamping ring. Additionally, the circled area in Figure 5.10(b) shows that the material is being pulled as evidenced by the speckle continuity across the pulled out region. Examining the photo shown in Figure 5.10(d), the circle shows an area where the material pulled through and did not deflect. This behavior is not observed in Figure 5.10(c).

In Figure 5.11, two cases are again shown, the pull-out and no pull-out. Figure 5.11(a) corresponds to a test where a plate pressure of 1.18 MPa was applied. The rates show very similar behavior and the maximum rates are comparable. While the shape of the response curve is similar as seen in Figure 5.9(b), pullout occurs in the x-direction and higher rates are measured. While pullout occurred at 1.76 MPa in this case, from the given experimental setup, it is not possible to know the exact pressure at which pull-out occurs. Several factors contribute to the pull out including,

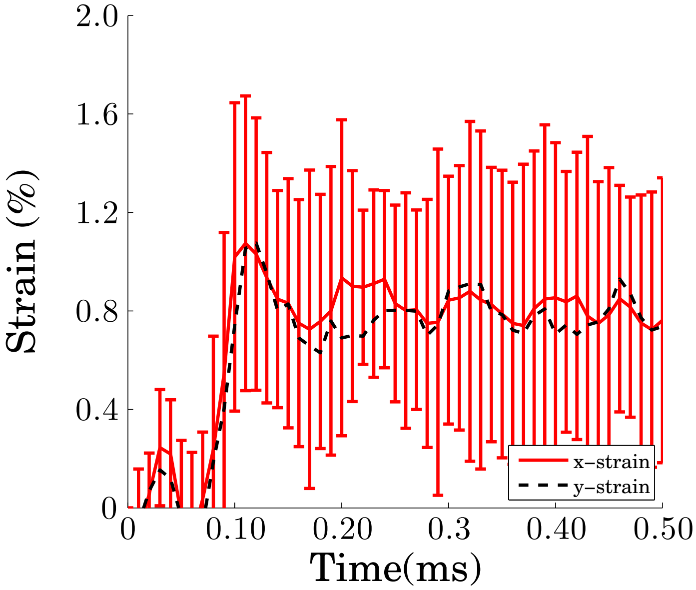

(a) A typical response at low pressures, shown here for 0.51 mm with a max plate pressure of 0.652 MPa

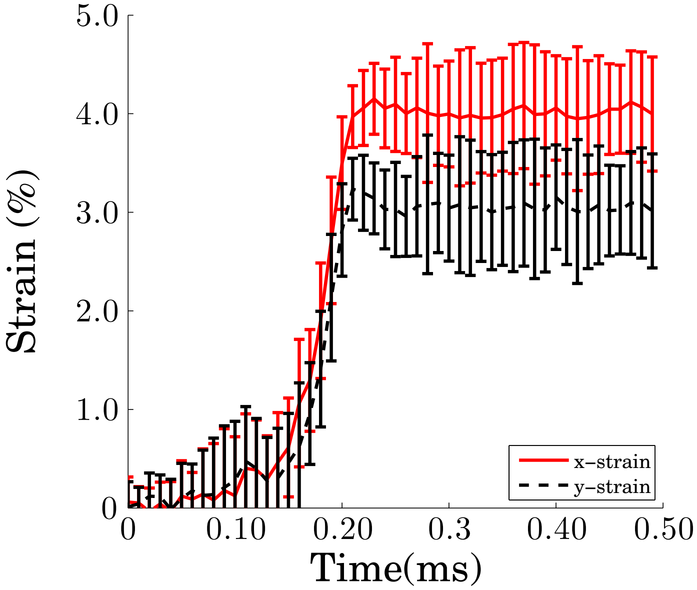

(b) A typical response at higher pressures demonstrating slight pullout, shown here for 0.64 mm with a max plate pressure of 1.19 MPa

Figure 5.9: Typical strain-time history response

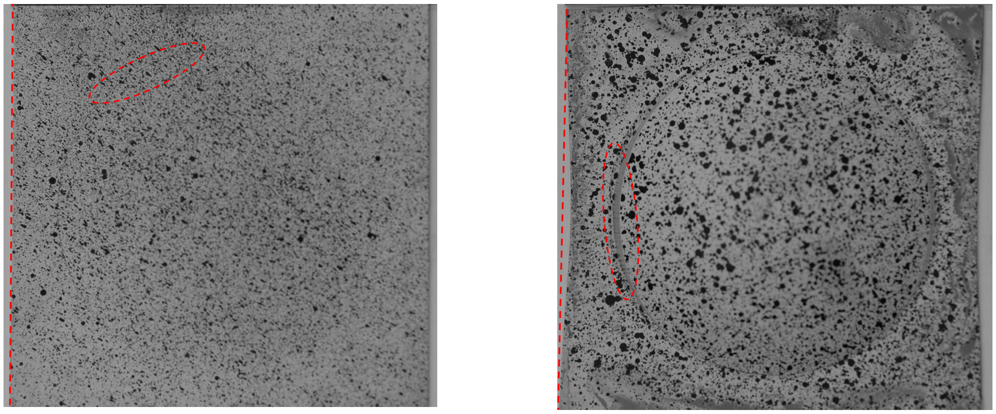

(a) A front view of a sample that has not demonstrated pullout (b) A front view of a sample that has demonstrated pull out

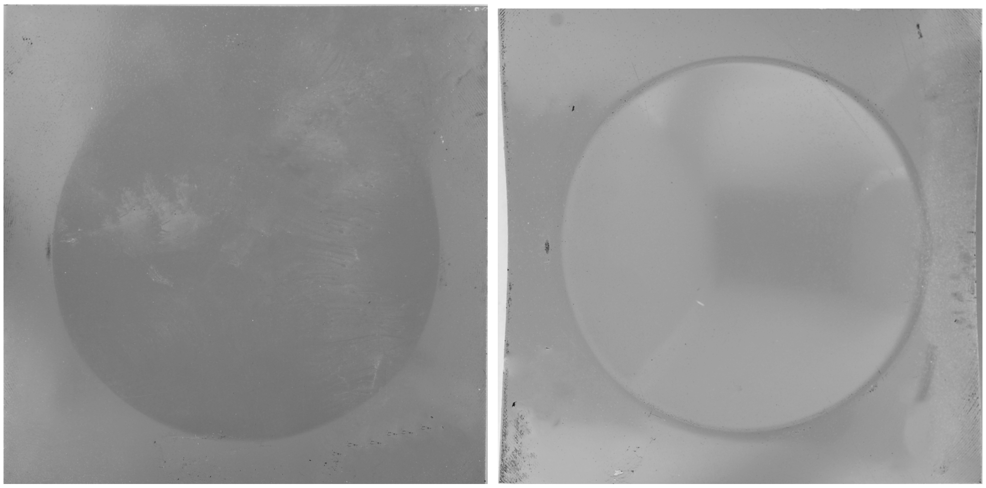

(c) A back view of a sample that has not demonstrated pullout (d) A back view of a sample that has demonstrated pull out

Figure 5.10: A comparison of samples showing pull out and no pull out

the size and orientation of the sample in the shock tube, and the clamping pressure applied by the clamping ring. In general, the shape of the response is similar across all samples. All the results for the out of the plane displacements and in plane strains and strain rates as determined by the DIC data is shown in Table 5.4. The strain rates were calculated by determining the change in strain as a function of the time step as determined by the experimental frame rate. Additionally, a sample strain field is shown in Figure 5.12. The results shown are the filtered results and show the general strain contours over the surface.

Each of the aforementioned techniques of visual observation, differences in strain fields, and differences in directional strain rate were used to determine the validity of the test. Only samples that did not experience pull-out or slight pull-out were used for the finite element modelling. A note should be made about the accuracy of the strain fields as determined by the DIC method. The DIC method is primarily used to measure local displacement fields. In this regard, the experimentally measured value is the out of plane displacement. The strain fields are derived through a numerical algorithm and is unique to each DIC software. The values of strain are raw and would require filtering, while the values of displacement do not require filtering of the raw measurements. For this reason, the out of plane displacement-time history was used as the primary metric for comparison between the experiment and simulation.

Thickness, mm (in)	Average Plate Pressure, MPa (PSI)	Max x Strain (%)	Max y Strain (%)	Max x Strain Rate (/s)	Max x Strain Rate (/s)
0.56 (0.022)	0.65 (94.6)	1.07±0.41	1.08±0.45	473	338
0.53 (0.021)	1.14 (165.1)	4.56±0.28	5.64±0.44	1171	1521
0.61 (0.024)	0.62 (89.8)	1.49±0.43	1.55±0.32	475	371
0.63 (0.025)	1.19 (172.0)	4.06±0.40	3.23±0.37	815	725
0.84 (0.033)	0.64 (92.3)	0.833± 0.64	1.30±0.59	380	570
0.84 (0.033)	1.19 (171.9)	2.37±0.68	2.68±0.76	750	707
0.82 (0.032)	1.94 (281.2)	3.32±0.64	4.81±0.59	875	930

Table 5.4: Results for strains and strain rates as measured by the DIC

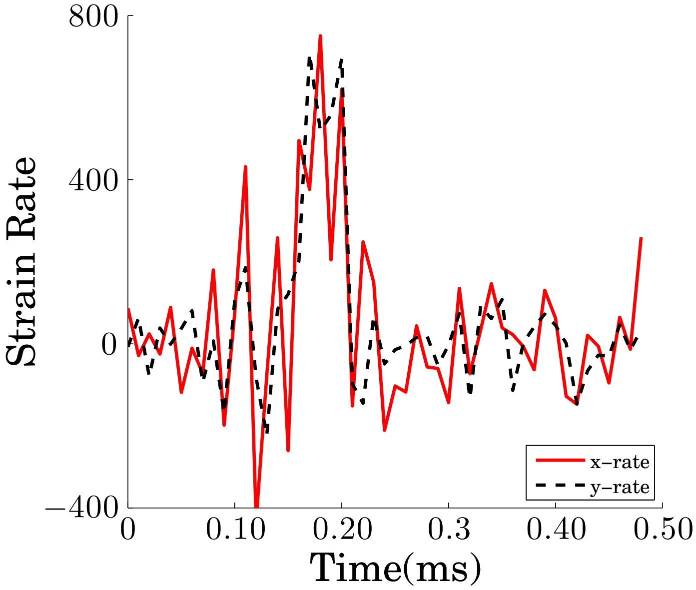

(a) Rate dependent results for no pull-out, shown here for 0.76 mm with a max plate pressure of 1.182 MPa

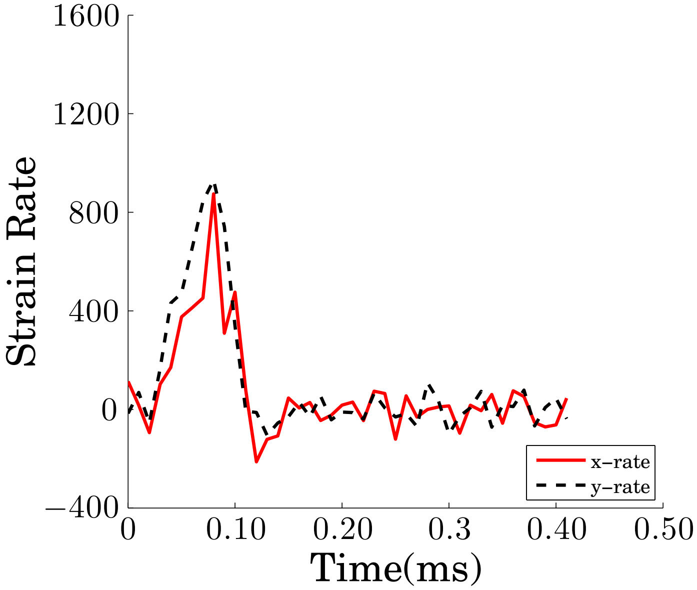

(b) Rate dependent results for no pull-out, shown here for 0.76 mm with a max plate pressure of 1.760 MPa

Figure 5.11: Typical strain rates

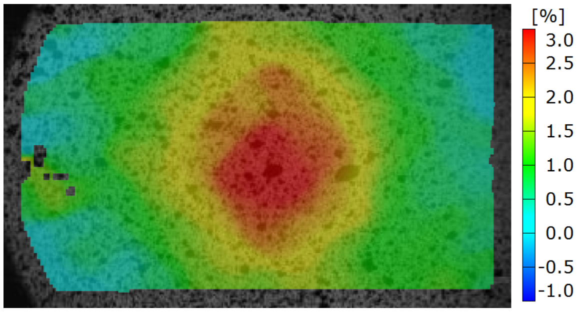

Figure 5.12: An typical strain field response

5.5 Computational Model

A computational model of the shock tube configuration was developed using the commercial software ABAQUS -Explicit [100]. The clamping ring was modeled as a rigid shell with an inner diameter of 76.2 mm (3 in), which is in frictionless contact with the aluminum specimen. The aluminum plate specimen was modeled using S3 triangular shell elements similar to the prior work of Pankow et. al. [84]. It should be noted at this point that the previous work of Pankow et. al. did not include rate dependency.

The plate was modeled as a 108mm x108mm (4.25in x 4.25in) shell and the thickness used was the average sample thickness measurements taken before testing. The plate was partitioned to include a 76.2 mm (3 in) diameter circle in the center of the plate which allowed for the loading to occur on the face as shown in Figure 5.14(b). A zero out-of-plane displacement boundary condition was applied to the area of plate that is not loaded on the edge, but allows in plane displacement. An additional circle of diameter 82.6 mm (3.25 in) was added to allow for material that will subsequently displace out-of-plane, if pull-through were to occur. A single model of the plate specimen was developed and the mesh consisted of 982 linear triangular elements of type S3 for the flat plate. A sample mesh is shown in Figure 5.14(a).This mesh was selected based on a test for convergence in which a number of different mesh sizes were used, the results of which are shown in Figure 5.13. It was found that the model stably

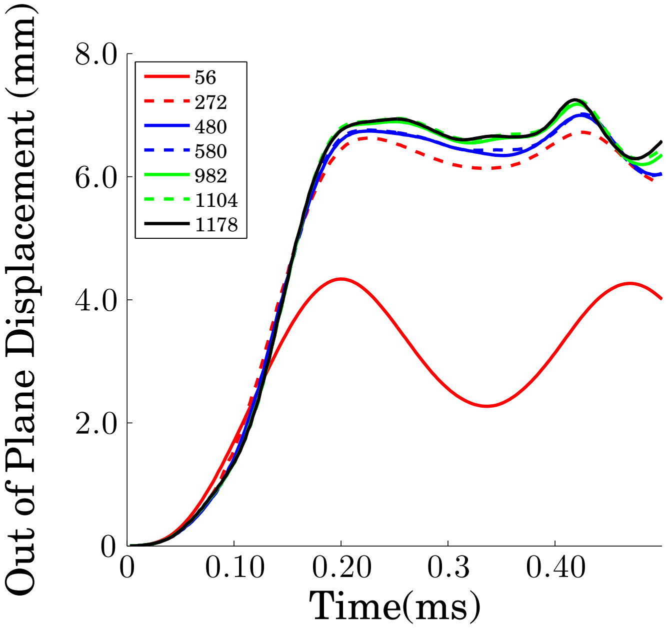

Figure 5.13: Convergence analysis of mesh based on the number of S3 elements

converged with 982 elements and with no significant gains by increasing the number of elements beyond that point.

The material properties used for the model are shown in Table 5.1. An elastic-plastic, small strain J2 flow theory representation of the aluminum was used with rate depended behavior incorporated by characterizing the yield stress ratio as a function of strain rate.

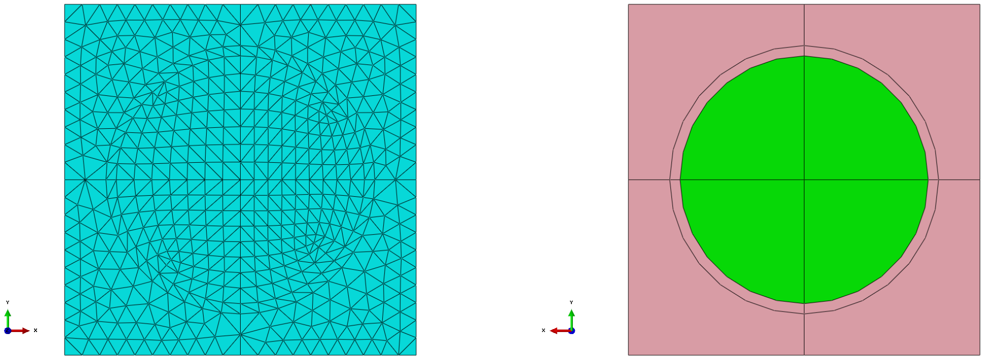

(a) Example of a sample mesh used in all models

(b) The partition of the geometry

Figure 5.14: Schematics of the geometry and mesh

The elastic-plastic model is described by equations 5.1,5.2, and 5.3. For values of stress, below the yield stress, the model follows a simple 1D Hooke Formulation where the stress is proportional the the strain by the modulus of elasticity as shown in equation 5.1. This relationship can then be inverted such that the elastic strain is written as a function of stress.

$$\sigma_{elastic} = E * \varepsilon_{elastic} \tag{5.1}$$

Upon yielding, the total strain is now the sum of two components, the elastic strain and the plastic strain as shown in equation 5.2.

$$\varepsilon_{total} = \varepsilon_{elastic} + \varepsilon_{plastic} \tag{5.2}$$

where

$$\varepsilon_{plastic} = K\sigma^{n}_{plastic} \tag{5.3}$$

In the current analysis, ABAQUS Explicit uses true stresses and true strains. True stress and true strain can be related to nominal stress and strain by equations 5.4 and 5.5.

$$\sigma_t = \sigma_n(1 + \varepsilon_{nom}) \tag{5.4}$$

$$\varepsilon_t = ln(1 + \varepsilon_{nom}) \tag{5.5}$$

Since the deviation between true stress and true strain is minimal during elastic loading, only the plastic regime needs to be considered. From the equations, if the plastic strain is sufficiently small, then deviation between true stress-strain and nominal stress-strain is negligible. For this work, it is assumed that the plastic strains are small.

The input for the plastic properties were determined from the stress-strain curve shown in Figure 5.1. The rate hardening was handled by using a yield ratio, R, which is shown in equation 5.6. For ABAQUS-Explicit, the input is tabular data of the yield ratio and strain rate, therefore, the input need not be a smooth function. What is shown in equation 5.6 is a modification of a traditional Power Law hardening where the rate hardening coefficient is normalized to unity thusly allowing a yield ratio of 1 to be obtained under static loading. For this work, it is assumed that Power Law hardening is observed with the material.

$$R = \frac{\sigma_y}{\sigma_o} = \dot{\varepsilon}^n \tag{5.6}$$

The amplitude of the pressure that was applied to the shell was taken directly from the experimentally measured data from the shock tube. With respect to the setup shown in figure 5.4, the applied pressure was the time-pressure history recorded during experimentation from pressure transducer 2. The use of this time-pressure history will be addressed further in the Computational Results section.

5.5.1 Optimization Technique

Previous work by Guo et. al. [26] did not determine the intermediate rate dependent behavior of Al-3003. In order to be able to determine the rate dependent behavior, an inverse modeling technique has been utilized, however, due to not knowing the exact values of the yield stress ratio as a function of strain rate, an optimization procedure was developed. The procedure would allow for an automated method of determining the optimized values of the yield stress ratio versus strain rate curve. In this technique, the output from the finite element analysis (FEA) is compared to the experimental results. The flow chart of the inverse modeling process is shown in Figure 5.15. The DIRECT algorithm, [44], has been used. It is a gradient free algorithm that is especially appealing for problems where no prior knowledge about the solution is available. The algorithm will converge to a global minimum provided sufficient iterations are allowed for. The process starts first with the selection of variables to be optimized, in this case, the yield stress ratio which is a function of the strain rate.

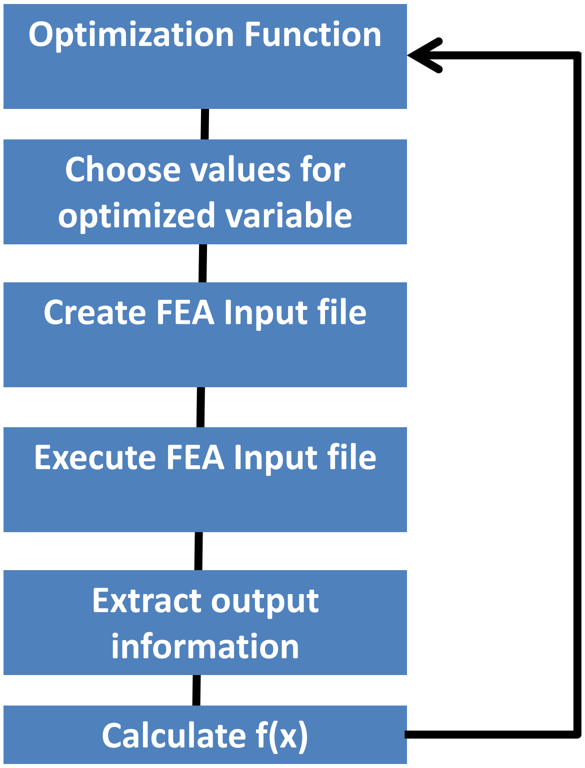

Figure 5.15: Flow chart for optimization technique

The goal of the optimization procedure was the determination of the yield ratio versus strain rate response curve. However, because the optimization algorithm only works with a finite number of degrees of freedom, data points were chosen to represent the yield stress ratio versus strain rate curve. Points in between where generated using a piecewise cubic hermitian interpolation. The points that were optimized were the selected strain rates at strains equal to 10, 50, 100, 200, 400, 600, 850 s^{-1} because the experimental strain rates fall into this interval. These values were determined from previous optimization runs that determined the range of strain rates observed during testing. Selection of points not within the actual range results in inaccurate data and does not determine an accurate response. The yield ratio curve consisted of 1000 data entries that were generated from interpolation. These data were programmed into the ABAQUS input file according to specification. The function that was attempted to be minimized is shown equation 5.7, where d_i^{exp} is the experimentally determined deflection and d_i^{num} were the numerical results from the finite element simulation. As shown in equation 5.7, three experimental cases were used to calibrate the model. These cases were diaphragm thicknesses of 0.53 mm, 0.63 mm, and .84 mm with maximum plate pressures of1.14 MPa, 1.19 MPa, 0.64 MPa respectively. These were selected because they produced the widest range of strain rates as observed in the experiment. The difference in the displacement between experimental and numerical results were minimized in a least-square sense. The three experimental results that were used for the optimization were selected to span different strain rate ranges. From this output, the optimization function compares the input to the constraints that were given in equations 5.8 and 5.9 to determine the validity of the points. .

$$f = \int_{0}^{3.5e-4} [(d_1^{exp} - d_1^{num})^2 + (d_2^{exp} - d_2^{num})^2 + (d_3^{exp} - d_3^{num})^2]dt \tag{5.7}$$

$$\begin{bmatrix} 1 & -1 & 0 & 0 & 0 & 0 & 0 \\ 0 & 1 & -1 & 0 & 0 & 0 & 0 \\ 0 & 0 & 1 & -1 & 0 & 0 & 0 \\ 0 & 0 & 0 & 1 & -1 & 0 & 0 \\ 0 & 0 & 0 & 0 & 1 & -1 & 0 \\ 0 & 0 & 0 & 0 & 0 & 1 & -1 \end{bmatrix} \begin{bmatrix} x_1 \\ x_2 \\ x_3 \\ x_4 \\ x_5 \\ x_6 \\ x_7 \end{bmatrix} \leq \begin{bmatrix} 0 \\ 0 \\ 0 \\ 0 \\ 0 \\ 0 \\ 0 \end{bmatrix} \tag{5.8}$$

The constraint in Equation 5.8 enforces that the yield stress ratios have to be monotonically increasing with strain rate. The constraint in Equation 5.9 enforces that the slope of the yield ratios decreases with higher strain rates.

$$\begin{bmatrix} \frac{1}{\delta\dot{\epsilon_1}} & \frac{-1}{\delta\dot{\epsilon_1}} - \frac{1}{\delta\dot{\epsilon_2}} & \frac{1}{\delta\dot{\epsilon_2}} & 0 & 0 & 0 & 0 \\ 0 & \frac{1}{\delta\dot{\epsilon_2}} & \frac{-1}{\delta\dot{\epsilon_2}} - \frac{1}{\delta\dot{\epsilon_3}} & \frac{1}{\delta\dot{\epsilon_3}} & 0 & 0 & 0 \\ 0 & 0 & \frac{1}{\delta\dot{\epsilon_3}} & \frac{-1}{\delta\dot{\epsilon_3}} - \frac{1}{\delta\dot{\epsilon_4}} & \frac{1}{\delta\dot{\epsilon_4}} & 0 & 0 \\ 0 & 0 & 0 & \frac{1}{\delta\dot{\epsilon_4}} & \frac{-1}{\delta\dot{\epsilon_4}} - \frac{1}{\delta\dot{\epsilon_5}} & \frac{1}{\delta\dot{\epsilon_5}} & 0 \\ 0 & 0 & 0 & 0 & \frac{1}{\delta\dot{\epsilon_5}} & \frac{-1}{\delta\dot{\epsilon_5}} - \frac{1}{\delta\dot{\epsilon_6}} & \frac{1}{\delta\dot{\epsilon_6}} \end{bmatrix} \begin{bmatrix} x_1 \\ x_2 \\ x_3 \\ x_4 \\ x_5 \\ x_6 \\ x_7 \end{bmatrix} \leq \begin{bmatrix} 0 \\ 0 \\ 0 \\ 0 \\ 0 \\ 0 \\ 0 \end{bmatrix} \tag{5.9}$$

where

$$\begin{bmatrix} \delta\dot{\epsilon_1} & \delta\dot{\epsilon_2} & \delta\dot{\epsilon_2} & \delta\dot{\epsilon_3} & \delta\dot{\epsilon_4} & \delta\dot{\epsilon_5} & \delta\dot{\epsilon_6} \end{bmatrix} = \begin{bmatrix} 40 & 50 & 100 & 200 & 200 & 250 \end{bmatrix} \tag{5.10}$$

Additionally, in order to accelerate the convergence of the DIRECT algorithm, the limits for the optimized value of the yield stress ratio were selected and shown in Equation 5.11. These values were selected based on the previous literature data reported in [26].

$$\begin{bmatrix} 1.05 \\ 1.05 \\ 1.05 \\ 1.07 \\ 1.14 \\ 1.20 \\ 1.25 \end{bmatrix} \leq \begin{bmatrix} x_1 \\ x_2 \\ x_3 \\ x_4 \\ x_5 \\ x_6 \\ x_7 \end{bmatrix} \leq \begin{bmatrix} 1.15 \\ 1.20 \\ 1.25 \\ 1.27 \\ 1.34 \\ 1.40 \\ 1.45 \end{bmatrix} \tag{5.11}$$

5.5.2 Computational Results

The optimization was able to converge in a stable manner to an "optimized" curve in 55 iterations. The total number of iterations used for the optimization was 999, which yielded the results shown in Figure 5.16. Additionally, the results of the optimization and the high rate results of Guo are combined and represented by a power law relationship shown in equation 5.12. The power law is valid for strain rates greater than 50.

$$\sigma_y = 110e6(\dot{\varepsilon})^{0.067} \tag{5.12}$$

It is worth noting however, that the optimized value at a strain rate of 10 is a fitting parameter necessary to meet the constraints because rates of $\frac{10}{s}$ are not seen in the FEA model. In Figure 5.16, the results of the optimization are shown with the results shown in [26]. The results of the optimized yield stress ratio response as a function of strain rate in seen to agree well with that reported in [26].

The first metric for comparison between the finite element model and experimental results is the comparison for out of plane displacements at the center of the panel shown in Figure 5.17. As seen in both Figure 5.17(a) and 5.17(b), there is, in general, good agreement between the samples. However, it is worth noting that there the

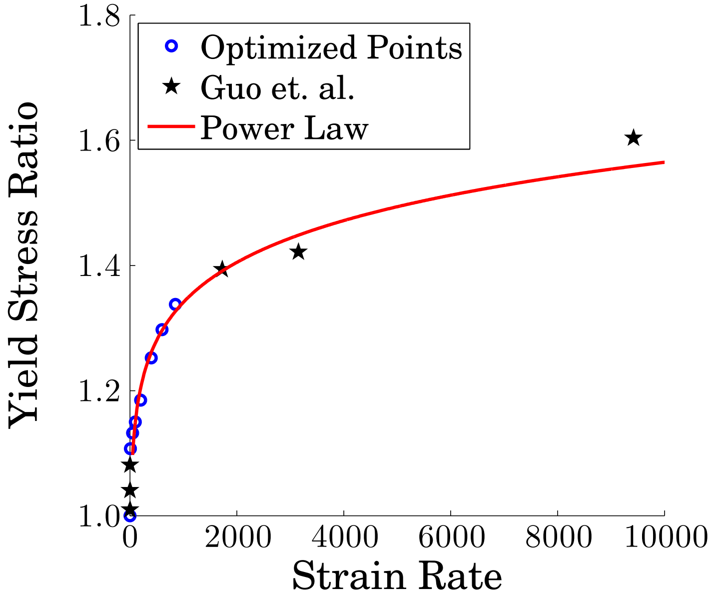

Figure 5.16: The results of optimization

model under predicts the out of plane displacement for the plate pressure equal to 1.760 MPa. At this high pressure, there was slight pullout of the diaphragm in one direction as discussed earlier, leading to the discrepancy. When examining figures 5.17, 5.17(a), 5.17(b), not only are the out of plane displacements comparable between the simulation and experiment, the rise times are nearly identical. When examining figure 5.5, it is clear that there is an initial loading on the plate that is not captured by pressure transducer 2 (the pressure-time history used for the input to the model). The agreement between the simulation and experiment suggests that the initial loading is not critical to capturing the proper rise time and out of plane deflection.

Thickness, mm (in)	Ave. Plate Pressure, MPa (PSI)	Experimental Displacement, mm (in)	Finite Element Displacement, mm (in)
0.56 (0.022)	0.65 (94.6)	7.02 (0.28)	7.04 (0.278)
0.83 (0.033)	1.14 (165.1)	10.91 (0.43)	10.91 (0.43)
0.61 (0.024)	0.62 (89.8)	6.41 (0.25)	6.58 (0.26)
0.63 (0.025)	1.19 (172.0)	10.29 (0.41)	10.1 (0.40)
0.84 (0.033)	0.64 (92.3)	4.96 (0.20)	5.07 (0.20)
0.84 (0.033)	1.19 (171.9)	7.58 (0.30)	7.95 (0.31)
0.82 (0.032)	1.94 (281.2)	11.10 (0.44)	11.50 (0.45)

Table 5.5: Comparison between FEA and DIC

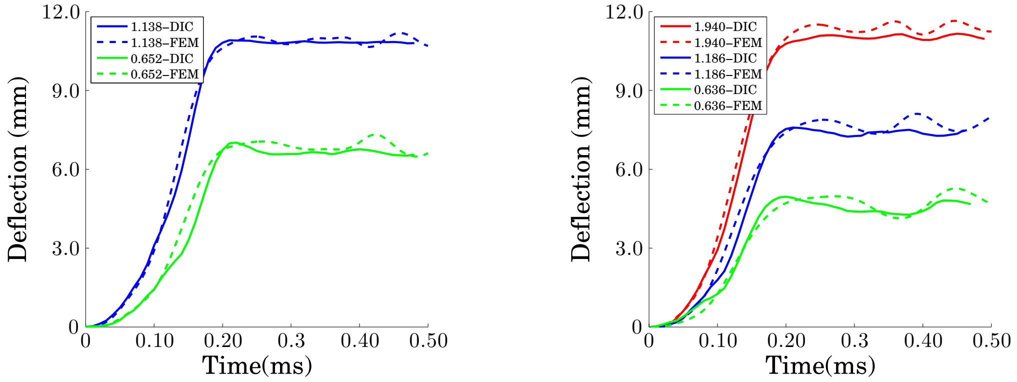

(a) Comparison between finite element simulation and experiment for 0.51 mm (0.020 in)

(b) Comparison between finite element simulation and experiment for 0.76 mm (0.030 in)

Figure 5.17: Comparison for finite element simulations and experiments

Because of the isotropic behavior of the material, the strains and rate rates are generally comparable and in some cases compare well against the experimental results as shown in Figure 5.18. The model did not capture the pull-out of the plate. This is due to the boundary conditions employed by the model. In order to accurately model the pull-out, more information would be needed about the clamping force, precise geometry of the plate, coefficient of friction, and orientation in the shock tube as the orientation affects the amount of clamping surface in a particular direction. From Figure 5.18, the strains in each direction are comparable as shown in Figure 5.18(a), which shows a small amount of oscillatory behavior. In the figure, the results for the plate pressures of 0.63 and 1.14 MPa are shown. Figure 5.18(b) shows a comparison between the filtered results of the finite element simulation and experiment for a 0.61 mm thick plate with a plate pressure of 0.612 MPa. Although not shown, the experiment and simulation are in agreement within experimental error.

The strain rates showed similar behavior as the strains and the results are given in Table 5.6. The values that are reported are maximum values that may have occurred during oscillations. However, the two directions show much less difference than the experimental results.

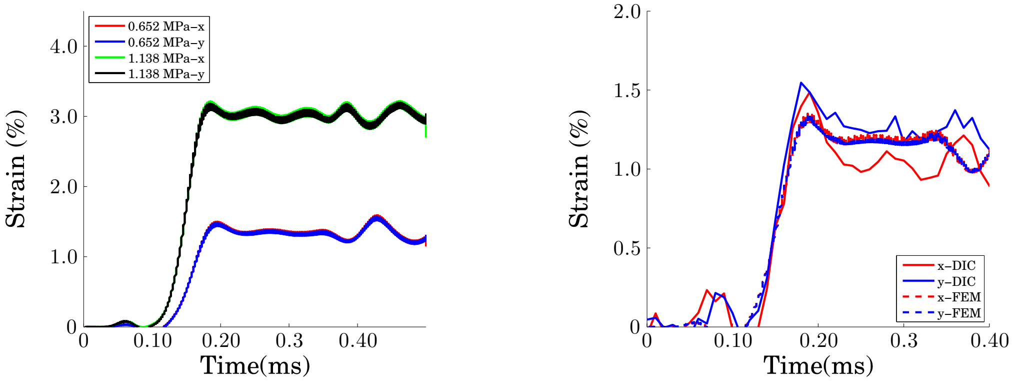

(a) Comparison between finite element simulation and experiment for nominal 0.51 mm (0.020 in)

(b) Comparison in strains between the filtered finite element simulation data and experiment for 0.61 mm (0.0240 in)

Figure 5.18: Results for strains in the finite element simulations

Thickness, mm (in)	Ave. Plate Pressure, MPa (PSI)	Max x Strain (%)	Max y Strain (%)	Max x Strain Rate ($\frac{}{s}$)	Max y Strain rate ($\frac{}{s}$)
0.56 (0.022)	0.65 (94.6)	1.55	1.53	335	332
0.53 (0.021)	1.14 (165.1)	3.22	3.18	732	722
0.61 (0.024)	0.62 (89.8)	1.35	1.33	280	276
0.63 (0.025)	1.19 (172.0)	2.65	2.58	567	551
0.84 (0.033)	0.64 (92.3)	0.906	0.896	174	174
0.84 (0.033)	1.19 (171.9)	1.69	1.67	292	300
0.82 (0.032)	1.94 (281.2)	3.27	3.23	607	602

Table 5.6: Results for strains and strain rates as determined by the FEA with smoothing

5.6 Conclusions

A shock tube facility has been used to examine the rate dependent multiaxial stress-strain response of thin aluminum sheet, in the strain rate range of $200-850s^{-1}$. Previous work was unable to capture data at intermediate strain rates due to limitations in testing techniques, namely the wave propagation issues at intermediate rates associated with SHPB. The shock-loading/inverse modeling technique has been shown to be capable of accurately determining the multiaxial consecutive response at intermediate strain rates. While the shock tube is able to also generate strain rates that are higher than 10^3s^{-1}, in this chapter, rates up to $850s^{-1}$ were observed. As demonstrated by the agreement between the strain profiles and out of plane displacements, the optimization technique presented in the paper was able to accurately determine the yield stress ratio as a function of strain rate. When compared to prior work, this intermediate rate dependent data fell within the previously determined rate dependent data shown in,[26].

CHAPTER VI

Shock Loading of 2D Plain Woven Textiles

In Chapter 3, the SHTB testing technique was introduced. SHTB is widely used to determine the 1D failure of materials at elevated strain rates. Chapter 5 introduced a new testing technique that creates a biaxial state of stress at the crown of a deforming plate. Through the use of aluminum testing, both testing techniques (SHTB and shock tube) were validated experimentally and in the case of the shock tube, an inverse modeling technique was used to extract rate dependent multi-axial response of aluminum. In order to examine the high strain rate properties of composite materials, the shock tube testing techniques developed in the previous chapters will be applied to composite materials. In this chapter, shock loading of plain woven textile composite materials is studied using a novel technique to induce damage initiation at the crown of the sample, where a biaixal state of stress is present.

6.1 Introduction

As shown in Chapter 5, shock tube testing is a convenient way to introduce blast loading of plates without having to use an explosive charge. The circular plate configuration when subjected to transverse shock pressure loading creates a state of biaxial stress at the crown in a deforming plate. With respect to composite materials, the most extensive research of blast loading is with underwater explosions. This was due in large part to development of marine structures with composite hulls for military applications.

While shock tube mechanics have been well understood and shock waves within a tube have been studied for the better part of 150 years, the application of a shock tube to induce shock wave pressure to transversely load plates is still relatively new. The first significant publication regarding the shock wave loading of plates was by Stoffel et al. [109] which validated the numerical and experimental results associated with testing layered materials. Early work on the blast response of composite materials was performed on using explosive charges underwater with a clamped plate. Mouritz examined the blast resistance using this technique in 1993 on graphite laminates [67] and later on stitched panels [66]. Early tests relied on post-test inspection of the panels and did not capture the failure of the plates. Later researchers, such as Leblanc and Shukla [53] were able to use further instrumentation such as strain gages and high speed cameras to image the response of plates and geometrically modified plates [54]. With increased fidelity of measurements in testing, the researchers were able to develop damage models. More recently, Schiffer and Tagarielli [98], developed techniques to measure wave propagation through the fluid and measure the blast response of carbon fiber plates while accounting for cavitation during testing.

The use of a shock tube to test the high strain rate performance of composite materials subjected to air blasts has been limited. On the contrary, the use of a shockwave to dynamically load a composite plate to failure has been used by many researchers, however, it is generally not in the context of a circular plate. Tekalur et al. have used the shock tube to cause failure in a dynamic three point bend test on a variety of materials [113], [114], [117]. In this test, a sample is set up flush with the shock tube on a simply supported test fixture. High speed imaging captures the dynamic deflections in the span. Subsequent studies by Jackson and Shukla used this technique to create a de facto dynamic compression after impact test for sandwich composites [42]. This technique allowed for a shock tube to be used to cause complete failure in a composite panel.

The use of a shocktube to generate an air-blast to examine high strain rate performance of circular composite plates is a relatively new application. Early work on air-blast loading on composites was performed by Leblanc et al. [55] examining 3D woven composites. 3D composites are ideal testing candidates because the ability to dissipate energy without catastrophic failure. Other high energy dissipating materials such as polyurea composites have been examined for their mechanical response to shock loading as reported in, [115]. Pankow et al. continued the study of 3D woven composite plates subjected to air-blast loading [79] and demonstrated novel testing techniques to develop low fidelity finite element models including damage that captured the initiation mechanisms observed in experiments, [82].

To date, most shock tube experiments have investigated the elastic-transient response while not examining the final failure of a plate when subjected to shock loading. While damage initiation has been established by previous researchers, there is a need to understand the response of composite plates subjected to transverse shock loading, until complete failure. The subsequent sections in this chapter will examine the shock wave loading response of a thin a textile plate that undergoes tensile rupture of the yarns with continued loading.

6.2 Experimental Details

As discussed in the previous chapter, the shock tube has a high degree flexibility in terms of how to control the shock wave that impacts the plate. One such way to do this is to use a different gas as the driver. From shock wave mechanics, the lighter gases produce faster shock waves that reflect at a greater rate. This results in very high pressures on the plate over a smaller time frame. When using a heavier gas, the reflected shock takes much longer to build to the maximum. The pressure traces for

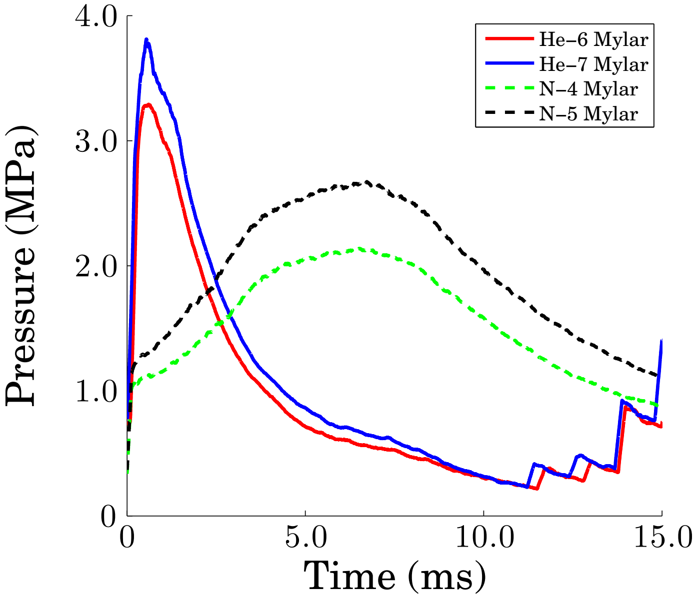

Figure 6.1: Comparison of reflected shock pressures on the plate, with the use of nitrogen and helium, as the driver gas

two different gases, helium and nitrogen, can be seen in Figure 6.1.

In Figure 6.1, two different driver gases are used with varying burst pressures. The burst pressure is controlled, in this case, by using different numbers of sheets of mylar separating the driver and driven sections (see chapter 5). It can be seen that the helium loads the plate very rapidly from the reflected shock, whereas the nitrogen reflected shock rises much slower over time. During the course of testing, there is an initial shock that impacts the plate in the Nitrogen case and pressure slowly builds up. Frequently, the maximum plate pressure seen by the sample is much later than this initial shock.

This is due to the fact that the out of plane deformation of the plate is dominated by inertial effects and is not as much a function of the reflected shock pressure. This is because the gas traveling in excess of Mach 1.0 creates a relatively strong inertial effect by accelerating the plate very rapidly. To demonstrate this, a test was performed in which the maximum imaging time of the camera relative to usable frames due to

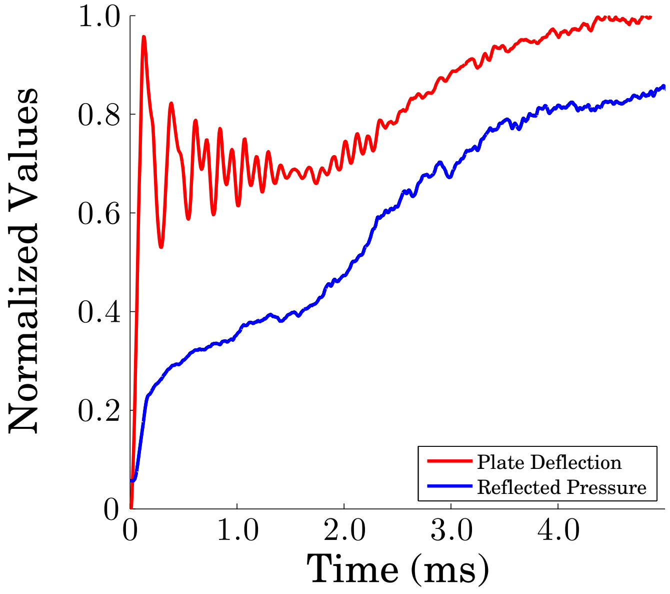

Figure 6.2: Comparison of reflected shock pressure to the out of plane displacements

the flash length was used to determine the out of plane deflection in a time span that corresponds with the rise time of the reflected shock. Figure 6.2 shows both the pressure-time history as measured from the test itself and the deflection-time history from the DIC results. Both of the results are normalized by their respective maximums. From this image, it is clear that while the initial pressure on the plate is between 20-30% of the maximum pressure, it allows for a deflection that is 95% of the maximum.

This result indicates that a better metric than the maximum plate pressure is needed to characterize the test conditions between tests that use different gases. In order to compare across different tests, shock strength is a better distinguishing parameter. Shock strength is a measure of the pressure differential across an unsteady shock wave propagating down a shock tube. The shock strength considers the Heat Capacity Ratio, γ and the shock speed, M_s. The relationship for shock strength is shown in Equation 6.1.

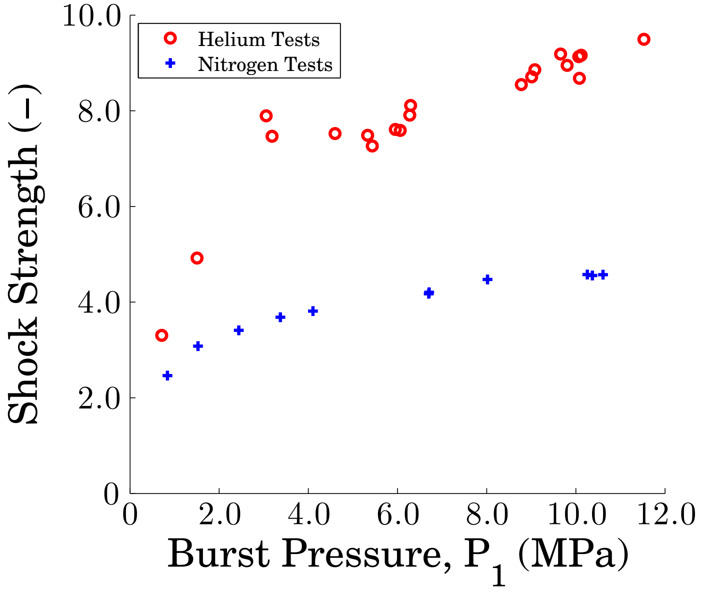

Figure 6.3: The shock strength versus burst pressure plot

$$ShockStrength = \frac{P_2}{P_1} = 1 + \frac{2\gamma_1}{\gamma_1 + 1}(M_s^2 - 1) \tag{6.1}$$

Figure 6.3 demonstrates the relationship between shock strength and burst pressure, P_1, as measured from all tests performed on the shock tube. The burst pressures were determined from the pressure readings in the driver section. The mach ratio was found by measuring the speed of the shockwave from the experiment and normalized by the speed of sound in air. Air was used because while the shock wave itself is propagating as a wave of driver gas, the medium in which it travels into is the air of the driven section. From this plot, it is clear that as the burst pressure is increased, there is diminishing returns. But what is clear is that different gases can be used to span different shock strengths. Also, this metric allows for a comparison between driver gases that incorporates more physical aspects of the wave itself.

6.2.1 Material

For this study, two material systems were examined, however, both were 4 ply plain woven samples of either IM7 carbon or S2 glass. The samples were manufactured at the United States Army Research Laboratory in Aberdeen Proving Ground, MD, and infused with SC-15 matrix via VARTM. The curing cycle that was described previously in Chapter 2 was used. After the cure, the samples had thicknesses of 2.84 mm (0.112 in.) and 1.02 mm (0.040 in.) for the glass and carbon respectively. From the bulk panel, samples were extracted using a diamond saw to sizes of 114.3 mm x 114.3 mm (4.5 in. x 4.5 in.).

6.3 Flat Plate Testing Results

Before full failure of the panel could be determined, it was necessary to test the flat plates themselves to determine the maximum strain rates that were achievable. Each plate was loaded sequentially with higher and higher burst pressures to create different shock strengths. The data was analyzed with DIC and when the sample no longer showed increases in the accumulated strain, then it was clear that punchout was beginning to occur. Post test inspection also confirmed the punchout effects near the clamped boundary. For these and all other tests, the stereo set of Photron SA.Xs were used at a frame rate of 150,000 FPS which yielded a resolution of 256x128 pixels. The data analysis was the same as described in the section on shock strength and in the previous chapter. The cameras were triggered by a TTL signal that was generated when the shock wave passed the pressure transducer closest to the plate as described in the previous chapter. It should be noted that previous research has shown that the use of a strain gage on plain woven materials results in varied measurements based upon the strain gage size as the heterogeneous nature of the material leads to large strain variations in the material [52]. Since DIC is non-contact, it will allow for better

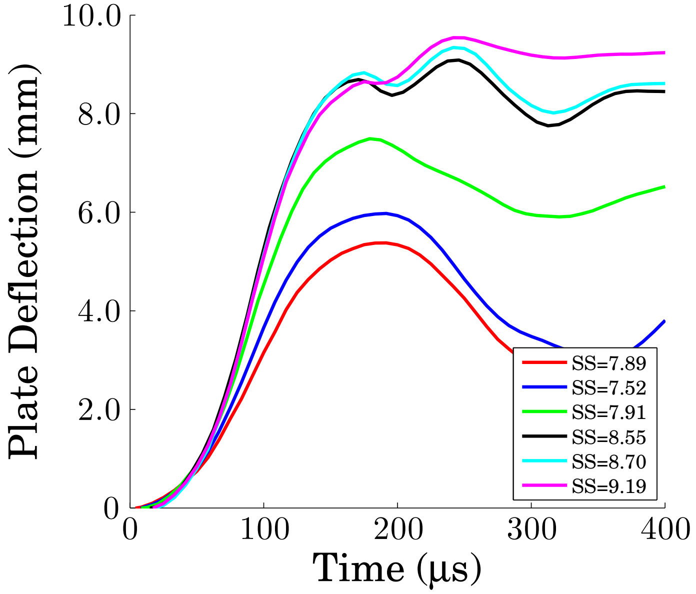

Figure 6.4: The deflection time histories for the flat glass plate

measurements than a strain gage. For further details about the validity of the DIC measurements at reduced resolution, See Appendix A.

6.3.1 Shock Loading of Flat Glass Plate

For the plain woven glass samples, 6 initial tests were run. The deflection time history for these plates is shown in Figure 6.4. In this figure, there are a a few points to note. As the shock strength is increased, so too is the maximum deflection. For shock strengths below 8.55, the maximum peak is seen in the first oscillation, however, above 8.55, there is an initial local maximum, followed by a further rise after which the deflection is seen to drop. Post test visual analysis suggests this is the beginning of delamination on the outer layer and is beginning to punch out. In order to establish this further, full images of the plate within the ring would be needed to plot the deflection across the section.

This effect from the delamination of the outer layer is seen in Figure 6.5 which show the strains in the x-direction, Figure 6.5(a), and the y-direction, Figure 6.5(b).

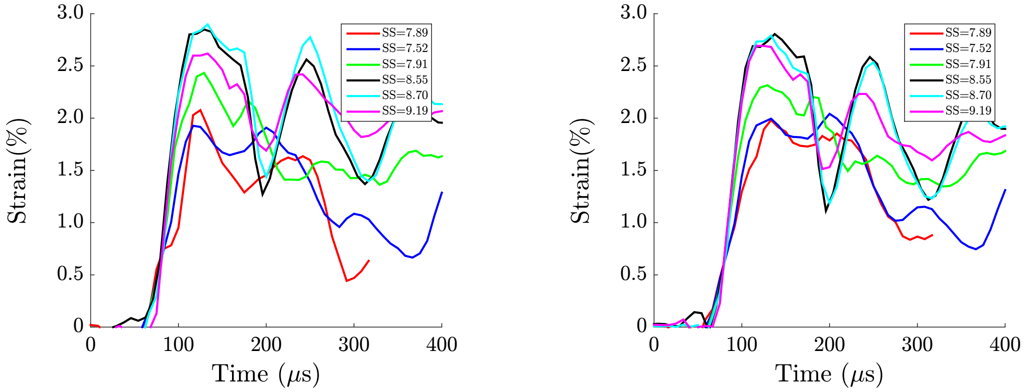

(a) The strain in the x-direction for the flat glass plates

(b) The strain in the y-direction for the flat glass plates

Figure 6.5: The strains from the flat plate testing–the yarns are aligned along the x-y axis

While the material does see higher deflections in Figure 6.4, this does not translate to higher strains in the plate in either direction. This is best seen in Figure 6.5(b) where the maximum strains are nearly identical for the shock strengths of 8.55, 8.70, and 9.19. Additionally, another observation from this testing is that there is general agreement between the two directions. This indicates that the damage accumulation is "isotropic", driven by the pressure loading which induces a equibiaxial state of stress. The relatively high degree of agreement suggests that damage is relatively diffuse and is 'isotropic'.

This agreement in the 'isotropy' of damage accumulation can be seen in Figure 6.6(a) where for many of the samples the directional strains are nearly identical. The strain rates in the sample can be determined from taking the slope of the strain time history. At the largest ends of the shock strengths, the strains are nearly identical because of the damage occurring on the outer layer. When examining the strain rates in Figure 6.6(b), it is clear that the maximum strain rate saturates at approximately 700/s. This is the maximum achievable strain rate in this material system since damage accumulation controls the maximum achievable strain rate.

The strain rate measure is of great interest in this work. While in the SHTB tests,

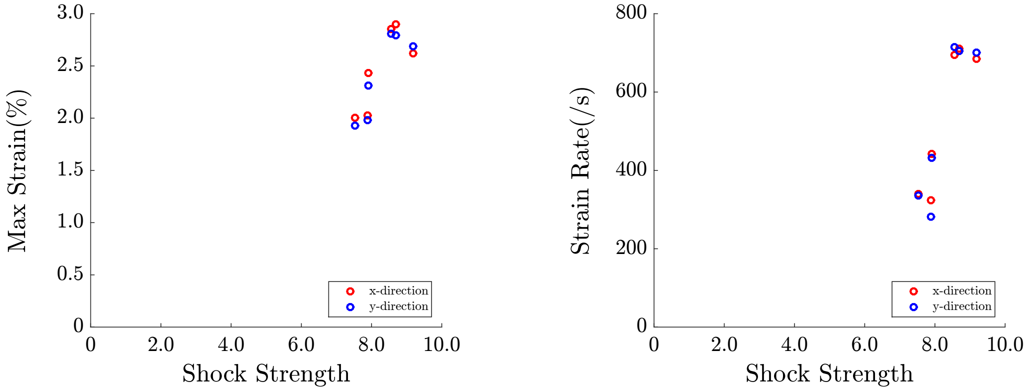

(a) The strain as a function of shock strength for the glass plates

(b) The strain rates as a function of shock strength for the glass plates

Figure 6.6: Comparison of strains and strain rates as a function of shock strengths

the results of the strain rate were consistent with a macroscopic measurement, this is not always the case as it relates to the plates when subjected to blast loading. In the case of the flat plates, the strain rates that are measured are again a macroscopic measurements because the plate does not experience significant damage. However, when the plate damages, further effects are observed and the measurement becomes a more local measurements as it is heavily affected by the localization of damage. This effect is described further in the progressive failure section.

The tested samples are shown in Figure 6.7. From this figure it is clear that damage is occurring on the outer layer as evidenced by the ring around the clamping. This effect is from the through-the-thickness shear stresses that push the outer layer through the ring. For this reason, higher strain rates cannot be achieved for the flat glass plates.

6.3.2 Shock Loading of Flat Carbon Plate

The same procedure was used used to load the carbon plates, however, since the plates were approximately a third of the thickness of the glass plates, special considerations were needed. The shock strengths that were used for the glass samples

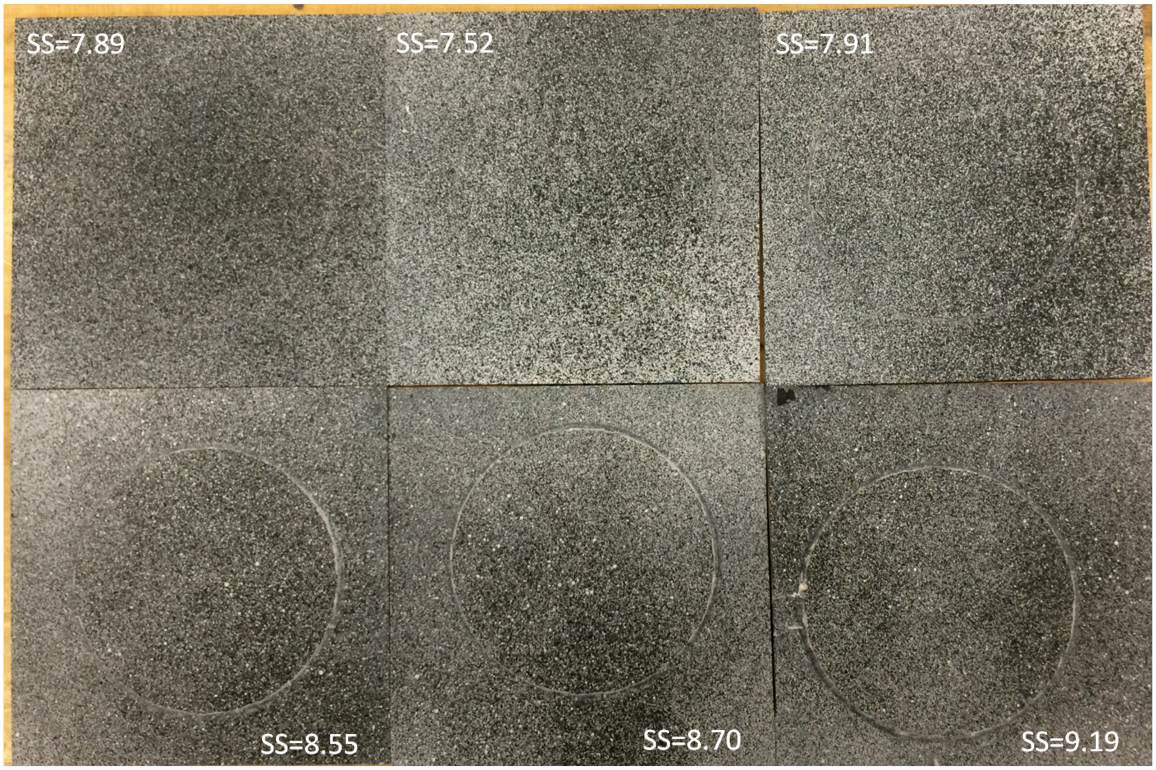

Figure 6.7: Photographs of the tested samples showing the increasing punchout

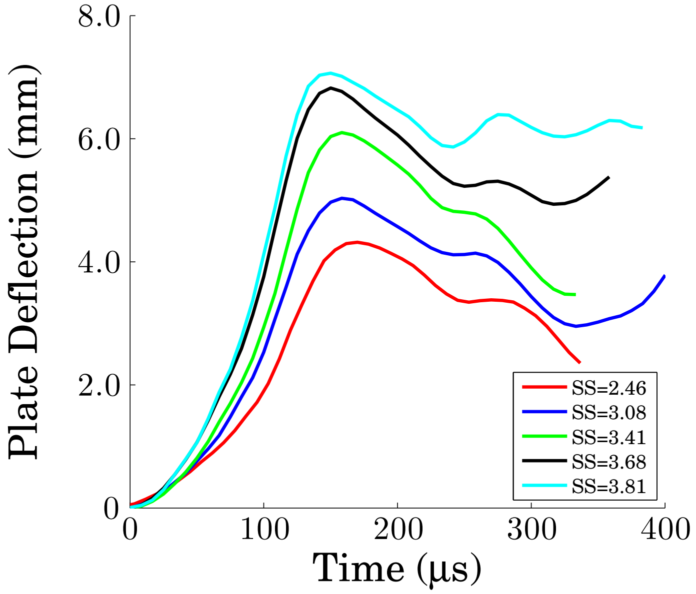

Figure 6.8: The deflection time histories for the flat carbon plates

would be too large for the carbon plates. It was determined through testing that the use of a helium shock was not possible because the reflected shock pressure and rise time was too fast for the plates and punchout occurred almost instantaneously, without straining of the plate. To prevent this effect, heavier gases of Argon and Nitrogen were examined, however, the shock speeds of the Argon were too slow. It was determined that Nitrogen gave the characteristics of the shock that were most desirable.

The deflection time histories for the carbon plates are shown in Figure 6.8. Like the glass plate tests of increasing shock strengths are shown, but as shown in Figure 6.3, as the burst pressure is increased, beyond a certain point, there is not a significant increase in shock strength. Also of importance is that these samples experienced final failure as the reflected pressure developed on the plate. This means that the plate was able to sustain load during the initial shock, but as the reflected shock pressure developed on the plate, the through thickness shear stresses at the boundaries ultimately led to punchout. The carbon plates show a characteristic increase in

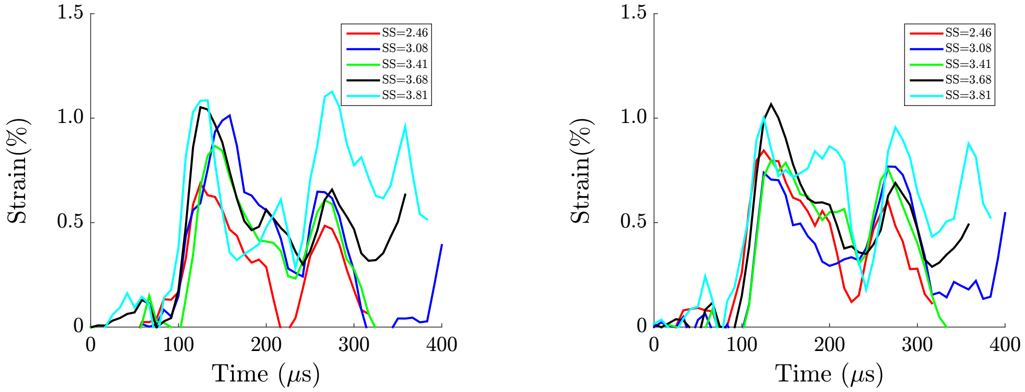

(a) The strain in the x-direction for the flat carbon plates (b) The strain in the y-direction for the flat carbon plates

Figure 6.9: The strains from the flat plate testing–the yarns are aligned along the x-y axis

deflection with increasing shock strength. While it was not visible as shown with the glass plates, the post peak behavior gives insight into how close the plate is to punching out. If the post peak behavior shows a flat slope, it is generally an indication that delamination is beginning to occur as the material is not straining further, and the deflection remains relatively unchanged.

This effect is further seen in the strain time history of the crown of the plate shown in Figure 6.9 which shows the strains in the x and y-direction respectively. Similarly to the glass samples, there is generally strong agreement between the two directions with respect to the strain-time history. This is an indication that any damage is occurring 'isotropically' in the material. Also, as expected with an undamaged material, as the shock strength increases so too does the strain in the samples. The comparison of strains as a function of shock strength is shown in Figure 6.10(a) which shows good agreement between the two strain fields. The strain rates generally increase with the shock strength as shown in Figure 6.10. Due to the testing difficulties discussed earlier, the maximum strain rate prior to punchout was not determined, but in this case, strain rates of up to 325/s were achieved without punchout.

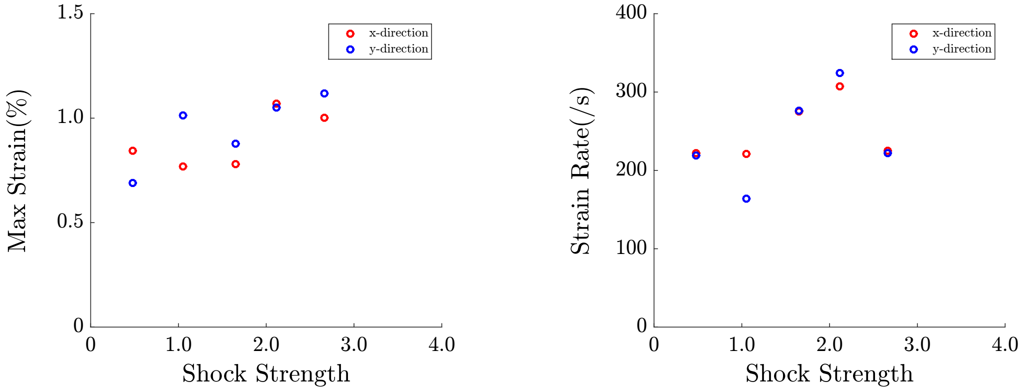

(a) The strain as a function of shock strength for the carbon plates

(b) The strain rates as a function of shock strength for the carbon plates

Figure 6.10: Comparison of strains and strain rates as a function of shock strengths

6.4 Thinned Plate Testing Results

While the flat plates showed interesting results, it was not able to achieve the tensile rupture of the yarns in the plate. As shown experimentally earlier with the composite plates and the aluminum sheets in the previous chapter, large through the thickness shear stresses develop along the edge of the clamping ring and creates competing mechanisms for the plate to fail. In order to induce tensile rupture, the strain at the crown of the plate needs to accumulate faster than the through the thickness shear stresses along the edge. One such way to do this is to thin the material in the middle of the plate to cause the strains to accumulate in the crown of the plate faster. With the composite plate, however, special attention needs to be paid to how the plate is thinned.

6.4.1 Thinning Technique

A centrally thinned sample would be able to deflect sufficiently in the center of the plate such that through-the-thickness shear stresses did not cause the plate to fail prematurely via punchout. To accomplish this, the plate needed to be machined to the the thickness of 1-ply in the center of the sample. Using a CNC lathe, a profile

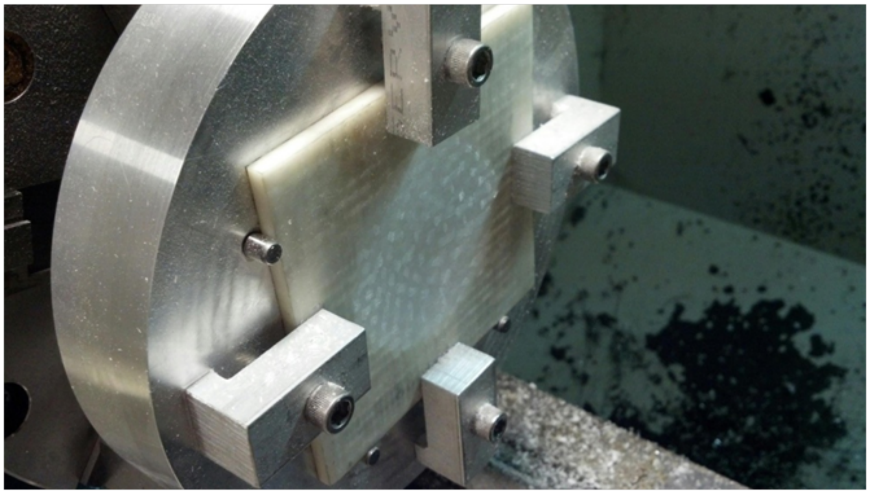

Figure 6.11: A photograph of a glass sample in the lathe after machining

was cut into each of the samples such that the 1 ply remained in the central portion. Additionally, to ensure that the yarns are not damaged, a 10% additional thickness is accounted for in the center of the plate. Since the yarns are not complete, the contribution to the stiffness is minimal. An image of the sample in the lathe fixture is shown in Figure 6.11.

In the original proof of concept tests, an initial batch was tapered to a profile in which the center had a diameter of 12.7 mm (0.5 in.). This will be termed the original geometry in the test results section and was only used for the glass fiber samples. After initial testing, the geometry was changed to have a center area of 25.4 mm (1.0 in.). This will be termed the final geometries and is used for both the carbon fiber and the glass fiber plates. After the machining operation, the thickness of the center of the plate was measured using a dial gage with resolution to 0.001 in. It was found that the plates were extremely consistent with the targeted thickness and the measurements were recorded prior to testing.

6.4.2 Initial Proof of Concept Tests

To prove this concept, an initial geometry was developed to thin the sample in the middle. The initial geometry was designed to include at least 4 Representative Unit

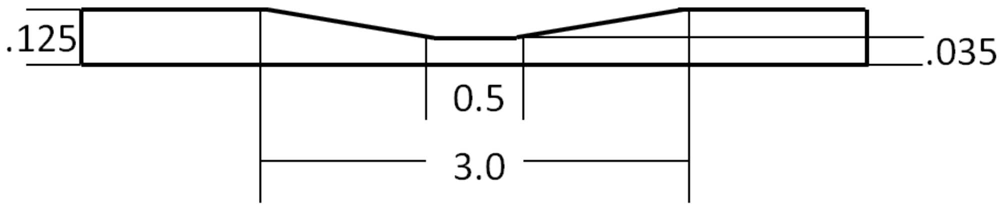

Figure 6.12: A schematic of the initial dimensions of the thinned plate (* not drawn to scale)

Cells (RUCs) across the diameter. This would give a more accurate representation of a panel level response. For this reason, a flat section of 12.7 mm (0.5 in.) diameter was cut into the center of the sample. A schematic of the the geometry is shown in Figure 6.12. For the proof of concept testing, only the glass plates were considered and a group of 6 initial plates was thinned to the described geometry.

To understand how the thinned plate deforms, the same procedure that was used for the flat plates was used. The plates were subjected to increasing shock strength to see if tensile rupture occurred at the crown of the plate. The deflection time history for the thinned plates is shown in Figure 6.13. The deflection-time history is very similar to that of the flat glass plates plates. As the shock strength is increased, so too is the out of plane deflection. With the thinned plates, higher deflections were observed without seeing the punchout effects that were observed with the glass plates. While punchout became visible on shock strengths over 8.0 for the flat plates, the thinned plate was subjected to shock strengths of almost 9.5 without observing punchout. Additionally, over the range of shock strengths tested, there did not appear to be a significant saturation effect in the out of plane deflection as seen with the flat plates.

One issue that was observed with the flat plates was that after the initial peak, a secondary peak is observed. In the flat plates this was observed to be an effect of the outer ply beginning to push out and was validated by the drop in strain in the sample. More generally, as the deflection increased, there was not an increase or

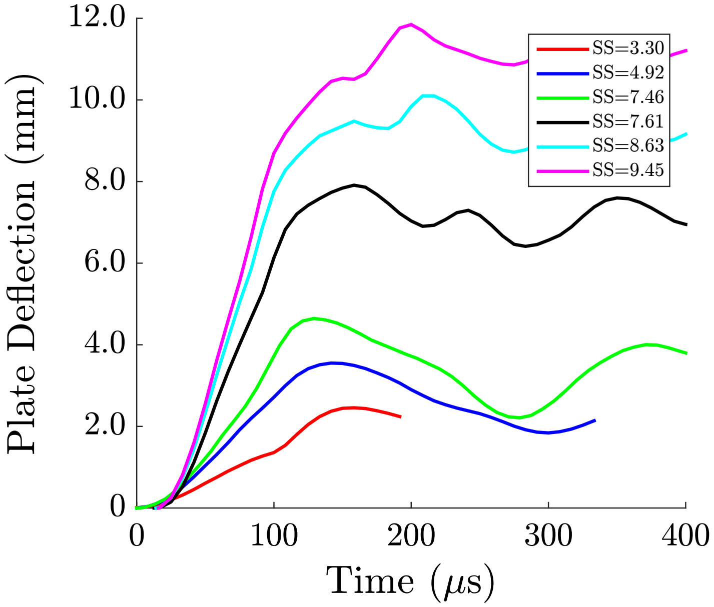

Figure 6.13: The deflection time histories for the initial thinned glass plates

constant strain observed, but rather a drop. In the thinned plates, at higher shock strengths, this same behavior of a local maximum followed by a rise was observed, but was not a result of punchout, but rather a function of the plate geometry. This is verified by the strain time histories shown in Figure 6.14. Instead of strains dropping during this additional rise, they are staying relatively stable. In the flat plates, strains of a little less than 3% were observed, however, in this loading, event, strains of 3.0% and higher are accumulated regularly within the plate and are enough to begin to damage the material. The elevated strains and relatively stable post peak response in the strain time histories is observed over a range of testing and is indicative of accumulated damage in the specimen.

To understand the effect of thinning the plate in the center, it is beneficial to compare the key data points from the tests. Among these are the deflection, strains, and strain rates in the material. The deflections as a function of the shock strength for the flat and thinned plate are shown in Figure 6.15(a). From this figure, it appears that the there is only a small increase in the maximum plate deflection between

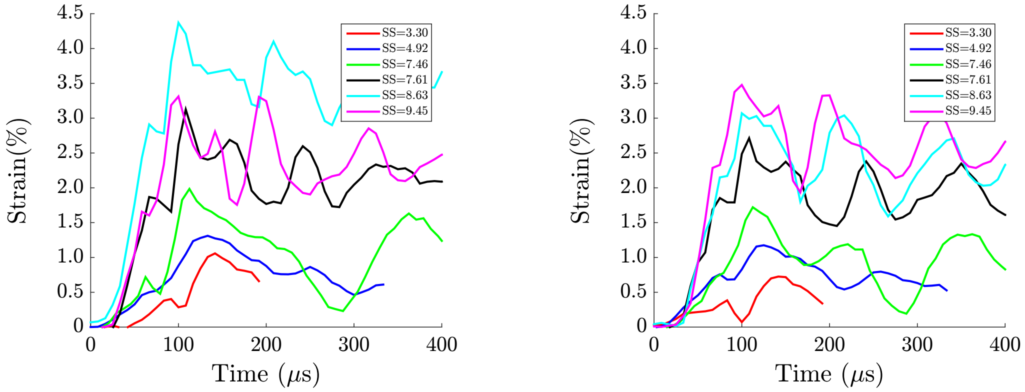

(a) The x-strain as a function of shock strength for the initial thinned glass plates

(b) The y-strain as a function of shock strength for the initial thinned glass plates

Figure 6.14: Comparison of the directional strains as a function of shock strengths for the thinned plates

the thinned samples and the flat plate, this does not give a true picture of what is gained by the thinning technique. Two key points points from the deflections need to be examined. The first is that while the slopes of the lines are similar, higher plate deflections were observed at the point where punchout was beginning to occur without observing any of the characteristics of the punchout. This is indicative of the fact that larger strains can accumulate in the crown of the deforming plate faster than the through thickness shear stresses. This allows for the test to come closer to achieving tensile rupture.

The second point that is of interest is that the deflection comparison between the two plates may not be a good indicator of what is occurring between the difference in the plates. Since the deflection of the plate is dependent on the flexural rigidity, this effect must be examined. Flexural rigidity is a function of both plate geometry, namely thickness, and the modulus of elasticity. While it is reasonable to assume that a 1ply sample has the same modulus of elasticity as an equivalent 4 ply sample, the thickness effect cannot be ignored. To demonstrate this effect, the deflections that are presented in Figure 6.15(a) have been normalized by the thickness of the plate at the center. The results of this are shown in Figure 6.15(b). From this figure, it

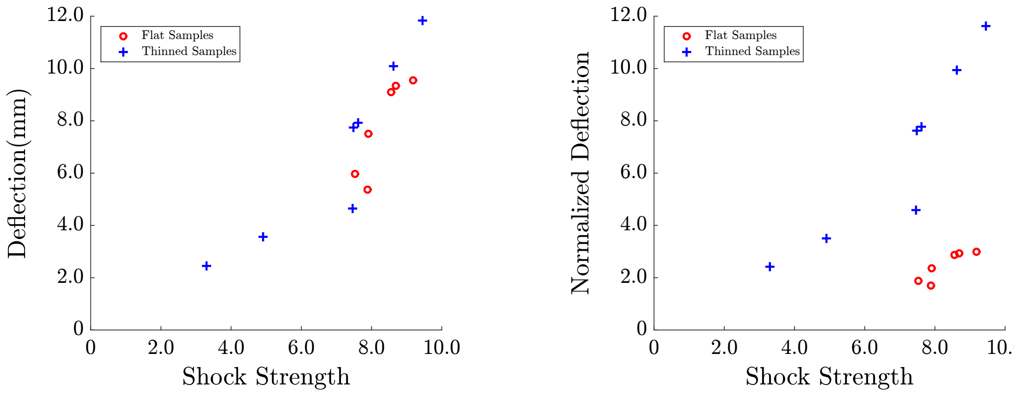

(a) The comparison of deflection as a function of shock strength for the flat and thin plates

(b) The comparison of deflection normalized by the thickness of the center

Figure 6.15: Comparison of flat and thinned deflection response

is clear that the slope of the thinned specimens is significantly higher than that of the flat samples. This indicates that for each increasing unit of shock strength, the deflection is much higher in the thinned plate relative to the flat plate.

This normalized effect is what allows for strain to accumulate to a great extent in the plate for the thinned samples than the flat plates. This is evidenced by the results shown in Figure 6.16 which shows the strains as a function of the shock strength for both types of plates. The thinned plates show much higher strains relative to the flat plates. This result is desirable because it indicates that the tensile strains on the outer surface are closer to failure and are damaging more than the yarns in the flat plate. This is further evidenced by the larger disagreement in the strain fields. While the agreement between strain in the two orthogonal directions was fairly consistent across the various tests initially, as the shock strength increases, the agreement becomes less suggesting 'orthotropy' in the damage accumulation leading to rupture. This is because the yarns in the textile plate are damaging resulting in a different response in the different directions. The damage accumulation is dictated by the strengths of the yarn, any manufacturing imperfections and the alignment of the yarns with respect to the plate boundaries. As damage accumulates, it does so non-isotropically.

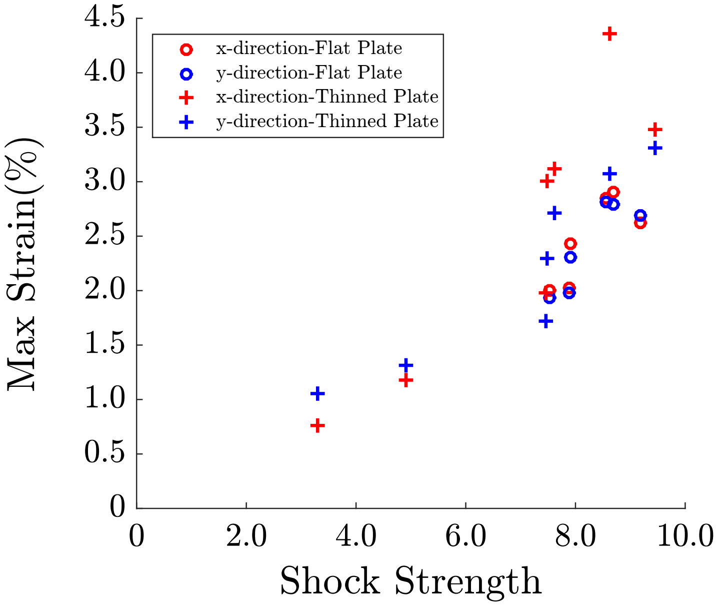

Figure 6.16: The directional strains for the flat and thinned plates

The effect of damage accumulation is further seen in Figure 6.17 which shows the strain rates in the sample as a function of shock strength. While the thinned samples experience higher amounts of strain, the strain rates are less than that of the flat plate for equivalent shock strengths. This is due to the damage accumulating in the yarns as it deforms rapidly which leads to local softening limiting the maximum achievable strain rate.

From these initial tests, it has been shown that thinning the samples does allow the sample to deflect to a higher amount without seeing the effects of punchout. The thinned samples accumulate higher amounts of strain than the flat plates, however, the strain rates are limited due to damage accumulation. The initial goal of achieving tensile rupture was not realized in the carbon plates. Using the information gained from the testing, a final test geometry was developed to include a larger area of thinned material. A schematic of the final geometry is shown in Figure 6.18. This geometry was used for the final tests presented in the subsequent sections.

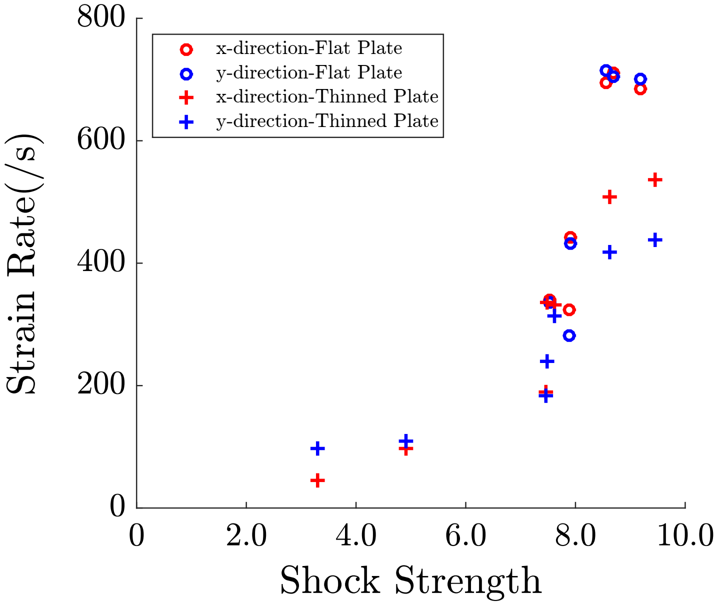

Figure 6.17: The directional strain rates for the flat and thinned plates

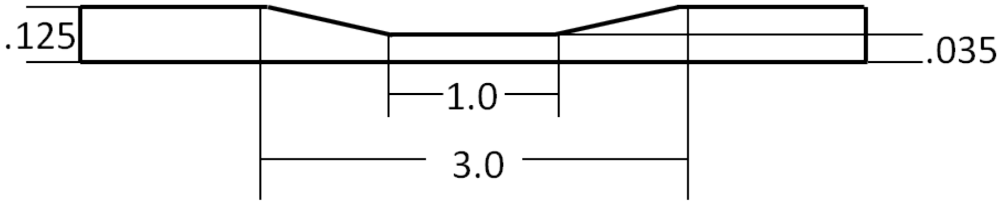

Figure 6.18: A schematic of the final dimensions of the thinned plate (* not drawn to scale)

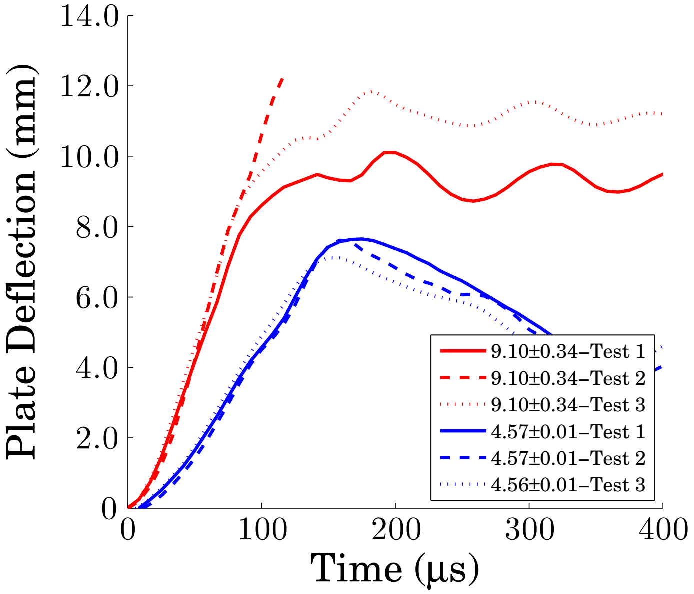

Figure 6.19: The triplicate testing for the final thinned glass plates

6.4.3 Thinned Glass Plate Testing Results

In order to understand the effects of the damage further, testing in triplicate was performed for the glass samples. However, due to limitations in material and safety considerations of the maximum operating pressures of the shock tubes, only two shock strengths were examined. The shock strengths tested were 4.57±0.01 and 9.10±0.34 and were accomplished by using Nitrogen and Helium respectively for the testing. These shock strengths were generated by targeting the same burst pressures in the driver section using the same number of mylar sheets, but heavier gases.

The results of the triplicate testing are provided in Figure 6.19 which show the deflection time history for the final geometry of the thinned plate. The samples that were tested at a shock strength of 4.57±0.01 showed a high degree of agreement between the three tests with nearly identical results in terms of the of the maximum deflection, rise time characteristics and post peak response. This was due to the fact that the burst pressures were all very close to each other demonstrating a high degree

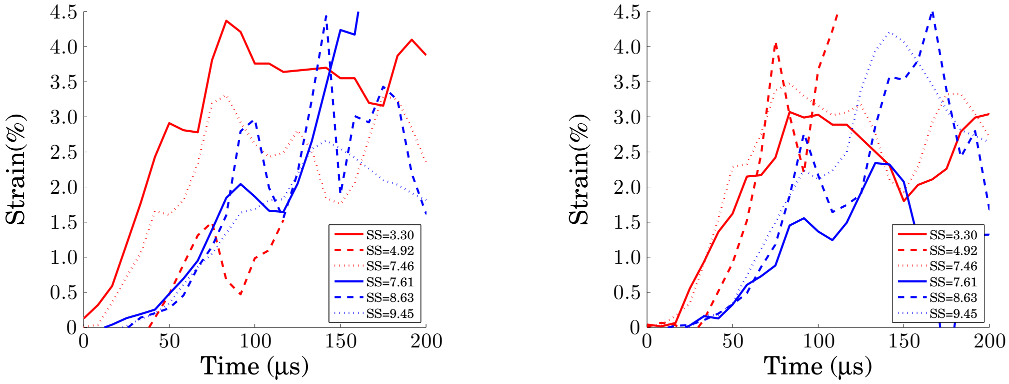

(a) The strains in the x-direction of the final thinned glass plates

(b) The strains in the y-direction of the final thinned glass plates

Figure 6.20: Comparison of strains and strain rates as a function of shock strengths

of repeatability in the sample.

The samples tested at the higher shock strength did not exhibit the same degree of agreement. There are two reasons for this. The first is the difference in burst pressures. While the number of sheets of mylar was held constant, the bust pressure may not always be consistent and is dependent on loading rate and other factors during testing. To achieve a high degree of repeatability, the gas should fill the driver section at a constant pressure. The incoming gas is regulated however, at these levels or pressures, it typically requires 2 cylinders of compressed helium since a higher pressure cylinders are not as readily available as the nitrogen. Because of this effect, there is a higher deviation in the burst pressure which can differ by as much as 25% between the highest and lowest burst pressure.

The second and more important reason why there is a larger difference is the damage accumulation in the samples subjected to the higher pressures which leads non-isotropic damage accumulation due to the localization of damage and subsequent progressive damage growth which do not occur identically from sample to sample. This is because of stochastically in sample internal architecture and the presence of any unintended manufacturing defects. This is evident in the directional strains

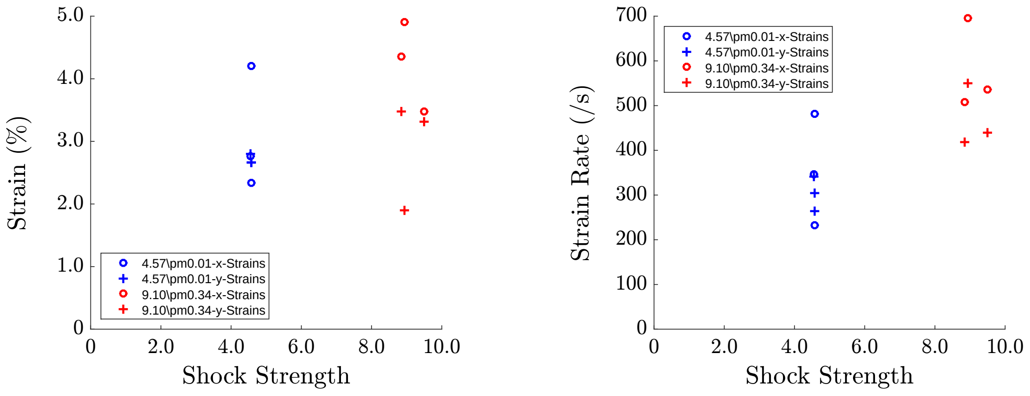

(a) The maximum strains in the thinned plate as a function of shock strength

(b) The strain rate as a function of shock strength for the thinned glass plates

Figure 6.21: Comparison of strains and strain rates as a function of shock strengths for the final thinned glass plates

shown in Figure 6.21. From this, it can be seen that for the samples that are subjected to a shock strength of 4.57, there is strong agreement between the tests and between the directions. As the shock strength is increased, the strain time histories show much less agreement due to the non-isotropic damage accumulation in the yarns. This is evidenced by the fact that the directional strains are much different and within the data set itself it is quite scattered.

The maximum strains and strain rates seen in the plate as a function of shock strength are shown in Figure 6.21(a) and Figure 6.21(b) respectively. The samples that were subjected to a shock strength of 4.57 experienced 2.91±0.65% and strain rates of 328.5±87.5. The samples with the 9.1 shock strength experienced an average strain accumulation in the crown of 3.57±1.0% and strain rates of 524.4±99.0.

Post test inspection revealed large amounts of longitudinal cracks in the samples subjected to higher pressures. At the higher pressure, transverse cracking of the yarns at the crown of the plate was observed, however, complete tensile failure was not observed. Due to the limitations in testing capabilities due to safety while operating the shock tube, further testing at even higher shock pressures could not be completed.

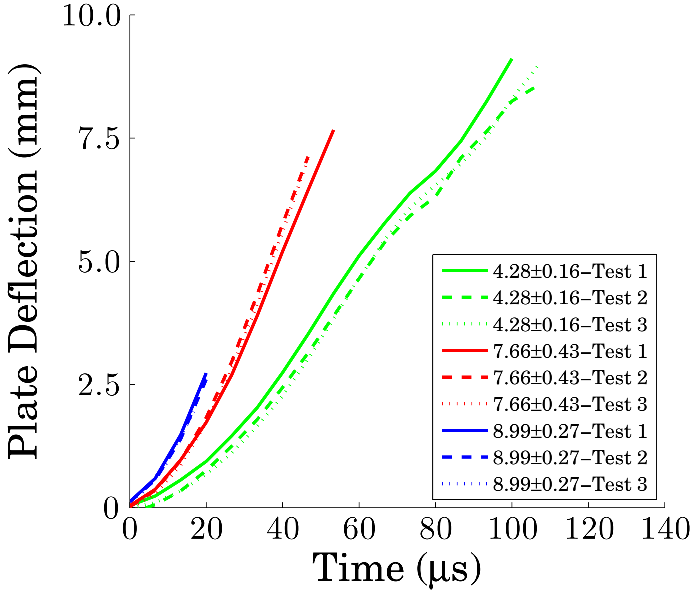

Figure 6.22: The triplicate testing for the final thinned carbon plates

6.4.4 Thinned Carbon Plate Testing Results

While complete tensile rupture of the glass was not achieved, the carbon samples offer a different response that is more conducive to complete tensile rupture. The glass has particularly high energy absorption characteristics and in comparison to the carbon, yields a much more compliant response. Since the carbon is relatively brittle by comparison, tensile rupture is a much more likely option. As shown in in chapter 2 on the unidirectional testing, the carbon fiber tows store large amounts of elastic energy and at rupture, dissipates energy rapidly due to localization. The ensuing ”‘rupture”’ waves cause additional failure in other area of the undamaged sample resulting in complete failure.

For the testing with carbon, three shock strengths were targeted since the failure occurs at shock strengths low enough to not affect the safety of testing. The shock strengths were 4.28±0.16, 7.66±0.43, and 8.99±0.27 and were generated with Nitrogen for the first strength and the final two being subjected to helium shocks. These

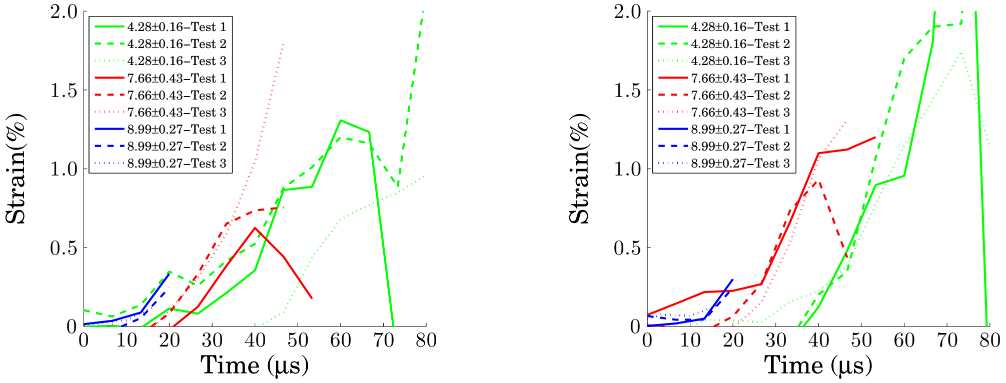

(a) The strains in the x-direction of the final thinned carbon plates

(b) The strains in the y-direction of the final thinned carbon plates

Figure 6.23: Comparison of strains and strain rates as a function of shock strengths

shock strengths allowed for a range of loading rates to be examined during the course of testing.

The deflection time histories for the thinned carbon plates are shown in Figure 6.22. The samples have a few features that are quite unique. The first is that the testing shows a high degree of repeatability between the samples as they fail. Over each set of the triplicate testing, the rise times and final deflections at failure are very consistent.

The second is, as the shock strength is increased, the failure deflection has an apparent decrease. While this effect is consistent with what was reported in the high strain rate properties, what is shown in this plot is the deflection at which the plate has completely failed. This is best exemplified by the tests that were performed at the 4.28 shock strength where each of the curves shows a slight hitch that happens at approximately 6.5 mm of deflection. At this point, there is visible confirmation of a crack forming in the strain fields, however, complete separation and failure does not occur until the point that is shown on the curve.

This general softening effect is further seen in the directional strain fields which are shown in Figure 6.24 for the x and y directions. In general, as the loading rate is

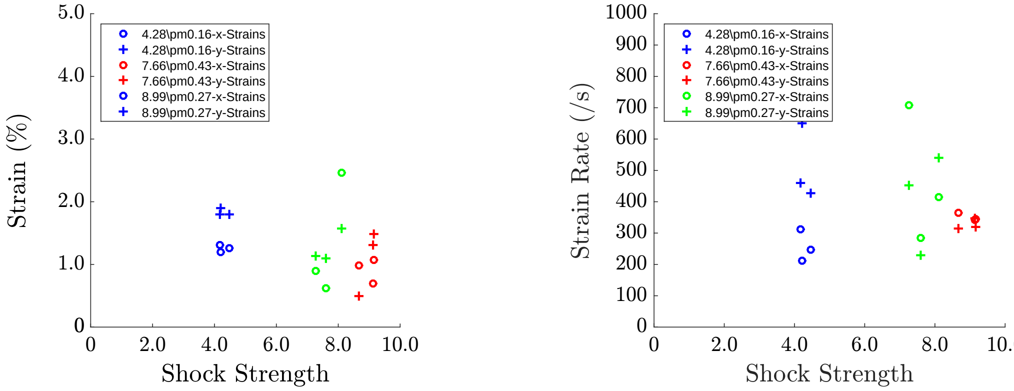

(a) The maximum strains in the thinned plate as a function of shock strength

(b) The strain rate as a function of shock strength for the thinned carbon plates

Figure 6.24: Comparison of strains and strain rates as a function of shock strengths for the final thinned carbon plates

Shock Strength	Strain Rate (/s)	Failure Strain (%)
4.28±0.16	384.5±162.2	1.55±0.32
7.66±0.43	338.6±18.2	1.00±0.37
8.99±0.27	438.3±173.8	1.29±0.65

Table 6.1: The average strain rates and failure strains in the carbon samples

increased, the failure strains decrease and exhibit very brittle behavior. During this test, there is good agreement between the strain fields. This indicates that there is not a significant amount of damage anisotropy that is present in the plate prior to failure.

The failure strains and strain rates are also shown in Table 6.1. It is worth noting that the error is quite large in this experiment because of the way in which the strain fields are measured. The first is the normal strains that are developed on the plate, however, once the plate begins to fail, cracks are created and contribute to the strain fields as a crack or crack opening strain. Figure 6.25(a) shows a deflection-time history for one of the samples with the strain fields. The image shows that as the material fails and cracks begin to open, the strain fields show large areas of high strain across the cracking surface. In turn, as the cracks open, it creates very large strains in a

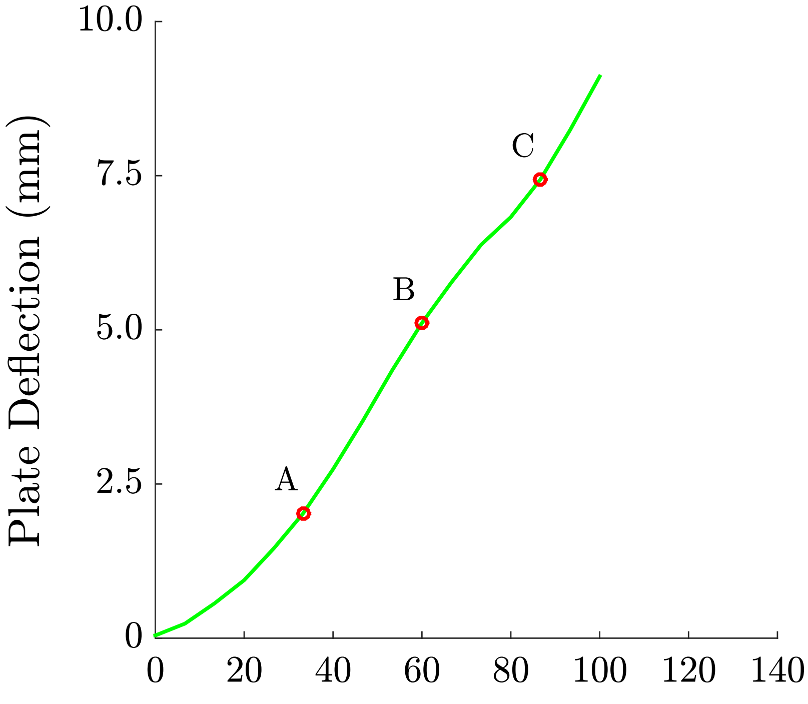

(a) Deflection time history of a damaging carbon plate showing the opening of the cracks

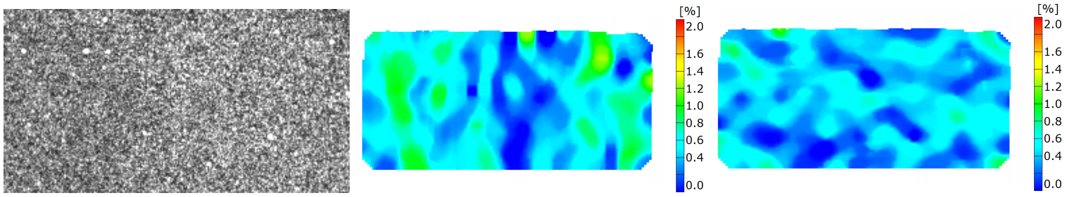

(b) Raw image at point A (c) X-direction strain at point A (d) Y-direction strain at point A

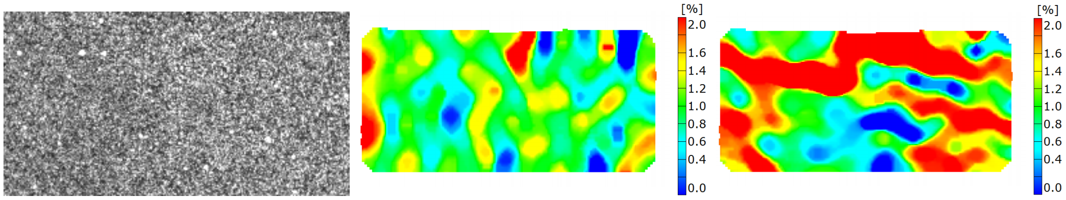

(e) Raw image at point B (f) X-direction strain at point B (g) Y-direction strain at point B

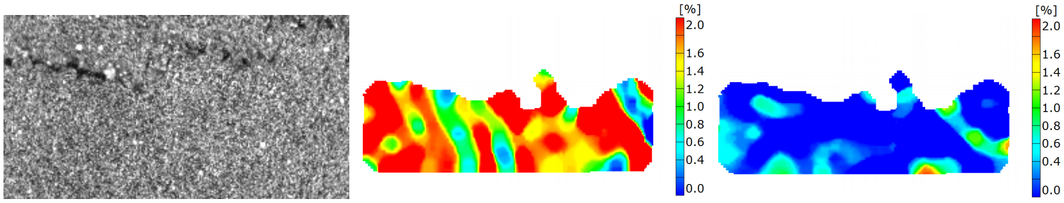

(h) Raw image at point C (i) X-direction strain at point C (j) Y-direction strain at point C

Figure 6.25: Schematic showing the progression of damage to a crossply glass sample at a strain rate of 705/s

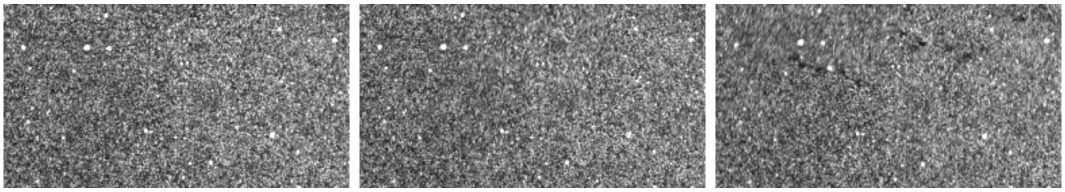

(a) Test 1-$t = t_{fail} - 6.6\mu$s (b) Test 1-$t = t_{fail}$ (c) Test 1-$t = t_{fail} + 6.6\mu$s

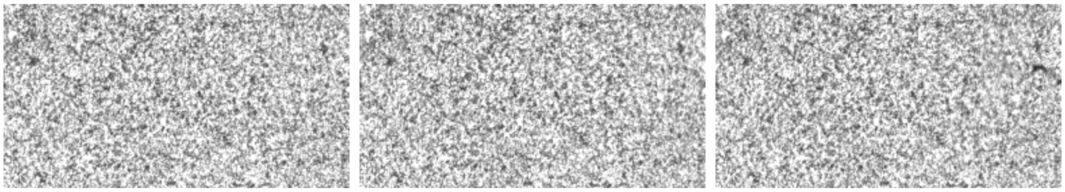

(d) Test 2-$t = t_{fail} - 6.6\mu$s (e) Test 2-$t = t_{fail}$ (f) Test 2-$t = t_{fail} + 6.6\mu$s

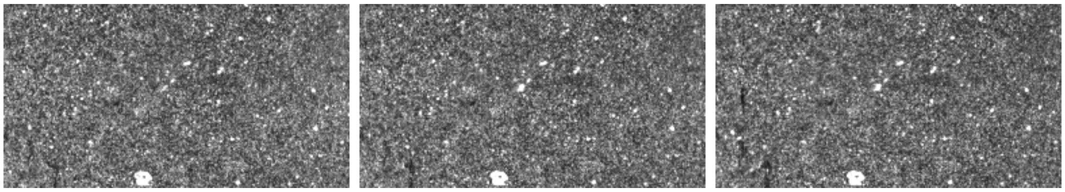

(g) Test 3-$t = t_{fail} - 6.6\mu$s (h) Test 3-$t = t_{fail}$ (i) Test 3-$t = t_{fail} + 6.6\mu$s

Figure 6.26: Failure images for the triplicate testing at shock strength of 4.28±0.16

short duration of time resulting in high strain rates. The values themselves give a good sense of the failure on the average, but in order to understand it further, the strain time history of each of the plates gives a better indication of what is really happening. This is the better metric for determining the plate response.

Figures 6.26, 6.27, and 6.28 show the raw images of the progression of failure for each of the triplicate testing. Each of the figures is shown as one frame before failure, at failure, and one frame after failure. With the given frame rate, each image is taken at 6.6 μs. Failure was determined from visual inspection coupled with loss of correlation in the DIC analysis. When examining the triplicate testing for the shock strength of 4.28±0.16, each of the plates showed a similar failure. This failure was characterized by a single failure across the plate with one opening strain. In Figure 6.26(c), a crack opens horizontally at approximately 2/3rds of the height of the image. In Figure 6.26(f), this crack is propagating at a similar height and can be seen on the righthand side of the plate. Finally, in the third test (Figure 6.26(i)), the crack

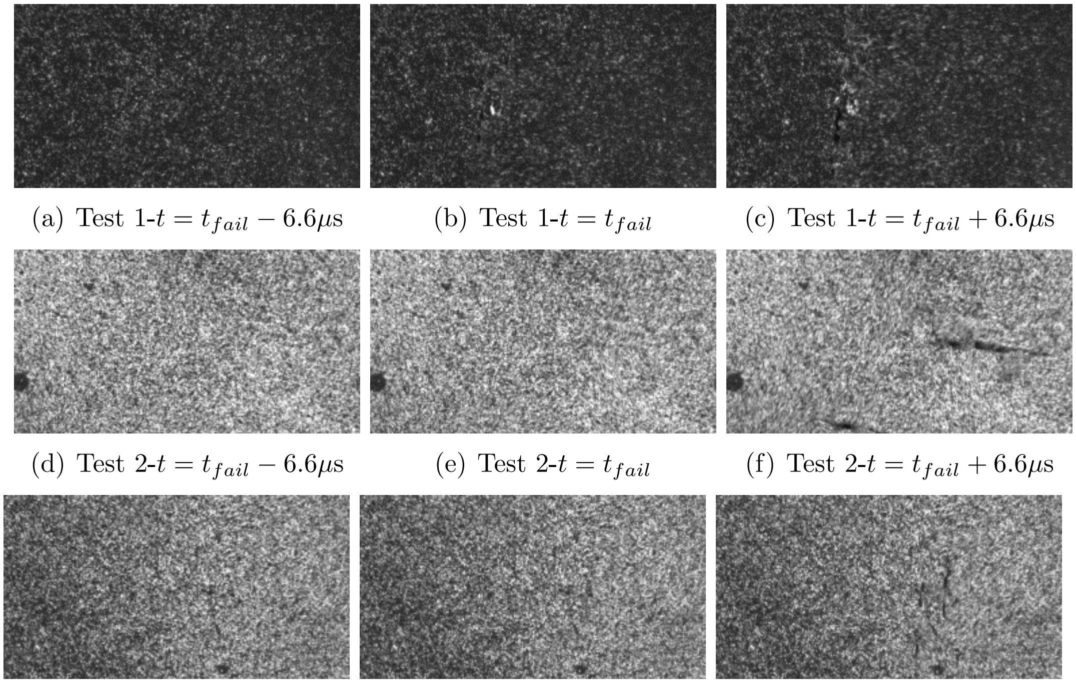

(a) Test 1-$t = t_{fail} - 6.6\mu$s (b) Test 1-$t = t_{fail}$ (c) Test 1-$t = t_{fail} + 6.6\mu$s

(d) Test 2-$t = t_{fail} - 6.6\mu$s (e) Test 2-$t = t_{fail}$ (f) Test 2-$t = t_{fail} + 6.6\mu$s

(g) Test 3-$t = t_{fail} - 6.6\mu$s (h) Test 3-$t = t_{fail}$ (i) Test 3-$t = t_{fail} + 6.6\mu$s

Figure 6.27: Failure images for the triplicate testing at shock strength of 7.66±0.43

propagates vertically on the left hand side of the image. Subsequent images show that this is the failure crack that opens without subcracks developing.

The failure images for a shock strength 7.66±0.43 shown in Figure 6.27 show similar behavior. In Figures 6.27(c) and 6.27(i), a vertical crack forms near the center of the plate and propagate vertically. The behavior in the second test is different though. Instead of a single crack forming, two cracks are seen in Figure 6.27(f). The first crack is horizontal along the center of the plate and the second one is also horizontal forming at the bottom of image.

When the shock strength is increased to 8.99±0.27. the failure is no longer limited to a single crack. In Figures 6.28(c), 6.28(f), and 6.28(i), many cracks are seen opening simultaneously. In general, the failure is almost a type of pedaling type behavior in which the center opens up along cracks that propagate from the center outwards. These failure images lend further insight into the ability of plain woven structure to dissipate energy. As the shock strength is increased, the plate has less ability

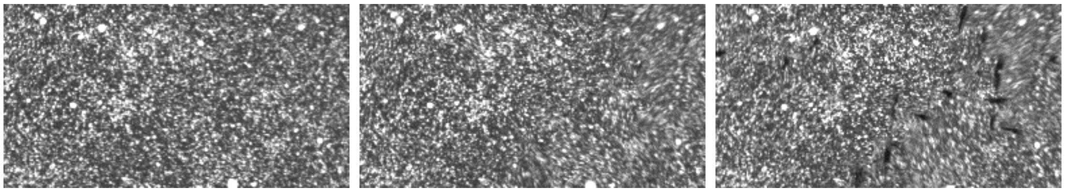

(a) Test 1-$t = t_{fail} - 6.6\mu$s (b) Test 1-$t = t_{fail}$ (c) Test 1-$t = t_{fail} + 6.6\mu$s

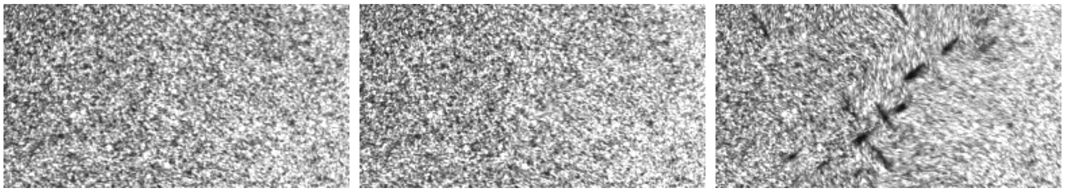

(d) Test 2-$t = t_{fail} - 6.6\mu$s (e) Test 2-$t = t_{fail}$ (f) Test 2-$t = t_{fail} + 6.6\mu$s

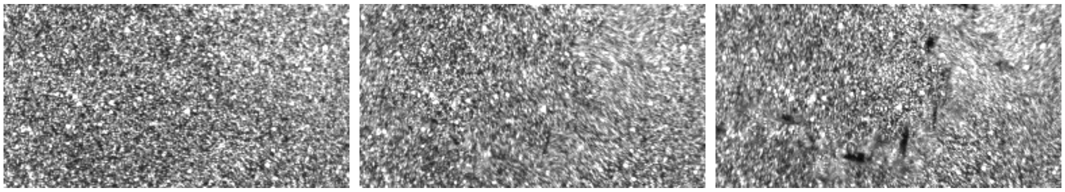

(g) Test 3-$t = t_{fail} - 6.6\mu$s (h) Test 3-$t = t_{fail}$ (i) Test 3-$t = t_{fail} + 6.6\mu$s

Figure 6.28: Failure images for the triplicate testing at shock strength of 8.99±0.27

to dissipate the stored energy and results in a more catastrophic failure due to the formation of increasing numbers of cracks.

6.5 Conclusions

In this chapter, flat plates of plain woven carbon and glass were subjected to shock loading to attempt to create tensile rupture of the yarns on the outside of the plate. After an initial round of testing, it was determined that the through the thickness shear stresses were large in comparison to the tensile stresses on the crown and would not be sufficient to cause tensile failure. In an attempt to reduce the effect of the through-the-thickness shear stresses, a novel testing technique was developed in which the center of the plate was thinned to the thickness of approximately one ply.

The thinned plate led to higher strain accumulation in the crown of the plate and higher deflections were achievable. After initial testing, a final geometry was developed and used to perform triplicate testing at two different loading rates for the glass plates and three loading rates for the carbon. Tensile rupture was acheived in the carbon plate, but not in the glass due to large amounts of energy dissipation. This allowed for a distinction to understand the difference between damage mechanics and failure mechanics as the glass samples experienced large amounts of matrix damage accumulation and the carbon samples did not.

CHAPTER VII

Creation of a Finite Element Model for IM7 Plain Woven Material

The previous chapters presented the experimental data from two sets of tests that can be used to determine the high strain rate tensile response of composite materials. While the split Hopkinson tensile bar (SHTB) gave information about the constituent level response, the shock tube tests gave more of a material level response. This chapter focuses on the development of a 3D Finite Element Model (FEM) of the plain weave samples. While up until this point, both carbon and glass samples have been examined, the carbon sample will be selected for modeling as tensile rupture failure was achieved in the testing.

7.1 Introduction

The plain weave is one of the most basic textile composite architectures and is of great interest because the geometry, in some regards, represents the most complex shape a textile laminate can be made to be by having the shortest frequency of the undulation. Furthermore, this relationship between the yarns as they pass over each other is an area where damage frequently occurs and is of great interest. In other woven systems such as twills and harness architectures, [95], this interaction between cross-over yarns is less prevalent in comparison to the plain weave.

Early analysis of plain woven structures was limited to understanding elastic effects. Naik and Ganesh performed extensive analysis to develop analytical solutions for the in plane stiffnesses [69], and thermal properties [70]. Analytical methods have also been developed for thermal conductivities in plane [73] and out of plane [74] for plane woven materials. Other researchers have proposed further techniques to develop analytical solutions including a Selected Averaging Method in which the unit cell is analyzed in slices and at the sub slice level [97]. Analytical solutions for plain woven composites have been well examined throughout the last two and a half decades. More recent work by Quek et al. [89], [88], and Kier et al. [48] have introduced an experimentally validated analytical method that can very quickly provide textile composite elastic properties fairly accurately.

More complicated loading conditions such as flexural testing, required the use of finite element modeling. For this reason, the concept of the Representative Volume Element (RVE) was developed. An RVE is considered to be a finite volume that accurately captures the physical response of the composite. Sankar and Marrey examined how a single RVE can be used to predict the flexural response in a plain woven beam [96]. Gowayed et al. used the RVE finite element approach to predict the elastic constants of many different 2D plain woven samples [24]. More recently, Zhang and Waas, [132] have presented an experimentally validated global-local model that can accurately capture textile composite flexural response.

While textile composites have been modeled for more than 20 years, many rely on what is considered the idealized architecture. This is due to the fact that the in-situ geometry is often difficult to model due to a manufacturing outcome referred to as nesting, [2]. Nesting occurs because of the manufacturing of the composites by VARTM as the VARTM process generally has a mold side and a bag side that is not pressed against a rigid part. When a vacuum is applied the compaction allows the yarns to deform against each other. While the vacuum does allow further compaction, it limits the ability to achieve high fiber content [126], and can lead to higher void content [51]. As early as 1993 researchers proposed techniques to measure yarn shapes and nesting of plain woven composites [128]. Subsequent work by Yurgaritis suggested techniques to measure fiber spatial distribution, small-angle fiber misalignment, yarn shape relative to nesting, and microcrack structures [127].

The relationship between in-situ architecture and the failure is not fully understood, but of great interest. Ganesh and Naik found that in-situ geometry can significantly affect plain woven materials in shear [19]. Pollock found experimentally that during the failure of plain woven carbon samples under tension, fiber bundles with large curvatures failed under shear loading [87]. Woo and Whitcomb examined the effect of tow misalignment and determined it had a significant effect on the elastic properties [122].

Failure of composites using RVE level modeling is a more recent occurrence. Whitcomb and Srirengan used a relatively simple failure model with coarse mesh to examine the effects of matrix damage and progressive failure in an RVE [119]. Karkkainen and Sankar used a higher fidelity plain woven RVE element to examine the failure of plain woven textiles under bending [46]. Damage models have been used for many loading conditions including tension [129], quasistatic punch shear [124], and compression [134]. However, many of these models tend to be matrix rich or based on idealized geometries and use linear elastic material response. An exception are the studies by Song et al., [103], [102], Pankow et al. [81], Huang and Waas, [38] and Zhang and Waas, [132], who have used both geometric and material nonlinearity to accurately model the mechanisms of damage accumulation and failure in textile composites.

Recently efforts have been made to understand more realistic geometries that include nesting. Bednarcyk et al. have used a Generalized Method of Cells technique to predict the damage in a plain weave with high accuracy by using a modified idealized architecture [6] that is representative of a more realistic geometry.

Software has been developed on the academic side of research to model these geometries. TexGen is a textile geometry generated by developed by the University of Nottingham Textile Composite Research Group allows for idealized architectures to be developed with relative ease [76]. Digital Fabric Mechanics Analyzer (DFMA) is another available software that produces high fidelity geometries by virtually weaving a textile, however, has difficulties in extracting usable geometry [64]. Extensive work has been done with KU Lueven's program WiseTex developed by Stepan Lomov [60]. WiseTex has been used in concert with python scripting to create realistic geometries in textile composites. Lomov has written two review articles that identify what are considered key points of interest when modeling textile composites [61], [59]. These can be summarized as follows:

1. Proper implementation of boundary conditions is necessary
2. The mesoscale can be used to model the elastic deformation and damage
3. The mesoscale can be used in concert with a multi-scale modeling to capture unique failures
4. Proper geometrical considerations, while sometimes can be difficult to mesh, offer a high degree of fidelity.

In this chapter, an RVE will be developed that contains both realistic and idealized features compared to a plain weave carbon sample identical to that used in the shock testing. This RVE will be subjected to planar tension loading, initially. An evaluation of many modeling factors including periodic boundary conditions, nonlinear geometry, and global-local modeling are presented. After investigation of the elastic properties, failure of the yarns is introduced via the smeared crack technique. In support of modeling, experimental results are also reported.

7.1.1 Experimental Testing

The plane weave material was extracted from the sample bulk plate that the shock tube specimens were extracted from. A simple diamond saw was used to cut the panel into strips that were 50.8 mm x 177.8 mm (2 in. x 7 in.) The width was chosen to be high to maximize the number of RVEs included in the configuration to be studied which was in excess of 15 RVEs. By having more than 4 RVEs, it is allows for the structural level response of the composite to be measured and is no longer heavily influenced by the architecture or local discontinuities. The strips were tested at a loading rate of 0.61 mm/min with the load and displacement being sampled at a rate of 10 Hz. High resolution images were taken at a rate of one photograph for every 5 seconds for the glass and one photograph every 3 seconds for the carbon samples. This was done to ensure that approximately 100 photographs were taken during the event to analyze the possibility of progressive damage in the sample. A total of 5 tests were conducted for each specimen, however, only 4 samples are shown in Figure 7.1 because the first test was omitted due to premature failure as a result of excess clamping force by the hydraulic grips.

From Figure 7.1 it is clear that a high degree of repeatability is achieved with the testing. The mechanical properties are shown in Table 7.1, which show the failure strength, the failure strain, and the modulus of elasticity. These will be the first metric that will be used when evaluating the efficiency of the model.

Sample	Modulus (GPa)	Failure Strain (%)	Failure Stress (MPa)
Carbon	48.3±4.0	1.03±0.10	484.7±31.9
Glass	21.3±0.9	1.76±0.24	322.7±35.3

Table 7.1: Material properties determined from testing of plain weaves

While response of the textile plate shows generally a linear elastic response until failure, which is generally seen in fiber dominated loading cases, there is still damage that accumulates in the material, albeit on a smaller scale. This is most evident by

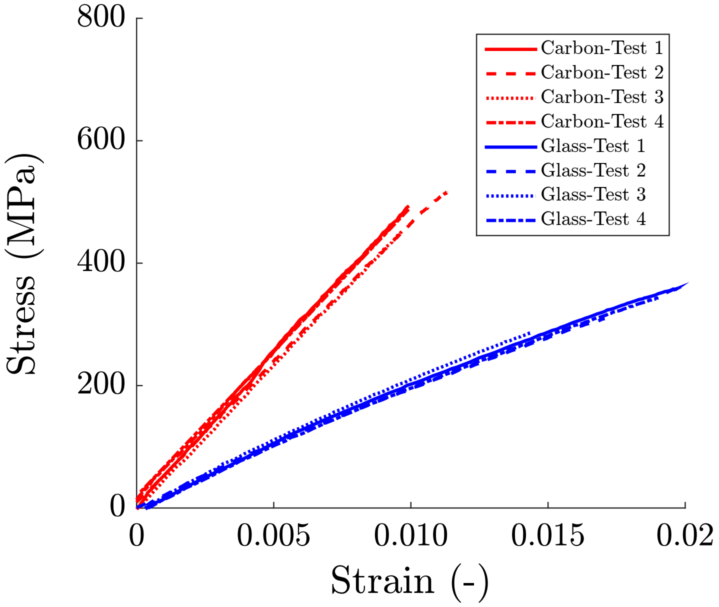

Figure 7.1: The stress-strain response of the carbon and glass samples

examining the strain fields of the DIC images shown in Figure 7.2(a) which shows the stress strain response for one of the tests.

While the total axial strain is on the order of 1%, the failure scale is set to 1.25% to show that there is a characteristic checkerboard pattern that develops during testing. The checkerboard pattern is higher strain than the axial strain that is applied and follows the pattern of the plain weave itself. These elevated strains are related to a few different aspects, but namely the damage of the matrix as it strains. The strain fields are further shown to be higher because the woven geometry creates matrix pockets, which are sites for strain concentration and is confirmed by the microscopic images shown previously in Figure 7.4(a) and in Chapter 2. As the material is strained from Figure 7.2(b) to 7.2(d) it is clear that a nearly periodic pattern is developing. By the ultimate failure shown in Figure 7.2(g), it is clear that a large portion of the sample is experiencing local strains that are higher than the global strain.

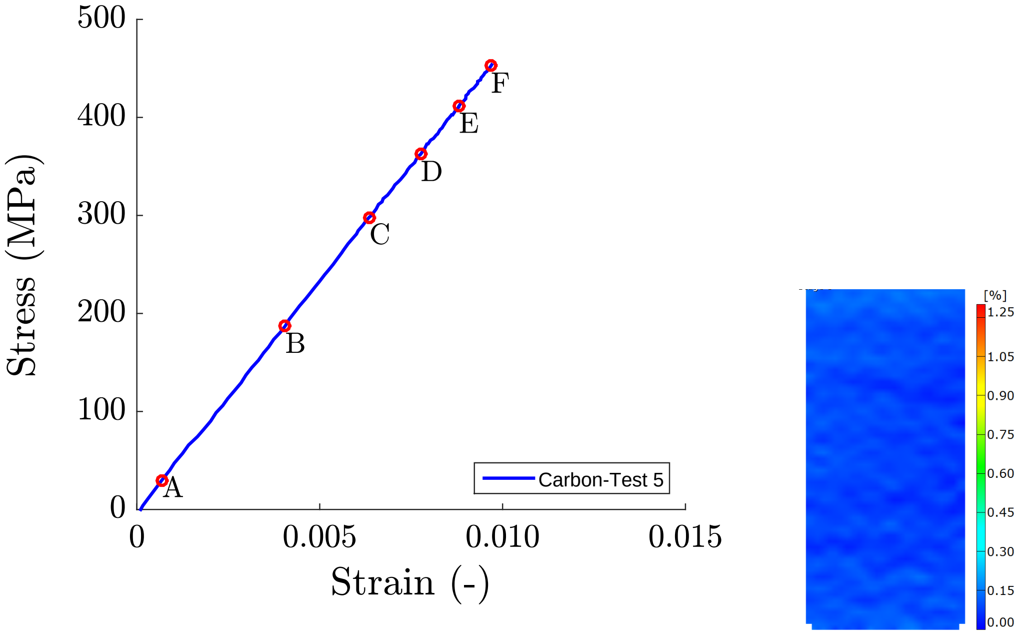

(a) The stress-strain response of a carbon sample

(b) Axial strain at point A

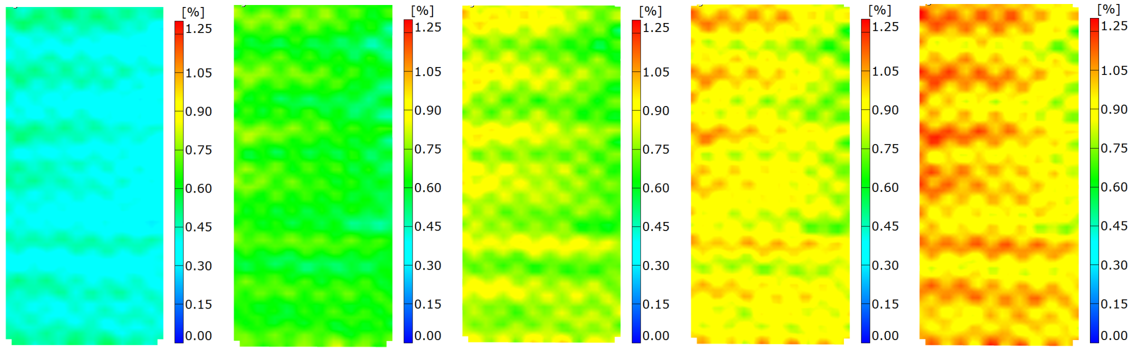

(c) Axial strain at point B

(d) Axial strain at point C

(e) Axial strain at point D

(f) Axial strain at point E

(g) Axial strain at point F

Figure 7.2: Schematic showing the progression of damage to a plain woven carbon sample

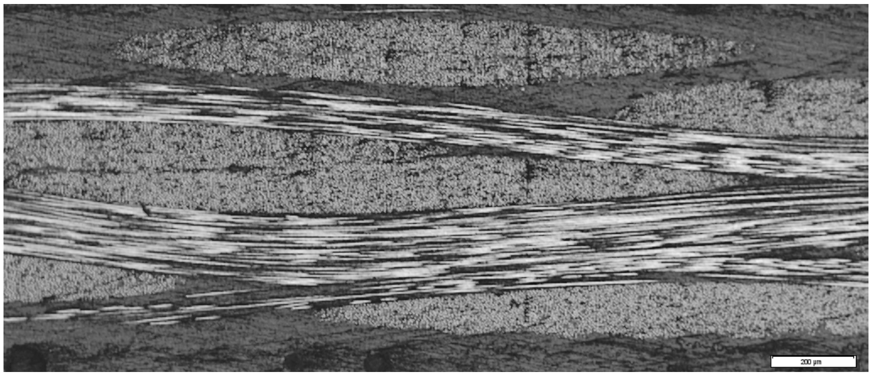

Figure 7.3: A carbon plain woven sample at 5x magnification

7.2 Optical Microscopy Results

In order to capture the accurate geometry of the textile composite, optical microscopy was performed. A plain woven samples was potted, ground, and polished to see the microstructure. A Olympus microscope with optical settings of 5x, 10x, 25x, 50x, and 100x were used and the microscope was fixed with a CCD that allowed for images to be taken. The Olympus microscope measuring system was precision calibrated using a micrometer ruler to set the pixel length. An image of the sample is shown in Figure 7.3.

From the four samples that were ground and polished, a total of 5 measurements were made from the 5x zoom. After further magnification, a sixth measurement was made. The measurements were as follows:

1. the thickness of a single ply, h
2. the major axis of the tow, a
3. the minor axis of the tow, b
4. the cross-sectional area of the tow, A
5. the distance between tows, d
6. the fiber volume fraction, V_f

(a) A microscope image at 5x magnification

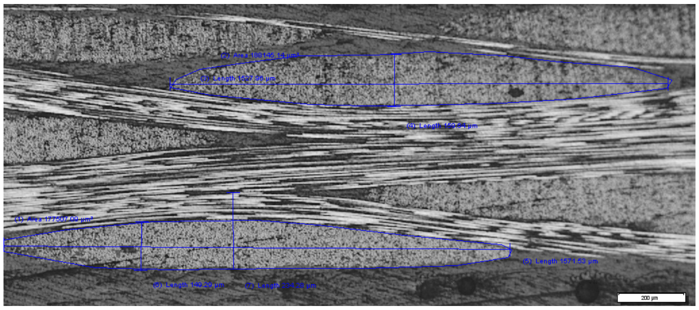

(b) A microscope image showing the measurements of the geometry

Figure 7.4: A comparison of the measurements for the textile composite

The first 5 measurements were made using the built in measuring tools within the Olympus post processing program an example of this process is shown in Figure 7.4. Figure 7.4(b) shows the measurements for the area of two tows, A, the major and minor axis, a and b, and the thickness of a ply, h. For each of the metrics, 6 measurements were taken to determine the average nested shapes that occur within the nested geometry. The results of the measurements are shown in Table 7.2

Ply Thickness h (μm)	Tow Major Axis a (μm)	Tow Minor Axis b (μm)	Tow Area A (μm^2)	Tow Separation d (μm)	Volume fraction V_f (%)
220.4±19.0	1653.7±109.7	156.0±15.7	181214.8±7105.8	384.6±69.1	62.0±1.3

Table 7.2: The results of the optical measurements for geometrical properties of the composite

The fiber volume fraction is measured optically using a MatLab technique developed by Mark Pankow, [83] In this technique, a fine image of the tow is taken such as that shown in Figure 7.5(a). Optical techniques are needed to create a high contrast

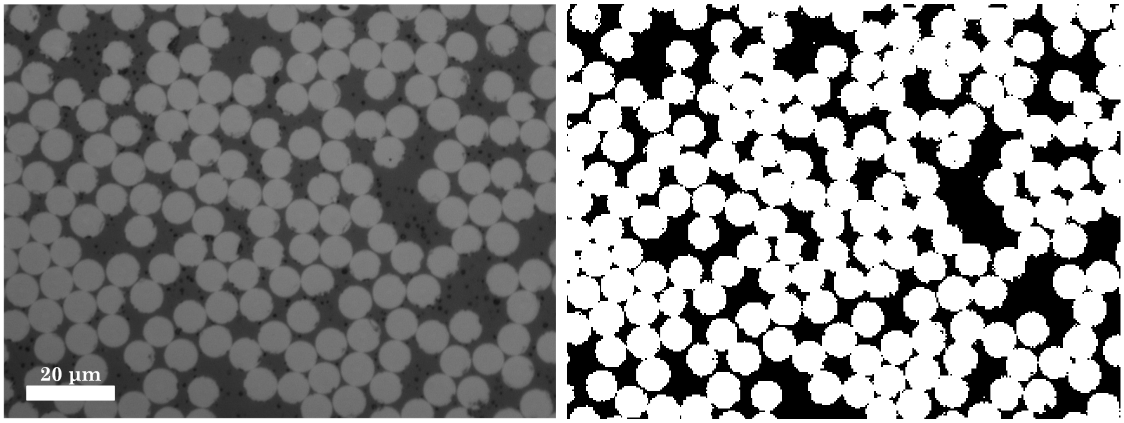

(a) A microscope image at 40x magnification of a carbon fiber tow (b) The result of image processing to convert to black or white

Figure 7.5: Example of fiber volume fraction of tow measured optically (66.5% for this carbon tow)

between the fibers and matrix. For this technique, the image is converted into a 256 grey scale set of pixels. The user then uses an input threshold grey scale level to serve as a point that separates the matrix from the fiber. The script then compares the grey scale levels and converts the image to either black or white depending on whether it is above or below the threshold. It then calculates the amount of white space to correspond to the fiber volume fraction. An example of this is shown in Figure 7.5(b). Note that the tow shown in this figure is for demonstration purpose only and not the tow measurement from the plain woven material.

7.3 Generation of 3D Geometry

As previously discussed, modeling of failure in textile composites frequently relies on idealized geometries that do not capture accurately the as nested geometry of the textile. The following sections demonstrate the shortfalls of using an idealized geometry and offer a step towards proper geometry by creating what is termed a 'Hybrid-Ideal Geometry'.

7.3.1 Idealized Geometry Generation

Many open source codes can be used to generate a finite element solid geometry of the plain weave. As mentioned previously, two widely used programs are WiseTex and TexGen. For this work, TexGen was used to generate a 2D plain weave. To generate this weave, TexGen requires inputs about the number of yarns in each direction, yarn spacing, yarn width, and fabric thickness. Additionally, there is a parameter that can be specified termed gap size. This parameter is a measure of the gap between yarns as the overlay each other. While the yarn spacing, width, and fabric thickness correspond to the measured values of d, a, and b, these values could not be used directly because they are considered to be as nested values and not idealized values. In order to create the the plain weave, parameters that were within the measured standard deviation were used. The properties that were used for the idealized structure as shown in Table 7.3

Yarn Spacing (mm)	Yarn Width (mm)	Fabric Thickness (mm)	Gap Size (mm)
315	1750	220	0.1

Table 7.3: Inputs for the TexGen idealized model

This geometry was then imported into Abaqus 6-12.1 where further operations were performed. Figure 7.6 shows many of the key geometric properties of the RVE. Figure 7.6(a) shows the weave and an empty matrix box. The weave was moved into place with the matrix box and the two parts were merged with intersections and boundaries being maintained. The purpose of this was to allow for easier applications of material assignments and orientations. Since the fiber tow is orthotropic, it is necessary to create a material orientation file. The material orientations are arranged such that the 1 direction is the fiber direction. Figure 7.6(b) shows the orientation as it has been assigned to the yarns in the geometry. A set of boundary conditions was made on the vertical direction to test the unidirectional tension case. The top face was prescribed a displacement of 0.1 mm, while the bottom face was simply supported. One node in the corner is fixed to prevent rigid body rotation. Finally the domain was meshed into 8000 tetrahedral elements and is shown in Figure 7.6(d).

The material properties are an important input to the model. The elastic constants for the tow were determined using the Concentric Cylinder Model (CCM) which was first proposed by Christensen and Waals [13]. The model treats a single fiber as a concentric cylinder with a cylindrical jacket of matrix. The radius of each cylinder is related to the fiber volume fraction of the tow. For this model, the fiber volume fraction was determined microscopically by the technique used previously. For the elastic constants, a fiber volume fraction of 63% was used and is within the measured error. The matrix elastic constants and the fiber properties were determined previously and shown in Chapter 2. The elastic constants are shown in Table 7.4.

E_{11} (MPa)	E_{22} (MPa)	G_{12} (MPa)	G_{23} (MPa)	ν_{12}	ν_{23}
174990	2868	1536	1192	0.3013	0.2028

Table 7.4: Elastic constants for a carbon fiber tow used for the model

At the completion of the analysis, the reaction forces perpendicular to the face in which the axial displacement was applied were extracted from a node set and the stress over the face was averaged. From this, a stress-strain curve was generated to determine if the results were within agreement with the static test. The comparison between the mechanical test and the idealized RVE is shown in Figure 7.7. From this figure, it is clear that the actual test shows a larger stiffness and it is not capturing the correct modulus of elasticity. While an attempt could be made to increase the fiber volume fraction that is used in the CCM elastic constants, this will create a fiber volume fraction that is inconsistent with what is measured in the tow.

From visual inspection and volume calculations, it was clear that the material response was not correct because the material was matrix rich, and minimized the

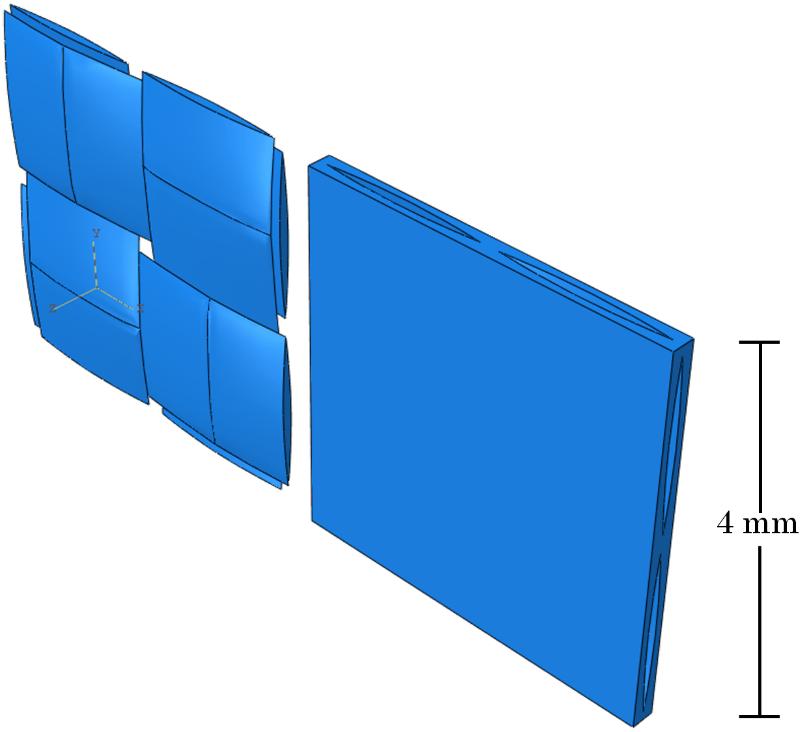

(a) An image showing the weave and the matrix before merging the geometry

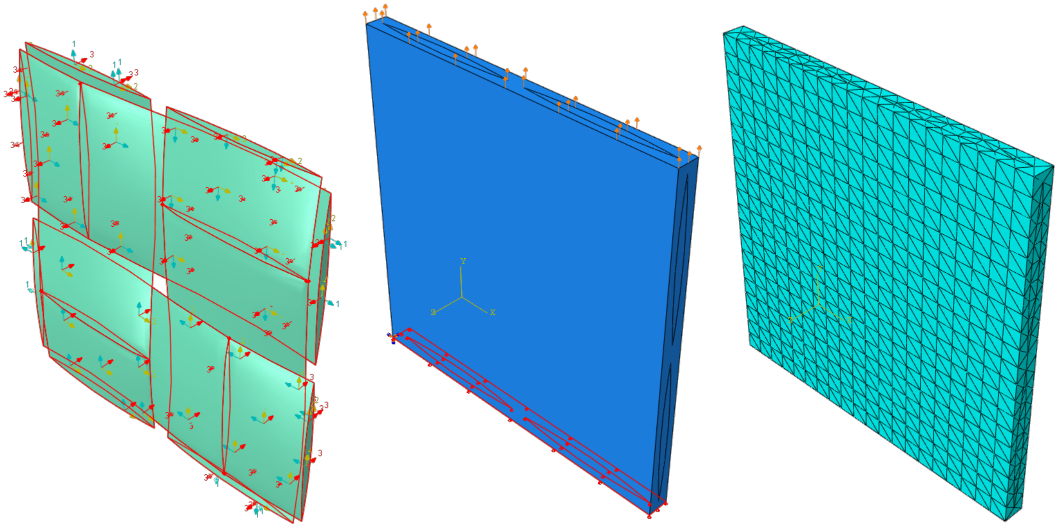

(b) Material orientations for the idealized RUC

(c) Boundary conditions for the idealized RUC

(d) Mesh for the idealized RUC

Figure 7.6: Key geometrical inputs for the idealized RUC

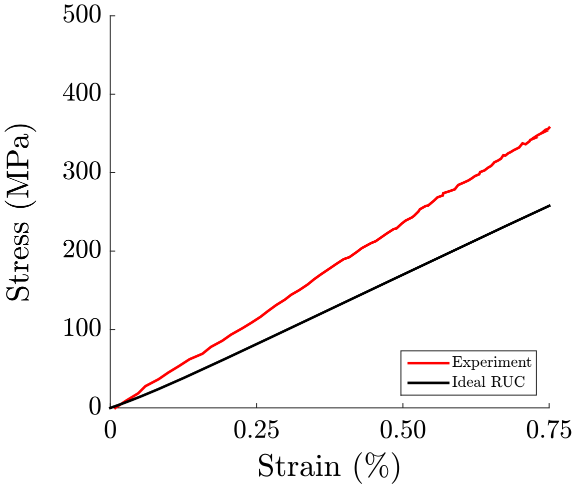

Figure 7.7: The stress-strain response of a plain weave test with the RVE

response of the tows relative to the matrix. The global fiber volume fraction in the idealized geometry was approximately 32.7%. While the mechanical properties of an individual fiber many vary, in order to get the correct stiffness, it is important to attempt to have a fiber volume fraction that is closer to an actual sample. For this reason, the Hybrid-Idealized Geometry was created.

7.3.2 Creation of Hybrid Idealized Geometry

In a panels that are manufactured via VARTM processes, it is common that one side of the panel has a fine finish due to the fact it is pressed against the tool, while the opposite side has a surface roughness that is consistent with the internal architecture. This is because this side is frequently bounded by a vacuum bag. Generally, the sides of these panels are referred to as the bag side and the tool side of the part. The tool side typically has a surface roughness that is consistent with the constituents and has a very strict adherence to the geometry of the part. It results in a very thin layer of matrix that follows the geometry of the weave. This is not captured in the RVE and frequently is neglected in simple ply models.

To capture this effect a new model was created in which an offset is created to allow

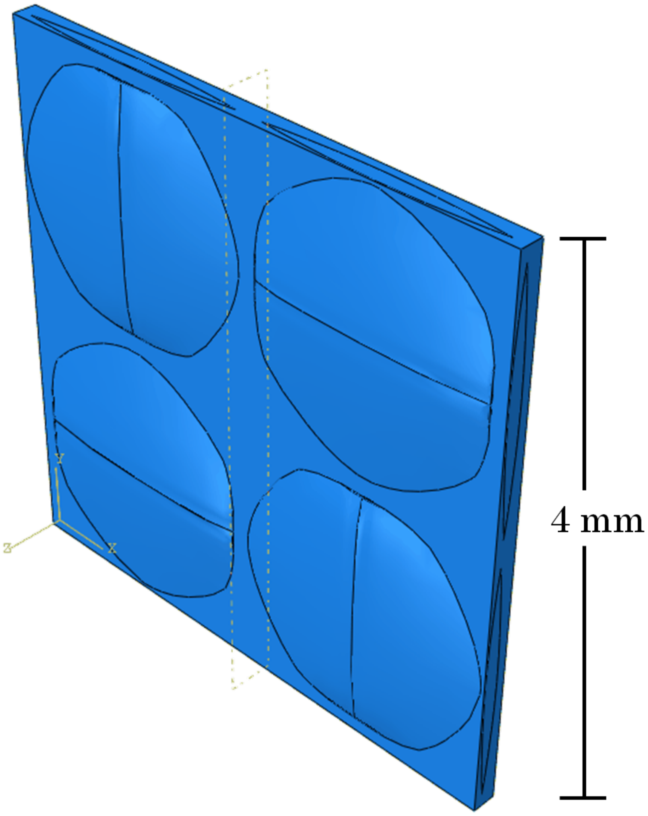

Figure 7.8: The geometry of the Hybrid Idealized Geometry.

for a surface roughness to be accounted for. The model is termed a Hybrid Idealized geometry because it contains aspects of both an idealized geometry and realistic geometry. While the yarns are modeled as constant cross-sectional ellipses along a line, the matrix contains realistic geometry features. An image of this geometry is shown in Figure 7.8. By doing this technique, the fiber volume fraction of the RVE was taken from the 32.7% in the original model to 45.5% in the hybrid idealized model. This volume fraction is generally consistent with what is observed with textile laminates manufactured by VARTM processes.

Material orientations and boundary conditions were applied in the same way as that described above. The mesh was finer than the previous model and contained 44271 quadratic tetrahedral elements of type C3D10. The finer meshing was necessary because the seeding was too coarse for the small areas of matrix outside the RVE.

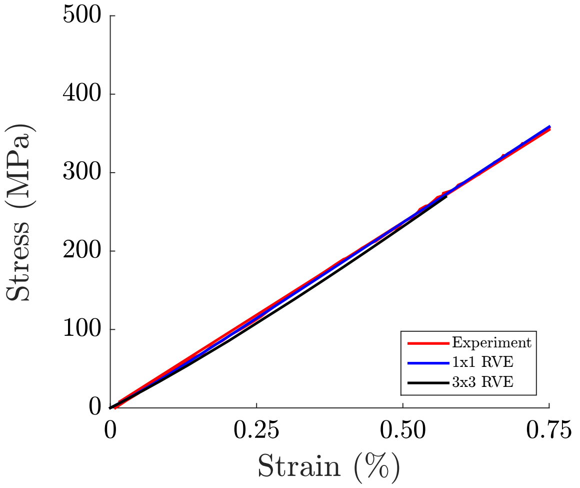

Figure 7.9: Comparison of the stress-strain response of the one RVE and 9 RVE to the experiment

The stress-strain curve was extracted in an identical manner as described previously. In addition to testing the RVE as itself, a 3x3 unit cell model was created to lend better insight into whether or not the geometry gave correct results. The stress-strain response is shown in Figure 7.9.

From Figure 7.9, it is clear that the stiffness of the RVE and the 3x3 RVE match well with the experiment. This result is not surprising given the fact that this response is a fiber dominated response and heavily dependent on the material properties and the geometry of the RVE. Since the RVE model had been proven to be effective, other model validation could then be examined in greater detail.

This modeling technique is unique to this problem because the material is thinned to the layer of one ply and the RVE could not be used for multiple plies. In order to use for multiply plies, the yarns would need to be further nested, however, the technique that was used to create a higher volume fraction by modeling the bag side of the composite could be used.

7.4 Model Validation

With a created geometry, it is necessary to determine that it accurately predicts the mechanical response of the plain weave. To do this, the model was tested against a simple tension test to determine the accuracy. Once this was determined, the RVE model was experimentally tested to determine if it accurately captured the response of the test. The sample was then tested virtually to determine the homogenized response and more specifically, the orthotropic elastic constants.

7.4.1 Effects of Periodic Boundary Conditions

Because the RVE may not be an accurate representation of a structural lever material, Periodic Boundary Conditions (PBCs) are frequently used. PBCs are used on structures that are periodic to represent the constraints that would be applied to the RVE by the surrounding material. It helps eliminate edge effects and generally is useful in shear dominated problems. While it might not be necessary for the current RVE because tensile response is the dominant response, it is worth investigating to determine whether or not the periodicity is important.

To implement the periodic boundary conditions, node pairs need to be identified along opposite faces. For true implementation, it is necessary that the meshes on either face be identical to one another. For full periodicity, PBCs need to be applied to all edges of the unit cell in the x, y, and z direction. In this study, it is only necessary to implement the boundary conditions in the in plane directions only as the structure is not periodic through the thickness.

In 2D, PBCs are developed through a set of constrain equations [23]. These equations are shown in Equations 7.1 and 7.2. The movement of any coordinate, u, can be defined in terms of X_n and Y_n. A node pair on opposite faces must remain at a distance equal to the length of the RVE and is constrained by the movement of the applied displacement. Likewise, the displacement of the node on the opposite face

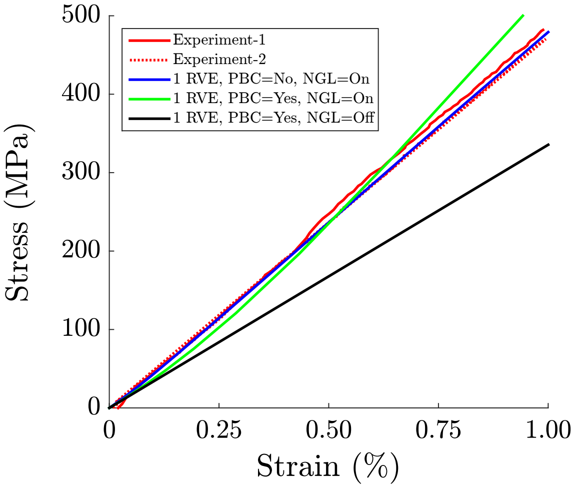

Figure 7.10: Comparison of the stress-strain response for a single RVE with periodic boundary conditions

must be confined to a traction free surface.

$$u(0, Y_1) - u(L_o, Y_1) = U_1 \tag{7.1}$$

$$u(X_1, 0) - u(X_1, L_o) = U_2 \tag{7.2}$$

where:

$U_1 = (0, \delta)$ $U_2 = (u_1, 0)$

From a textile perspective, PBCs have been implemented by Heinrich [31]. To investigate this effect, periodic boundary conditions for all three directions were applied to the faces which were periodic and not applied to in the through thickness direction. This is because the through thickness direction is not periodic.

The single RVE stress-strain response is compared under a variety of simulation conditions. Figure 7.10 shows the results of the simulations. While the initial simulation uniquely captured the stiffness nearly identically to the experiment, when periodic boundary conditions are applied, it results in a much larger non-linear behavior

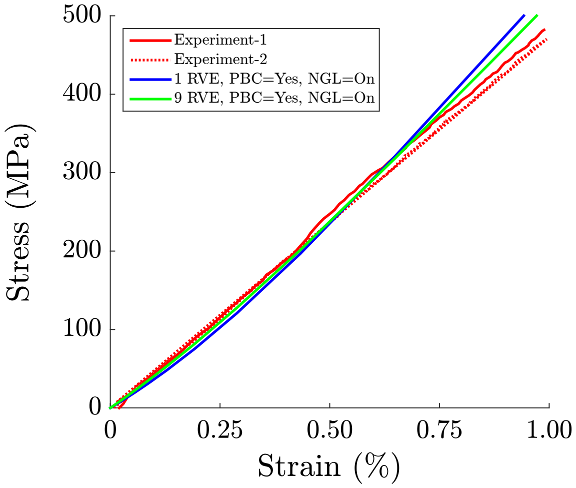

Figure 7.11: Comparison of the stress-strain response for a single RVE and 9 RVE with periodic boundary conditions

in which the stiffness is initially more compliant, but then stiffens significantly. This is the result of the nonlinear geometry. To understand this effect, the same model was run without nonlinear geometry, and displayed purely linear elastic behavior. This behavior though is significantly less stiff than either of the experiments. This suggests that for this problem, nonlinear geometry is important to the response of the textile.

The stress rises rapidly because as the RVE is deformed, without damage or failure, it creates very large internal stresses as the tows deform to straighten themselves against restraint placed by the internal architecture. To verify this, a nine RVE simulation was run with the same loading and boundary conditions, and also with periodic boundary conditions. Nonlinear geometry was still used. Figure 7.11 shows the result of this virtual test. From this Figure, it is clear that the 9 RVE sample displays less nonlinearity in comparison to the 1 RVE. This is because the deformation is more diffuse in the 9 RVE so that stresses associated with the nonlinear geometry do not accumulate as quickly within this model when compared against a 1RVE model.

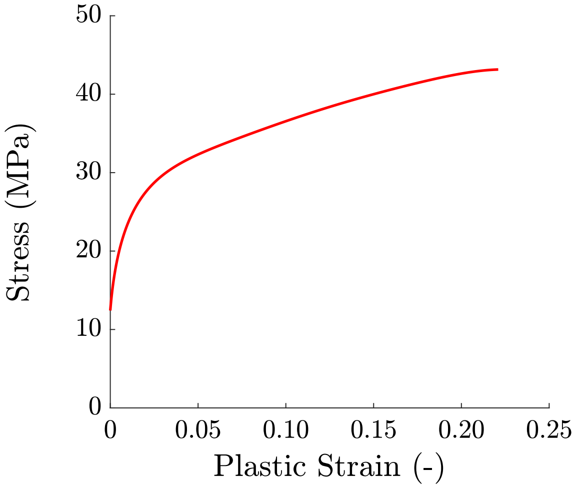

Figure 7.12: The non-linear matrix response used as an input for the simulation

7.4.2 Effects of Matrix Non-Linearity

As seen from the experimental results, the matrix experiences a high degree of strain and needs a non-linear matrix response in order to capture the actual behavior of the RVE. To do this, the stress-strain curve of the in-situ matrix plastic strain properties are determined by breaking the strain into the plastic and elastic strain components based on the modulus of elasticity. The results of this process are shown in Figure 7.12. This stress-plastic strain response was assigned to the matrix in the hybrid idealized geometry. It was not used to determine any non-linearity in the tows because the effect of the matrix damage on the tow's tensile response is minimal.

The RVE was exactly the same, however, it was tested in two different loading conditions, however, periodic boundary conditions are not used for this section of analysis. In the first one, nonlinear geometry was suppressed to examine what the effect would be on the RVE. In the second iteration, nonlinear geometry is active. It produced two different results. The results are shown in Figure 7.13. The results demonstrate an interesting finding. Though matrix nonlinearity is now included in the model, a non-linear result is only obtained when the geometry is considered

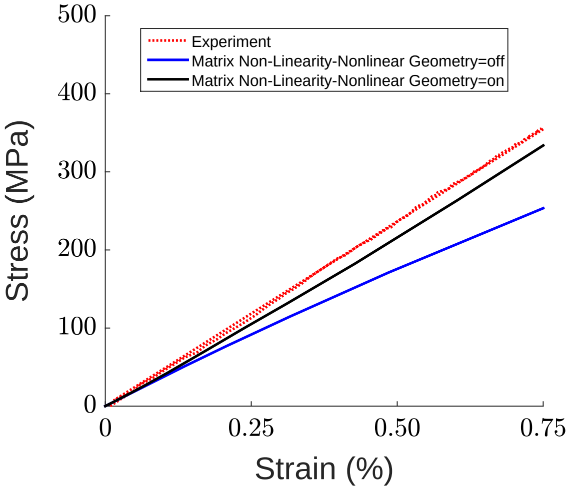

Figure 7.13: Results of the different runs using non-linear geometry

to be linear. Conversely, when nonlinear matrix properties are applied in concert with nonlinear geometry, a linear elastic response is obtained. This is because the "'hardening"' effect of the nonlinear geomtery is offset by the "'softening"' effect of the matrix.

Table 7.5 shows the results of the modulus of elasticity measurements of the non-linear geometry results. As shown previous, the modulus of elasticity ranges between 44.3-52.3 GPa. When incorporating the nonlinear matrix response, nonlinear geometry must be incorporated to capture the proper value of the curve. Between this and the previous study, it established that nonlinear geometry must be included to accurately capture the results.

Experiment (GPa)	Nonlinear Geometry=Off (GPa)	Nonlinear Geometry=On (GPa)
46.7	35.8	44.8

Table 7.5: Stiffness of the various models incorporating matrix non-linearity

7.4.3 Coupled Periodic Boundary Conditions and Non-Linear Matrix Response

The final analysis before moving on to failure of the RVE was to determine the effects on the model of the periodic boundary conditions coupled with matrix nonlinearity. To do this, the 9 RVE model that was used previously had the matrix nonlinearity curve shown in Figure 7.13 applied to it. The results are shown in Figure 7.14. From Figure 7.14(a), it is seen that the initial nonlinearity in the stiffness has been reduced further, however, after initial plasticity effects, the model hardens rapidly at the sample slope as the model without matrix nonlinearity. A close up of the initial stiffness is shown in Figure 7.14(b). The initial stiffness is matched quite well.

From the series of virtual tests, it was established that the geometry is sufficient for further analysis and will be preserved throughout this chapter.

7.5 Development of a Global-Local Model for Failure Analysis

The global local modeling is a technique that has been widely used to model composite damage and failure. Global local models typically involve the use of two or more scales to utilize computational efficiency while improving fidelity in areas of interest. This is generally implemented in one of two ways. The first way is by having two models at two different scales in which the stress and strain fields are passed between the two models. This technique has been used in composites. The methodology for textiles is reported by Whitcomb et in [120] and more specifically 2D plain weaves in ref [104]. Generally, this technique would now be called "multiscale analysis" since they rely on running two simulations simultaneously at different scales.

The second way of utilizing a global local technique involves the linking of length

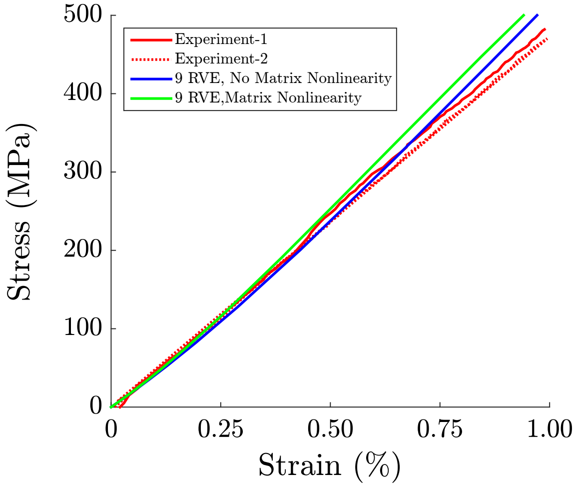

(a) Macro comparison of stress-strain response

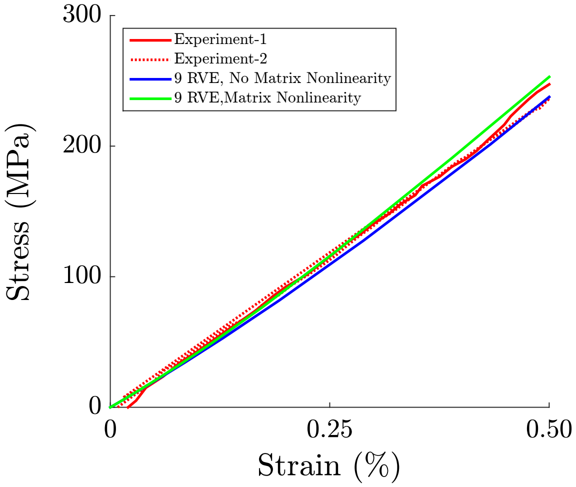

(b) A view of the initial response

Figure 7.14: The effects of applying periodic boundary conditions and matrix nonlinearity

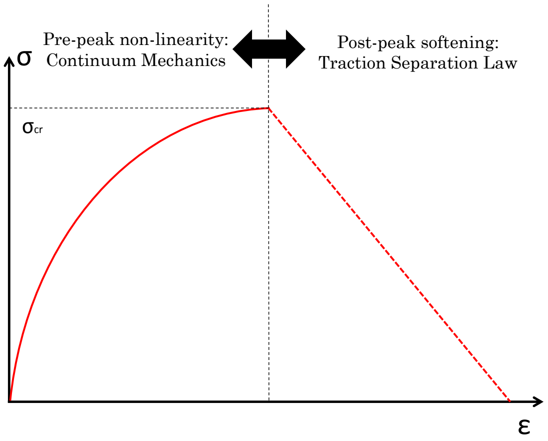

Figure 7.15: A schematic showing the smeared crack approach

scales in a single model. For this work, the macro-scale is linked with the mesoscale to determine the mechanical response of the material. This technique is particularly useful because it allows for localization of the failure within the mesoscale but has relatively high computational efficiency in comparison to the full mesoscale model. This technique has been shown by Zhang and Waas for bending applications of 3D textiles [132].

7.5.1 Smeared Crack Formulation

The smeared crack formulation was developed by Rots et al. in 1985 to examine the tensile failure of concrete [94]. The basic notion of the smeared crack is that instead of modeling a discrete crack in a model, cracking can be smeared over an element or group of elements to capture the failure of a material. More details of the smeared crack formulation can be found in, [32], [93], [130].

Figure 7.15 shows a general schematic of how the smeared crack approach is formulated. This formulation is derived around the assumption that upon failure initiation, the total strain can be decomposed into two parts: The continuum strain, ϵ^{co} and the cracking strain, ϵ^{cr} as shown in Equation 7.3. Within the continuum sense, all applicable continuum strains can be applied including built-in functions for elasticity and plasticity response. The post peak response is governed by a traction separation law. It should be noted that ϵ is used to denote the global coordinate system whereas ε is used for the local coordinate system.

$$\epsilon = \epsilon^{co} + \epsilon^{cr} \tag{7.3}$$

While the total strain is given on the global coordinate, it is necessary to transform the results to the local coordinate system in order to smear the crack across the element. The cracking strains can be further decomposed into the opening strains, ε^{cr}_{norm}, and sliding strains, γ^{cr}_{t1} and γ^{cr}_{t2}. The equation is shown in Equation 7.4. N is a transformation matrix that takes the strains from the global to the local coordinate system.

$$\epsilon_{cr} = N\varepsilon^{cr} = N \begin{bmatrix} \varepsilon^{cr}_{norm} \\ \gamma^{cr}_{t1} \\ \gamma^{cr}_{t2} \end{bmatrix} \tag{7.4}$$

In a similar manner, the stresses can be transformed from the global to the local system using the transpose N matrix and is shown in Equation 7.5.

$$s_{cr} = N^T\sigma^{cr} = N^T \begin{bmatrix} \sigma^{cr}_{norm} \\ \tau^{cr}_{t1} \\ \tau^{cr}_{t2} \end{bmatrix} \tag{7.5}$$

In order to initiate failure, the Rankine criterion of maximum principle stress is used which in turn affects how the transformation matrix, N is formulated. This criteria is used because the highest principle stress directions helps determine crack directions. In order to relate the crack interface stresses to the crack strains, an additional matrix, D^{cr}, is needed. D^{cr} is secant stiffness matrix for the material.

Additionally, as the material damages, there is a loss of positive definiteness in the stiffness matrix which can lead to large oscillations between between time steps. To combat this effect, a damping matrix D^{da} needs to be introduced. Considering this factor, the relation between the cracking stresses and crack strains is related by Equation 7.6.

$$s_{cr} = D^{cr}\varepsilon^{cr} + D^{da}\dot{\varepsilon^{cr}} \tag{7.6}$$

where $\dot{\varepsilon^{cr}}$, is a simple backward difference formulation shown in Equation 7.7

$$\dot{\varepsilon^{cr}} = \frac{\varepsilon^{cr}(t+\delta t) - \varepsilon^{cr}(t)}{\delta t} = \frac{\varepsilon^{cr} - \varepsilon^{cr}_{old}}{\delta t} \tag{7.7}$$

By combining Equations 7.6 and 7.7, it can produced the complete relationship for the crack stress shown in Equation 7.8.

$$s^{sr} = D^{cr}\varepsilon^{cr} + \frac{1}{\delta t}D^{da}\varepsilon^{cr} - \frac{1}{\delta t}D^{cr}\varepsilon^{cr}_{old} \tag{7.8}$$

In the global sense, the constitutive relationship for the continuum can be written as show in Equation 7.9 where D_{co} is the secant stiffness of the continuum. However, the continuum strain ϵ^{co} can be decomposed using the relationship from Equation 7.3.

$$\sigma = D^{co}\epsilon^{co} = D^{co}[\epsilon - \epsilon^{cr}] = D^{co}[\epsilon - N\varepsilon^{cr}] \tag{7.9}$$

From combining the above equations, an implicit relationship between the local crack strains the total strains can be shown to be Equation 7.10

$$\varepsilon^{cr} = [D^{cr} + N^T D^{co} N + \frac{1}{\delta t}D^{da}]^{-1}[N^T D^{co}\epsilon + \frac{1}{\delta t}D^{da}\varepsilon^{cr}_{old}] \tag{7.10}$$

By substituting Equation 7.10 into Equation7.9, the relationship between the stress and strain can be computed for the damaging behavior and is shown Equation 7.11

$$\begin{aligned}\sigma = [D^{co} - DcoN(D^{cr} + N^T D^{co} N + \frac{1}{\delta t} D^{da})^{-1} N^T D^{co}]\epsilon \\ -\frac{1}{\delta t}[D^{cr}\varepsilon^{cr} + N^T D^{co} N + \frac{1}{\delta t} D^{da}]^{-1} D^{da} \varepsilon^{cr}_{old}\end{aligned} \tag{7.11}$$

Since the components of D^{cr} are bound by the traction separation law describe earlier, the crack strain becomes a non-linear equation. This equation can be solved using Newton's Method and minimizing the function shown as follows:

$$f(\varepsilon^{cr}) = [D^{cr}(\varepsilon^{cr}) + N^T D^{co} N + \frac{1}{\delta t} D^{da}]\varepsilon^{cr} - N^T D^{co}\epsilon - \frac{1}{\delta t} D^{da} \varepsilon^{cr}_{old} = 0 \tag{7.12}$$

This equation can be solved iteratively where each iteration is governed by Equation 7.13

$$[\varepsilon^{cr}]^{(k+1)} = [\varepsilon^{cr}]^{(k)} - [\frac{df}{d\varepsilon^{cr}}]^{-1} f(\varepsilon^{cr})^k \tag{7.13}$$

In order to preserve mesh objectivity (e.g. the size of the mesh does not affect the final answer) a characteristic length, h, is incorporated into the formulation. This characteristic length is determined by the requirement of energy dissipation continuity between the continuum elements and and the cohesive element of the same size. In a finite element framework, this length is the length of the element normal to the crack surface. The characteristic length is incorporated into the formulation via the traction separation law. Generally, the area under the curve of a traction separation law is equivalent to the critical crack energy release rate or G_{IC} during Mode I fracture. The separation, δ, can be written as a function of the crack strain, ε^{cr}_{norm} and characteristic length, such that Equation 7.14 is satisfied.

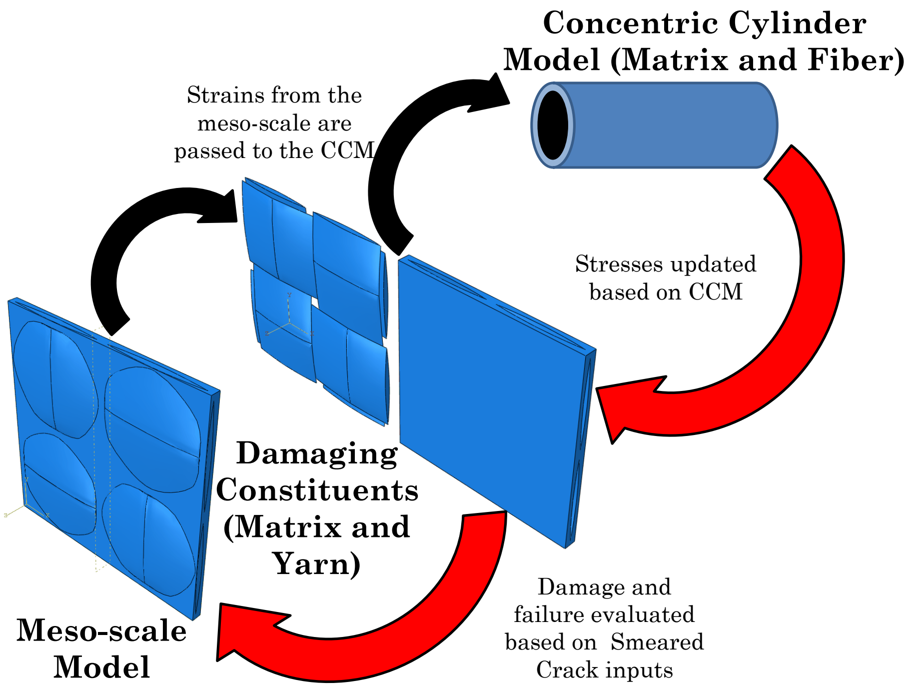

Figure 7.16: A schematic showing how the multi-scale framework is implemented

$$G_{IC} = \int_{0}^{\delta_{ult}} \sigma d\delta = \int_{0}^{\varepsilon_{ult}^{cr}} \sigma h d\varepsilon^{cr} \tag{7.14}$$

7.5.1.1 Smeared Crack in a Multi-Scale Approach

The multi-scale framework for this Smeared Crack approach was developed by Zhang, [130], with details provided in Zhang and Waas, [132]. This technique uses smeared crack technique over the meso-scale by incorporating damage in the micro-scale. Figure 7.16 gives a schematic overview on how the multi-scale framework is developed.

The multi-scale process begins with identification of the damaging geometries that will be incorporated into the smeared crack failure technique. For this work, the matrix and the fiber tow are treated as separate constituents. When a strain is applied to the RVE, the framework considers the strain applied to the tow and matrix individually. For the tow, the strains for each integration point are passed to a Concentric Cylinder Model. This CCM incorporates the elastic properties of the fiber, and the elastic and non-linear behavior of the matrix as well. Using a closed-form solution for the damaged elastic constants (secant values), the stresses are then calculated and returned to the meso-scale damaging constituents. At this point, the stress states are compared to the given failure values for the smeared crack techniques. If the sample has reached the failure stress, it then enters the post-peak traction-separation law that was described earlier. The novelty of this framework is that the micro-scale model developed by Zhang and Waas [131] is a closed form solution so it allows for a high degree of computational efficiency for large meshes and in conjunction with a multi-scale framework.

The matrix non-linearity considered in the model was based on in-situ properties. The relationship for the nonlinear stress-strain relationship was characterized using an exponential relationship shown in Equation 7.15

$$\sigma_{eq} = \sigma_y - \frac{K_1}{K_2}(e^{-K_2 \epsilon_{eq}} - e^{-K_2 \frac{\sigma_y}{E_e}}) \tag{7.15}$$

where σ_{eq} and ϵ_{eq} is the equivalent stress and strain from J2 plasticity. σ_y is the yield stress and K_1 and K_2 are material constants that describe the nonlinear behavior. The inputs for the smeared crack failure for the matrix are shown in Table 7.6. The initial properties for the failure via smeared creak formulation were selected from ref. [130] which were shown to work well for 3D hybrid textiles in bending applications.

σ_y (MPa)	K_1 (MPa)	K_2 (-)	σ_{cr} (MPa)	G_{IC} (N/mm)
25	1700	40	50	1.5

Table 7.6: The smeared crack inputs for matrix failure

The failure stresses for the carbon fiber tow are shown in Table 8.4. It should be noted that in order not to set off the critical failure stress in compression, a value of

-10,000 MPa was used in the simulations.

σ_{11}^{T} (MPa)	σ_{11}^{C} (MPa)	σ_{22} (MPa)	τ_{12} (MPa)	τ_{12} (MPa)	G_{IC} (N/mm)
3000	-1000	7000	3700	3200	40

Table 7.7: The smeared crack critical strengths for the tow.

7.5.2 3 RVE Global-Local Model

To begin to analyze failure of the textile, a preliminary global-local model was developed. For this model, 3 RVEs are used and wedged in between a homogeneous material. The geometry is shown in Figure 7.17(a) along with how the material sections have been assigned in Figure 7.17(b). From Figure 7.17(b) it can be seen that two scales are bridged during this analysis, the meso-scale and the macro-scale. In the meso-scale, two different material assignments have been made. In the center of the sample, the smeared crack formulation has been used, while on the edges, the elastic properties used in the RVE analysis were used. The purpose of this is because when the smeared crack formulation is applied to a single RVE, failure tends to occur near the edges. By using a global-local approach, this effect is not seen.

The geometry was assembled in 5 pieces. The mesh that is used for the RVEs is identical to that used previously. The homogeneous material is seeded with the same dimensions to ensure continuity in the mesh. All interfaces are tied together. The homogenized material properties were assigned based on the experimentally determined values. While in general, the material is orthotropic, within the plane itself, when subjected to uniaxial loading, many of the elastic constants are negligible and the material can be treated as isotropic with material constants determined from the testing both virtually and experimentally. The homogeneous material was assigned a stiffness of 48000 MPa and a Poisson's ratio of 0.046.

The requirements for the smeared crack portion, the multi-scaling technique de-

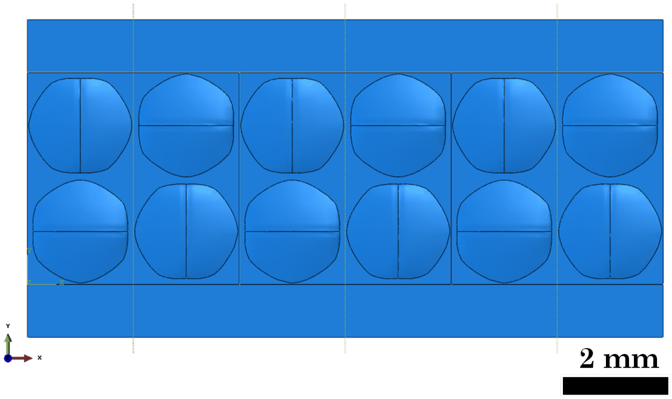

(a) The geometry from FE

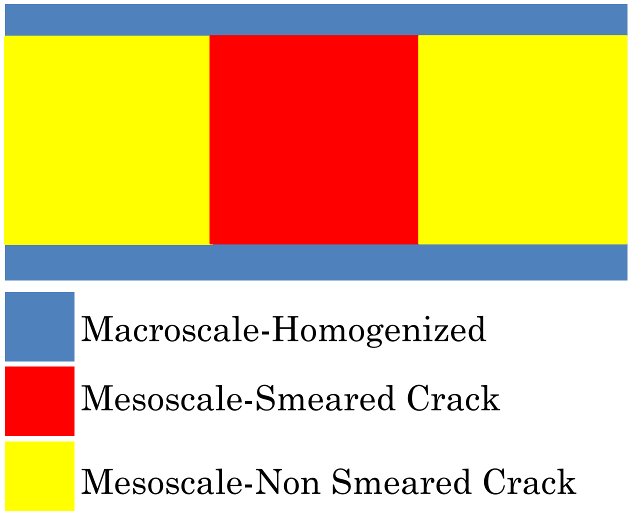

(b) A schematic showing how the smeared crack is applied to the geometry

Figure 7.17: The geometry for the 3 RVE global local model

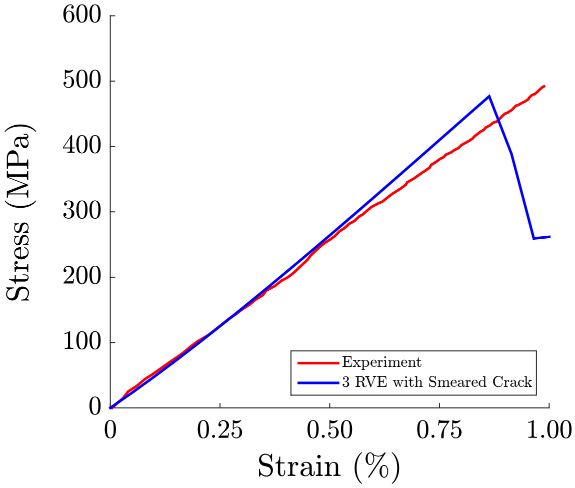

Figure 7.18: A comparison between the experiment and the 3 RVE model

scribed previously relied solely on the fiber and matrix parameters, however, for this analysis the failure to the matrix was not considered. The matrix is allowed to damage and be described as in the work by Zhang and Waas, [132]. To ensure that the matrix did not fail, an arbitrarily high tensile failure stress was selected for the material.

The results of the simulation in comparison to the experimental work is shown in Figure 7.18. The failure stress for the simulation was 476.7 MPa, which is well within the experimentally determined value of 484.7±31.9. While the initial stiffness is nearly identical, at approximately 0.50% strain, the slope begins to show a hardening effect. From the previous results, it is reasonable to assume that the stiffening is a result of the nonlinear geometry. For this reason, the failure strain in the simulation of 0.86% is not within agreement of the experimental values. It should be noted that due to the homogenized section, a vertical load drop is not observed. This is because the model is a displacement controlled and the homogenized section does not have failure, when the sample fails, the load is transmitted through the elastic medium. A load drop is observed, however, it is not exactly as it is seen in the experiment and is merely an artifact of the modeling.

Figure 7.19 shows the exposed yarns as they are loaded. At the load drop shown in

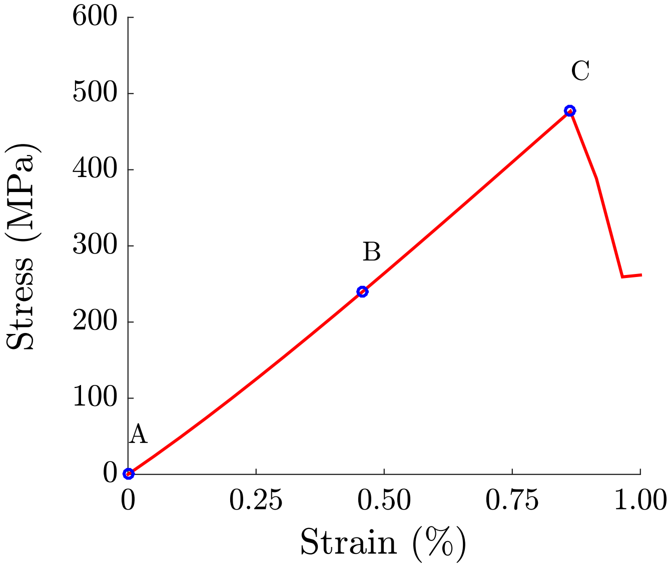

(a) The stress-strain response of the 3x1 RVE tensile test

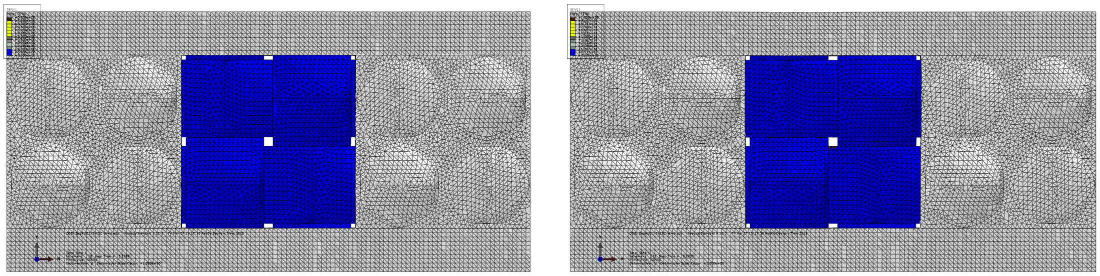

(b) The tensile yarn damage from the simulation at point A

(c) The tensile yarn damage from the simulation at point B

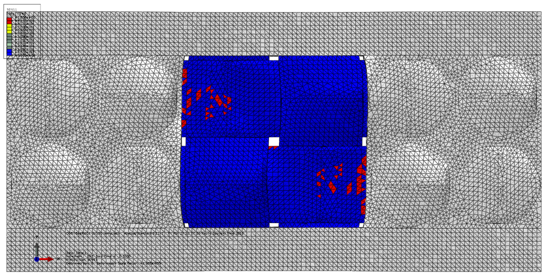

(d) The tensile yarn damage from the simulation at point D

Figure 7.19: The geometry for the 3 RVE global local model

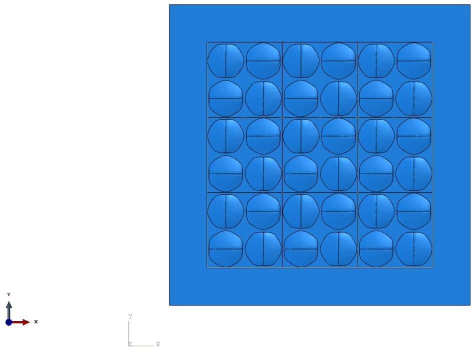

Figure 7.20: A comparison between the experiment and the 9 RVE model with and without matrix failure

Figure 7.19(d), it can be seen that the yarn is damaged in a number of areas relating to geometrical features of the yarn including the in center of the yarn and when the yarn reaches a local maximum or minimum. Also of interest, as the yarn fails, the loss in stiffness results in a distortion to the architecture.

7.5.3 9 RVE Global-Local Model

While the 3 RVE model performed well in terms of predicting the stiffness and failure load of the textile, the effects of the nonlinear geometry were still observable. To minimize this effect, additional RVEs were added to make a total of 9 RVEs in the model. Similar to the 3 RVE model, the smeared crack formulation was applied to the middle cells in each of the three rows. The other instances of the RVE had elastic properties. Finally, a picture frame type boundary was applied around the 9 RVEs to not apply a load directly to the boundary. The total assembly is shown in Figure 7.20.

The 9 RVE sample was tested in two configurations, the first was with matrix and tow failure, the second was with tow failure only. The results of this are shown in Figure 7.21. While the sample has experienced a number of failures in matrix, it does not have any effect on the stiffness. This further confirms that the model is fiber dominated and treating the matrix as a nonlinear solid without the smeared

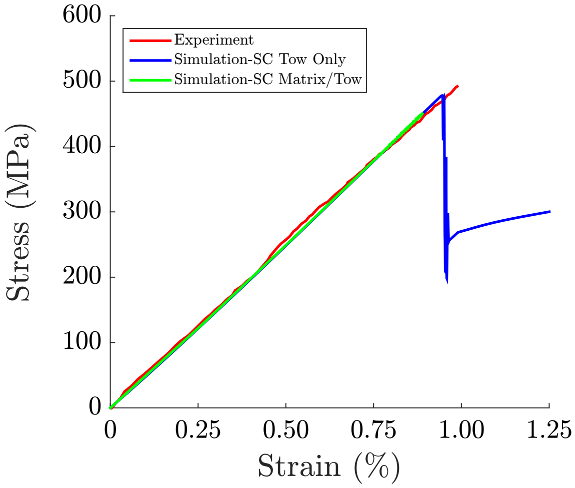

Figure 7.21: A comparison between the experiment and the 9 RVE model with and without matrix failure

cracks model is acceptable. With progressive matrix failure, it exponentially increases computational time. From this figure, it is clear that there is very good agreement between the 9 RVE model and the experiment. The stiffness is nearly identical and the simulation had a failure stress of 477 MPa compared to that of the experimental value of 484.7±31.9. The failure strain was also in good agreement. The non-linearity that was observed with the 3 RVE sample was not seen in the 9 RVE sample.

A good comparison that can be made though about the importance of the matrix cracking relative to the mechanics of the RVE can be seen in Figure 7.22. This figure shows the comparison of the cracking patterns (shown in red) between the front of the RVE (Figure 7.22(a)) and the back of the RVE (Figure 7.22(b)). The matrix first fails at the point where the matrix layer is the thinnest (when the yarns are the the top of their amplitude). It then spreads between local maximum and minimum to create the characteristic checkerboard pattern that is observed in the experiment.

The final examination of the RVE was with the tow failure and the matrix damaging, however, the matrix cannot fail. The result of this can be seen in Figure 7.23. In this image the axial strain of the fiber tow is shown next to the damage. As the

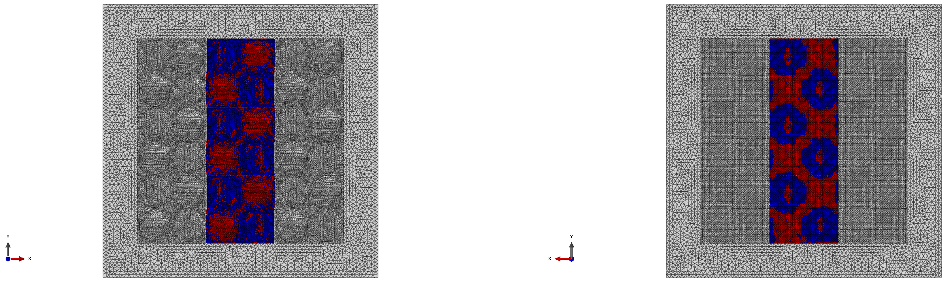

(a) The matrix failure (red) on the front of the sample (b) The matrix failure (red) on the back of the sample

Figure 7.22: The matrix cracking patterns in 9 RVE Model in final frame

material begins to strain more, strain concentrations within the yarn are observed on the insertion points in which the yarns interact. Ultimately as this strain concentration develops, the tow fails as seen in Figure 7.23(i) and is responsible for the load drop. As seen in the previous 3 RVE model, two piece failure is not observed and the homogenized material quickly carries the load. However, the simulation showed a high degree of agreement with the experiment.

7.6 Conclusions

In this chapter, a finite element model was developed that included aspects of real geometry and idealized geometry of a plain woven carbon composite sample. The idealized geometry was developed from the measurements of optical microscopy. The model was tested for elastic response in comparison to a plain woven sample and it was found that it performed well against the experiment. To understand how the RVE reacts, it was subjected to many loading cases to determine the effects of periodic boundary conditions, nonlinear geometry, and matrix nonlinear effects. When these aspects were understood, a global-local model was developed to examine the failure using the smeared crack formulation. With the smeared crack, the failure strength, and strain were predicted to within 5% of the experimental average. This degree of agreement lends further insight into the modeling strategy that has been developed.

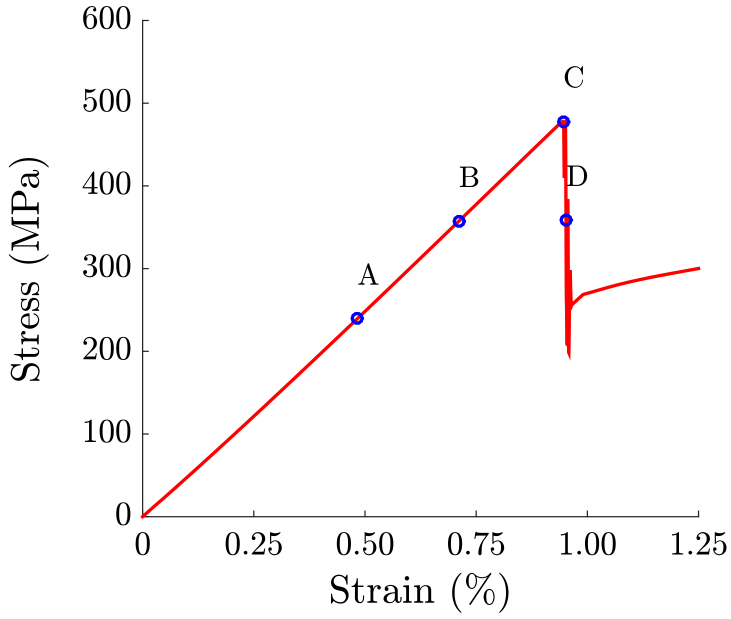

(a) The stress-strain response of the 9 RVE tensile test

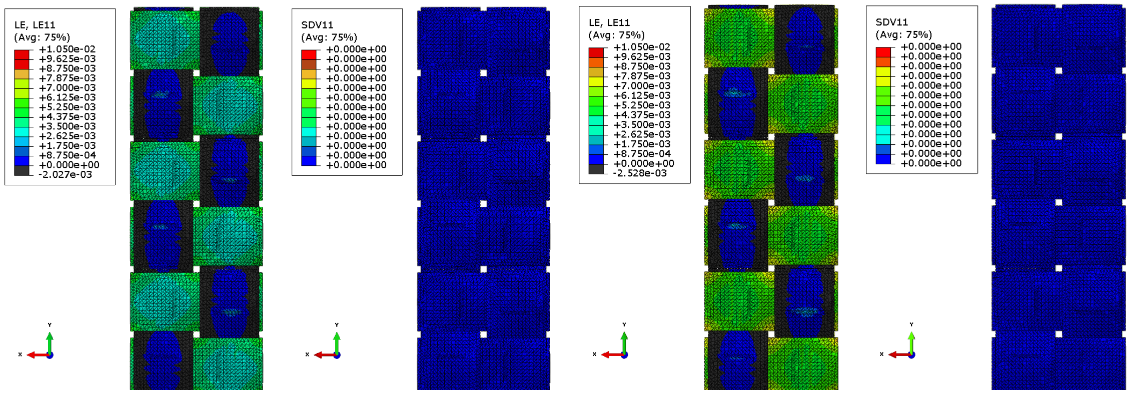

(b) The tensile strains at point A (c) The tensile yarn damage at point A (d) The tensile strains at point A (e) The tensile yarn damage at point B

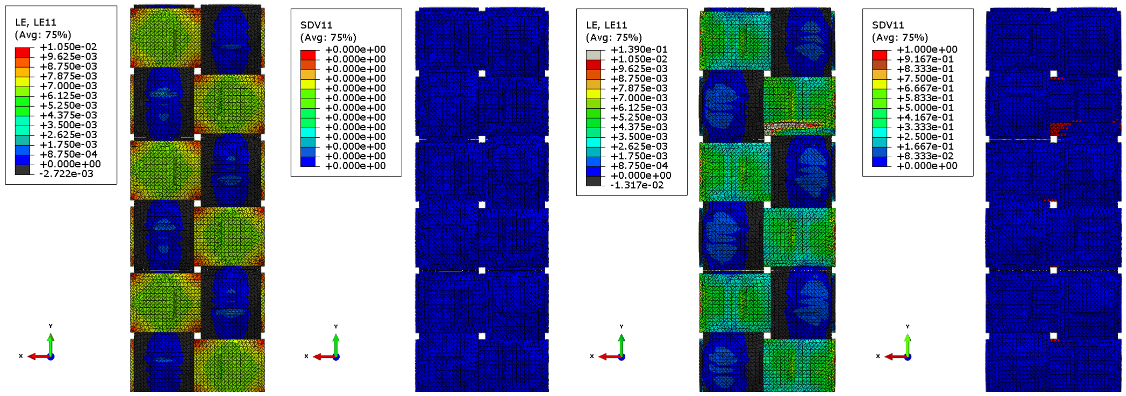

(f) The tensile yarn damage from the simulation at point C (g) The tensile strains at point C (h) The tensile yarn damage at point D (i) The tensile strains at point D

Figure 7.23: The progressive failure and damage in the RUC

CHAPTER VIII

Modeling of Shockwave Loading Carbon Plates

In the previous chapter, the RVE geometry was developed and analyzed to determine its capability for simulating failure in a global-local model. Using this geometry and the experimental results from the previous chapters, a global-local model will be used to simulate a textile composite panel subjected to shock loading conditions. This is done in order to determine the rate dependent failure of the yarns under multi-axial loading and to establish if the results obtained from the 1-D experiments can be used to develop a constitutive model that can predict response under multi-axial loading states.

8.1 Introduction

While there have been numerous examples of shock wave transverse loading of plates of various materials, there has been little past literature with respect to modeling the response of the plate and even less literature that reports examining damage and failure. Much like the experimentation, a majority of the work towards modeling of shock loading tends towards under water blast. Leblanc and Shukla developed a finite element model to analyze the failure of composite laminates subjected to underwater blast loading using a simple layered model in LS-Dyna [53]. Batra and Hassan developed a damage model that was able to show matrix cracking in composite plates during underwater blast loading [5].

Air blast loading is generally more limited. Stoffel developed sets of analytical failure criteria for a number of plates, both isotropic and anisotropic, subjected to shock loading [110]. In references [45] and [85], the use of models for understanding the strain rate dependent effects in plates has been shown to be effective by matching the deflection-time histories of experimental data against analysis models. With respect to composite plates, Pankow et al. predicted the onset of damage in a textile composite panel through a validated user material [82], however, complete failure was not considered. Additionally, a psuedo-laminated model was developed that did not incorporate the architectural details of the microstructure.

To date, researchers have yet to develop a robust finite element framework at the meso-scale to examine the complete failure of a woven composite plate. The following sections discuss the development of a global-local model that incorporates the smeared crack formulation with the full mesoscale architecture. In this chapter, the previous experimental work is now coupled with the high strain rate multiaxial response of the plate to determine if the failure laws developed earlier have accurately captured the failure mechanics of the shock loaded panels.

8.2 Virtual RVE Testing for Homogeneous Material Properties

In order to implement a global-local framework for shock loading of composite panels, the homogenized orthotropic material constants of the textile plate are required. To obtain these constants, the RVE that was discussed in the earlier chapter was loaded in different configurations to determine the elastic constants. From general orthotropic linear elasticity, a 6x6 matrix can be developed for an orthotropic material where extension-shear is not coupled, as shown in Equation 8.1.

$$\begin{Bmatrix} \sigma_1 \\ \sigma_2 \\ \sigma_3 \\ \sigma_4 \\ \sigma_5 \\ \sigma_6 \end{Bmatrix} = \begin{bmatrix} C_{11} & C_{12} & C_{13} & 0 & 0 & 0 \\ C_{21} & C_{22} & C_{23} & 0 & 0 & 0 \\ C_{31} & C_{32} & C_{33} & 0 & 0 & 0 \\ 0 & 0 & 0 & C_{44} & 0 & 0 \\ 0 & 0 & 0 & 0 & C_{55} & 0 \\ 0 & 0 & 0 & 0 & 0 & C_{66} \end{bmatrix} \begin{Bmatrix} \epsilon_1 \\ \epsilon_2 \\ \epsilon_3 \\ \epsilon_4 \\ \epsilon_5 \\ \epsilon_6 \end{Bmatrix} \tag{8.1}$$

By applying ϵ_1 and assuming symmetry conditions, the elastic constant C_{12} is equal to C_{21}. Similarly C_{13} is equal C_{31}. Also, the response is the same in the in plane directions. Therefore this loading condition allows for determination of the C_{11}, C_{12}, C_{13}, and C_{22}constants. To determine the lower part of the extension portion of the stress-strain matrix relation, through thickness tension is acheived by applying a strain in the 3 direction (ϵ_3). This allows for determination of the C_{33} and C_{23} constants with C_{32} being the same as C_{23} based on symmetry. The shear responses can be found by applying ϵ_4, ϵ_5, and ϵ_6 individually to the RVE, and reading off the reaction forces from which the stresses and hence the corresponding elastic constants are obtained.

$$[S_{ij}] = \begin{bmatrix} S_{11} & S_{12} & S_{13} & 0 & 0 & 0 \\ S_{21} & S_{22} & S_{23} & 0 & 0 & 0 \\ S_{31} & S_{32} & S_{33} & 0 & 0 & 0 \\ 0 & 0 & 0 & S_{44} & 0 & 0 \\ 0 & 0 & 0 & 0 & S_{55} & 0 \\ 0 & 0 & 0 & 0 & 0 & S_{66} \end{bmatrix} = \begin{bmatrix} \frac{1}{E_1} & -\frac{\nu_{12}}{E_1} & -\frac{\nu_{13}}{E_1} & 0 & 0 & 0 \\ -\frac{\nu_{12}}{E_1} & \frac{1}{E_2} & -\frac{\nu_{23}}{E_3} & 0 & 0 & 0 \\ -\frac{\nu_{13}}{E_1} & -\frac{\nu_{23}}{E_3} & \frac{1}{E_3} & 0 & 0 & 0 \\ 0 & 0 & 0 & \frac{1}{G_{12}} & 0 & 0 \\ 0 & 0 & 0 & 0 & \frac{1}{G_{13}} & 0 \\ 0 & 0 & 0 & 0 & 0 & \frac{1}{G_{23}} \end{bmatrix} \tag{8.2}$$

The C_{ij} matrix can be inverted to determine the compliance matrix, S_{ij}. The compliance matrix can be related to the orthotropic material constants by using

Equation 8.2. From this relationship, the orthotropic constants were determined and shown in Table 8.1. These are the constants that were used for the homogenized plate response.

E_{11} (MPa)	E_{22} (MPa)	E_{33} (MPa)	ν_{12} (-)	ν_{13} (-)	ν_{23} (-)	G_{12} (MPa)	G_{13} (MPa)	G_{23} (MPa)
48022	48022	1936	.1982	.4836	.2716	942	765	765

Table 8.1: The homogenized orthotropic material constants

8.3 Shock Loading of Homogenized Plain Woven Plates

Using the homogenized material constants that are shown in Table 8.1, a finite element model was created to simulate the deflection response of the plate under blast loading. This information is necessary to develop the global-local framework that is needed for failure analysis. To do this, a mesh of the 101.6x101.6 mm (4 in. x 4in.) fully 3D plate was generated with a thickness of 1.016 mm (0.040 in.). It was possible to use shell elements for this simulation, however, for the global-local framework, a shell cannot be used because the panel does not have constant thickness. This plate is identical in dimensions to the plates tested in the shock tube shown in Chapter 6. A material orientation was assigned such that the in-plane directions are '1' and '2'. The through the thickness direction was the '3' direction. The plate was then sectioned such that boundary conditions could be applied. A 76.2 mm (3 in.) circle was placed at the center of the plate to allow for alignment with the clamping ring on the front and back surface. A clamping ring was made as an analytical rigid shell. Frictionless contact was applied to the surfaces that interacted.

The geometry was meshed with 17452 quadratic tetrahedral elements of type C3D10. A picture of the partitioned plate and the mesh is shown in Figure 8.1. The clamping ring was meshed with 750 elements: 736 linear quadrilateral elements of type R3D4, and 14 linear triangular elements of type R3D3. Because the plates failed at a

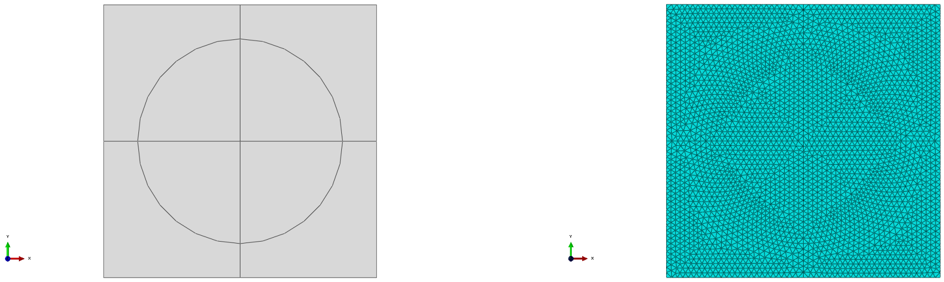

(a) The partitioned plate geometry (b) The partitioned plate mesh

Figure 8.1: The partitioned geometry and mesh used for the flat plate testing

later point in the laboratory tests, the complete plate pressure-time history for each test could not be obtained from the reflected pulse. For this reason, 5 tests with increasing number of sheets of mylar, identical to what was tested with the carbon plates, were examined with a ”‘rigid”’ sample to get the reflected shock pressures on the plate. The ”‘rigid”’ sample is a thick steel end plate that is instrumented with pressure sensors (see Chapter 5). This pressure-time history is what is used in the finite element model. It should be noted that for each of the failed samples presented later, this was the sample procedure that was used to get a pressure-time history of the plate since failure does not allow for capturing of the reflected shock pressure.

This pressure-time history was applied to the back of the plate in the section defined by the 76.2 mm circle in the center of the plate. The area outside the ring was restricted to move in the plane only ($U_3 = 0$) and the clamping ring was fixed to give the same boundary conditions as those described in Chapter 5. A node-set was created at the center of the plate to measure the deflection-time history similar to the experimental procedure. The results of the simulation for a shock strength of 3.68 are shown in Figure 8.2.

From the results shown in Figure 8.2, it is clear that the the response is more compliant in the simulation in comparison to the experiment, however, key attributes of the simulation have been captured. In particular the slope of the curve is nearly identical. This is a good indication that the material properties are correct, however,

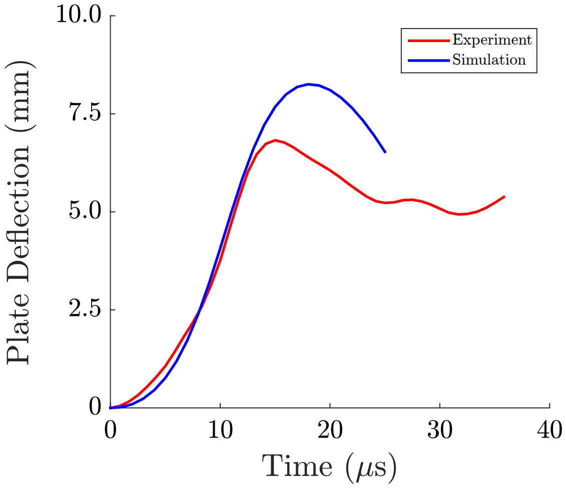

Figure 8.2: A comparison of the finite element simulation to the experimental results for a shock strength of 3.68

the boundary conditions might not be entirely correct.

8.3.0.1 Evaluation of Boundary Conditions

The exact boundary conditions, particularly the in-plane restraint at the clamping ring boundary, for the shocktube test are unknown. While previous results have shown that the way to model it described above has proven successful in the past, [45], the boundary conditions may be more problem dependent and not necessarily correct for this application. Since the strain rates determined experimentally were rather low, it is reasonable to assume that any strain rate effects are generally small and are not responsible for what is preventing the more compliant response. While the area outside of the deformed area was considered to be simply supported, the actual boundary condition might differ from that.

To analyze this effect, a clamped boundary condition was applied to the area outside the center circle, all other factors were held constant. Figure 8.3 shows a comparison of the two different boundary conditions. The clamped boundary condition has a deflection that is less than that of the experiment, whereas the simply

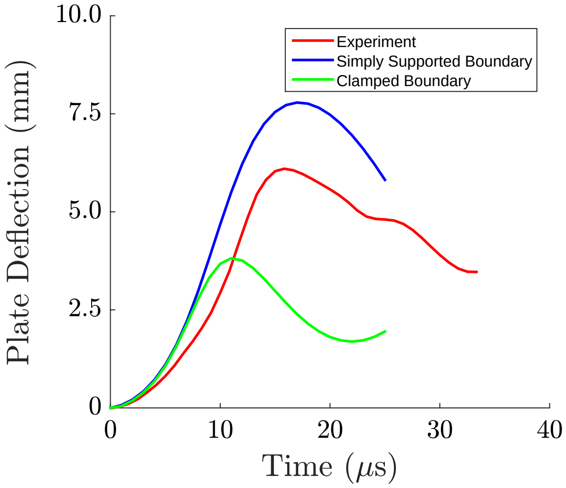

Figure 8.3: A comparison of various boundary conditions for the flat plate subjected to a shock strength of 3.41

supported boundary condition has a larger deflection. This indicates that the true boundary condition falls between these two loading conditions.

	Experiment (mm)	Simulation (mm)	% Difference
Shock Strength=2.46	4.32±0.03	4.46	3.0
Shock Strength=3.08	5.03±0.04	5.64	12.0
Shock Strength=3.41	6.10±0.04	6.34	3.9
Shock Strength=3.68	6.82±0.05	6.67	2.2
Shock Strength=3.81	7.07±0.03	6.98	1.2

Table 8.2: Comparison of out of plane deflection of the experiment and simulation with an in-plane spring support

In an attempt to find the proper boundary conditions, an in-plane linear spring was added as a boundary condition to restrict the out of plane deflection by adding resistance to the sliding of the plate in plane. The stiffness of the spring needed was tuned to a value between the maximum stiffness (the clamped condition) and the minimum stiffness (simply supported). After some trial and error, a final stiffness for the spring was selected to be 5000 N/mm. The results of the comparison between the experiments and simulations is shown in Table 8.2. Generally, the results differed by less than 4%, however, the shock strength of 3.08 differed by 12%. This may have

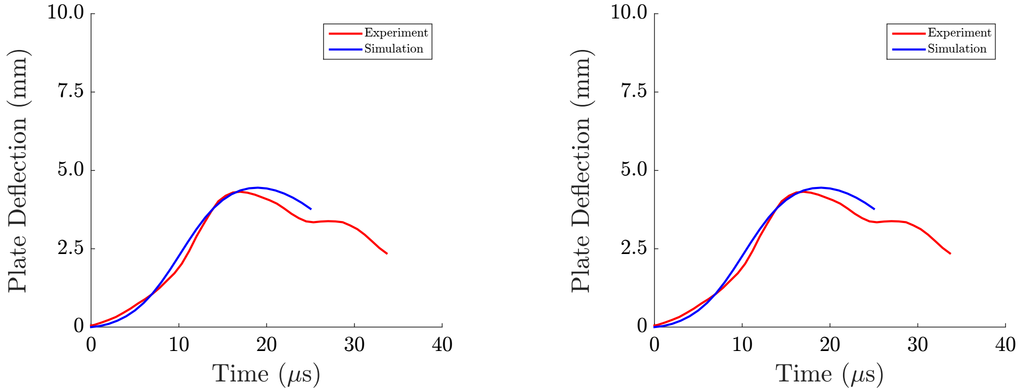

(a) A comparison of the simulations to the experiment for a shock strength of 2.46

(b) A comparison of the simulations to the experiment for a shock strength of 3.68

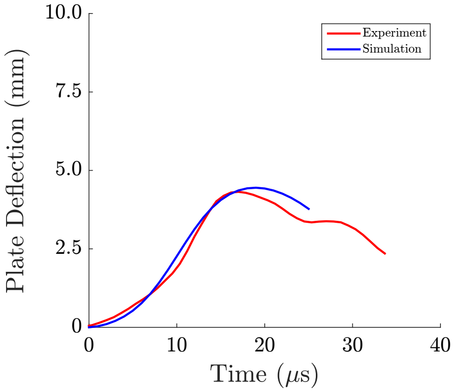

(c) A comparison of the simulations to the experiment for a shock strength of 3.81

Figure 8.4: A comparison of the deflection time history of the experiment and simulation with in plane springs

been a result of not having the exact pressure-time history.

Figure 8.4 shows the deflection-time history for the experiment and the simulation using an in plane spring for shock strengths of 2.46, 3.68, and 3.81. There is good agreement between the maximum deflection as well as the rise characteristics. From these simulations, the developed material model and boundary conditions used for the flat plate replicate the experimental results well. These properties will be used for the global-local model presented in subsequent sections.

8.4 Shock Loading of Plates Using the Global-Local Model

In the previous chapter, a global-local model was introduced that incorporated the use of an RVE meso-scale model nested in a homogenized material and was shown to be used in concert with the smeared crack formulation to replicate the results of experimental testing. In the current chapter, the homogenized material was extended to include orthotropic behavior and through analysis that modeled the uncertain boundary conditions, it was shown that the plate response replicated the experimental results closely. In the following sections, a shock tube global-local simulation will be presented in concert with the smeared crack formulation to predict the onset of tensile failure in the carbon plates of non-uniform thickness (center is thinner than the outer edges) subjected to shock loading.

8.4.1 Model Geometry

To create the global portion of the global-local model, the geometry that was used for the flat plate was modified in two ways. The first way was to include the final thinned profile of the plate. This was created by using a revolving cut from the center of the plate. The second operation was a cut through the thickness to allow for a total of 16 RVEs in a 4 row and 4 column pattern to be inserted. Figure 8.5 shows the front and back of the geometry that is used for the global portion of the global-local model. Seen in Figure 8.5(a), the partitioning of the face is held constant between the flat plate and thinned plate. This is used to align the model correctly with the fixed ring. In Figure 8.5(b), the thinned profile can be seen. The inner ring was thinned to the average measured thickness of the carbon plates. It is a constant thickness section of 0.381 mm (0.015 in.). A taper was then applied to second ring at a diameter of 76.2 mm (3 in.).

The second part of the model was the addition of the RVEs. The RVEs were arranged in a 4x4 configuration and interfaces were tied together. Since the meshes

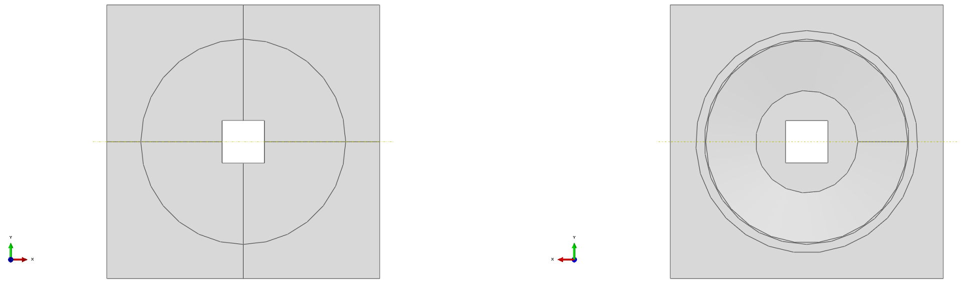

(a) The front of the final global geometry (b) The back of the final global geometry

Figure 8.5: The final geometry for the global local model for shock loading

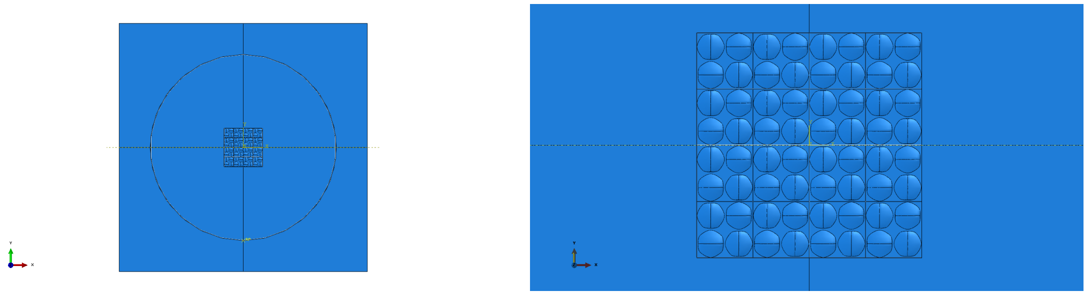

(a) The front of the full global local model (b) A close up view of the global local model

Figure 8.6: The global local model for shock loading

were the same between the RVEs, it allows for good adherence to continuity of displacements across the various RVEs. The edges of the 4x4 RVE block was then tied to the surface of the global model. The bag side of the RVE was selected to be oriented in the positive '3' direction to maintain consistently in the models between the global and local material coordinate system. Figure 8.6 shows the full geometry of the global-local model along with a close-up view of the 4x4 RVEs in the center of the global model.

The model was meshed to ensure continuity of displacement across the tie nodes, but also to ensure computational efficiency. For this reason, the end of the global portion of the model was seeded with the same mesh density as the RVE, however, a different seeding was applied further away from the center of the model. Each of the RVEs was meshed with 44,286 linear tetrahedral elements of type C3D4, while the global model was meshed with 49,130 linear tetrahedral elements of type C3D4.

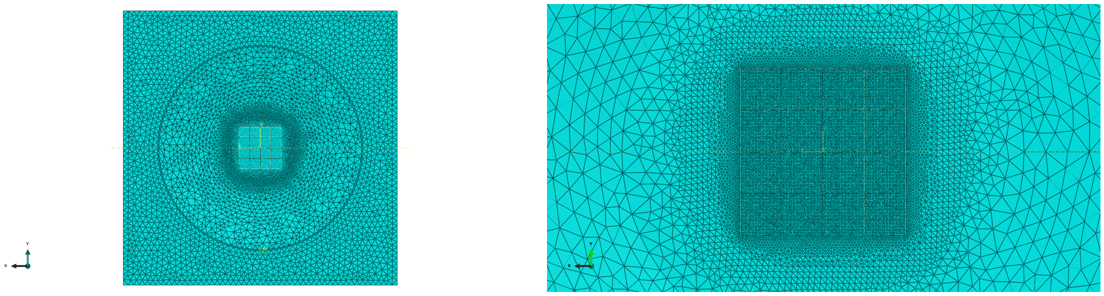

(a) The mesh for the global local model

(b) A close up view of the global local mesh at the interface between the global and local model

Figure 8.7: The mesh used for the global-local simulations

The entire model consisted of 757,706 elements. An image of the mesh along with a closeup of near the interface between the global and local model can be seen in 8.7

The pressure-time history was applied to the back of the plate in the tapered region as well as the back of the RVEs. Movement in the '3' direction was restricted and an in-plane spring with a stiffness of 5,000 N/mm was applied to the global section of the model. The boundary conditions for the ring and contact were the same as what was described previously for the flat plate.

8.4.2 Initial Results for Each Loading Case

Further validation of this global-local model was needed to ensure that the model is correctly capturing the mechanics of the test. To do this, the model was subjected to loading in two different configurations. The first configuration assumes the model is linear elastic without damage. This will help ensure that the initial response of the plate is consistent between the test and simulation. The second is to add the smeared crack formulation to the tows to simulate two-piece tow failure.

8.4.2.1 Elastic Response of the Global Local Model

The three loading cases considered for the fully elastic model were with shock strengths equal to 4.28, 7.66, & 8.99. The time history of the center deflection consisted of data computed at every 1 μs. Output frames were requested every 6.66 μs

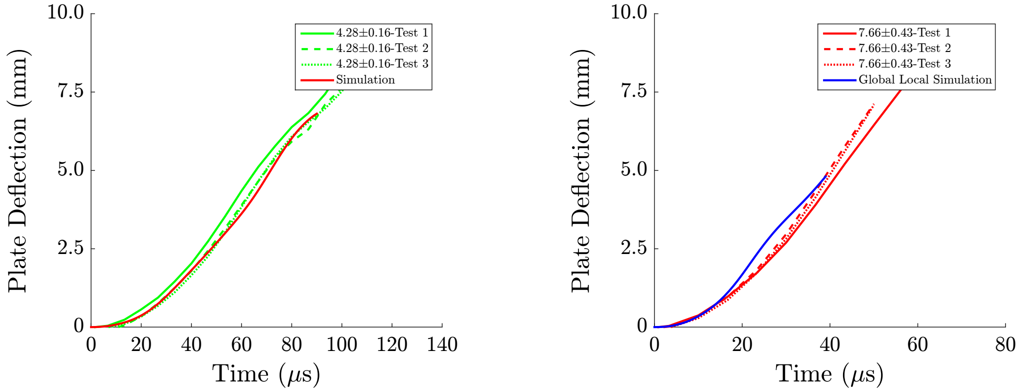

(a) Comparison between the elastic finite element model and the triplicate experiment for a shock strength of 4.28

(b) Comparison between the elastic finite element model and the triplicate experiment for a shock strength of 7.66

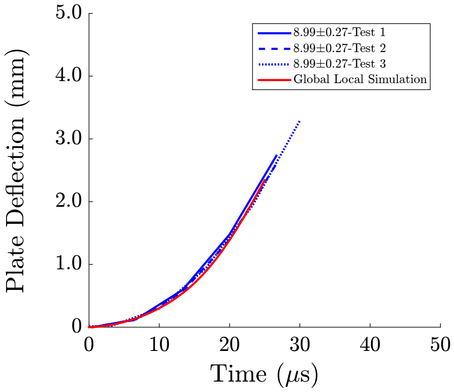

(c) Comparison between the elastic finite element model and the triplicate experiment for a shock strength of 8.99

Figure 8.8: A comparison of elastic finite element model to the experiments

to allow for a comparison to be made between the experimental results and the FE simulation. Each of the elastic simulations was run on 16 processors and took approximately 1 hour to run depending on the loading case. Depending on the amount of simulated time and non-linearity of the geometry at maximum deflection, the processing time could be as low as 20 minutes.

The results for the center deflection of the global-local model are shown in Figure 8.8 for the three loading cases. The model shows a high degree of agreement between the simulation and global-local model. In each of the simulations, the rise time and slope of the rise time are consistent with the experiment. Additionally, in the case of the shock strength of 8.99 shown in Figure 8.8(c), the response of the model is nearly identical to the triplicate testing. Figure 8.9 shows the comparison between the deflection profile for the simulation and experiment for the a shock strength of 8.99. The experimental deflection field limits were used for the finite element model limits. The deflection fields show good agreement between the experiment and simulation. Additionally, as the plate defects, there is a strong continuity of the displacement gradients across the global-local model boundary.

In addition to getting the deflection of the center of the plate, an accurate measure of the strain rate in the sample can be determined by taking the slope of the strain-time history of the crown. The strain-time histories for the two orthotropic material directions are shown in Figure 8.10. The strain-time history shows strong agreement between the two directions and this is to be expected for an elastic medium without damage.

Table 8.3 shows the two components of the directional strain for the simulations. As the shock strength is increased, so too is the strain rate. The average strain rate for the simulations range from 250/s to 528/s. These strain rates will be used later to establish the strain rate hardening parameter for the failure of the tow and conversely to check if the rate dependent information extracted from the 1-D SHPB experiments carries through for a biaxial simulation as is done here.

Shock Strength	Simulation- X-strain Rate (/s)	Simulation- y-strain Rate (/s)	Average Strain Rate (/s)
4.28	242	258	250
7.66	470	500	485
8.99	556	500	528

Table 8.3: The measured directional strain rates for the simulation

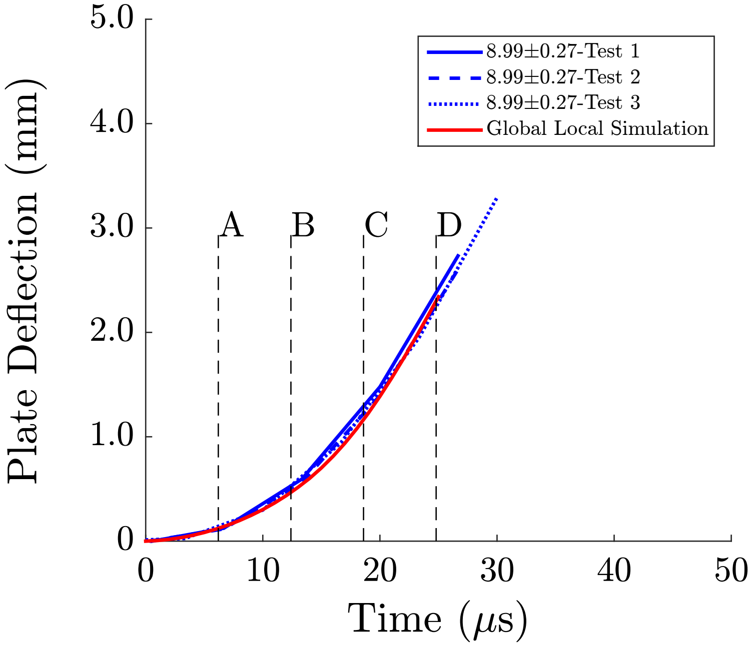

(a) Comparison between the deflection profile of the elastic finite element model and the triplicate experiment for a shock strength of 4.28

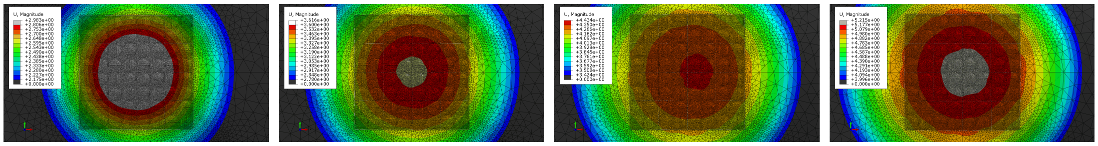

(b) Simulation deflection profile at A (c) Simulation deflection profile at B (d) Simulation deflection profile at C (e) Simulation deflection profile at D

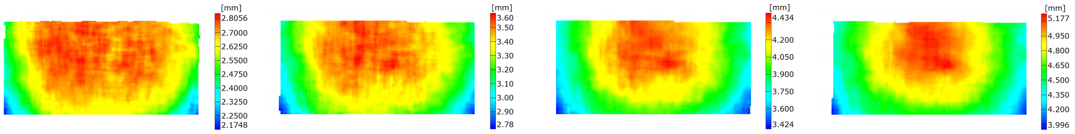

(f) Experimental deflection profile at A (g) Experimental deflection profile at B (h) Experimental deflection profile at C (i) Experimental deflection profile at D

Figure 8.9: A comparison of elastic finite element model to the experiments

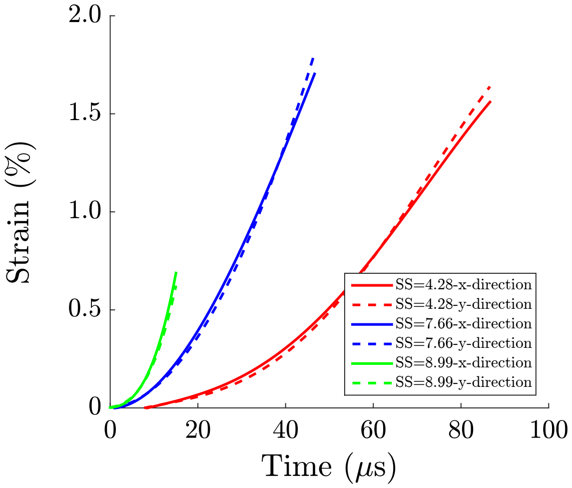

Figure 8.10: The directional strain time histories for the global-local elastic model

8.4.2.2 The Global-Local Model with Smeared Crack

To simulate the two-piece failure of the yarn, the smeared crack formulation was applied to the center 4 RVEs. The 12 RVEs that surround it was considered to be entirely elastic since it was shown in the previous section that the elastic model matched the center deflection-time history quite well. Additionally, since it was also shown previously that the matrix non-linearity had little effect on tensile rupture of the yarns and decreased computational efficiency, the smeared crack model was only applied to the yarns. The input parameters for the smeared crack portion of the model is shown again in Table 8.4.

σ_{11}^{T} (MPa)	σ_{11}^{C} (MPa)	σ_{22} (MPa)	τ_{12} (MPa)	τ_{12} (MPa)	G_{IC} (N/mm)
3000	-1000	7000	3700	3200	40

Table 8.4: The smeared crack critical strengths for the tow

As with the previous elastic example, output information was computed at a rate of 1 frame every 6.66 μs, and the onset of failure in the yarns was examined. When failure was observed, the yarn was considered to have failed in a manner that is

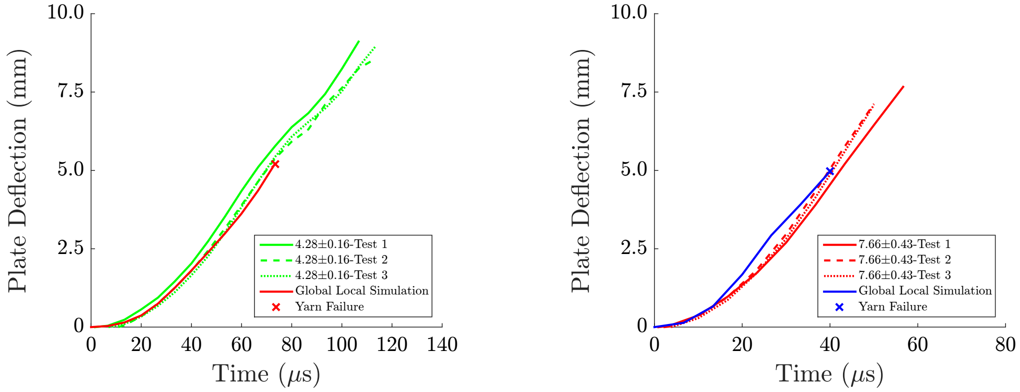

(a) Failure in the finite element model and the triplicate experiment for a shock strength of 4.28

(b) Failure in the finite element model and the triplicate experiment for a shock strength of 7.66

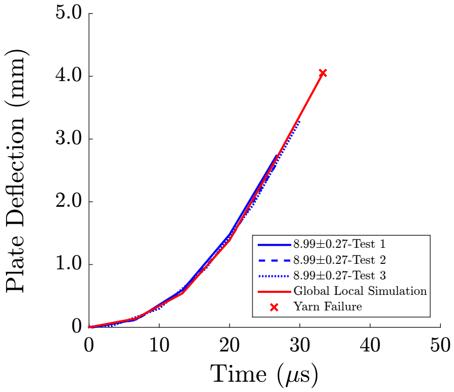

(c) Failure in the finite element model and the triplicate experiment for a shock strength of 8.99

Figure 8.11: A comparison of the yarn failure in the element model to the experiments

identical to that in the experiment. Figure 8.11 shows the comparison between the onset of yarn failure in the finite element model with the smeared crack formulation and the the triplicate experiment.

For a shock strength of 4.28 shown in Figure 8.11(a), the simulation with a failure strength of 3,000 MPa for the yarn, under-predicts the failure of the yarn. This same effect is observed in the middle loading case of a shock strength of 7.66 (Figure 8.11(b)). Of interest is the failure of the yarn for the highest shock strength of 8.99. It is seen that the deflection corresponding to failure is over predicted relative to the experiment. This may be a function of the difficulty of accurately establishing two-piece failure in the experiment, and will be addressed further in a subsequent section.

8.5 Incorporation of Strain Rate Dependent Behavior with Smeared Crack

Since the failure deflections were generally under predicted, it was necessary to incorporate rate dependent behavior into the smeared crack formulation. Since the code does not consider strain rate dependent behavior, each of the loading cases was considered to be rate-independent. Rate dependency obtained from the 1D SHTB studies (see chapter 4) were used establish the critical rate-dependent tensile strength of the yarns, S_{11}^{T}. The selected values are shown in Figure 8.12. It should be noted in this figure that the behavior and fit of the trend line is dependent on the highest strain rates measured during SHTB testing, and that the failure strength does not tend to infinity. If higher strain rates were achieved in the SHTB testing, this representation would not have the same characteristics and would most likely result in a tensile strength ratio saturating at a given value.

Also shown on this figure is a line of best fit. The line of best fit is shown in Equation 8.3.

$$R = 1.132 * exp^{(9.56e-4)\dot{\epsilon}} \tag{8.3}$$

From the elastic simulations, the strain rates were determined to be 250, 485, 528/s. These strain rates were used in Equation 8.3 to determine the failure ratio of the yarn at that given strain rate. It should be noted that the failure stress for the SHTB work was much lower than the initial failure stress of the smeared crack formulation. The ratio however, may still be an accurate representation of what the yarn in the textile composite experiences at high strain rates. Table 8.5 shows the

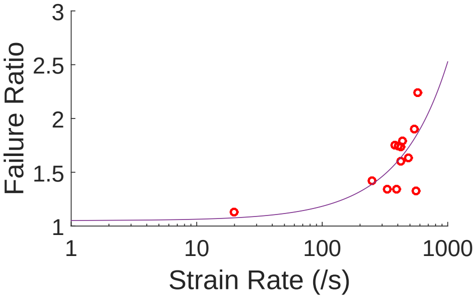

Figure 8.12: The tensile failure strength ratio as a function of strain rate

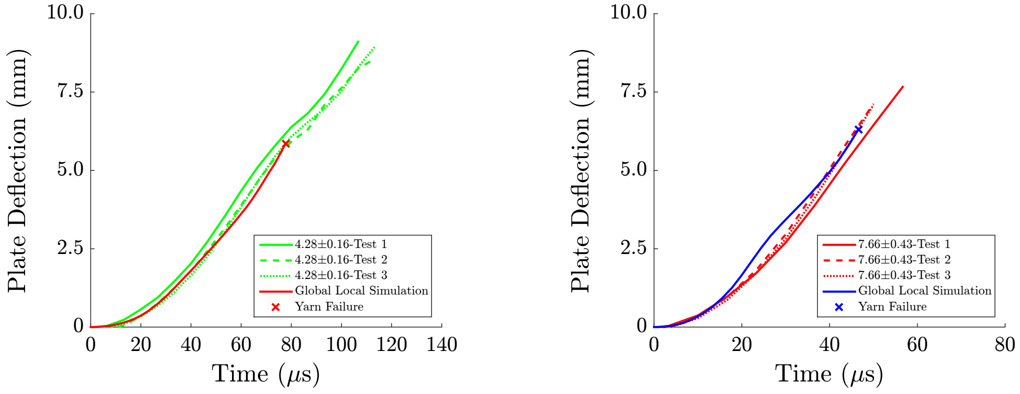

(a) Failure with strain rate dependence in the finite element model and the triplicate experiment for a shock strength of 4.28

(b) Failure in the finite element model and the triplicate experiment for a shock strength of 7.66

Figure 8.13: A comparison of the strain rate dependent failure in the finite element model to the experiments

failure ratios and the tensile strengths that were used for the three loading cases to analyze the rate dependent behavior. These failure strengths were written into the input file for each of the three loading cases.

Strain Rate (/s)	Failure Strength Ratio	Failure Strength (MPa)
250	1.44	4314
485	1.80	5400
528	1.88	5625

Table 8.5: The failure ratios for the final smeared crack critical strengths

The simulations were run with all other parameters kept the same as before, except for the incorporation of rate-dependency. It was requested that frames be computed and written out at every 2.2 μs to find the onset of failure accurately.

Figure 8.13 shows the results for the two smaller shock strengths of 4.28 and 7.66. The onset of failure of the 4.28 shock strength corresponds well with the physical features of the deflection-time history of the triplicate experiments. In the experiments, there is a knee right around the point of failure in the experiments. At this point, the plate is beginning to fail, however, correlation is still observed in the plate during

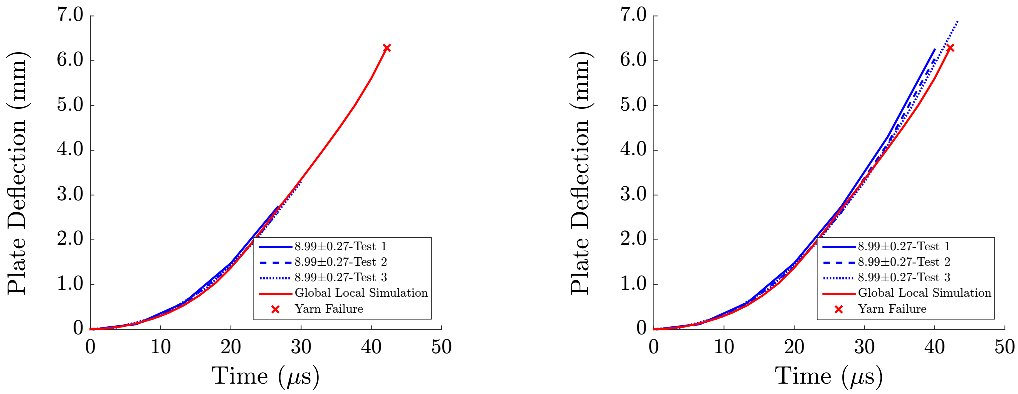

(a) Failure with strain rate dependence in the finite element model and the triplicate experiment for a shock strength of 8.99

(b) Failure in the finite element model and the triplicate experiment for a shock strength of 8.99 with two more frames included

Figure 8.14: A comparison of the strain rate dependent failure in the finite element model to the experiments

the experiment. The simulation has good agreement with the experiment.

Similarly, Figure 8.13(b) shows a comparison between with the strain rate dependent smeared crack and the triplicate experiment for the shock strength 7.66 case. The failure deflection that is predicted by the model is 6.314 mm and is still slightly under predicted relative to the triplicate testing average of 7.30±0.31.

The results corresponding to the highest shock strength between the simulation and the experiment is shown in Figure 8.14(a). The failure is over predicted in comparison to the triplicate experiment. While the failures for the two lower pressures predicted the behavior reasonably well, the over prediction of the highest pressure should be addressed. This could be an effect of one of two factors: difficultly in identifying failure of the plate, or experimental error in the SHTB testing.

Figure 8.14(b) shows the deflection-time history of the plate by including the deflections of the plate for two additional frames. When identifying failure of the plate through the experiments, deviations in the strain fields coupled with visual inspection of the images was used to determine the failure of the plate. The images shown in Chapter 6 indicated the failure of the samples and in many of the samples, a clear crack is not observed, particularly in the case of the shock strength=8.99 samples, however, in the subsequent frame, separation has occurred. With the relative large slope of the deflection time history and low framing rate, it is difficult to pinpoint the exact time of failure.

The second reason is the accuracy of the fit for the strain rate dependent response. Figure 8.12 shows the failure strength ratio as a function of strain rate. While there is a clear trend towards hardening within the yarns with respect to the failure strength, there is quite a bit of scatter in the data. The exact fit for the line to determine the relationship is affected by the number of data points. Additionally, for the points of failure for the above 500/s (in the simulations, the strain rate was approximately 528/s) there are three points which range from 1.3-2.3 times larger than the static strength. These two effects together make it difficult to fully assess the failure at the high rates without further experimental information.

8.6 Conclusions

In this section, the response of carbon textile panels subjected to high rate loading using a shock wave in a shock tube was modeled using a number of different techniques. The flat plate was simulated and determined that the boundary conditions in the experiment were neither simply supported or purely clamped, but rather at a state in between. To remedy this, an in-plane spring was added to simulate the boundary conditions and had agreement with the experiments to within 4% of measured values in plate deflections. To simulate the response of the thinned carbon plate, a global-local model was created that included 16 RVEs in the center of a homogenized plate. The plate was subjected to shock loading and it was determined that the elastic response was nearly identical to that of the experiment. The smeared crack formulation was added to determine the predicted failure of the yarns. When the plate failure deflection was generally under predicted, it was determined that strain rate hardening of the failure stress of the yarn in tension was needed to be added. To choose the values of the failure stress at elevated loading rates, the experimental fit to the 1D SHTB experimental results was used as input into the model. For the two lower shock strengths, the failure deflections were in good agreement with the experiments, while the high shock strength over predicted the deflection corresponding to when failure occurred. Reasons for this discrepancy were discussed.

CHAPTER IX

Concluding Remarks

In this thesis, the response of fiber reinforced polymer matrix composites at elevated loading rates was examined with a particular focus on the tensile response. To study this effect, experimentation in concert with finite element modeling was used. Selected material systems of IM7 carbon fiber and S2 glass fiber with SC-15 matrix were tested. The quasi-static response of the composite materials was first examined to establish a baseline response for the materials. Through the use of traditional mechanical testing, the failure strength of cross-ply composites was evaluated and the matrix material response in tension and compression was established, while the in-situ matrix response was examined using the $[+45/-45]$ test.

While a number of researchers have examined the high rate response of composites subjected to tension, there is no clear consensus about the influence of rate on the material response. A literature survey revealed that there is little consistency between past work with regard to the trends observed at elevated rates. In this thesis, Split Hopkinson Tensile Bar (SHTB) testing techniques were used with the Digital Image Correlation technique to study elevated rate response of composite materials. By first validating with aluminum specimens, an Enhanced Split Hopkinson Tensile Bar data analysis technique was developed to determine the high strain rate response. From the testing, it was shown that as the strain rate increases, for the IM7/SC-15 material system, so too does the failure stress and modulus of elasticity, however, the failure strain generally decreases. Likewise, for the S2/SC-15 material system, the failure stress and modulus of elasticity increase, however, the failure strain was generally rate insensitive. These results were consistent with a few of the results reported by researchers with similar techniques.

The SHTB produces an approximately one-dimensional state of strain, while shock tube testing has been shown to be a way to dynamically load a plate to produce a multi-axial state of strain. By first using commercial aluminum, it was shown that a shock tube can be used to extract the multi-axial rate dependent response by using an inverse modeling technique. This technique demonstrated that shock tube testing is repeatable, reliable, and predictable to a high degree. After successfully demonstrating this effect, thin plates of plain woven IM7/SC-15 and S2/SC-15 were subjected to shock loading. It was found that in order to rupture the yarns at the crown of the plate, strains must accumulate faster at the crown than through the thickness to prevent a punch out shear response at the plate boundary. In order to accomplish this, a thinning technique was proposed and tested which allowed the multi-ply sample to be thinned to the thickness of a single ply at the center of the sample. After testing with both material systems, it was determined that the energy absorption in the S2glass material system was too high to safely rupture, requiring very high shock tube driver gas pressures, however, the carbon system was able to fail consistently at operational driver pressures that were safe between 6.2-10.3 MPa (900-1500 PSI). Within the carbon system, triplicate testing offered insight into failure over a number of multi-axial high strain rate configurations.

To model the strain rate effects on failure within the plain weave carbon samples, a finite element model was developed from detailed optical microscopy images. First, it was demonstrated that an ideal geometry did not properly capture the mechanics of the composite because it was too matrix rich. In order to achieve a higher global volume fraction, a hybrid geometry was made that incorporated realistic geometries with idealized yarn features to create a representative volume element (RVE). The RVE was virtually tested without failure and determined that the stiffness matched the experimental stiffness. The smeared crack formulation was then used in the model and it was able to predict the failure load within 5% of the experimentally measured in-plane tensile failure strengths. Importantly, it was shown that strain localizes at the crimp points where the yarns intersect in the tow geometry, and this was captured as observed in experiments. This is a unique and novel contribution that has hitherto not been modeled in the manner shown in this thesis.

Virtual testing was next performed to study the shock tube model that was experimentally examined. The effect of boundary restraint, which is intermediate between a clamped and a simple-support, was modeled by an in-plane spring with an appropriate stiffness. This proved to be successful as the less than 4% difference between the experimental deflection and modeling deflection was seen for four of the five loading cases.

A global-local finite element model was next developed to incorporate the geometry of multiple RVEs into the shock tube plate configuration. After establishing that the elastic response matched well with the experimental results, a rate dependent smeared crack formulation was implemented for the carbon fiber plain weave textile material. It was found that the failure deflections were generally consistent with that of the experiment. Additionally, it also appears that the smeared crack formulation is able to provide a good estimate of the failure strength under high rate loading. The simulations gave a good indication that the use of the strain rate dependent data, extracted from the 1D SHPB test and its utilization for multiaxial modeling was correctly capturing the panel response.

9.1 Future Work

This thesis outlines a number of novel experimental and modeling techniques, however, what has been presented is only a fraction of the possible capabilities with respect to understanding the failure of textile composites under elevated loading rates. The following subsections contain proposed future work that can build on the work of this thesis to lend further insight into this important engineering problem.

9.1.1 High Strain Rate Testing

The Hopkinson bar and Shock Tube testing in concert with the Digital Image Correlation Technique offered great insight into the failure of textile composites at high strain rates, but they were not without limitations.

9.1.1.1 Hopkinson Bar Testing

The results of the tensile Hopkinson bar testing were unique and offered a new examination into the failure of crossply composites. This technique can be improved by incorporating a number of lessons learned through the course of the testing and validation. One of the key assumptions from the original Kolsky test was that the bar is free to move in plane and that during dynamic equilibrium, the sample is free of inertial effects. As the diameter of the bar increases, so too does the mass. This increases the friction and the inertial effects of the bar. For each Hopkinson bar test setup, an analysis of the friction free conditions and inertia effects should be conducted on the setup prior to testing. This ensures that the data collected is as accurate as possible.

Secondly, the Enhanced Split Hopkinson Bar data analysis technique requires further refinement to eliminate the need for the transmitted bar signals. Researchers have shown in the past that the bar signals can differ greatly from the in-situ measurements made by a strain gage or a non-contact strain measurement by DIC. Further investigation with this technique into highly heterogeneous materials will give new insight into strain rate dependent response in these materials.

The cross-ply system is a good example of a heterogenous material that has wave speeds of different magnitudes throughout. While the wave speed of the carbon fiber is much faster than that of the matrix at the mirco-scale, the wave speed of a ply could be quite different depending on whether it is longitudinal or transverse. As a wave passes through a layered system, it is currently unknown whether or not this effect is important and if the wave separation occurs due to different wave speeds in the material. There has yet to be conclusive proof that traditional wave analysis correctly captures the homogenized response. The use of experimental results using DIC and finite element modeling will offer further insight into this aspect.

9.1.1.2 Shock Tube Testing

Shock tube testing is one of the most promising techniques to evaluate high strain rate properties at multiaxial loading rates. It has been shown to be repeatable, predictable, and offer a high degree of fidelity for the testing that helps to translate well into modeling applications. In past thesis work by Mark Pankow, repeated (multiple loading of the same panel) blast loading is introduced, however, it is not fully investigated. As 3D textiles are inserted in larger applications, one of the key points to understand is the damage tolerance to the matrix. While the focus of this thesis was based on the tensile response of the composite which minimized the matrix effect, other applications are more dependent on the toughness of the matrix. Since the shock tube test has a high degree of repeatability, a detailed study on matrix microcracking and crack propagation of the matrix as subjected to shock loading would be a way to understand the progressive damage of the matrix at elevated multiaxial loading rates.

9.1.2 Modeling of Textile Composites

In this thesis, the modeling of textile composites used a hybrid RVE that incorporated real features of the composite with an idealized yarn texture. Through modeling, it was shown that strain localizes at the crimp points were the yarns intersect in the idealized tow geometry. This feature has been noted by a number of researchers and is not fully understood. To fully understand the failure of textile composites, careful attention must be paid to the geometry of the textile itself. In order to achieve a more realistic as-manufactured geometry, researchers are beginning to model the weaving process to gather information about the crimping of the yarns and local deviations from idealized architecture. This process can be quite time consuming, and sometimes a result is needed in a more timely manner.

In the following subsection, a technique is proposed to show how to develop a nested geometry by allowing the yarns of an RVE to deform into one another.

9.1.2.1 Proposed Technique for As Nested Geometry Generation

In order to achieve a deformed state within the yarns, a psuedo-thermal cycle was applied to the yarns. It is important to emphasize that the parameters that were used were arbitrary and were used to create the nested geometry. They have no physical representation and are simply numerical to achieve a realistic shape. The following section describes how this process was done to achieve the final geometry. This procedure is similar to what has been proposed in the past by Stig and Hallstrom [108].

The geometry that was developed in TexGen was exported as a step file to ABAQUS. An imported file from TexGen can be seen in Figure 9.1. Figure 9.1 shows a mid yarn cut to show the geometry. As can be seen from the image, while the geometry looks correct, it is missing many few geometrical points that have to be addressed further as the yarn fraction is not correct. It can also be seen that the

Figure 9.1: A mid-yarn cut showing the cross-section of initial geometry

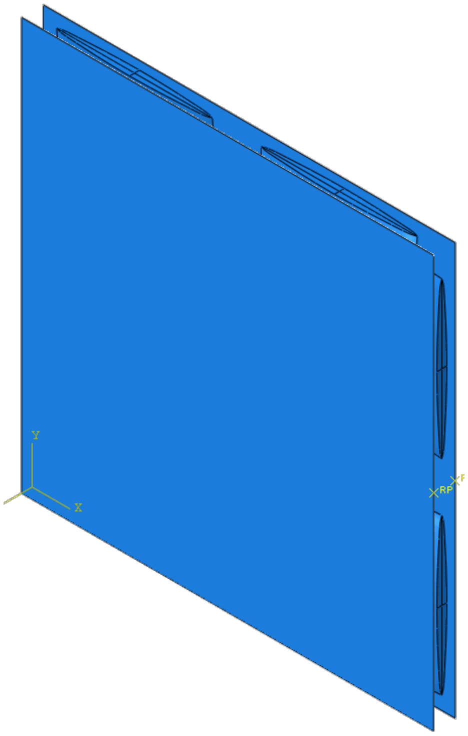

Figure 9.2: A schematic of RVE wedged between the rigid plates

geometry has a small gap between the yarns. It is important for the contact algorithm to have this effect.

To do this, two rigid plates were created and offset by the thickness of one ply or approximately 0.215 mm. The geometry by the idealized RUC was placed in between the plates to allow the yarns deform into the plate. An image of this is shown in Figure 9.2. The plates were fixed at the reference points. A node set was created on the center of the face of each of the yarns. The node set was fixed to prevent the yarns from sliding as they deform, while allowing the free expansion to occur. A thermal load of 6000 was applied to each of the ends of the yarns.

In order to create this simulation, a material model was needed to be developed. While many of these values were selected to be arbitrary, they were modeled after aluminum in order to have realistic ratios of properties. Since expansion along the yarns was not desirable, orthotropic expansion coefficients were given as 0, 2.31e-5, 2.31e-5 for the 1, 2, and 3 directions. A material coordinate system was given to the yarns such that the 1 direction was along the yarns. Plasticity was used to slow the expansion at some point such that the expansion was not uncontrolled, however, ended up only contributing minimally to the final geometry.

Thermal Conductivity	Density	Young's Modulus	Poisson's Ratio
159	2730	68.9e9	.33

Table 9.1: Inputs for the FE simulation

Each yarn was meshed into 3020 linear tetrahedral elements of type C3D4T and the rigid plates were meshed into 6400 linear quadrilateral elements of type R3D4. Two types of contact were used for this simulation. The first was self contact using a surface to surface discretization method with normal and tangential frictional behavior defined. The second was a pure master-slave surface to surface contact that was described for the rigid plate and the surface of the yarns. The rigid plate was the master and the yarn surface was the slave. The same normal and tangential frictional behavior was used for this contact. A coupled temperature-displacement step was created for a time period of 1000 seconds solving for the steady state response. Nonlinear geometry was used in the simulation as was automatic stabilization. Due to the large amounts of contact during the initial steps, a small time increment is needed to begin the solution. Stabilization allows for dissipation of energy to allow for the solution to converge faster. While this may not always be a recommended step, it is satisfactory since a deformed geometry is what is desired. The simulation ran on 4 CPUs for 4 hours to complete the job on a standard Dell workstation.

A comparison between the initial and the final geometry is shown in 9.3. Figure 9.3(a) shows the undeformed yarns cut at 1/4 the length of the RVEs whereas Figures 9.3(b), 9.3(c), and 9.3(d) show cuts along the deformed shape at 1/4, 1/2 and 3/4s the


(a) Initial undeformed geometry

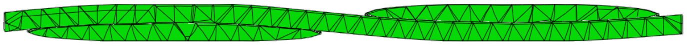
(b) Deformed RUC cut at 1/4 the RUC length


(c) Deformed RUC cut at 1/2 the RUC length

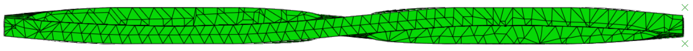
(d) Deformed RUC cut at 3/4 the RUC length

Figure 9.3: Comparison between the undeformed and deformed shape

RUC length. The deformed shape shows aspects that were missing from the idealized geometry. Namely, the yarn is deformed when it is at either the top or the bottom of the sinusoidal shape. It flattens at the top, however, when the yarn is in the middle of the RUC, it maintains its elliptical shape.

As seen in Figure 9.3, the RVE now has a more realistic geometry that incorporates more aspects of the crimping. This technique could allow for further insight into the failure of the textile composites without the time constraints of simulation the weaving process.

APPENDICES

APPENDIX A

Validity of Reduced Resolution Optical Strain Measurements

One common issue that continues to be of interest to the mechanics community is the validity of DIC measurements. While it has become one of the most widely used tools in material testing, many have questioned the validity of the measurements relative to a strain gage. This uncertainty is sometimes exacerbated by the reduced resolution photographic techniques such as those in high strain rate testing. For this reason, it is necessary to establish the validity of the strain measurements.

A.1 Experimental Details

To examine the validity of the results, a simple tension test was conducted with a certified piece of aluminum 6061-T651 as its mechanical properties are generally well understood. To mimic the results of what is observed in the high strain rate testing, the same experimental parameters were used. The Photoron SA.X was set to a frame rate of 60 FPS, but to match the resolution of a shock tube test run at 150,000

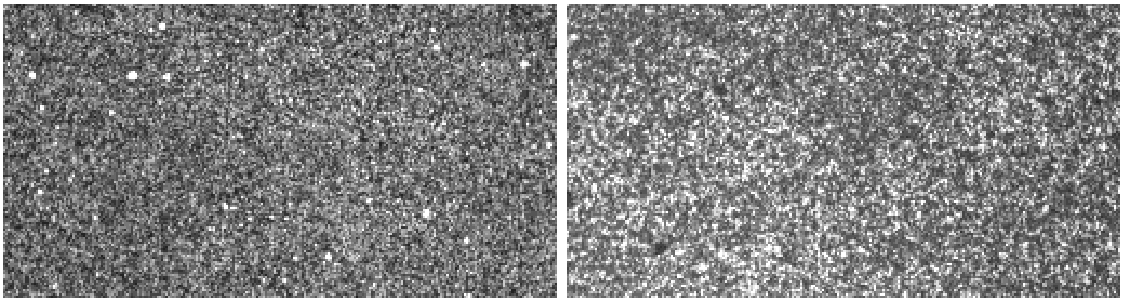

(a) An image taken from shock tube testing (b) A comparable image with same resolution of aluminum

Figure A.1: Comparison of resolution and speckle for the validity analysis

FPS, the resolution was set to 256x136 pixels. A 180 mm lens was used at a focal length of 44", the same length as that used in a shock tube. A random speckle pattern was applied to the aluminum in the same manner as the that of the shock tube specimen. A sample of the focus and the speckle pattern is shown in Figure A.1.

The sample was pulled at a quasi-static rate of 0.0004 in/s on a hydraulically activated load frame and images were taken at a frequency of 60 hertz. The load and displacement were recorded at a rate of 10 hertz. The images were saved and run through the ARAMIS DIC software to determine the mechanical properties. For consistency, the DIC facet size of 17x17 pixels and step size of 2 pixels was kept identical to that of the shock tube tests. Strain gages were attached in the center of the sample in the loading and transverse directions and recorded at a frequency of 10 hertz as well.

A.2 Results

After testing, the images were aligned and run through the ARAMIS

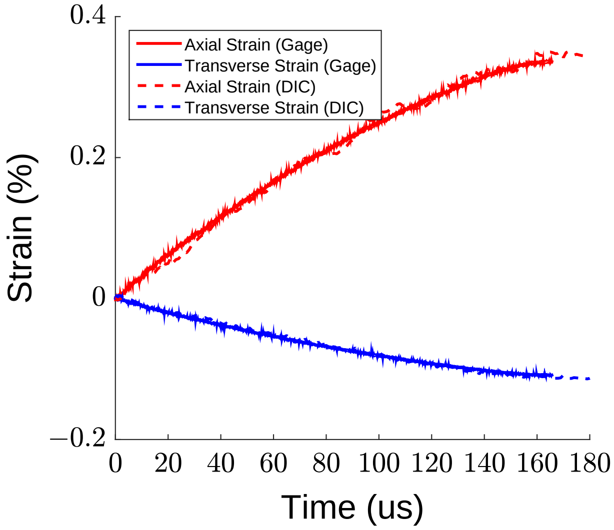

Figure A.2: A comparison of the transverse and longitudinal strains as measured by the DIC and strain gage

DIC software. It is important to note that what is being shown is the raw strains without filtering, though GOM, the manufacturer of ARAMIS generally recommends filtering strains. The reason the strains are not filtered is because at high framing rate tests, the strains are generally not filtered as they may remove important localized information. This maintains the integrity of this investigation by changing none of the parameters between the static test and the high rate tests.

A comparison of the axial and transverse strains from the DIC and strain gages is shown in Figure A.2 as a function of time. As seen in this plot, there is a high degree of agreement between the strain gages and the DIC. While there is some error in the measurement with the DIC, it matches the trend nearly identically. With slight filtering, this would yield a nearly identical result.

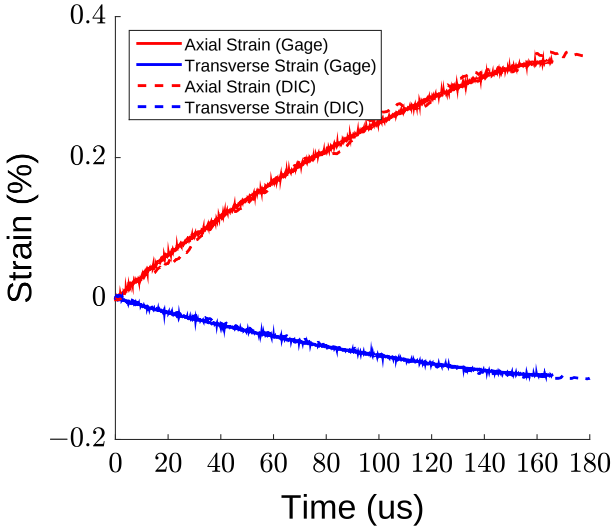

Figure A.3: A comparison of the transverse-longitudinal strains to determine Poisson's ratio

The strains signals were then used to determine the Poisson's ratio of the material. This was done by plotting the transverse strain against the axial strain. This is shown in Figure A.3. To determine Poisson's ratio, the slope of that line is taken. From Figure A.3, it is clear that on the average, the results are very similar. Again, the DIC shows a larger amount of error, however, the trend is captured correctly.

Finally, the stress-strain response was plotted in two ways by using the strain gage strain and the DIC strain. The results of this are shown in Figure A.4. Additionally, the reported value of the modulus of elasticity is also plotted. Both of strain measurement techniques showed a less stiff response than that of the reported value, however, both samples show nearly identical trends.

These results indicate accuracy of the DIC is not sensitive to the

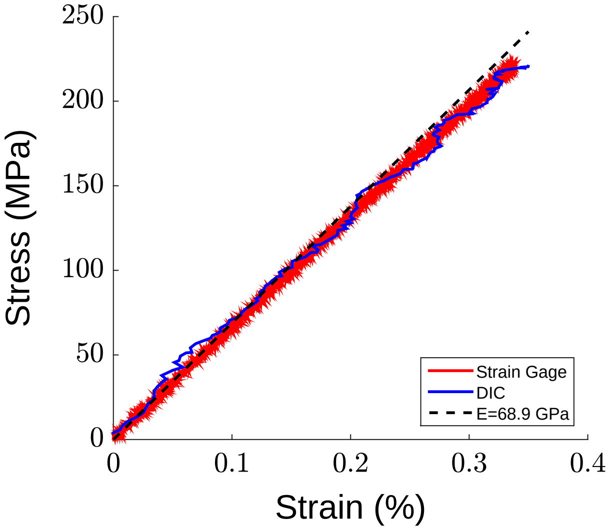

Figure A.4: The stress-strain response of the aluminum 6061-T651 using DIC and strain gages

reduced resolution.

APPENDIX B

MatLab and Python Script

B.1 MatLab Script for Align and Crop Raw Images

```
function Crop_Photos_v1

    %% Inputs
    st=3;  % Starting img num
    en=55; % End img num
    interval=1; % Picture interval
    save_loca='#################';



    imshow('DSC_0003.JPG')
    clicks=ginput(2);
    disp('click for rotation adjustment')
    x1=clicks(1,1); x2=clicks(2,1);
    y1=clicks(1,2); y2=clicks(2,2);
    rot_degree=atand((y2-y1)/(x2-x1));
```

```
imshow('DSC_0003.JPG')
disp('click for Crop Size')
clicks=ginput(2);
x=[clicks(1,1);clicks(2,1)];
y=[clicks(1,2);clicks(2,2)];
xmin=min(x);
ymin=min(y);
width=abs(x(1)-x(2));
heighth=abs(y(1)-y(2));
crop_size=[xmin ymin width heighth];


%%
for i=1:1:(en-st+1)/interval
    cam_pic_nums(i)=st+(i-1)*interval;  %Camera Pic Number
end


%%
for it=1:1:length(cam_pic_nums)
    picnum=num2str(cam_pic_nums(it)); %Camera Pic Number String

    if (cam_pic_nums(it) < 10)
        picname=strcat('DSC_000',picnum,'.jpg');
    elseif (cam_pic_nums(it) < 100)
        picname=strcat('DSC_00',picnum,'.jpg');
    else
```

```
            picname=strcat('DSC_0',picnum,'.jpg');
        end
    %% Image Adjustment
        refimage=imread(picname,'jpg');
        refrotate = imrotate(refimage,rot_degree);
        refcrop = imcrop(refrotate,crop_size);


    %% Image Rename
        testnum=num2str(it);
        testname=strcat('PK',testnum,'.jpg');
    %% Image Save Location


        testname=strcat(save_loca,'\',testname);




        imwrite(refcrop, testname,'JPG');




    end
end
```

B.2 MatLab Script for Split Hokinson Tensile Bar Data Analysis

```
INPUTS: Oscilloscope data, in .csv format.
       Column 1: Time (s)
       Column 2: Channel 1 - Incident Bar (V)
       Column 3: Channel 2 - Transmitted Bar (V)
 OUTPUTS: A .csv file containing the following
       Column 1: Time (us)
       Column 2: Strain (-)
       Column 3: Stress (MPa)
       Column 4: Strainrate (-/s)
 1. Copy this file into a folder along with the channel data files.
 2. Match the names of the channel files with those in this program.
 3. Enter specimen length, diameter, mass, estimated modulus
    information into the program code
 4. Run the program.
 5. Select beginning and end points of incident wave.
 6. Iterate (Rerun program) -  Shifting by changing error values to
    establish equilibrium if possible.
 7. Output is the polynomial fit data

 Plots:
 1. Incident and Transmitter Bar strain gage signals
 2. Incident Gage - Requires user inputs to window the incident pulse
 3. Pulse Orientation - Gauge of pulses in relation to entire signal
 4. Incident, Transmitted and Reflected Pulses - After shift is applied
 5. Force Balance - Equilibrium Check
 6. Stress-Strain Curves (Polynomial fit and original)
```

 7. Strainrate-Strain Curves (Polynomial fit and original)

```
function SHPB_Data_Analysis
clear all;
close all;
clc;
```

1 Data Read In

```
 Read in Strain Gage Signals - file 'name-of-file.csv'
inbar = csvread('######.csv',23,0);
```

2 Specimen, Pressure Bar, Amplifier Specifications

```
 Specimen Information
l_spec = .5*.0254;            % Output Meters
d_spec = .0625*.0254*.350*.0254;             % Output Meters
m_spec = .8041*.001;            % Output Kilograms
E_spec_guess = 100*1e09;        % Output Pa (Pick one to use for every
                                              iteration)

rho_spec = m_spec / (l_spec*d_spec^2);  % Kg / m^3
A_spec = d_spec;                      % Meters Sq

c_spec = sqrt(E_spec_guess /  rho_spec);    % m/s
tau = l_spec / c_spec;                      % sec

 Amplifier Information
num_gage_inc = 1;       % Quarter Bridge = 1
```

```
num_gage_tra = 1;       % Quarter Bridge = 1
gain = 500;             % Gain
v_exc = 10;             % Excitation Voltage
```

Pressure Bar Information

```
l_incident = 96 * .0254;
l_trans = 70 * .0254;

E_al=68e9;
E_steel = 220e09;
d_bar = 1.5 * 0.0254;
A_bar = pi*(d_bar/2)^2;
v_sound = 5416.67;
v_sound_al = 4877;
c_bar = v_sound;
rho_bar = 7500;
rho_bar_al = 2698.9;
```

3 Data Breakout

Separating the single input file into multiple arrays

Split loaded data into time and voltage vectors for each wave

```
t_inc = inbar(:,1);
t_ref = t_inc;
t_tra = t_inc;

v_inc = inbar(:,2);
v_tra = inbar(:,3);
```

```
v_ref = v_inc;


figure(1)
plot(t_inc,v_inc, t_inc, v_tra)
xlabel('Time (s)','FontSize',18); ylabel('Voltage (V)','FontSize',18)
title('Strain Gage Raw Signals','FontSize',18)
legend('Incident Bar Gage','Transmitter Bar Gage')
```

4 Noise Correction - Simple average of closest 7 data points

```
for k=4:(length(v_inc)-4)
    v_inc(k) = (v_inc(k-3)+v_inc(k-2)+v_inc(k-1)+v_inc(k)+v_inc(k+1)
    +v_inc(k+2)+v_inc(k+3))/7;
end
for k=4:(length(v_ref)-4)
    v_ref(k) = (v_ref(k-3)+v_ref(k-2)+v_ref(k-1)+v_ref(k)+v_ref(k+1)
    +v_ref(k+2)+v_ref(k+3))/7;
end
for k=4:(length(v_tra)-4)
    v_tra(k) = (v_tra(k-3)+v_tra(k-2)+v_tra(k-1)+v_tra(k)+v_tra(k+1)
    +v_tra(k+2)+v_tra(k+3))/7;
end
```

5 Establish Incident Wave Beginning and End - Manual Inputs Needed

Beginning - Typically when wave begins to ramp up is - approx 250mv
End - Big Bar: Wave peak, before any noise
      Small Bar: After wave has finished level portion and begins to decrease to 0

Incident Wave

```
figure(2);
grid on;
plot (t_inc,v_inc);
xlabel('Time (s)','FontSize',18); ylabel('Voltage (V)','FontSize',18)
title('Incident Pulse Windowing','FontSize',18)
grid on;
uiwait(msgbox('Select the BEGINNING and END of INCIDENT wave'));
[t_beg, v_beg] = ginput(1);
inc_beg = find(t_inc < t_beg);
inc_beg = max(inc_beg);
[t_end, v_end] = ginput(1);
inc_end = find(t_inc < t_end);
inc_end = max(inc_end);
```

6 Reflected and Transmitted Wave Determination

Time Shift Method for Determining Start Points of Waves

Reflected Wave Determination

```
error_ref = #####;
t_shift_ref = l_incident / v_sound + error_ref;
ref_beg = find(t_inc < (t_inc(inc_beg) + t_shift_ref));
ref_beg = max(ref_beg);
ref_end = ref_beg + (inc_end - inc_beg);
```

Transmitted Wave Determination

```
error_tra = ####;
```

```
t_shift_tra = ((l_incident/2 + l_trans/2) / c_bar + l_spec / c_spec)
 + error_tra;
tra_beg = find(t_tra < (t_inc(inc_beg) + t_shift_tra));
tra_beg = max(tra_beg);
tra_end = tra_beg + (inc_end - inc_beg);

7 Pulses in Relation to Total Signal - Plot for Visualization

figure(3)
hold on;
plot(t_inc,v_inc, t_inc, v_tra)
plot(t_inc(inc_beg:inc_end),v_inc(inc_beg:inc_end),'m',...
     t_inc(ref_beg:ref_end),v_inc(ref_beg:ref_end),'m--',...
     t_inc(tra_beg:tra_end),v_tra(tra_beg:tra_end),'m:','LineWidth',3)
grid on;
legend('Incident Bar Gage Signal','Transmitted Bar Gage Signal',
       'Transmitted Pulse','Reflected Pulse','Transmitted Pulse')
xlabel('Time (s)','FontSize',18); ylabel('Voltage (V)','FontSize',18)
title('Pulse Orientation','FontSize',18)

% 8 Normalizing Waves

 Convert time arrays into microseconds (s -> us)
t_inc = (inbar(:,1) - inbar(1,1))*1e06;
t_ref = (inbar(:,1) - inbar(1,1))*1e06;
t_tra = (inbar(:,1) - inbar(1,1))*1e06;

 Create Arrays for only Pulse Segment
l=0;
```

```
for k = inc_beg:inc_end-1

    l = l+1;

    t_wave_inc(l) = t_inc(k);

    v_wave_inc(l) = v_inc(k);

end


l=0;

for k = ref_beg:ref_end-1

    l = l+1;

    t_wave_ref(l) = t_ref(k);

    v_wave_ref(l) = v_ref(k);

end


l=0;

for k = tra_beg:tra_end-1

    l = l+1;

    t_wave_tra(l) = t_tra(k);

    v_wave_tra(l) = v_tra(k);

end


 Saving length of time array of each wave for later use

inc_size = size(t_wave_inc);

ref_size = size(t_wave_ref);

tra_size = size(t_wave_tra);


 Normalize Wave Start Times to Zero Time - Aligning Beginnings

t_wave_inc = t_wave_inc - t_wave_inc(1);

t_wave_ref = t_wave_ref - t_wave_ref(1);

t_wave_tra = t_wave_tra - t_wave_tra(1);
```

```
 Plot of aligned pulses
figure(4)
plot(t_wave_inc,v_wave_inc,'g',t_wave_ref,-v_wave_ref,'b',
     t_wave_tra, v_wave_tra,'r','LineWidth',2)
legend('Incident','Reflected','Transmitted')
xlabel('Time (us)','FontSize',18); ylabel('Voltage (V)','FontSize',18)
title('Pulses Overlay','FontSize',18)

 Times are now a percent of the total time of the incident wave
t_nor_inc = t_wave_inc / max(t_wave_inc);
t_nor_ref = t_wave_ref / max(t_wave_inc);
t_nor_tra = t_wave_tra / max(t_wave_inc);

 Determining the shortest wave, in order to set limit of integration
if ref_size(2) <= inc_size(2)
    if ref_size(2) >= tra_size(2)
        time_per = t_nor_tra;
    else
        time_per= t_nor_ref;
    end;
else if inc_size(2) <ref_size(2)
        if inc_size(2) < tra_size(2)
            time_per = t_nor_inc;
        else
            time_per = t_nor_tra;
        end;
    end;
end;
```

Time array ends with the shortest wave

```
time = time_per.*max(t_wave_inc);
t_end = size(time);
```

9 Compare the Simulated Transmitted Wave from Theory with Experimental

```
F = (rho_bar * c_bar * A_bar) / (rho_spec * c_spec * A_spec);
v_wave_tra_g = 4 * F / (1 + F)^2 * v_wave_inc;
t_wave_tra_g = t_wave_inc;

figure(7)
plot(t_wave_tra_g,v_wave_tra_g,'r',t_wave_tra,v_wave_tra,'g')
legend('Theoretical','Measured-Shifted');
```

10 Calculating Specimen Stress, Strainrate and Strain

Calculating the strain values from each gage, over the entire wave

```
strain_inc = (v_wave_inc/v_exc)*(4/2.11)*(num_gage_inc/gain);
strain_ref = (v_wave_ref/v_exc)*(4/2.11)*(num_gage_inc/gain);
strain_tra = (v_wave_tra/v_exc)*(4/2.11)*(num_gage_tra/gain);

for k=1:t_end(2)
    force_inc(k) = E_steel * (strain_inc(k)) * pi * d_bar^2 / 4;
    force_ref(k) = E_steel * (strain_ref(k)) * pi * d_bar^2 / 4;
    force_1(k) = E_steel * (strain_inc(k) + strain_ref(k)) * pi
                 * d_bar^2 / 4;
    force_tra(k) = E_al * (strain_tra(k)) * pi * d_bar^2 / 4;
    ref_theo(k) = force_inc(k)-force_tra(k);
```

```
    error(k) = ref_theo(k) + force_ref(k);
end


 Equilibrium Check Plot
 Trans/Spec is linearly related to the Transmitted pulse.
figure(5)
plot(time, force_inc,’g’, time, -force_ref, ’b’, time, force_1,
     ’k’, time,force_tra,’r’, time, ref_theo, ’b--’, time, error,
     ’c’,’Linewidth’,2)
legend(’Incident’,’Reflected’,’Force Inc/Spec’,’Force Trans/Spec’,
     ’Theo Reflected’,’Error in Ref’);
xlabel(’Time (us)’,’FontSize’,18); ylabel(’Voltage (V)’,’FontSize’,18)
title(’Equilibrium Check’,’FontSize’,18)


 Calculating Stress - Non-uniform and Uniform Deformation
for k = 1:t_end(2)
    stress(k)=  1/2*(A_bar/A_spec)* (E_al*strain_tra(k)+(E_steel*
    (strain_inc(k)+strain_ref(k))));
    stress_uni(k) = E_al * (A_bar/A_spec) * strain_tra(k);
end


 Calculating Strainrate - Non-uniform and Uniform Deformation
for k = 1:t_end(2)
    strainrate(k) =  -2 * v_sound / l_spec * (strain_ref(k));
    strainrate_uni(k) = -2 * v_sound / l_spec * (strain_ref(k));
end


Calculating Strain in the Specimen-Non-uniform and Uniform Deformation
strinc= cumtrapz(time,v_wave_inc(1:t_end(2)));
```

```
strref = cumtrapz(time,v_wave_ref(1:t_end(2)));
for k = 1:t_end(2)
    strain(k) = ((v_sound/l_spec-E_steel/E_al*v_sound_al/l_spec)*
    strinc(k)/v_exc* (4/2.11) * 1/gain)-((v_sound/l_spec+E_steel/E_al*
    v_sound_al/l_spec)* strref(k)/v_exc* (4/2.11) * 1/gain);
    strain_uni(k) = ((v_sound/l_spec-E_steel/E_al*v_sound_al/l_spec)*
    strinc(k)/v_exc* (4/2.11) * 1/gain)-((v_sound/l_spec+E_steel/E_al*
    v_sound_al/l_spec)* strref(k)/v_exc* (4/2.11) * 1/gain);;
end
```

11 Polynomial Fitting of Stress and Strainrate Data

This will also include shifting of data to go through origin for stress-strain curve

Setting up arrays for polynomial fitting

```
A=size(strain);
for i=1:A(1,2)
    strain_poly(i,1)=strain(1,i)*1e-06-strain(1,1)*1e-06;
    strain_poly_uni(i,1)=strain_uni(1,i)*-1e-06-strain_uni(1,1)*-1e-06;
    stress_poly(i,1)=stress(1,i)*1e-06-stress(1,1)*1e-06;
    strainrate_poly(i,1)=strainrate(1,i)*1-strainrate(1,1)*1;
    stress_poly_uni(i,1)=stress_uni(1,i)*1e-06-stress_uni(1,1)*1e-06;
    strainrate_poly_uni(i,1)=strainrate_uni(1,i)-strainrate_uni(1,1);
end
```

Polyfit Stress and Strainrate

```
A=polyfit(strain_poly,stress_poly,10);
stress_poly_new=polyval(A,strain_poly);
```

```
B=polyfit(strain_poly,strainrate_poly,10);
strainrate_poly_new=polyval(B,strain_poly);
C=polyfit(strain_poly_uni,stress_poly_uni,10);
stress_poly_uni_new=polyval(C,strain_poly_uni);
D=polyfit(strain_poly_uni,strainrate_poly_uni,10);
strainrate_poly_uni_new=polyval(D,strain_poly_uni);
```

12 Plotting Stress-Strain and Strainrate-Strain Curves

```
 Finding max values for axes limits
stress_limit = max(stress_poly_new);
strain_limit = max(strain_poly);
strainrate_limit = max(strainrate_poly_new);

 Plotting original and poly/shifted stress-strain curves
figure(6)
hold on;
plot(strain*1e-06, stress*1e-06,'b')
xxx=smooth(strain, 1000)
yyy=smooth(stress, 1000)
plot(xxx*1e-06, yyy*1e-06,'r')
plot(strain_poly,stress_poly_new,'r','Linewidth',2)
plot(strain_uni*1e-06, stress_uni*1e-06,'k','Linewidth',2)
axis([0 strain_limit 0 stress_limit])
xlabel('Strain(-)','FontSize',18); ylabel('Stress(MPa)','FontSize',18);
title('Stress-Strain Polynomial Fit and Shift','Fontsize',18)
legend('Original','Polynomial Fit + Shifted')

 Plotting original and poly/shifted strainrate-strain curves
```

```
figure(7)
hold on;
plot(strain*1e-06, strainrate*1,’b’)
plot(strain_poly,strainrate_poly_new,’r’,’Linewidth’,2)
plot(strain_uni*1e-06, strainrate_uni*1,’k’)
axis([0 strain_limit 0 strainrate_limit])
xlabel(’Strain(-)’,’FontSize’,18); ylabel(’Strainrate(-/s)’,
       ’FontSize’,18);
title(’Strainrate-Strain Polynomial Fit and Shift’,’Fontsize’,18)
legend(’Original’,’Polynomial Fit + Shifted’)

figure(8)
hold on;
plot(time,strain*1e-06,’b’)
axis([0 200 0 strain_limit])
xlabel(’Time(us)’,’FontSize’,18); ylabel(’Strain(-)’,’FontSize’,18);
title(’Strain-Time History’,’Fontsize’,18)


13 Data Read Out - Non-uniform
for k = 1:t_end(2)
    data_saved(k,1) = time(k);                      us
    data_saved(k,2) = strain_poly(k,1);             (-)
    data_saved(k,3) = stress_poly_new(k,1);         MPa
    data_saved(k,4) = strainrate_poly_new(k,1);     (-/s)
    data_saved(k,5) = strain_poly_uni(k,1);         (-)
    data_saved(k,6) = stress_poly_uni_new(k,1);     MPa
    data_saved(k,7) = strainrate_poly_uni_new(k,1); (-/s)
    data_saved(k,8) = strain(k)*1e-06;              (-)
```

```
    data_saved(k,9) = stress(k)*1e-06;               MPa
end



csvwrite('######-out.csv',data_saved,0,0);
```

B.3 MatLab Script for Optical Fiber Volume Fraction Measurement

```
clear all

close all

clc




I=imread ('####.jpg');

%If your image is in RGB then you need to convert!

%J=rgb2gray(I);

J=imcrop(I);

%Sharpen Image

H=fspecial('unsharp');

S=imfilter(J,H,'replicate');

%Find Cut off level

level=graythresh(S);

K=im2bw(S,level-.1);

% [X,map] = imread('trees.tif');

% gmap = rgb2gray(map);

% figure, imshow(X,map), figure, imshow(X,gmap


scrsz = get(0,'ScreenSize');


figure('Position',[scrsz(3)/4 scrsz(4)/3 scrsz(3)/2 scrsz(4)/2])

ax(1)= subplot(1,2,1);

imshow(S);

ax(2)=subplot(1,2,2);
```

```
imshow(K);

histo=imhist(K);

Vol_Fiber=histo(2,1)/(histo(1,1)+histo(2,1
```

B.4 Python Script for Periodic Boundary Conditions

```
##def applyPBC():

if 1:


    from abaqus import *

    from abaqusConstants import *

    import __main__

    import section

    import regionToolset

    import displayGroupMdbToolset as dgm

    import part

    import material

    import assembly

    import step

    import interaction

    import load

    import mesh

    import job

    import sketch

    import visualization

    import xyPlot

    import displayGroupOdbToolset as dgo

    import connectorBehavior


    #from sys import path

    #path.append('C:\Python24\Lib\site-packages')

    #from numpy import *


    modelName='Smaller RUC'
```

```
partName='Part-6'


#'clean up'
for key in mdb.models[modelName].parts[partName].sets.keys():
    if 'nodes' in key:
        del mdb.models[modelName].parts[partName].sets[key]
for key in mdb.models[modelName].constraints.keys():
    if 'PBCConstraint' in key:
        del mdb.models[modelName].constraints[key]



#Tolerance for matching nodes
tol=2e-5


nodes={
    'x0':mdb.models[modelName].parts[partName].sets['setx0'].nodes,
    'x1':mdb.models[modelName].parts[partName].sets['setx1'].nodes,
    'y0':mdb.models[modelName].parts[partName].sets['sety0'].nodes,
    'y1':mdb.models[modelName].parts[partName].sets['sety1'].nodes}


if not len(nodes['x0'])==len(nodes['x1']):
    #or not len(nodes['y0'])==len(nodes['y1'])
    or not len(nodes['z0'])==len(nodes['z1']):
    print 'Warning: number of nodes is different'
    print len(nodes['y0']), len(nodes['y1'])
    raise KeyboardInterrupt


#check that bottom left is (0,0)
allNodes=mdb.models[modelName].parts[partName].nodes
```

```
xmin=1e9
ymin=1e9
zmin=1e9
for i in range(len(allNodes)):
    coord=allNodes[i].coordinates
    xmin=min(xmin,coord[0])
    ymin=min(ymin,coord[1])
    zmin=min(zmin,coord[2])
if xmin<-tol or ymin<-tol or zmin<-tol:
    print 'Warning: Corner not at (0,0,0)'
    raise KeyboardInterrupt



#Side length of the brick/ rectangle
sideLength={'x':0.0,'y':0.0,'z':0.0}
#For readibility...
for node in nodes['x1']:
        sideLength['x']=max(node.coordinates[0],sideLength['x'])
for node in nodes['y1']:
        sideLength['y']=max(node.coordinates[1],sideLength['y'])
#for node in nodes['z1']:
        #sideLength['z']=max(node.coordinates[2],sideLength['z'])

print 'lx='+str(sideLength['x'])+', ly='+str(sideLength['y'])+ ',
lz='+ str(sideLength['z'])

p=mdb.models[modelName].parts[partName]

nodesLib={'x0':{},'x1':{},'y0':{},'y1':{},'z0':{},'z1':{}}
```

```
#create the sets and note down their names and coordinates
for key in nodes.keys():
    for i in range(len(nodes[key])):
        myNode=nodes[key][i:i+1]
        myLabel=nodes[key][i].label
        p.Set(nodes=myNode, name=key+'nodes'+str(myLabel))
        nodesLib[key][myLabel]=nodes[key][i].coordinates


import sets
# | union, & intersection, - difference
#find the faces
noEdge={}
noEdge['x']=list((set(nodesLib['x0'].keys())|set(nodesLib['x1']
    .keys()))-(set(nodesLib['y0'].keys())|set(nodesLib['y1']
    .keys())|set(nodesLib['z0'].keys())|set(nodesLib['z1']
    .keys())))
noEdge['y']=list((set(nodesLib['y0'].keys())|set(nodesLib['y1']
    .keys()))-(set(nodesLib['x0'].keys())|set(nodesLib['x1']
    .keys())|set(nodesLib['z0'].keys())|set(nodesLib['z1']
    .keys())))
noEdge['z']=list((set(nodesLib['z0'].keys())|set(nodesLib['z1']
    .keys()))-(set(nodesLib['x0'].keys())|set(nodesLib['x1']
    .keys())|set(nodesLib['y0'].keys())|set(nodesLib['y1']
    .keys())))



#find the corners
corners={
```

```
    'x0y0z0':(),
    'x0y0z1':(),
    'x0y1z0':(),
    'x0y1z1':(),
    'x1y0z0':(),
    'x1y0z1':(),
    'x1y1z0':(),
    'x1y1z1':()}

for key in corners.keys():
    corners[key]=list(set(nodesLib[key[0:2]].keys())&set(nodesLib
    [key[2:4]].keys()))[0]

#find the edges
edges={
    'x0y0':(),
    'x0y1':(),
    'x1y0':(),
    'x1y1':(),
    'x0z0':(),
    'x0z1':(),
    'x1z0':(),
    'x1z1':(),
    'y0z0':(),
    'y0z1':(),
    'y1z0':(),
    'y1z1':()}

for key in edges.keys():
```

```
    edges[key]=list((set(nodesLib[key[0:2]].keys())
    &set(nodesLib[key[2:4]].keys()))-set(corners.values()))

pairs={'x':[],'y':[],'z':[]}



#match the nodes
for key in pairs.keys():
    for i in nodesLib[key+'0'].keys():
        if i in noEdge[key]:
            nodesLib1keys=nodesLib[key+'1'].keys()
            for j in nodesLib1keys:
                diff=         abs(nodesLib[key+'1'][j][0]
                -nodesLib[key+'0'][i][0])
                diff=diff+    abs(nodesLib[key+'1'][j][1]
                -nodesLib[key+'0'][i][1])
                diff=diff+    abs(nodesLib[key+'1'][j][2]
                -nodesLib[key+'0'][i][2])
                diff=abs(diff-sideLength[key])
                if diff<tol:
                    pairs[key].append((i,j))
                    break
                #When this is true, the code failed to find
                a partnering node
                # if j==nodesLib1keys[-1]:
                  #  print 'Could not find partnering node',
                   j, i, key
                   # raise KeyboardInterrupt
```

```
constraintNumber=0

#create the equations on faces
myKeys=pairs.keys()
myKeys.sort()
for key in myKeys:
    for i in range(len(pairs[key])):
        name1=partName+'-1.'+key+'1nodes'+str(pairs[key][i][1])
        name0=partName+'-1.'+key+'0nodes'+str(pairs[key][i][0])
        for j in [1,2]:
            mdb.models[modelName].Equation(name='PBCConstraint'+
                str(constraintNumber), terms=(
                (1.0 ,name1, j),
                (-1.0,name0, j),
                (-1.0,'setrp'+key,j)))
            constraintNumber=constraintNumber+1

#create equations on corners
#all nodes are either in x0 or xl
for key in corners.keys():
    if corners[key] in nodesLib['x0'].keys():
        name=partName+'-1.x0nodes'+str(corners[key])
    elif corners[key] in nodesLib['x1'].keys():
        name=partName+'-1.x1nodes'+str(corners[key])
    else:
        print 'Corner keys wrong!'
        raise KeyboardInterrupt
```

```
    for i in [1,2]:
        mdb.models[modelName].Equation(name='PBCConstraint'+
            str(constraintNumber), terms=(
            (1.0 ,name, i),
            (-float(key[1]),'setrpx',i),
            (-float(key[3]),'setrpy',i)))
        constraintNumber=constraintNumber+1

#create equations for all edges
for key in edges.keys():
    if key[1]=='0' and key[3]=='0':
        continue
    for nodeNumber in edges[key]:
        name1=partName+'-1.'+key[0:2]+'nodes'+str(nodeNumber)
        #find the corresponding node number in the zero side
        zeroEdgeNodes=edges[key[0]+'0'+key[2]+'0']
        if key[1]=='0':
            myNodesLib=nodesLib[key[2]+'1']
        else:
            myNodesLib=nodesLib[key[0]+'1']

        for zeroEdgeNode in zeroEdgeNodes:
            diff=abs(abs(myNodesLib[nodeNumber][0]-
                nodesLib[key[0]+'0'][zeroEdgeNode][0])
            +abs(myNodesLib[nodeNumber][1]-nodesLib[key[0]+'0']
            [zeroEdgeNode][1])
            +abs(myNodesLib[nodeNumber][2]-nodesLib[key[0]+'0']
            [zeroEdgeNode][2])
            -sideLength[key[0]]*float(key[1])-sideLength[key[2]]
```

```
                        *float(key[3]))
                if diff<tol:
                    name0=partName+’-1.’+key[0]+’0nodes’
                    +str(zeroEdgeNode)
                    break
                # if zeroEdgeNode==zeroEdgeNodes[-1]:
                  #  print ’Could not match edges nodes’
                   # raise KeyboardInterrupt
            rpname0=’setrp’+key[0]
            rpname1=’setrp’+key[2]
            coeff0=-float(key[1])
            coeff1=-float(key[3])

            for j in [1,2]:
                mdb.models[modelName].Equation(name=’PBCConstraint’
                +str(constraintNumber), terms=(
                    (1.0 ,name1, j),
                    (-1.0 ,name0, j),
                    (coeff0,rpname0,j),
                    (coeff1,rpname1,j)))
                constraintNumber=constraintNumber+1
    print ’\n\n\nfinished’

##if __name__ == "__main__":
##    applyPBC()
```

BIBLIOGRAPHY

BIBLIOGRAPHY

[1] *Atlas of Stress-Strain Curves.* ASM-International, 2002.

[2] Jeffrey A. Acheson, Pavel Simacek, and Suresh G. Advani. The implications of fiber compaction and saturation on fully coupled vartm simulation. *Composites Part A: Applied Science and Manufacturing*, 35(2):159 – 169, 2004.

[3] Haider Al-Zubaidy, Xiao-Ling Zhao, and Riadh Al-Mahaidi. Mechanical characterisation of the dynamic tensile properties of cfrp sheet and adhesive at medium strain rates. *Composite Structures*, 96:153–164, 2013.

[4] A.E. Armenkas and C.A. Sciammarella. Response of glass-fiber-reinforced epoxy specimens to high rates of tensile loading. *Experimental Mechanics*, 13(10):433–440, 1973.

[5] R.C. Batra and N.M. Hassan. Response of fiber reinforced composites to underwater explosive loads. *Composites Part B: Engineering*, 38(4):448 – 468, 2007.

[6] Brett A. Bednarcyk, Bertram Stier, Jaan-W. Simon, Stefanie Reese, and Evan J. Pineda. Meso- and micro-scale modeling of damage in plain weave composites. *Composite Structures*, 121(0):258 – 270, 2015.

[7] D. Bonorchis and G.N. Nurick. The effect of welded boundaries on the response of rectangular hot-rolled mild steel plates subjected to localised blast loading. *International Journal of Impact Engineering*, 34(11):1729 – 1738, 2007.

[8] P. Broomhead and RJ Grieve. The effect of strain rate on the strain to fracture of sheet steel under biaxial tensile stress conditions. *Journal of Engineering Materials and Technology*, 104:101–106, 1982.

[9] Chamis and Smith. Environmental and high strain rate effects on composites for engine applications. *AIAA Journal*, 22:128–134, 1864.

[10] Weinong W. Chen and Bo Song. *Split Hopkinson (Kolsky) Bar-Design, Testing and Applications.* Springer.

[11] Y. Chen, A.H. Clausen, O.S. Hopperstad, and M. Langseth. Stressstrain behaviour of aluminium alloys at a wide range of strain rates. *International Journal of Solids and Structures*, 46(21):3825 – 3835, 2009.

[12] Seong Sik Cheon, Tae Seong Lim, and Dai Gil Lee. Impact energy absorption characteristics of glass fiber hybrid composites. *Composite structures*, 46(3):267–278, 1999.

[13] RM Christensen and FM Waals. Effective stiffness of randomly oriented fibre composites. *Journal of Composite Materials*, 6(3):518–535, 1972.

[14] R.M. Davies. A critical study of the hopkinson pressure bar. *Proc. R. Soc.*, A240:375–457, 1948.

[15] H Eskandari and JA Nemes. Dynamic testing of composite laminates with a tensile split hopkinson bar. *Journal of composite materials*, 34(4):260–273, 2000.

[16] American Society for Testing and Materials. Astm d3039: Standard test method for tensile properties of polymer matrix composites, 2000.

[17] American Society for Testing and Materials. Astm d638: Standard test method for tensile properties of plastics, 2002.

[18] American Society for Testing and Materials. Astm d695: Standard test method for compressive properties of rigid plastics, 2008.

[19] V.K. Ganesh and N.K. Naik. Failure behaviour of plain weave fabric laminates under in-plane shear loading: effect of fabric geometry. *Composite Structures*, 30(2):179 – 192, 1995.

[20] Robert Gerlach, Clive R Siviour, Jens Wiegand, and Nik Petrinic. In-plane and through-thickness properties, failure modes, damage and delamination in 3d woven carbon fibre composites subjected to impact loading. *Composites Science and Technology*, 72(3):397–411, 2012.

[21] A. Gilat, T.E. Schmidt, and A.L. Walker. Full field strain measurement in compression and tensile split hopkinson bar experiments. *Experimental Mechanics*, 49(2):291–302, 2009.

[22] Amos Gilat, Robert K Goldberg, and Gary D Roberts. Experimental study of strain-rate-dependent behavior of carbon/epoxy composite. *Composites Science and Technology*, 62(10):1469–1476, 2002.

[23] Carlos Gonzalez and Javier LLorca. Mechanical behavior of unidirectional fiber-reinforced polymers under transverse compression: Microscopic mechanisms and modeling. *Composites Science and Technology*, 67(13):2795 – 2806, 2007.

[24] Yasser A. Gowayed, Christopher Pastore, and Carl S. Howarth. Modification and application of a unit cell continuum model to predict the elastic properties of textile composites. *Composites Part A: Applied Science and Manufacturing*, 27(2):149 – 155, 1996.

[25] V Grolleau, G Gary, and D Mohr. Biaxial testing of sheet materials at high strain rates using viscoelastic bars. *Experimental Mechanics*, 48:293–306, 2008.

[26] W.G. Guo, X.Q. Zhang, J. Su, Y. Su, Z.Y. Zeng, and X.J. Shao. The characteristics of plastic flow and a physically-based model for 3003 almn alloy upon a wide range of strain rates and temperatures. *European Journal of Mechanics - A/Solids*, 30(1):54 – 62, 2011.

[27] AL-Zubaidy Haider, Xiao-Ling Zhao, and Riadh Al-Mihaidi. Mechanical behaviour of normal modulus carbon fibre reinforced polymer (cfrp) and epoxy under impact tensile loads. *Procedia Engineering*, 10:2453–2458, 2011.

[28] J Harding and LM Welsh. *Impact testing of fibre reinforced composite materials.* University of Oxford Department of Engineering Science, 1982.

[29] J. Harding and L.M. Welsh. A tensile testing technique for fibre-reinforced composites at impact rates of strain. *Journal of Materials Science*, 18(6):1810–1826, 1983.

[30] Steven Van Hayes and DF Adams. Rate sensitive tensile impact properties of fully and partially loaded unidirectional composites. *Journal of Testing and Evaluation*, 10:61–68, 1982.

[31] C Heinrich, M Aldridge, AS Wineman, J Kieffer, AM Waas, and K Shahwan. The influence of the representative volume element (rve) size on the homogenized response of cured fiber composites. *Modelling and Simulation in Materials Science and Engineering*, 20(7):075007, 2012.

[32] Christian Heinrich and Anthony M Waas. Investigation of progressive damage and fracture in laminated composites using the smeared crack approach. In *53rd AIAA/ASME/ASCE/AHS/ASC Structures, Structural Dynamics and Materials Conference 20th AIAA/ASME/AHS Adaptive Structures Conference 14th AIAA*, 2012.

[33] C.T. Herakovich. *Mechanics of Fibrous Composites.* Wiley, 1997.

[34] Hexcel. Hextow im7 carbon fiber. Electronic.

[35] C.P. Hinesley and J.G. Morris. The effect of structure on the strain rate sensitivity of 3003 al-mn alloy. *Materials Science and Engineering*, 6(1):48 – 54, 1970.

[36] Bertram Hopkinson. A method of measuring the pressure produced in the detonation of high explosives or by the impact of bullets. *Philosophical Transactions of the Royal Society*, A213:437–456, 1914.

[37] John Hopkinson. Further experiments on the rupture of iron wire (1872). *Original Papers-by the late John Hopkinson*, 2, 1901.

[38] Hsengji Huang and Anthony M Waas. Compressive response of z-pinned woven glass fiber textile composite laminates: Modeling and computations. *Composites Science and Technology*, 69(14):2338–2344, 2009.

[39] Werner Hufenbach, Maik Gude, and Christoph Ebert. Hybrid 3d-textile reinforced composites with tailored property profiles for crash and impact applications. *Composites Science and Technology*, 69(9):1422–1426, 2009.

[40] H Huh, WJ Kang, and SS Han. A tension split hopkinson bar for investigating the dynamic behavior of sheet metals. *Experimental Mechanics*, 42(1):8–17, 2002.

[41] G.T. Gray III and J.C. Huang. Influence of repeated shock loading on the substructure evolution of 99.99 wt. *Materials Science and Engineering: A*, 145(1):21 – 35, 1991.

[42] Matthew Jackson and Arun Shukla. Performance of sandwich composites subjected to sequential impact and air blast loading. *Composites Part B: Engineering*, 42(2):155 – 166, 2011.

[43] George C Jacob, J Michael Starbuck, John F Fellers, Srdan Simunovic, and Raymond G Boeman. Strain rate effects on the mechanical properties of polymer composite materials. *Journal of Applied Polymer Science*, 94(1):296–301, 2004.

[44] Donald R. Jones. *Encyclopedia of Optimization.* Kluwer Academic Publishers, 1999.

[45] B Justusson, M Pankow, C Heinrich, M Rudolph, and AM Waas. Use of a shock tube to determine the bi-axial yield of an aluminum alloy under high rates. *International Journal of Impact Engineering*, 58:55–65, 2013.

[46] Ryan L. Karkkainen and Bhavani V. Sankar. A direct micromechanics method for analysis of failure initiation of plain weave textile composites. *Composites Science and Technology*, 66(1):137 – 150, 2006.

[47] Subhash C Khatri and Michael J Koczak. Thick-section as4-graphite/e-glass/pps hybrid composites: Part i. tensile behavior. *Composites science and technology*, 56(2):181–192, 1996.

[48] Zachary T Kier, Amit Salvi, Geoffrey Theis, Anthony M Waas, and Khaled Shahwan. Estimating mechanical properties of 2d triaxially braided textile composites based on microstructure properties. *Composites Part B: Engineering*, 68:288–299, 2015.

[49] H Kimura, M Itabashi, and K Kawata. Mechanical characterization of unidirectional cfrp thin strip and cfrp cables under quasi-static and dynamic tension. *Advanced Composite Materials*, 10(2-3):177–187, 2001.

[50] H Kolsky. An investigation of the mechanical properties of materials at very high rates of loading. *Proceedings of the Physical Society. Section B*, 62(11):676, 1949.

[51] Nina Kuentzer, Pavel Simacek, Suresh G. Advani, and Shawn Walsh. Correlation of void distribution to vartm manufacturing techniques. *Composites Part A: Applied Science and Manufacturing*, 38(3):802 – 813, 2007.

[52] Eric J. Lang and Tsu-Wei Chou. The effect of strain gage size on measurement errors in textile composite materials. *Composites Science and Technology*, 58(34):539 – 548, 1998.

[53] James LeBlanc and Arun Shukla. Dynamic response and damage evolution in composite materials subjected to underwater explosive loading: An experimental and computational study. *Composite Structures*, 92(10):2421 – 2430, 2010.

[54] James LeBlanc and Arun Shukla. Dynamic response of curved composite panels to underwater explosive loading: Experimental and computational comparisons. *Composite Structures*, 93(11):3072 – 3081, 2011.

[55] James LeBlanc, Arun Shukla, Carl Rousseau, and Alexander Bogdanovich. Shock loading of three-dimensional woven composite materials. *Composite Structures*, 79(3):344 – 355, 2007.

[56] M.M. LeBlanc and D.H. Lassila. Dynamic tensile testing of sheet material using the split-hopkinson bar technique. *Experimental Techniques*, 17(1):37–42, 1993.

[57] Hu S. Liu, X. Wave propagation characteristics in cone bars used for variable cross-sectional shpb. *Explosion and Shockwaves*, 20:110–114, 2000.

[58] DJ Lloyd. The deformation of commercial aluminum-magnesium alloys. *Metallurgical Transactions A*, 11(8):1287–1294, 1980.

[59] Stepan V. Lomov, Dmitry S. Ivanov, Ignaas Verpoest, Masaru Zako, Tetsusei Kurashiki, Hiroaki Nakai, and Satoru Hirosawa. Meso-fe modelling of textile composites: Road map, data flow and algorithms. *Composites Science and Technology*, 67(9):1870 – 1891, 2007.

[60] S.V. Lomov, A.V. Gusakov, G. Huysmans, A. Prodromou, and I. Verpoest. Textile geometry preprocessor for meso-mechanical models of woven composites. *Composites Science and Technology*, 60(11):2083 – 2095, 2000.

[61] S.V. Lomov, G. Huysmans, Y. Luo, R.S. Parnas, A. Prodromou, I. Verpoest, and F.R. Phelan. Textile composites: modelling strategies. *Composites Part A: Applied Science and Manufacturing*, 32(10):1379 – 1394, 2001.

[62] G Marom, E Drukker, A Weinberg, and J Banbaji. Impact behaviour of carbon/kevlar hybrid composites. *Composites*, 17(2):150–153, 1986.

[63] AGY Advance Materials. S-series high performance materials. Electronic.

[64] Kansas State University Fabric Mechanics. Digital fabric mechanics analyzer.

[65] R. Moulart, F. Pierron, S.R. Hallett, and M.R. Wisnom. Full-field strain measurement and identification of composites moduli at high strain rate with the virtual fields method. *Experimental Mechanics*, 51(4):509–536, 2011.

[66] A.P. Mouritz. The damage to stitched {GRP} laminates by underwater explosion shock loading. *Composites Science and Technology*, 55(4):365 – 374, 1995.

[67] A.P. Mouritz. The effect of underwater explosion shock loading on the fatigue behaviour of grp laminates. *Composites*, 26(1):3 – 9, 1995.

[68] A.D. Mulliken and M.C. Boyce. Mechanics of the rate-dependent elasticplastic deformation of glassy polymers from low to high strain rates. *International Journal of Solids and Structures*, 43(5):1331 – 1356, 2006.

[69] N.K. Naik and V.K. Ganesh. Prediction of on-axes elastic properties of plain weave fabric composites. *Composites Science and Technology*, 45(2):135 – 152, 1992.

[70] N.K. Naik and V.K. Ganesh. Prediction of thermal expansion coefficients of plain weave fabric composites. *Composite Structures*, 26(34):139 – 154, 1993.

[71] S. Nemat-Nasser. *Introduction to High Strain Rate Testing*, volume 8 of *ASM Handbook*. ASM International, 2000.

[72] Wei H. Ng, Amit G. Salvi, and Anthony M. Waas. Characterization of the in-situ non-linear shear response of laminated fiber-reinforced composites. *Composites Science and Technology*, 70(7):1126 – 1134, 2010. Special issue on Chiral Smart Honeycombs.

[73] Qiong-Gong Ning and Tsu-Wei Chou. Closed-form solutions of the in-plane effective thermal conductivities of woven-fabric composites. *Composites Science and Technology*, 55(1):41 – 48, 1995.

[74] Qiong-Gong Ning and Tsu-Wei Chou. A general analytical model for predicting the transverse effective thermal conductivities of woven fabric composites. *Composites Part A: Applied Science and Manufacturing*, 29(3):315 – 322, 1998.

[75] Suppliers of Advanced Composite Materials Association. Tensile properties of oriented cross-plied fiber-resin composites, 1994.

[76] University of Nottingham Textile Composite Research. Texgen.

[77] L. Djapic Oosterkamp, A. Ivankovic, and G. Venizelos. High strain rate properties of selected aluminium alloys. *Materials Science and Engineering: A*, 278(12):225 – 235, 2000.

[78] Anthony Owens. Development of a split hopkinson tension bar for testing stress-strain response of particulate composites under high rates of loading. 2007.

[79] M. Pankow, B. Justusson, A. Salvi, A.M. Waas, Chian-Fong Yen, and Seth Ghiorse. Shock response of 3d woven composites: An experimental investigation. *Composite Structures*, 93(5):1337 – 1346, 2011.

[80] M Pankow, A Salvi, AM Waas, CF Yen, and S Ghiorse. Resistance to delamination of 3d woven textile composites evaluated using end notch flexure (enf) tests: Experimental results. *Composites Part A: Applied Science and Manufacturing*, 42(10):1463–1476, 2011.

[81] M Pankow, A Salvi, AM Waas, CF Yen, and S Ghiorse. Split hopkinson pressure bar testing of 3d woven composites. *Composites Science and Technology*, 71(9):1196–1208, 2011.

[82] M. Pankow, A.M. Waas, Chian-Fong Yen, and Seth Ghiorse. Shock loading of 3d woven composites: A validated finite element investigation. *Composite Structures*, 93(5):1347 – 1362, 2011.

[83] Mark Pankow. *The Deformation Respose of 3D Woven Composites Subjected to High Rates of Loading.* PhD thesis, University of MIchigan, 2010.

[84] Mark Pankow, Brian Justusson, and Anthony M Waas. Three-dimensional digital image correlation technique using single high-speed camera for measuring large out-of-plane displacements at high framing rates. *Applied Optics*, 17:3418–3427, 2010.

[85] Mark Pankow, Anthony M Waas, and Brett Bednarcyk. Blast loading of epoxy panels using a shock tube. Technical report, NASA/TM2010-216941, 2010.

[86] Anthony K. Pickett, Thomas Pyttel, Fabrice Payen, Franck Lauro, Nikica Petrinic, Heinz Werner, and Jens Christlein. Failure prediction for advanced crashworthiness of transportation vehicles. *International Journal of Impact Engineering*, 30(7):853 – 872, 2004. ¡ce:title¿Fifth International Symposium on Impact Engineering¡/ce:title¿.

[87] Peter B Pollock. Tensile failure in 2-d carbon-carbon composites. *Carbon*, 28(5):717 – 732, 1990.

[88] Shu Ching Quek, Anthony Waas, Khaled W Shahwan, and Venkatesh Agaram. Compressive response and failure of braided textile composites: Part 2computations. *International Journal of Non-Linear Mechanics*, 39(4):649–663, 2004.

[89] Shu Ching Quek, Anthony M Waas, Khaled W Shahwan, and Venkatesh Agaram. Compressive response and failure of braided textile composites: Part 1experiments. *International Journal of Non-Linear Mechanics*, 39(4):635–648, 2004.

[90] JP Quinn, AT McIlhagger, and R McIlhagger. Examination of the failure of 3d woven composites. *Composites Part A: Applied Science and Manufacturing*, 39(2):273–283, 2008.

[91] Maziar Ramezani and Zaidi Mohd Ripin. Combined experimental and numerical analysis of bulge test at high strain rates using split hopkinson pressure bar apparatus. *Journal of Materials Processing Technology*, 210(8):1061 – 1069, 2010.

[92] Ethirajan Rathakrishnan. *Applied Gas Dynamics*. John Wiley and Sons, 2010.

[93] Jan G Rots. Smeared and discrete representations of localized fracture. In *Current Trends in Concrete Fracture Research*, pages 45–59. Springer, 1991.

[94] JG Rots, P Nauta, GMA Kuster, and J Blaauwendraad. Smeared crack approach and fracture localization in concrete. *HERON, 30 (1), 1985*, 1985.

[95] S. K. Malhotra Sabu Thomas, Kuruvilla Joseph. *Polymer Composites: Volume I: Macro- and Microcomposites*. Wiley, 2012.

[96] Bhavani V. Sankar and Ramesh V. Marrey. A unit-cell model of textile composite beams for predicting stiffness properties. *Composites Science and Technology*, 49(1):61 – 69, 1993.

[97] Bhavani V. Sankar and Ramesh V. Marrey. Analytical method for micromechanics of textile composites. *Composites Science and Technology*, 57(6):703 – 713, 1997.

[98] A. Schiffer and V.L. Tagarielli. The response of circular composite plates to underwater blast: Experiments and modelling. *Journal of Fluids and Structures*, 52(0):130 – 144, 2015.

[99] Mahmood M. Shokrieh and Majid Jamal Omidi. Tension behavior of unidirectional glass/epoxy composites under different strain rates. *Composite Structures*, 88(4):595 – 601, 2009.

[100] Simulia. Abaqus/explict 6.10, 2010.

[101] R. Smerd, S. Winkler, C. Salisbury, M. Worswick, D. Lloyd, and M. Finn. High strain rate tensile testing of automotive aluminum alloy sheet. *International Journal of Impact Engineering*, 32(14):541 – 560, 2005. ¡ce:title¿Fifth International Symposium on Impact Engineering¡/ce:title¿.

[102] Shunjun Song, Anthony M Waas, Khaled W Shahwan, Omar Faruque, and Xinran Xiao. Compression response of 2d braided textile composites: single cell and multiple cell micromechanics based strength predictions. *Journal of composite materials*, 2008.

[103] Shunjun Song, Anthony M Waas, Khaled W Shahwan, Xinran Xiao, and Omar Faruque. Braided textile composites under compressive loads: modeling the response, strength and degradation. *Composites Science and Technology*, 67(15):3059–3070, 2007.

[104] Kanthikannan Srirengan, John Whitcomb, and Clinton Chapman. Modal technique for three-dimensional global/ local stress analysis of plain weave composites. *Composite Structures*, 39(12):145 – 156, 1997.

[105] George H Staab and Amos Gilat. High strain rate characterization of angle-ply glass/epoxy laminates. In *Proceedings of the Ninth International Conference on Composite Materials: ICCM-9: Metal Matrix Composites*, volume 1. McGraw Hill Professional, 1993.

[106] George H Staab and Amos Gilat. High strain rate response of angle-ply glass/epoxy laminates. *Journal of Composite Materials*, 29(10):1308–1320, 1995.

[107] G.H. Staab and A. Gilat. A direct-tension split hopkinson bar for high strain-rate testing. *Experimental Mechanics*, 31(3):232–235, 1991.

[108] Fredrik Stig and Stefan Hallström. Spatial modelling of 3d-woven textiles. *Composite Structures*, 94(5):1495–1502, 2012.

[109] M. Stoffel, R. Schmidt, and D. Weichert. Shock wave-loaded plates. *International Journal of Solids and Structures*, 38(4243):7659 – 7680, 2001.

[110] Marcus Stoffel. Experimental validation of anisotropic ductile damage and failure of shock wave-loaded plates. *European Journal of Mechanics - A/Solids*, 26(4):592 – 610, 2007.

[111] Norihiko Taniguchi, Tsuyoshi Nishiwaki, and Hiroyuki Kawada. Experimental characterization of dynamic tensile strength in unidirectional carbon/epoxy composites. *Advanced Composite Materials*, 17(2):139–156, 2008.

[112] GOM Optical Measuring Techniques. Aramis v6.11. Computer Software, 2012.

[113] Srinivasan Arjun Tekalur, Alexander E. Bogdanovich, and Arun Shukla. Shock loading response of sandwich panels with 3-d woven e-glass composite skins and stitched foam core. *Composites Science and Technology*, 69(6):736 – 753, 2009. {ONR} - Dynamic Failure and Durability.

[114] Srinivasan Arjun Tekalur, Kunigal Shivakumar, and Arun Shukla. Mechanical behavior and damage evolution in e-glass vinyl ester and carbon composites subjected to static and blast loads. *Composites Part B: Engineering*, 39(1):57 – 65, 2008. Marine Composites and Sandwich Structures.

[115] Srinivasan Arjun Tekalur, Arun Shukla, and Kunigal Shivakumar. Blast resistance of polyurea based layered composite materials. *Composite Structures*, 84(3):271 – 281, 2008.

[116] Vikrant Tiwari, Michael A. Sutton, S.R. McNeill, Shaowen Xu, Xiaomin Deng, William L. Fourney, and Damien Bretall. Application of 3d image correlation for full-field transient plate deformation measurements during blast loading. *International Journal of Impact Engineering*, 36(6):862 – 874, 2009.

[117] Erheng Wang, Nate Gardner, and Arun Shukla. The blast resistance of sandwich composites with stepwise graded cores. *International Journal of Solids and Structures*, 46(1819):3492 – 3502, 2009.

[118] Erheng Wang and Arun Shukla. Analytical and experimental evaluation of energies during shock wave loading. *International Journal of Impact Engineering*, 37(12):1188 – 1196, 2010.

[119] John Whitcomb and Kanthikannan Srirengan. Effect of various approximations on predicted progressive failure in plain weave composites. *Composite Structures*, 34(1):13 – 20, 1996.

[120] John Whitcomb, Kanthikannan Srirengan, and Clinton Chapman. Evaluation of homogenization for global/local stress analysis of textile composites. *Composite Structures*, 31(2):137 – 149, 1995.

[121] T. Wierzbicki and G.N. Nurick. Large deformation of thin plates under localised impulsive loading. *International Journal of Impact Engineering*, 18(78):899 – 918, 1996.

[122] Kyeongsik Woo and John D. Whitcomb. Effects of fiber tow misalignment on the engineering properties of plain weave textile composites. *Composite Structures*, 37(34):343 – 355, 1997.

[123] Xcitex. Proanalyst. Computer Software, 2012.

[124] J.R. Xiao, B.A. Gama, and J.W. Gillespie Jr. Progressive damage and delamination in plain weave s-2 glass/sc-15 composites under quasi-static punch-shear loading. *Composite Structures*, 78(2):182 – 196, 2007.

[125] Murat Yazici. Loading rate sensitivity of high strength fibers and fiber/matrix interfaces. *Journal of Reinforced Plastics and Composites*, 2008.

[126] Bekir Yenilmez, Murat Senan, and E. Murat Sozer. Variation of part thickness and compaction pressure in vacuum infusion process. *Composites Science and Technology*, 69(1112):1710 – 1719, 2009. ¡ce:title¿Experimental Techniques and Design in Composite Materials (ETDCM8) with Regular Papers¡/ce:title¿.

[127] S.W. Yurgartis. Techniques for the quantification of composite mesostructure. *Composites Science and Technology*, 53(2):145 – 154, 1995. Mesostructures and Mesomechanics in Fibre Composites.

[128] S.W. Yurgartis, K. Morey, and J. Jortner. Measurement of yarn shape and nesting in plain-weave composites. *Composites Science and Technology*, 46(1):39 – 50, 1993.

[129] Masaru Zako, Yasutomo Uetsuji, and Tetsusei Kurashiki. Finite element analysis of damaged woven fabric composite materials. *Composites Science and Technology*, 63(34):507 – 516, 2003.

[130] Dianyun Zhang. *Progressive Damage and Failure Analysis of 3D Textile Composites Subjected to Flexural Loading*. PhD thesis, University of Michigan, 2014.

[131] Dianyun Zhang and Anthony M Waas. A micromechanics based multiscale model for nonlinear composites. *Acta Mechanica*, 225(4-5):1391–1417, 2014.

[132] Dianyun Zhang, Anthony M Waas, and CF Yen. Progressive damage and failure response of hybrid 3d textile composites subjected to flexural loading: Part ii: Mechanics based multiscale computational modeling of progressive damage and failure. *International Journal of Solids and Structures (In Revision)*, 2015.

[133] Xin Zhang, Hui Li, Hui Li, Hui Gao, Zhi Gao, Ying Liu, and Bo Liu. Dynamic property evaluation of aluminum alloy 2519a by split hopkinson pressure bar. *Transactions of Nonferrous Metals Society of China*, 18(1):1 – 5, 2008.

[134] Yuan Zhou, Zixing Lu, and Zhenyu Yang. Progressive damage analysis and strength prediction of 2d plain weave composites. *Composites Part B: Engineering*, 47(0):220 – 229, 2013.

[135] Yuanxin Zhou, Sajedur Rahman Akanda, Shaik Jeelani, and Thoms E. Lacy. Nonlinear constitutive equation for vapor-grown carbon nano fibers-reinforced sc-15 epoxy at different strain rates. *Material Science and Engineering A*, 465:238–246, 2007.

[136] Yuanxin Zhou, Farhana Pervin, Mohammad A. Biswas, Vijaya K. Rangari, and Shaik Jeelani. Fabrication and characterization of montmorillonite clay-filled sc-15 epoxy. *Materials Letters*, 60(7):869 – 873, 2006.